



**HAL**  
open science

# Manipulation of the illumination of an Adaptive Optics Flood Illumination Ophthalmoscope for functional imaging of the retina in-vivo

Elena Gofas Salas

► **To cite this version:**

Elena Gofas Salas. Manipulation of the illumination of an Adaptive Optics Flood Illumination Ophthalmoscope for functional imaging of the retina in-vivo. Optics / Photonics. Sorbonne Université, 2019. English. NNT: . tel-02489710v1

**HAL Id: tel-02489710**

**<https://theses.hal.science/tel-02489710v1>**

Submitted on 28 Jun 2019 (v1), last revised 24 Feb 2020 (v2)

**HAL** is a multi-disciplinary open access archive for the deposit and dissemination of scientific research documents, whether they are published or not. The documents may come from teaching and research institutions in France or abroad, or from public or private research centers.

L'archive ouverte pluridisciplinaire **HAL**, est destinée au dépôt et à la diffusion de documents scientifiques de niveau recherche, publiés ou non, émanant des établissements d'enseignement et de recherche français ou étrangers, des laboratoires publics ou privés.



# Sorbonne Université

Doctoral School ED 394 : *Physiologie, Physiopathologie et Thérapeutique*

*Institut de la Vision / PARIS Group*

*ONERA- The French Aerospace Lab*

## **Manipulation of the illumination of an Adaptive Optics Flood Illumination Ophthalmoscope for functional imaging of the retina *in-vivo***

By Elena Gofas Salas

Doctoral thesis in Physics

Supervised by Serge Meimon and Michel Paques

Submitted and publicly defended in Paris on January 8<sup>th</sup> 2019

Reviewer :	M.	Arnaud DUBOIS	Institut d'Optique Graduate School
Reviewer:	M.	Claude BOCCARA	ESPCI
Examiner :	M.	Gilles TESSIER	Sorbonne Université
Examiner :	Mme.	Alexandra FRAGOLA	Sorbonne Université
Examiner:	M.	Ethan ROSSI	University of Pittsburgh
Supervisor:	M.	Serge MEIMON	ONERA
Supervisor :	M.	Michel PAQUES	Sorbonne Université



## Declaration of Authorship

I, Elena GOFAS SALAS, declare that this thesis titled, “Manipulation of the illumination of an Adaptive Optics Flood Illumination Ophthalmoscope for functional imaging of the retina *in-vivo*” and the work presented in it are my own. I confirm that:

- This work was done wholly or mainly while in candidature for a research degree at this University.
- Where any part of this thesis has previously been submitted for a degree or any other qualification at this University or any other institution, this has been clearly stated.
- Where I have consulted the published work of others, this is always clearly attributed.
- Where I have quoted from the work of others, the source is always given. With the exception of such quotations, this thesis is entirely my own work.
- I have acknowledged all main sources of help.
- Where the thesis is based on work done by myself jointly with others, I have made clear exactly what was done by others and what I have contributed myself.

Signed:

---

Date:

---



*“The two things in life you are in total control over are your attitude and your effort.”*

Billy Cox



# Abstract

As the only transparent optical window of our body, the eye gives a unique access to the observation of neural and vascular networks. Today however, a new era is opening up for high-resolution imaging, which should no longer be limited to giving access to tissue structures, but may also tackle their functions. In fact, biomarkers for the functioning of the whole human body can be found in retinal imaging. Neurodegenerative diseases (Parkinson's, Alzheimer's) or arterial hypertension could thus be diagnosed early by high precision imaging of the retina. Adaptive optics, applied to retinal imaging as early as 1997, significantly improved the spatial resolution of retinal images, leading to many retinal studies by ophthalmoscopy. In particular, it was coupled with the scanning ophthalmoscope, which became the most popular choice for its superior spatial resolution and in optical sectioning compared to full-field.

However, unlike scanning systems, the full-field ophthalmoscope produces wide-field images with a high rate of acquisition and without distortion. In my thesis work, I intended to show how such a system, associated to imaging modalities adjusting geometrical settings of the illumination, could contribute to research on the retina.

To achieve this ambitious goal, we modified the full-field ophthalmoscope built at the National Hospital Center of Quinze-Vingts with a specific image processing and two new instruments inspired by full-field microscopy. We have integrated these instruments into the illumination path of the ophthalmoscope to manipulate the geometry of the retinal illumination. These new implementations allow us to make use of more advanced imaging techniques, such as dark field imaging or noninvasive near infrared angiography. These imaging modalities have been exploited to image the retina functionally. We focused mainly on the light coupling function of photoreceptors and on blood perfusion.



## Résumé en Français

L'œil étant la seule fenêtre optique transparente de notre corps, il donne un accès unique à l'observation de réseaux neuronaux et vasculaires. Mais aujourd'hui une nouvelle ère s'ouvre pour l'imagerie haute résolution, qui ne doit plus se contenter de donner accès aux structures des tissus, mais aussi d'en apprécier les fonctions. En effet, on peut trouver dans l'imagerie rétinienne des biomarqueurs du fonctionnement de l'ensemble du corps humain. Des maladies neurodégénératives (Parkinson, Alzheimer) ou l'hypertension artérielle pourraient être ainsi précocement diagnostiquées par une imagerie de haute précision de la rétine. L'optique adaptative, adaptée à l'imagerie rétinienne dès 1997, a amélioré nettement la résolution spatiale des images rétiniennes entraînant la multiplication des études de rétine par ophtalmoscope. Elle a notamment été couplée avec l'ophtalmoscope à balayage, qui devint le choix le plus populaire par sa supériorité en résolution spatiale et sectionnement optique par rapport au plein champ.

Cependant, contrairement aux systèmes à balayage, l'ophtalmoscope plein champ produit des images grand champ à forte cadence d'acquisition et sans distorsion. Dans mon travail de thèse, j'ai cherché à montrer qu'un tel système, associé à des modalités d'imagerie jouant sur la géométrie d'éclairage, pourrait apporter à la recherche sur la rétine.

Pour atteindre cet objectif ambitieux, nous avons modifié l'ophtalmoscope plein champ construit au Centre Hospitalier National des Quinze-Vingts avec un traitement d'image spécifique et deux nouveaux instruments inspirés de la microscopie plein champ. Nous avons intégré ces instruments dans le trajet d'illumination de l'ophtalmoscope afin de manipuler la géométrie de l'éclairage de la rétine. Ces nouvelles implémentations nous permettent de mettre en œuvre des techniques d'imagerie plus avancées, comme par exemple l'imagerie en champ sombre ou l'angiographie non invasive en proche infrarouge. Ces modalités d'imagerie ont été exploitées pour imager la rétine de façon fonctionnelle. Nous nous sommes intéressés principalement à la fonction de couplage de lumière des photorécepteurs et à la perfusion sanguine.



## *Acknowledgements*

I am very grateful to all the people who supported me and helped me to achieve this work. In the first place, I thank my supervisors, Serge Meimon and Michel Paques for creating this project and letting me pursue the research under their supervision. I also thank the reviewers Arnaud Dubois and Claude Boccara for accepting to read and examine my manuscript as well as the other members of the committee, Alexandra Fragola, Gilles Tessier and Ethan Rossi, for coming to my thesis defence. I am very lucky to have been given the chance to work at ONERA (the French Aerospace Lab) where I enjoyed an environment of collaboration and group work I have never seen before. I was also able to work with people with amazing scientific skills from whom I have learnt a lot. In particular, I would like to express my special thanks to the following persons:

Laurent Mugnier, who has supervised the subjects of my thesis concerning image processing. You have always been patient and available to guide me through the complicated parts. Thanks to your kindness and advice I did not give up, and for that I will always be extremely thankful.

Fred Cassaing, you always had your door open when questions about optical problems popped up in my mind. I think doodling optical setups and equations on the white board with you has been one of the funnest parts of my work. In particular, I felt each time I gave my opinion that you would listen and take it into account even if I was a student and you had more experience. This feeling of being treated with that respect has been one of the most satisfying of my career so far.

Olivier Herscovici-Schiller, I am so grateful that you were a PhD student during the same period. I want to thank you for always having your door open when I wanted to talk about, well... either about math or just nothing and everything. Coffee breaks would not have been the same without you.

I am indebted to the other researchers at ONERA, Aurelie, Nicolas, Vincent, Klelia, Beatrice, Jean Marc, Caroline and Thierry for their constant support, constructive criticism and interesting conversation during these three years. I would like to thank also the PhD students, Yann, Antoine, Laurie, Chloe and Matthieu for their laughs, crosswords, lending their ears or shoulder and for supporting each other during a period that can be as beautiful as it can be hard.

I am also grateful to the people I worked with at the Quinze Vingts Hospital. In particular, I thank Kate Grieve, one of the kindest and most humble persons I have ever met. You have always stopped what you were doing to answer my questions, or discuss a problem with me. You have read every abstract, article, manuscript, undecipherable doodle, etc. that I had given you. I am grateful for having you as a colleague all these years and hope to keep working with you in the future. I thank Celine, who is one of the most fun and great persons in the world. You have been there for all my accidents and helped me with such kindness. Working with you has also been incredibly nice and I am so impressed of the knowledge you have accumulated and I hope to keep learning from you in the future. You are just too cool for school! Finally, I would like to thank the rest of the hospital personnel who has always helped me, in particular Chiara, who has always listened and given me advice when needed. Finally, the last co worker I want to thank is the one I am most grateful for, Pedro Mecê. Pedro, what can one say about you? You are kind, generous, ethical and wise... You taught me to learn my strengths and thanks to you I started to trust myself more and work my own way, pursuing the results using my best skills. When I look at all the results I obtained after listening to you I can only be incredibly thankful to have had such guidance. Guidance that I will carry on in the rest of my career. Besides helping me through the rough times, I am just thankful for having worked with you because I just

had so much fun! Planning experiments, building set ups with catchy music in the background, laughs coming from despair of long working hours and lack of results or reaching unexpected results. I consider you such a good friend, and I hope one day we can work together again.

Now, all these people above I have met at work have helped me to reach my goal, but I could not have done it without the people at home, my family and friends. I want to start this section by thanking my parents. They have always done everything for me, sacrificing money, time and peace of mind so I would succeed. I thank my mum, who has endlessly talked with me on the phone during these three years, helping me to keep my confidence up when someone surrounding me pushed me down and made me feel worthless. She helped me fight my ghosts and taught me how to be fearless like her. I thank my dad, who has always been there to help me through all my studies from writing a cover letter, to build a CV or to fumigate my apartment from bed bugs. I know I can always count on him, and I understand what a luxury that is. I thank my brother, who doesn't really talk much but all he says to me comes from love. I know I have an ally in him, and without much to say he says a lot. "Thanks bro". I want to thank the rest of my family, cousins, uncles and aunts to always be there asking news about me and cheering me up. I am particularly grateful for Manolo and Marisol who came to my thesis defence and made me laugh and relax until the last second when I started to speak on the stage and without whom I don't think my presentation would have been as good as it was. I thank my cousins Cristina and Mariola, who are sisters to me and who have always been there, day or night, to check on me, to listen and reassure me. I love them so much and because of them I have never felt alone. I know Mariola could not come to the defence but I know she was with me in spirit. I thank Cristina for coming, for taking a whole month of extra hours at the hospital so they let her a two day leave to come and support me. I had so much fun, and you made this scary experience of defending three years of work in one hour such a beautiful fun one. Finally I want to thank my grandparents, to whom I dedicate this manuscript. They have inspired me by how they have lived their lives but also for their constant support. My "abuela Carmen", thank you for your constant praying and love. Nicole, even though you are not here any more you have been there at the beginning of my studies, cheering me at every step. Maria, thank you for always being there, helping me with to pay a tuition or with sound advice. I hope you know how much you mean to me. And Phanis, thank you for being such an inspiration of work ethic and adventurous spirit, I am very proud of being your granddaughter.

I want to thank my friends, here in France or abroad, for their words, love and faith. I am especially grateful for the lot here below:

Aude, Chrystelle and Thibault who have through countless dinners heard everything and nothing along these three years,

Fred and Mickael who have always cheered me up when most needed,

Miou, you are my best friend and the coolest guy, our pizza and tv shows nights have saved my life, your mija thank you for being there,

Ana, my Latina girl, who taught me to laugh things off,

Melissa and Tyler, this power couple that has listened and cared for me since we met, and always provided excellent advice.

Finally, I would like to end by thanking my boyfriend Ossian. You came into my life in my last year of the PhD and have helped me through the most complicated moments with love, patience and kind optimism. I love you and I am so grateful to have achieved this milestone with your support.

To all the people that helped me and believe in me, thank you.

# Contents

<b>Declaration of Authorship</b>	<b>iii</b>
<b>Abstract</b>	<b>vii</b>
<b>Résumé en Français</b>	<b>ix</b>
<b>Acknowledgements</b>	<b>xi</b>
<b>Introduction</b>	<b>1</b>
<b>I Context</b>	<b>5</b>
<b>1 The Human retina</b>	<b>7</b>
1.1 The human eye . . . . .	7
1.1.1 Optics of the eye . . . . .	7
1.1.2 Eye movements . . . . .	8
1.1.3 Ocular aberrations . . . . .	8
1.2 Retinal structure and function . . . . .	10
1.2.1 Cellular organization . . . . .	10
Nerve fiber bundles . . . . .	11
Photoreceptors . . . . .	11
Retinal pigment epithelium (RPE) . . . . .	12
Vascular network . . . . .	12
1.2.2 The visual cycle . . . . .	13
Photoreceptor orientation . . . . .	14
Perfusion . . . . .	14
<b>2 Structural imaging of the retina <i>in-vivo</i></b>	<b>15</b>
2.1 Clinical retinal imaging systems . . . . .	15
2.1.1 Fundus camera . . . . .	15
2.1.2 OCT . . . . .	15
2.2 High resolution retinal imaging . . . . .	15
2.2.1 Adaptive Optics . . . . .	15
Principle . . . . .	16
Adaptive optics applied to retinal imaging . . . . .	16
2.2.2 Off-axis techniques . . . . .	18
Dark-field or off-set aperture . . . . .	18
Split-detection . . . . .	19
Multi-offset . . . . .	19
<b>3 Functional imaging of the retina <i>in-vivo</i></b>	<b>21</b>
3.1 Definition of functional imaging . . . . .	21
3.2 The ideal functional imaging technique for the retina . . . . .	21
3.3 Scan versus Full-Field . . . . .	22

<b>II Adaptive optics system: optimization &amp; add-on</b>	<b>27</b>
<b>4 Optimization and exploitation of an AO FIO</b>	<b>31</b>
4.1 Introduction to the peer-reviewed article . . . . .	31
4.2 <i>Peer-reviewed Article: High loop rate adaptive optics flood illumination ophthalmoscope with structured illumination capability</i> . . . . .	31
4.3 Conclusion . . . . .	40
<b>5 Designing a new illumination for AO-FIO</b>	<b>41</b>
5.1 Inspiration from microscopy . . . . .	42
5.1.1 Oblique back-illumination . . . . .	42
5.1.2 Structured Illumination Microscopy . . . . .	45
5.2 Building a new illumination path . . . . .	47
5.2.1 Deriving two illumination geometries . . . . .	47
5.2.2 Optical design . . . . .	48
5.2.3 Implementation . . . . .	51
Optical elements of the path . . . . .	51
Alignment procedure . . . . .	53
5.2.4 Difficulties and limitations . . . . .	55
5.3 Structured Illumination Imaging . . . . .	55
5.4 Conclusion . . . . .	56
<b>III Imaging instruments: Design, integration &amp; testing</b>	<b>57</b>
<b>6 Developing a dark-field modality in full field ophthalmoscope</b>	<b>61</b>
6.1 Introduction to the article . . . . .	61
6.2 <i>Article in Progress: Dark-field imaging using an Adaptive Optics Flood Illumination Ophthalmoscope</i> . . . . .	62
6.3 Conclusion . . . . .	74
<b>7 Developing pseudo-confocal modality</b>	<b>75</b>
7.1 Description of pseudo-confocal imaging technique . . . . .	75
7.1.1 Principle of confocality and near-confocality . . . . .	75
Confocal scanning systems . . . . .	75
Near-confocal line scanning systems . . . . .	76
7.1.2 Implementation in the PARIS AO-FIO . . . . .	78
7.2 Proof of concept in the photoreceptor layer . . . . .	78
7.2.1 Optical sectioning . . . . .	81
7.2.2 Limitations . . . . .	82
7.3 Conclusion . . . . .	83
<b>8 Developing a Retinal Goniometer</b>	<b>85</b>
8.1 Description of the technique . . . . .	86
8.1.1 Phase imaging in the retina by oblique illumination . . . . .	86
8.1.2 Implementation in the PARIS AO-FIO . . . . .	86
8.2 Proof of concept in artificial eye . . . . .	89
8.3 Test in humans . . . . .	92
8.4 Conclusion . . . . .	95

<b>IV Clinical application: From structure to function</b>	<b>97</b>
<b>9 Extracting neural retinal biomarkers</b>	<b>101</b>
9.1 Structural biomarkers	101
9.1.1 Photoreceptors	101
Clinical interest	101
Biomarker	102
9.1.2 Nerve fibers	102
Clinical interest	102
Biomarker	103
9.1.3 Comparison with AO-SLO	104
9.2 Functional biomarkers	104
9.2.1 Clinical interest	104
9.2.2 Biomarker: Photoreceptor brightness at various illumination incidences	105
9.3 Conclusion	110
<b>10 Extracting vascular retinal biomarkers</b>	<b>111</b>
10.1 Structural biomarkers	111
10.1.1 Clinical interest	111
Vascular biomarkers	112
Comparison with AO-SLO	115
10.2 Functional biomarkers	116
10.2.1 Reading guide	116
10.2.2 <i>Peer reviewed Article: Near Infrared Adaptive Optics Flood Illumination Angiography</i>	117
10.3 Conclusion	132
<b>11 Pigment epithelium imaging with two complementary techniques</b>	<b>133</b>
11.1 Clinical application of the AO-FIO dark-field images	134
11.1.1 Clinical interest	134
11.1.2 Retinal pigment epithelium biomarkers	134
11.1.3 Extraction of density biomarker of the RPE mosaic	134
11.1.4 Comparison with AO SLO	135
11.1.5 Conclusion	136
11.2 Autofluorescence imaging of the retinal pigment epithelium with AO-SLO	136
11.2.1 Reading guide	136
11.2.2 <i>Peer-reviewed Article: In vivo near-infrared autofluorescence imaging of retinal pigment epithelial cells with 757nm excitation</i>	137
11.3 Comparing two complementary imaging techniques of RPE	154
11.4 Conclusion: Towards functional imaging	155
<b>Conclusion and Perspectives</b>	<b>157</b>
<b>A Ocular safety for the Paris AO-FIO system</b>	<b>159</b>
A.1 Context:	159
A.2 ISO 15004-2 norm (2007):	159
<b>Bibliography</b>	<b>161</b>



*To my grandparents, Carmen, Nicole, Maria and T  ophanis, who always encouraged me  
to be brave and follow my dreams wherever they take me.*



# Introduction

The eye is the only optical window to the human body, providing a non invasive access to both neural and vascular networks in vivo. Indeed the retina constitute a neuro-vascular network that can be considered as an extension of the brain, sharing some of the same structures as well as some of its pathologies. Neuro-degenerative diseases such as Alzheimer[1] or vascular pathologies such as arterial hypertension[2] could be early diagnosed thanks to a high performance imaging of the retina[3–5]. Additionally, as functional deterioration may precede significant structural changes in many retinal pathologies[6], an even more precocious diagnosis along with a better understanding of neuro-vascular connections could be achieved by not just giving access to tissue structures, but to their function.

Functional imaging is carried out through the extraction of retinal biomarkers which evaluate the correct performance of physiological mechanisms and therefore implies the detection of microscopic and very rapid structural variations. Although the introduction of Adaptive Optics (AO) in ophthalmic imaging led to diffraction-limited retinal images with cellular resolution[7], many retinal structures still remained hard to visualize because of their low reflectance. This issue was partially resolved by implementations inspired by microscopy on the AO Scanning Laser Ophthalmoscope (SLO) [8], where the addition of a confocal pinhole further improved retinal images contrast and optical sectioning. Then, the development of off-axis techniques like dark-field [9–12] and split-detection [11, 13] exploiting the multiply scattered light achieved phase contrast of the most transparent structures[14, 15]. Because this system provided retinal images with unprecedented quality it has often been adopted to perform functional imaging on various structures of the retina such as intrinsic signals from human cone photoreceptors [16], or the characterization of retinal perfusion [9, 17]. Similarly, Optical Coherence Tomography (OCT)[18] has also benefited from AO technology [19] and is sensitive to phase changes, which can be exploited for the imaging of transparent retinal structures. Like AO-SLO, OCT and its version upgraded with adaptive optics has also been employed to characterize neural and vascular function [20–23], as well as imaging transparent cells such as ganglion neurons [24, 25]. However, both of these techniques suffer from limitations arising from the scanning nature of the systems which introduces image distortion and restricts the maximum pixel rate. Multiple groups have found methods to correct the artifacts due to distortion which provoke an uncertainty of the imaged retinal topometry [26–28]. Similarly, the lack of temporal resolution implies a substantial difficulty in tracking the more rapid functional processes [29].

On the contrary, an AO Flood Illumination Ophthalmoscope (FIO)[7, 30] generates images free from distortion and provides a large field of view and higher temporal resolution more adapted to the dynamic nature of the rapid retinal processes. A commercial AO-FIO system (RTX1) was implemented by the French company Imagine Eyes and has been clinically exploited to study pathologies such as Age Macular Degeneration[31], hypertension[2] or Stargardt disease[32]. However because it achieves a lower contrast than AO-SLO, it has been scarcely developed since the introduction of the AO technology. The aim of this thesis is to show that with an improvement of contrast this wide field system

could become a valuable tool to achieve functional imaging of the retina by combining a high image quality with a great temporal performance and a reliable topometry of the retinal structures. Inspired by the development of the AO-SLO system achieved through the implementation of modalities translated from scanning microscopy, we explore the potential combination of an AO-FIO system with full-field microscopy modalities in order to reach a higher imaging performance (e.g. explore different illumination and detection configurations and geometries).

This thesis manuscript is divided into four parts:

First, an introduction to the scientific notions addressed throughout the manuscript is presented in Part I. Chapter 1 describes the eye and particularly the retinal structural organization and function, which we aim to image. The high resolution imaging of retinal structure is detailed in Chapter 2, in particular the principle of AO which enables the lateral resolution at a cellular level. Finally, Chapter 3 defines the concept of functional imaging and explores the ideal imaging technique to carry it out.

Part II focuses on the required optimization and modification of an AO-FIO for the purpose of improving its contrast. Chapter 4 shows how, contrary to most scanning ophthalmoscopes AO technology, our AO-FIO was optimized with a fast and robust AO loop as an effective correction of the aberrations is necessary due to the impact of the out of focus light on image contrast. Additionally, the illumination beam was aberration corrected ensuring a control of the illumination geometry which, similarly to what exists in the microscopy field, would be manipulated to improve the contrast of the system. In Chapter 5 two illumination geometries are described introducing an asymmetry of the illumination beam inspired from the oblique back-illumination microscopy and structured illumination microscopy. The implementation of these two modulations of the illumination beam respectively in the focal and pupil plane of the AO-FIO system are described.

Part III describes three modalities improving AO-FIO image contrast developed thanks to these manipulations of the illumination. The modulation in the focal plane that led to the first dark-field images on AO-FIO revealing previously invisible retinal structures such as capillaries or retinal pigment epithelium is presented in Chapter 6. Chapter 7 describes the other imaging modality ensuing from this illumination modulation, a pseudo-confocal technique, which achieves a partial optical sectioning similar to the confocal pinhole in scanning systems but without of the scanning raster limitations. Finally in Chapter 8 the pupil modulation, which led to the exploitation of multiply scattered light by achieving differential phase contrast, is introduced along with its implementation in the AO-FIO system.

The other application of the instrument achieving a modulation of the illumination at the pupil plane is presented in Chapter 9 of Part IV. Indeed, Part IV refers to the clinical applications of the implementations described in the previous part and Chapter 9, along with the description of neural structural biomarkers, explains the use of this instrument to exploit the directionality of the back-scattered light from photoreceptors in order to achieve a functional analysis of their orientation. Chapter 10 focuses on the extraction of biomarkers of the vascular network. In particular, it describes a specific image processing developed to achieve blood flow characterization, meaning the mapping of the retinal perfusion at the microvascular level as well as the computation of erythrocyte velocity. Finally, in Chapter 11, the clinical interest of visualizing retinal pigment epithelium with a dark-field modality in AO-FIO is discussed. The generation of pigment epithelium cell images with near-infrared autofluorescence is described and the complementarity of the modalities is shown. These three Chapters show how these modalities improved the image quality of the AO-FIO leading to the extraction of structural and functional biomarkers of

the retina which represent valuable indicators of retinal pathologies that could be used for structural and functional analysis of the human retina *in-vivo*.



**Part I**

**Context**



## Chapter 1

# The Human retina

## 1.1 The human eye

### 1.1.1 Optics of the eye

The human eye is the organ that enables us the visualization of the outside world. It is an effective imaging system that adapts itself to a range of visual configurations such as dark or bright environments or close or longer distances to the imaged object. The eye structure is shown in Fig. 1.1. The optical system consists in two lenses, the cornea and the crystalline lens, an aperture or pupil whose diameter is defined by the iris and the retina serving as photodetector. The eye can image objects at different distances by varying the refractive power of the crystalline lens through the ciliary muscle. This accommodation can go from punctum remotum (absence of accommodation) when the refractive power of the eye is about 60 dioptres to the punctum proximum (focusing on a close object) increasing the refractive power up to 15 dioptres.

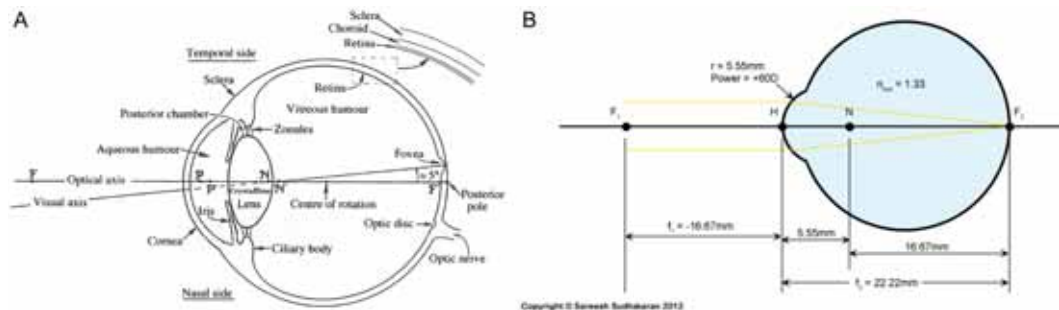


FIGURE 1.1: Two schematic layouts of the structure and optics of the eye. (A) Horizontal cross-section of the right eye as seen from above [33]. Simplified model of the eye presenting a single refractive index of 1.33.

The light crosses the refractive optics of the eye and the vitreous humour, i.e. a viscous liquid filling the eye and separating the optics of the eye, before reaching the retina. Then, the retina detects the light signal converting it in nerve impulse that is transported to the brain converting it into visual perception.

Finally, the external covering of the eye is provided by a two layer wall. The sclera, the external layer, is a structure supporting the wall of the eyeball and has therefore a resistant and elastic tissue composed mainly by collagen fibers. The internal layer laying next to the sclera is the choroid layer, which with a rich vascular network, provides nutrients and oxygen to other tissues of the eye.

The optical system of the eye is complex and presents several indices of refraction depending on the ocular tissue[34]. In 1952 Emsley presented a simplified model shown in Fig. 1.1(B) which reduces the system to a refractive surface providing a refractive power of 60D between the air and a ocular medium of 1.33 refractive index leading to a focal

length of 16.67 mm. A circular aperture defines the pupil at the top of the refractive lens. This simplified model will be adopted throughout the manuscript.

### 1.1.2 Eye movements

The eye is always in motion with both voluntary and involuntary movements ensuring efficient fixation and tracking of a visual stimuli. Voluntary eye movements such as rotation, torsion or pursuit are carried out by extraocular muscles shown in Fig.1.2. The involuntary eye movements, also known as fixational movements can be divided into three categories: drift, tremor and microsaccades [35]. Drift is a smooth and slow motion of the eye when fixed on an object. Tremor is a fast shake centered around a point and still in average. Finally microsaccades are very fast and large movements deviating the fixation suddenly.

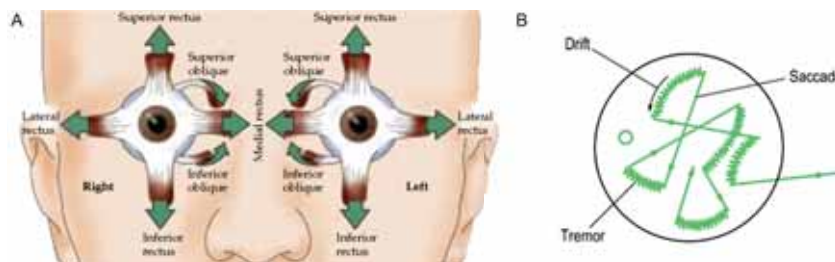


FIGURE 1.2: (A) Schematic drawing showing the six extraocular muscles in each eye responsible for the ocular motion [Credits:<http://www.speedyeyes.com/learn-eye-movement-training/>]. (B) Diagram of the typical displacements of the optical image on the retina due to involuntary eye movements of the eye (tremors, drifts and saccades) while fixing a stationary object for approximately a 10 seconds period. The large black circle represents 10 minutes of arc in diameter and the small green circle represents the size of a single cone. [36]

### 1.1.3 Ocular aberrations

The optics of the eye are far from perfect and thus introduce aberrations in the optical path of the eye. The effect of these aberrations is shown in Fig. 1.3 where the point spread function (PSF) of a perfect eye is compared to the PSF of an eye with typical aberrations for various pupil sizes. Optical aberrations can be decomposed into a linear combination of the Zernike polynomials. Figure 1.4 shows the first 21 of these polynomials.

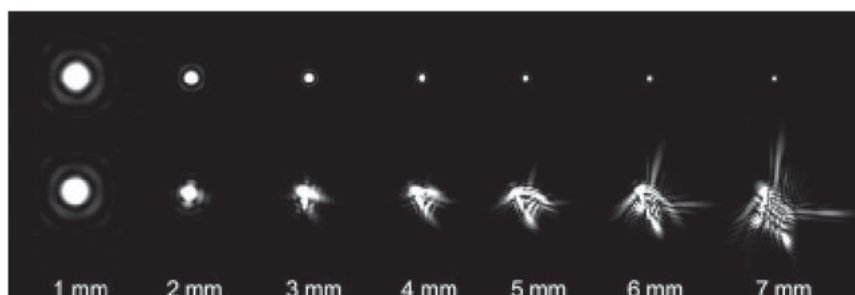


FIGURE 1.3: The top row shows the point spread function of an eye with no aberrations. As the pupil size increases the Pupil Spread Function (PSF) decreases in size, offering the potential for higher resolution. The lower row shows the point spread functions for an eye with typical aberrations. In this case aberrations, particularly for the larger pupil sizes, blur the PSF.[37]

These polynomials are well adapted to the wavefront analysis of optical aberrations of the eye as they form an orthonormal base with a circular aperture and the first polynomials corresponds to standard aberrations. For instance, the eye can present a degree of asymmetry with one of its optic surfaces slightly inclined or shifted with respect to the optical axis which would lead to astigmatism, described by Zernike polynomials  $Z_5$  and  $Z_6$ . Similarly, a variation of the axial length of the eye can introduce defocus aberration described by Zernike polynomial  $Z_4$ . The rest of the optical aberrations of the eye of higher order are described as well by this base. These optical aberrations lead to a lateral resolution of the images of the eye fundus of about  $20\mu\text{m}$ , which does not allow cellular resolution.

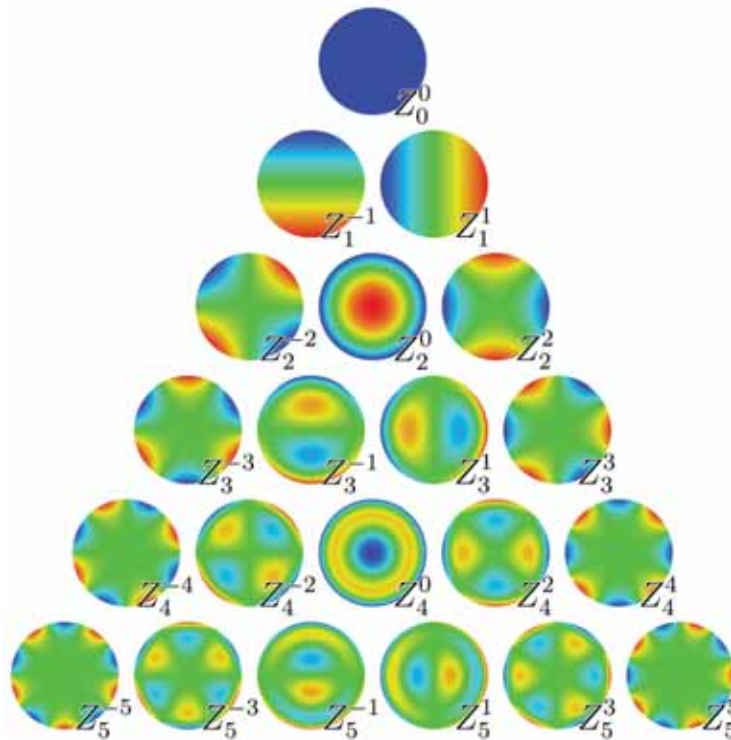


FIGURE 1.4: (A) The first 21 Zernike polynomials, ordered vertically by radial degree and horizontally by azimuthal degree

There are three categories of ocular aberrations: static, dynamic and chromatic aberrations.

Static aberrations in the eye are what we know as the standard vision problems overcome with glasses. These aberrations are often expressed in power unit (i.e. equal to the opposite correction to provide) and defocus and astigmatism are the two best known.

Dynamic aberrations are aberrations with a temporal dependence, meaning that they evolve in time. Such temporal evolution of ocular aberrations has been observed, even during fixation. A range of potential origins of dynamic ocular aberrations have been identified such as lacrimal film or the fluctuation of the accommodation [38, 39].

The eye presents two chromatic aberrations which are due to ocular dispersion, i.e. the refractive index variations of the optics of the eye with the wavelength. In particular, the dispersion in different mediums can be described by the Cauchy equation  $n(\lambda) = A + B/\lambda^2 + C/\lambda^4 + D/\lambda^6$  (see [40] for its application to the ocular medium).

The first is the longitudinal chromatic aberration (LCA) leading to a depth of focus varying with the wavelength. It varies from one individual to another with an average

value of 1.3 dioptres for the wavelength range [450nm,650nm] [41, 42] The second is the transverse chromatic aberration (TCA) due to the 5° angle between the optical axis and the visual axis. This leads to a lateral magnification variation of the image with wavelength (with the red image larger than the blue image). Contrary to LCA, the TCA varies very much according to the individual [42].

## 1.2 Retinal structure and function

### 1.2.1 Cellular organization

As mentioned before, the retina detects the light signal and converts it to nerve impulses. This organ is therefore composed of photosensitive cells connected to neuronal cells. Figure 1.5 shows an illustration of the cellular organization of the retina. The region containing synapses linking the photoreceptors with bipolar and horizontal cell dendrites is known as the outer plexiform layer or Outer Nuclear Layer (ONL), the area where the bipolar and amacrine cells connect to the ganglion cells is the inner plexiform layer or Inner Nuclear Layer (INL). The inner nuclear layer, contains one to four types of horizontal cells, 11 types of bipolar cells and 22 to 30 types of amacrine cells. The surface layers of the retina are the Ganglion Cells Layer (GCL), containing about 20 types of ganglion cells and the nerve fiber layer (NFL), going from the eye to the brain through the optic nerve head.

These four neural layers are separated by three vascular layers, the Superficial, Intermediate and Deep layers. Under the ONL lies the photoreceptor layer identified in Fig.1.5(B) as Inner Segments (IS)/ Outer Segments (OS). Finally, the last retinal layer over the choroid is the Retinal Pigment Epithelium (RPE).

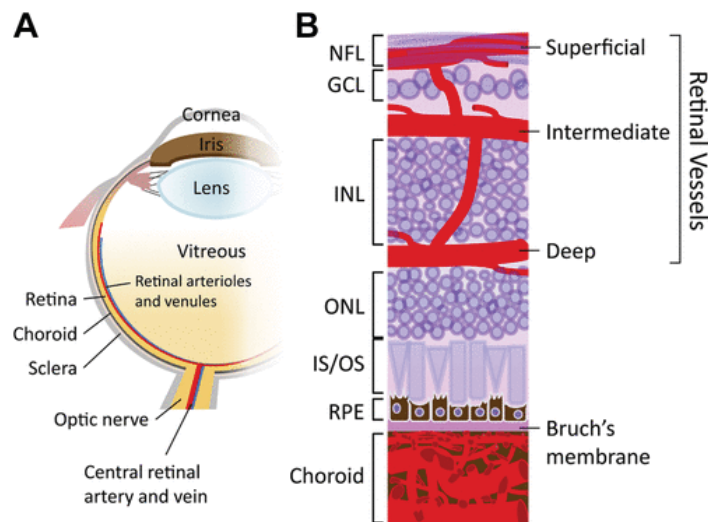


FIGURE 1.5: (A) Schematic drawing showing a cross-section of an eyeball in a top view. (B) Schematic layout showing a cross-sectional view of the retinal and choroidal layers. [43]

The following paragraphs provide more details about the retinal structures, between the ones described above, that are addressed in this work:

### Nerve fiber bundles

The axons of the optic nerve are extensions of the retinal ganglion cells whose unmyelinated axons form much of the nerve fiber layer of the neural retina. The axons or “nerve fibers” then enter the optic disc by making a sharp turn, where they continue as a series of fascicles or bundles [44]. Nerve fiber bundles from a group of retinal ganglion cells travel together with little tendency to disperse laterally as they course into the optic nerve head [45], which collects all the axons of the ganglion cells.

### Photoreceptors

The photoreceptors are light sensitive cells and there are two categories: cones and rods. Cones, responsible for daylight vision have a higher density in the central region of the retina, the macula, to ensure accurate vision. The fovea, the center of the macula, contains only cones. The cone photopigments (opsins) are sensitive to a range of wavelengths. There are three type of cones, Long, Middle and Short wavelength sensitive, depending on their peak wavelength. Cones diameter is 1-4 $\mu\text{m}$  at the fovea and over 4 $\mu\text{m}$  outside this region. Rods, more adapted to night vision, have approximately a diameter of 1 $\mu\text{m}$ . Their density is maximum at approximately 6 mm from the center of the retina and decreases towards the periphery of the retina (see Fig.1.6 (B))[46].

Photoreceptors are composed of three main layers: 1) the cell nuclei, 2) the inner segment, which encloses the cell machinery, and 3) the outer segment that contains photosensitive pigment (see Fig. 1.6 (A)). The outer segment corresponds to discrete disks saturated with a photosensitive molecule called rhodopsin in the case of the rods, and forms a series of folds containing similar photosensitive molecules in the case of cones. The outer segment absorbs photons, which initiates an electrochemical transmission through the cells and retinal nerve fibers, up into the brain [47].

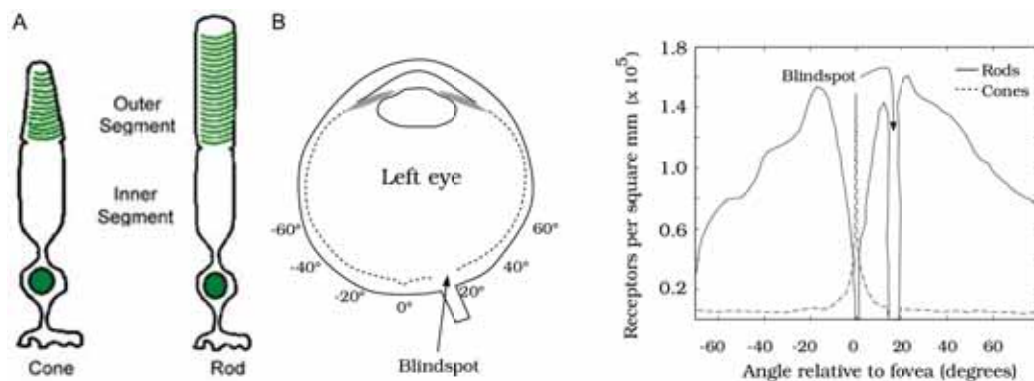


FIGURE 1.6: (A) Schematic illustration of a cone (left) and a rod (right) showing the three main sections: 1) the outer nuclear layer, containing the nuclei 2) the inner segment and 3) the outer segment that contains photosensitive pigment.[47] (B) Density of rod and cone photoreceptors across the human retina as a function of eccentricity (in degrees of visual angle relative to the position of the fovea) for the left eye. Cones are concentrated in the fovea while rods are absent from the foveal region and reach their highest density 10 to 20 degrees peripheral to the fovea. No photoreceptors are present in the blindspot.[46]

### Retinal pigment epithelium (RPE)

The RPE is the pigmented cell layer located between the light-sensitive outer segments of the photoreceptors and blood supply of the choroid. The RPE is composed of a single layer of hexagonally packed, tight-junction, connected, single sheet of cells with pigment granules and organelles for digestion of photoreceptor outer segment membranes into phagosomes [48].

### Vascular network

The central retinal artery and the choroidal blood vessels are the two sources of blood supplying the human retina. The largest blood flow is provided by the choroid (65-85%) and maintain principally the outer retina, and photoreceptors in particular. The retinal artery provides the rest of the blood flow (20-30%) and enters the retina through the optic nerve head, supplying the inner layers[49]. Figure 1.7 shows the vascular network model of the retina proposed by Campbell et al.[50](left) and Fouquet et al.[51](right). In both studies the central retinal artery supplies four retinal vascular networks: 1) The radial peripapillary capillaries (RPCs), which is the most superficial layer of capillaries lying in the inner part of the nerve fiber layer (this layer is presented in [50] but does not appear in Fig. 1.7(A) as the images are not acquired near the optic disk, where the RPC layer lies). 2) The Superficial Vascular Plexus, located at the ganglion cell layer. 3) The Deep Capillary Plexus or Intermediate Vascular Plexus located above the inner nuclear layer. 3) The Deep Capillary Plexus or Deep Vascular Plexus, located below the inner nuclear layer.

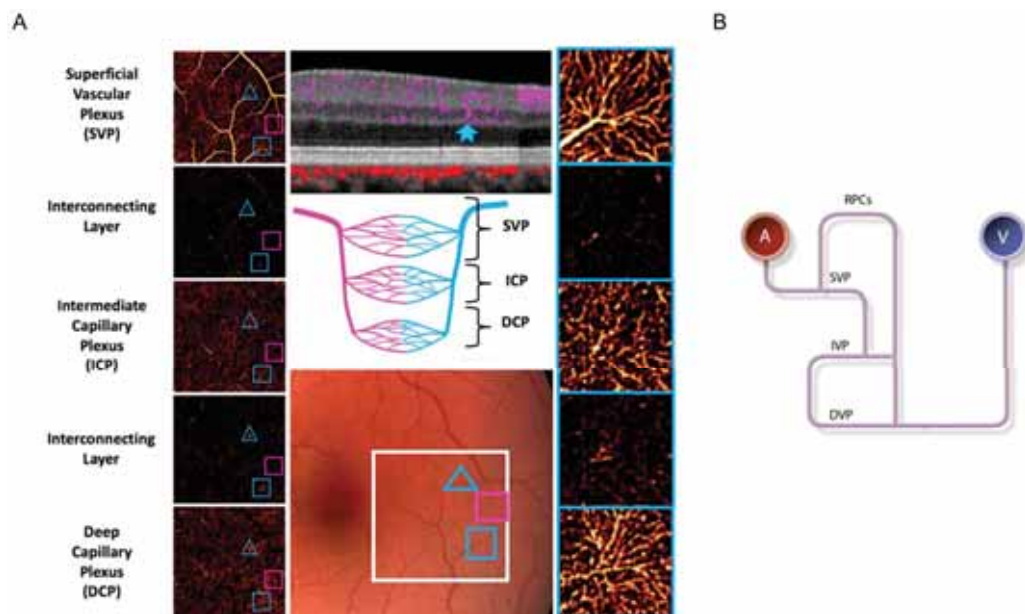


FIGURE 1.7: (A) Middle bottom panel: Color fundus photograph. Left panels: En-face PR-OCTA, which are arrayed from the most superficial on top to the deepest at the bottom. Right panels: En-face PR-OCTA slabs. Middle top panel: Cross-sectional PR-OCT. Center panel: Cartoon depicting the anatomical relationships between arterial and venous systems in the three vascular plexuses and the interconnecting layers.[50]. (B) Proposed 2D model of the retinal microcirculation in the pig retina close to the optic disc [51]. RPCs: Radial peripapillary capillaries, SVP: Superficial Vascular Plexus, IVP: Intermediate Vascular Plexus, DVP: Deep Vascular Plexus.

### 1.2.2 The visual cycle

The processing of visual information begins in the retina with the detection of light by photoreceptor cells. In humans, two specialized types of photoreceptors detect light under different conditions. Rod photoreceptors are highly sensitive and mediate vision in dim light, while cone photoreceptors function in bright light and mediate both high acuity and color vision. To detect light, both rods and cones exploit the unique properties of a vital molecule, retinal, a photosensitive derivative of vitamin A which initiates the phototransduction and is produced by the retinal pigment epithelium (RPE) [52]. Retinal molecules are recycled back into the RPE.

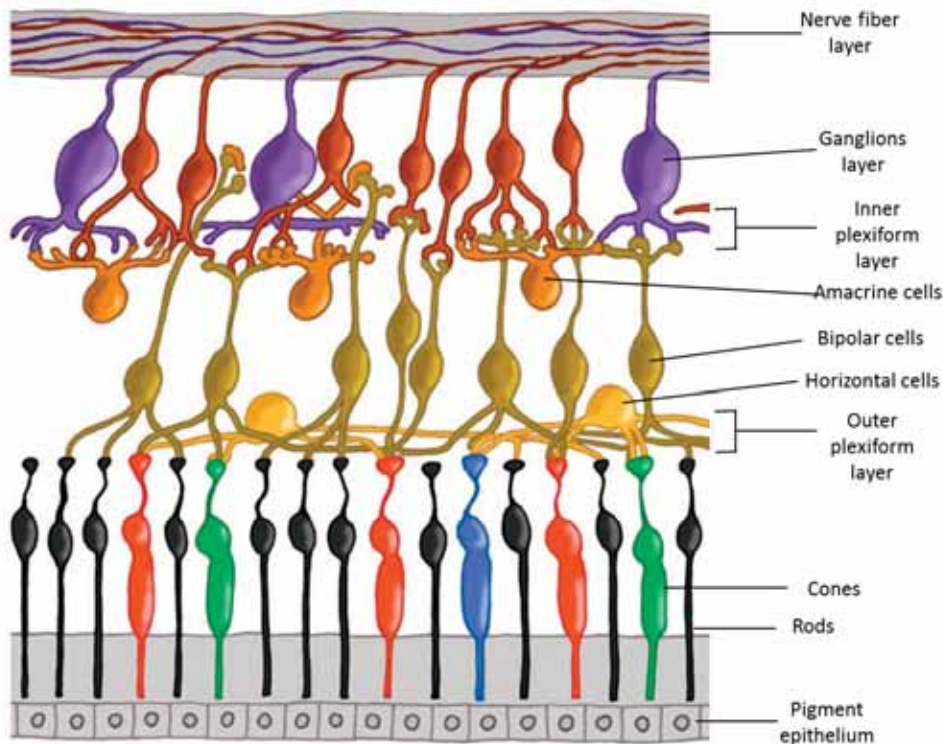


FIGURE 1.8: Schematic illustration of intricately wired neurons in the retina. Signals pass from the photoreceptors through a series of neural connections toward the surface of the retina, where the ganglion-cell nerve-fiber layer relays the processed information to the optic nerve and into the brain.

Then, neurons in the outer layer respond to stimulation originated in the photoreceptors and continues the transmission through the visual pathway to the inner layer and finally the ganglion cells. Finally, impulses from the ganglion cells travel to the brain via more than a million optic nerve fibers (cf. Fig. 1.8). Although the visual function is composed by the parallel or successive mechanisms described above, there are other structures carrying functions just as critical to the balance of the visual cycle. For instance, the RPE has another role essential to the normal function and survival of photoreceptors which is to facilitate photoreceptor cell renewal. Indeed, rod and cone photoreceptor cells undergo a daily regeneration process wherein about 10% of their OS volume is shed, subsequently phagocytosed by adjacent RPE cells [53]. Another key function to maintain this balance is the vascular perfusion which provides the retinal cells involved in the cycle in oxygen and nutrients.

All these sub-functions, either with direct or indirect intervention in the visual cycle, are involved in some way.

This thesis manuscript describes, among other developments, the first steps of functional imaging undertaken with the implementations carried out during these three years. From the multiple functions leading to the visual cycle or indirectly maintaining its physiological balance, the following are going to be addressed in this work:

### **Photoreceptor orientation**

The photoreceptors carry out the transduction, which is the conversion of the light to electrical signal. They have therefore a key function in the visual cycle. In the case of a healthy retina they should be oriented towards the center of the pupil (with a deviation of less than a millimeter). It has been hypothesized that a loss of this orientation is associated with a loss in visual capacity. Even though this hypothesis has not been validated yet, we aim to study this orientation which we believe could be a biomarker to evaluate the correct functioning of the photoreceptor cells.

### **Perfusion**

Perfusion, i.e. the supplying of oxygen and nutrients to retinal cells, is carried out by the vascular network. This structure does not directly participate in the visual cycle, but a failing in its function would affect structures which do. Therefore, in this work we aim to characterize this indirect function, in particular at the microvascular level where tissue exchanges take place.

## Chapter 2

# Structural imaging of the retina *in-vivo*

## 2.1 Clinical retinal imaging systems

### 2.1.1 Fundus camera

A fundus camera is a specialized low power microscope with an attached camera. The main structures that can be visualized on a fundus photography are the central and peripheral retina, optic disc and macula. Fundus photography can be performed with colored filters, or with specialized dyes including fluorescein and indocyanine green. Its optical design is based on the indirect ophthalmoscope. Fundus cameras are described by the angle of view - the optical angle of acceptance of the lens. An angle of 30°, considered the normal angle of view, creates a film image 2.5 times larger than life.

### 2.1.2 OCT

Optical Coherence Tomography (OCT), consists in producing interferences between the light coming back from the sample (the retina in our case) and a part of the illumination beam used as a reference. By modulating the wavelength (Fourier or Spectral Domain OCT) or the position of the reference beam (Time Domain OCT), the recorded interference pattern gives access to propagation time difference between the sample and the reference beams, and thereby on the depth of the layers constituting the retina. This technique enables an axial resolution worth a few microns, typically ten times better than classical (incoherent) imaging.

## 2.2 High resolution retinal imaging

### 2.2.1 Adaptive Optics

Adaptive optics enables the real time correction of the wavefront aberrations introduced by the optics of the eye thanks to the following components:

- 1) The Wavefront sensor (WFS) which measures the wavefront aberrations. From the range of existing WFS, the most commonly used is the Hartmann-Shack, which is the one that will be used in this work.
- 2) The Wavefront corrector, in our case a deformable mirror, which compensates the measured aberrations introduced by the optics of the eye and the optical system.
- 3) The Real time calculator (RTC) which converts the measures into voltage commands and is used to pilot the wavefront corrector.

## Principle

The principle of adaptive optics applied to retinal imaging is presented in Fig.2.1. The system is composed of the elements of the AO loop previously mentioned forming a closed loop configuration with the deformable mirror upstream from the WFS, a beacon illuminating the retina and an imaging camera. The illumination beacon is known as the WFS source and creates a point source in the retina. This illumination beacon is then back-scattered by the retina through the eye and propagates through the optical system towards the WFS. The deformation measured by the WFS is transmitted to the real time calculator which computes the voltage commands that are sent to the deformable mirror. Both the WFS and deformable mirror are placed at the pupil plane of the system. The deformable mirror surface is modified in order to compensate the measured aberrations of the WFS. This correction is applied to the wavefront of the back-scattered photons coming from the large illumination source leading to a high resolution image of the retina.

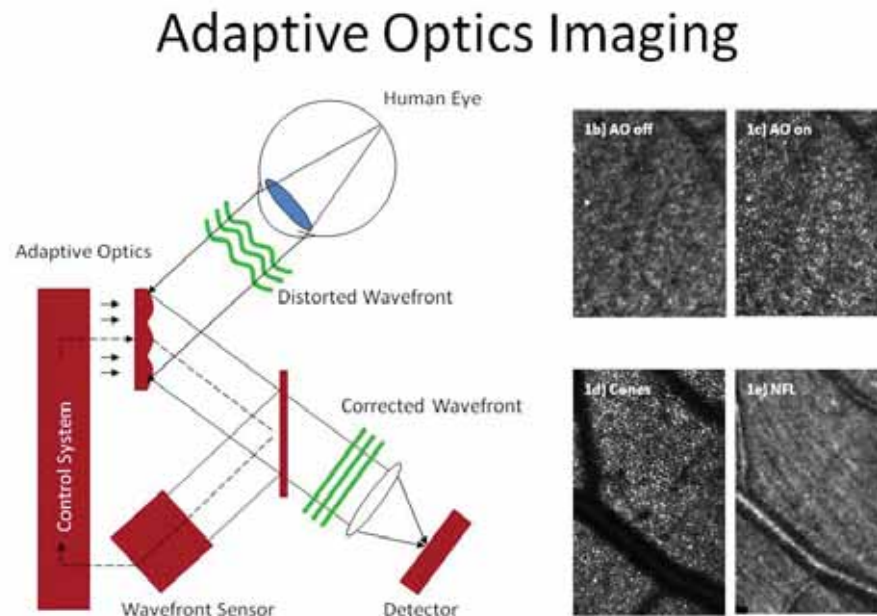


FIGURE 2.1: Schematic drawing describing the Adaptive Optics (AO) principle [Credits: <http://www.opt.indiana.edu/people/faculty/burns/CenterForOphthalmicImaging/AOSLO.html>].

## Adaptive optics applied to retinal imaging

### *Adaptive Optics Flood Illumination Ophthalmoscope (AO-FIO)*

Adaptive Optics was translated to retinal imaging in 1997 by Liang et al. [7]. They used adaptive optics (AO) to compensate for monochromatic aberrations of the eye. The quality of retinal images obtained on a CCD fundus camera was greatly improved so as to visualize cellular structures of just a few microns such as photoreceptors in human retina *in-vivo*. AO-FIO devices were further improved and their applications multiplied leading to a commercial system developed by the French company Imagine Eyes used now in a clinical setting [54].

### *Adaptive Optics Scanning Laser Ophthalmoscope (AO-SLO)*

The adaptive technology was subsequently introduced in scanning laser ophthalmoscope (SLO) as well. The SLO was invented by Webb et al. [55] and represented a major advance with respect to the wide field ophthalmoscope. This system presents an improved efficiency in light collection and real-time imaging, in particular thanks to the use of a confocal pinhole which enhances the image contrast compared to flood illuminated imaging as well as optically sectioning the retina. By adding AO technology to the SLO [8], the SLO's spatial resolution, of 20  $\mu\text{m}$  and 200  $\mu\text{m}$  lateral and axial respectively, evolved to 2.5  $\mu\text{m}$  and 100  $\mu\text{m}$ .

The introduction of a confocal pinhole in microscopy led to an improvement in image quality arising from an enhancement in spatial resolution as well as optical sectioning [56]. The ophthalmoscope combined with the lens of the eye can be seen as a microscope imaging the retina and thus in 1987 Webb et al. developed the confocal scanning ophthalmoscope improving the contrast of retinal images [57]. This confocal configuration was later implemented on the AO-SLO leading to an instrument acquiring highly contrasted images of microstructure of the retina *in-vivo*. However, as mentioned before, these confocal systems are limited by the speed of the resonant scanner, which additionally is slower than the involuntary fixational movements of the eye leading to distortion artifacts.

### *Adaptive Optics Line Scanning Ophthalmoscope (AO-LSO)*

Another confocal regime, known as line scanning ophthalmoscopy, has been developed to try to overcome these limitations as well as to simplify the complexity of these scanning systems.

Several variations of line scanning imaging systems have been investigated to improve the imaging speed and applied first to the cSLO and then to the cAOSLO in order to render these systems less susceptible to eye motion. The idea first introduced by Hammer et al. [58, 59] was to use a line illumination instead of a "flying spot" and named this new configuration the line scanning ophthalmoscope (LSO). This implementation simplified the system to a configuration where only one of the two scanners, a galvanometer, is used thus increasing the imaging speed with limited reduction in the confocality. Further simplification and speed improvement of the system was achieved by completely avoiding the use of scanners. The galvanometer is replaced by a Digital Micromirror Device (DMD), a spatial light modulator which consists in an array of micromirrors that can be set to two positions allowing the projection of specific illumination patterns. In the case of the LSO it is set to rapidly project a single line to the retina and synchronizing the acquisition with the rolling shutter of the camera [60, 61]. Finally, faster imaging was achieved by acquiring in parallel multiple lines within the field of view [29, 62].

Although the line scanning, whether it is applied to cSLO or cAO-SLO, leads to high contrast images, it has been acknowledged that the cross-talk along the imaging line reduce the confocal imaging mechanism in the direction of the light line [29].

### *Adaptive Optics Optical Coherence Tomography (AO-OCT)*

A combination of the adaptive optics and Optical Coherence Tomography (OCT) technologies was first proposed by Miller et al. [63]. These two technologies have complementary strengths in lateral and axial resolution respectively. AO-OCT has enabled the visualization of retinal structures previously only visible with histology and has been used to study the optical properties of individual cone photoreceptors, the capillaries that form

the foveal avascular zone, and retinal nerve fiber bundles from the optic disc to the fovea. Indeed, this AO-OCT system can provide high 3D resolution ( $3 \times 3 \times 3 \mu\text{m}^3$ ) and high speed imaging (10 times faster than a commercial OCT). It enables phase-sensitive imaging detecting optical length changes down to half a micron [64]. However AO-OCT is a scanning system and requires volume acquisition to reconstruct en face imaging which can take a long time.

### 2.2.2 Off-axis techniques

The introduction of adaptive optics technology enabled the imaging of several retinal cellular structures such as photoreceptors, due to their waveguiding properties or nerves fiber bundles which are very reflective. Nevertheless, a range of transparent structures remained invisible or with too low a contrast due to masking from highly reflective waveguiding photoreceptors. The off axis techniques described hereafter helped overcome this issue. They are presented in the chronological order of their development.

#### Dark-field or off-set aperture

Dark-field imaging is a modality first developed in the microscopy field in which the ballistic photons (unscattered by the beam) are excluded from the image. This method was first contemplated in ophthalmic imaging by Webb et al. [57] where they stop the direct back-scattered light using an aperture block. Widely adopted in AO-SLO by shifting the detection confocal pinhole, dark-field imaging has enabled the imaging of transparent retinal structures such as small capillaries [9] or retinal pigment epithelium [12].

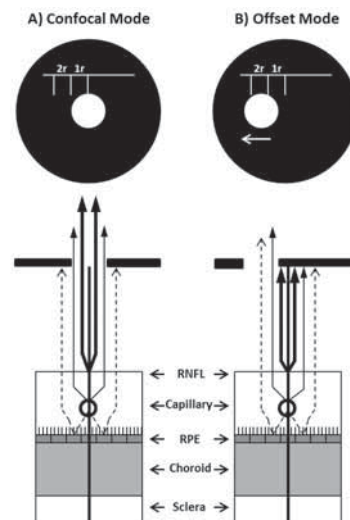


FIGURE 2.2: Schematic drawing illustrating the off-set (or dark-field) technique in an AO-SLO system as it depicts the effect of offsetting the confocal pinhole on the visibility of the capillaries. (A) shows a centered aperture. The specular reflection from the retinal nerve fiber layer (RNFL) (heavy arrows) decreases the contrast of the capillary. (B) The pinhole is laterally shifted leading to offset imaging. Specular reflection from the RNFL is blocked by the offset aperture, allowing more multiple scattered light (dashed arrows) to return back to the detector [9].

### Split-detection

Another off-axis technique improving retinal image contrast is split-detection modality [11].

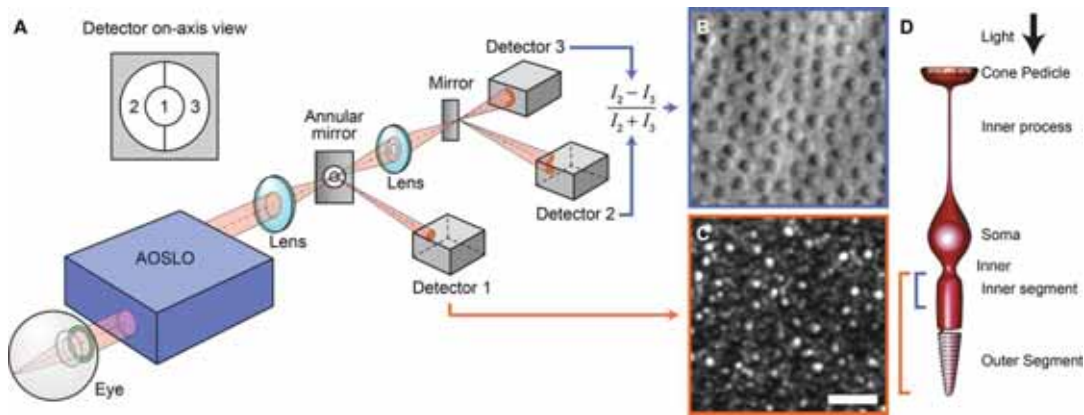


FIGURE 2.3: Schematic drawing illustrating the split-detector technique. (A) AO-SLO schematic with an annular reflective mirror separating the confocal from the multiple-scattered light. Multiply scattered photons are equally split between two light detectors. Detector 1 captures the confocal signal. Detectors 2 and 3 respectively capture each divided multiply scattered beam. The split-detector signal results from the subtraction of the two multiply scattered intensities divided by their sum at every pixel. (B) Typical split-detector image of the photoreceptor inner segment mosaic. (C) Simultaneously recorded confocal image showing cones with varying reflectivity surrounded by rods. Scale bar is  $25 \mu\text{m}$ . (D) Photoreceptor schematic shows the likely origin of the light back reflections [14].

This method, inspired as well from microscopy, consists in the subtraction of two images acquired with two halves of the whole detector (Detectors 2 and 3 in Fig. 2.3) and divided by the sum of these images. It is a differential phase technique, meaning the two images subtracted have opposite phases and the same absorption contribution leading to a final generated image where the phase contrast is enhanced and the background contribution canceled.

### Multi-offset

A development of the differential phase imaging, known as multi-offset imaging, in the retina has enabled the visualization of very transparent retinal feature such as ganglion cells [15]. This multi-offset approach relies in the combination of multiple offset apertures displaced by an optimal shift adapted to the imaged structures leading to the enhancement of structural contrast.



## Chapter 3

# Functional imaging of the retina *in-vivo*

### 3.1 Definition of functional imaging

Achieving functional imaging means being able to evaluate retinal function, i.e. to understand the mechanisms participating in the visual cycle and to be able to tell as soon as possible that a function is failing. To “visualize” these functions we need to extract functional biomarkers. Biomarkers are defined as “a characteristic that is objectively measured and evaluated as an indicator of normal biological processes, pathogenic processes, or pharmacologic responses to a therapeutic intervention” [65]. For instance, Duan et al [66] uses the variation of the lumen size as a biomarker for the evaluation of the function of perfusion when optically stimulating the retina. A reduced variation could indicate that the area observed is not being perfused correctly. It is important not only to select an appropriate biomarker but to assess the nominal value of this biomarker when the function it evaluates works fine. For instance using the same example of the variation of capillary lumen as a biomarker, several measurements on healthy subjects need to be done to determine this nominal value and then tests must be done on patients to observe a variation from this value and assess if the biomarker is sensitive enough.

In our case, we are looking to be able to extract biomarkers evaluating the functions of transduction and perfusion. Even though these biomarkers are not directly related to the visual cycle, i.e. a small lumen or dim cone does not necessarily imply poor vision, they provide information about structures and mechanisms whose failing would indirectly impact the visual cycle. Therefore, we consider here the computation of "indirect" functional biomarkers, evaluating for instance retinal perfusion, a functional analysis of the retina. The computation of said biomarkers means that we need to be able to detect a variation in size, intensity or shape of the structures carrying out these functions. Therefore we have to reach an image quality such as to resolve the structures of interest and above all their spatial or temporal variation.

### 3.2 The ideal functional imaging technique for the retina

We are interested in two kinds of retinal structures: neural structures such as photoreceptors or ganglions cells and supplier structures such as capillaries and RPE. We are particularly interested in photoreceptors and capillaries for two main reasons. First, ganglions and RPE are hard to image as they are transparency and they are masked by other retinal structures, making the detection of spatial or temporal variation extremely difficult. Since structures like photoreceptors and capillaries have been well characterized, it makes sense

to try to detect their variations first. Table 3.1 shows the two function concerning photoreceptors and capillaries and some examples of possible biomarkers. It displays the order of magnitude of the variations we would need to be able to detect to achieve functional imaging.

Function	Structure	Size	Example of biomarkers	Order of magnitude
Perfusion	Capillary	3-10 $\mu\text{m}$	Lumen variation	$\sim$ 4%-10% lumen[66]
	Erythrocyte	8 $\mu\text{m}$	Erythrocyte speed	0.3-3 mm/s[67]
Transduction	Photoreceptors	2-3 mm	Intensity variation	(slow ) s to min[68, 69] (fast ) few 100s[70, 71]

TABLE 3.1: Examples of functions and possible biomarkers with an order of magnitude of their spatial and temporal variation

After analyzing the order of magnitude of the variations, spatial and temporal, we are looking to detect, we have summarized the various characteristics our ideal functional imaging technology would need. It should have a high temporal and spatial resolution in the order of the millisecond and the micron respectively. It should also have a high contrast and optical sectioning of the order of a few microns. Finally it must be able to resolve transparent structures.

Besides the characteristics we derive from the functions of interest, we need an instrument that can be used in a clinical setting for humans. This implies that it must comply with ocular safety standards and it should be comfortable for the patients. Also, it should have a wide field of view and a fast image processing in order to reduce the lengths of the imaging sessions.

#### The need for AO

The imaging technique used for functional imaging needs a high lateral spatial resolution close to the micron. The only existing systems reaching this spatial lateral resolution are those corrected by adaptive optics.

Thus, we believe adaptive optics corrected ophthalmoscopes are the best suited systems to carry out functional imaging of the retina.

### 3.3 Scan versus Full-Field

The high spatial and temporal resolution reached with AO-corrected ophthalmoscopes can help us achieve our ultimate goal of conducting functional imaging of the retina *in vivo*. Of the current state-of-the-art two types of AO-corrected ophthalmoscopes, the AO-SLO achieves the highest image quality in terms of resolution and contrast, which should make it the obvious choice for retinal structural and functional imaging *in vivo*. Additionally, this system enables fairly easy implementations of imaging techniques from the microscopy field such as dark-field or autofluorescence. The easy handling of this technology leads not only to an improvement in contrast but also to the achievement of complementary contrasts allowing the visualization of low-contrast retinal features. Nevertheless, the AO-SLO system suffers from limitations associated to its scanning nature such as distortion and low pixel rate; limitations that have not been overcome yet despite the continuous research of the field.

In this Chapter we explain why, despite AO-SLO's outstanding imaging qualities, such as high spatial resolution and contrast, we did not consider this technique to be well-adapted to the dynamic nature of functional imaging, where not only we are interested in spatial

details but also want to resolve temporal variations. Furthermore, we describe the limitations concerning the clinical use of this technique.

	<b>AO-FIO</b>	<b>AO-SLO</b>
<b>Strengths</b>	High pixel rate (high temporal resolution and large field of view)	Adaptation of microscopy field inspired techniques (eg confocal hole, off-axis,etc)
	Reliable topometry (NO distortion)	High contrast
		Higher axial resolution
<b>Shortcomings</b>	Low contrast	Out of focus light filtered out
	Background noise due to out of focus light	Low pixel rate
	Low axial resolution	Distortion
		Resonant scanner

TABLE 3.2: Comparing strengths and shortcomings of the two adaptive optics ophthalmoscope: Adaptive Optics Flood Illumination Ophthalmoscope (AO-FIO) and Adaptive Optics Scanning LAser Ophthalmoscope (AO-SLO)

AO SLO has enabled several groups to study the human retina in vivo at a cellular level. AO SLO strengths can be summarized in the two following characteristics: high lateral spatial resolution and high contrast.

Thanks to the AO correction, AOSLO is able to resolve down to  $2 \mu\text{m}$  features, which enables the imaging of cones and even rods at a few eccentricities. High contrast in AO SLO comes from implementations of a series of features inspired from microscopy. For instance, the implementation of a confocal configuration improves optical sectioning, as the out of focus light is filtered by a hole conjugated to the focal plane, leading to an enhanced contrast. The contrast of the AO SLO can also be improved by off-axis techniques implementations like off-set aperture or split-detection (cf.Ch. 2) which leads to the observations of retinal details like vessels walls or small capillaries previously concealed by the strong back scatter of deeper layers of the retina such as the retinal pigmented epithelium.

Finally, other implementations enable the detection of signals other than the light back scattered by the retina and thus showing a different contrast. For instance autofluorescence image of Retinal Pigment Epithelium (RPE) cells imaging is an example of such a technique. It leads to the observation a different contrast coming from the excitation of certain fluorophores inside the RPE instead of relying in the reflectance signal, in which RPE signal is sometimes masked by photoreceptor cells strong back scattering.

These strengths are extremely useful for functional imaging as we mean to detect microscopic variations in structures. A high resolution and contrast are key to be able to achieve these measurements with sufficient accuracy. Moreover, some of the structures of interest, such as retinal pigmented epithelium, ganglion cells or capillaries, display a weak signal that is often screened by stronger ones, like photoreceptors. The relatively easy handling of AO SLO has lead to a range of implementations showing various type of contrasts and thus allowing the detection of these structures with weak reflectance signal.

Although AO SLO is a great instrument for retinal microstructure imaging because of its high contrast and resolution, two main shortcomings have been identified limiting its dynamic applications: the image distortion generated by the scan raster and the low pixel rate.

Distortion is an artifact produced in an image obtained with a retinal scan when the eye moves during the acquisition of a frame [72, 73]. An example on our AO SLO system (cf.Ch.2), of a distortion in an image sequence is shown in Fig.3.1. In this figure, (A) shows a distorted frame. The deformation is especially noticeable when looking at the vessel indicated by the yellow arrowhead, as well as on the photoreceptors which appear elongated in (A) compared to their round shapes in (B) (see zooms from yellow boxes)

Even though image processing has been developed to correct this aberration, leading to the fine imaging of many retinal structures, like photoreceptors or vessels, it remains that this limitation has not been completely overcome yet. The main difficulties generated by this aberration are the following. On the one hand, when there is a deformation in a retinal structure, there is an uncertainty regarding whether it comes from distortion or has physiological origin. On the other hand, to correct distortion on all the frames in an image sequence, the user must select a reference frame. However, there may not be a working reference in every acquisition. Carroll et al.[27], concluded that in some acquisitions even the least-distorted image in a sequence may be unacceptably distorted to be reference, which is often the case in acquisitions on pathological eyes. Furthermore they noticed that quite frequently manually selected reference frames were rejected by the algorithm they implemented, which is based on intraframe motion, to achieve the same selection. This implies that any metrics extracted from those processed images are likely to be confounded by significant local distortions, caused for instance by a disease, which can lead to a poor understanding of the organization of the retina or a wrong diagnostic. This team suggests using an undistorted template acquired with an AO FIO on the same region for determining distortions in their AO SLO images.

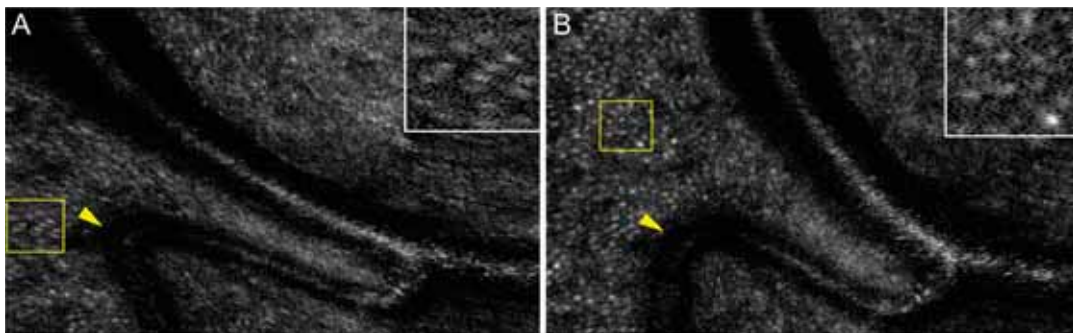


FIGURE 3.1: Two consecutive frames from an image sequence of peripheral retina acquired with AO SLO showing a deformation due to distortion artifact. The yellow arrowhead indicate the vessel distorted in A with respect to the normal position shown in B. A yellow box has been zoomed to appreciate the deformation on photoreceptors, more elongated in A while showing their typical round shape in B.

The second disadvantage of using AO SLO is the low pixel rate. This limitation translates into a compromise that must be done between having a larger field of view or a higher acquisition rate. Moreover, since scan rasters have reached their maximum speed capacity, even when restricting the field of view the temporal resolution that can be achieved is limited.

The MAORI platform accommodating the AO SLO has a 1024 by 1024 pixels field of view that can be adapted to a size range going from 1° to 5° and an acquisition rate of 24 frames per second, i.e. 24Hz. Since the scanner speed remains the same when varying the size of the field of view, the trade-off consists in the decrease in resolution going from 2  $\mu\text{m}$  for the 1° field of view to 6  $\mu\text{m}$  for the 5° field of view.

So, on the one hand, at this acquisition rate, a frame of the sequence is obtained every 40ms approximately which is higher than the typical time constants in functional imaging. On the other hand, if we select the smaller field of view (in order to reach the highest resolution), the imaging of large portions of retina would imply long imaging sessions as well as longer image processing times.

Concerning functional imaging, the scanning technique is also limited for blood flow dynamics studies. Because the scan raster is slower than the blood flow speed, a blood cell can not be followed from one frame to the next one. Indeed, as the blood cell moves in the field of view the scanner will detect it several times in the same frame, making any temporal analysis of the sequence quite difficult. Thus, not only might the temporal resolution be too low to follow the blood cells, but the resulting image shows this effect of shape distortions due to the scanning of a flow. An alternative technique has been developed to extract the velocity of blood cells using AO SLO, but it requires a small field of view in order to reach the highest scan speed.

AO-SLO has benefited from several implementations that have improved its contrast over the years. Nevertheless, in spite of these improvements it seems its main limitations have not been overcome yet. On the contrary, the AO-FIO, which benefits from the same high spatial lateral resolution than the scanning ophthalmoscope, can reach nowadays a high temporal resolution thanks to the development of cameras. However, when comparing state-of-the-art AO-SLO and AO-FIO we can identify the main shortcoming of the full field ophthalmoscope as its low optical sectioning, in particular when comparing it to the confocal version of the AO-SLO. Indeed, contrary to AO-SLO, AO-FIO has not been extensively developed since its first implementation by Williams et al. Therefore, if the full field technique were to be developed in the same manner the AO-SLO has been we could maybe achieve similar levels of contrast while keeping the advantages particular to the full field systems of a high temporal resolution and distortion free images with large fields of views.

In order to assess the feasibility of this objective and explore the prospective ways to achieve it, an AO-FIO system has been exploited and optimized towards this goal before examining the different implementations within our reach.



## **Part II**

# **Adaptive optics system: optimization & add-on**



In this Part we mean to demonstrate what the Adaptive Optics Flood Illumination Ophthalmoscope (AO-FIO) can bring to the retinal research by pushing its limits in order to match the Adaptive Optics Scanning Laser Ophthalmoscope (AO-SLO)'s best characteristics while exploiting the AO-FIO strengths. In order to achieve this challenging goal we modified the Paris AO-FIO built at the Quinze-Vingts Hospital by integrating a new illumination path in the ophthalmoscope that allowed the manipulation of the illumination geometry. This part describes the manipulations of the system: On the one hand it specifies the optimization of the system and image processing required to approximate the contrast of the AO-SLO images as well as to obtain a robustness allowing high image quality everywhere in the retina. On the other hand it details the manipulation of the illumination geometry along with the particular microscopy techniques on which this manipulation is inspired.



## Chapter 4

# Optimization and exploitation of an AO FIO

### 4.1 Introduction to the peer-reviewed article

Functional imaging requires a high spatio-temporal imaging system as well as high contrast images. Although AO-FIO reaches diffraction limited resolution and benefits from the ever growing high temporal resolution of current camera technology, the lack of optical sectioning leads to high background noise that deteriorates contrast. However, we believe that this limitation could be overcome. Inspired by the great development in image quality of the AO-SLO achieved thanks to the translation of scanning microscopy technique such as confocal pinhole, we explore the possibility of drawing from full-field microscopy to improve AO-FIO image quality.

The Paris Adaptive Optics Retinal Imaging & Surgery (PARIS) AO-FIO built in the Quinze-Vingts National Ophthalmology Hospital [74][38] has been used as full field system for this development.

The aim of this Chapter is to optimize the AO-FIO in order to allow the implementation of microscopy inspired techniques which improve its image quality (contrast, resolution etc.). Different aspects have been undertaken during this optimization. On the one hand we have improved the AO-FIO adaptive optics loop to make it more robust and achieve the best possible correction. On the other hand we have improved the image processing, for instance by correction of the inhomogeneous background. Finally, an important aspect of this AO-FIO is the correction of the illumination beam from ocular aberrations. This correction is necessary in order to control the illumination geometry which will be used in the following Ch. 5 to translate particular microscopy techniques to this ophthalmic system. The description of the resulting AO-FIO system along with the first exploration of a range of different regions and depths of the retina have been summarized in a scientific paper published in *Applied Optics* in July 2018 and presented in the following section.

I participated in the data acquisition, processing and analysis of the generated retinal images. I contributed to the experimental optimization of the system and image processing, as well as to the writing of the article.

### 4.2 *Peer-reviewed Article: High loop rate adaptive optics flood illumination ophthalmoscope with structured illumination capability*



# High loop rate adaptive optics flood illumination ophthalmoscope with structured illumination capability

ELENA GOFAS-SALAS,<sup>1,2,6,†</sup> PEDRO MECÈ,<sup>1,3,6,†</sup> CYRIL PETIT,<sup>1,6</sup> JESSICA JAROSZ,<sup>1,3</sup>  
LAURENT M. MUGNIER,<sup>1</sup> AURÉLIE MONTMERLE BONNEFOIS,<sup>1</sup> KATE GRIEVE,<sup>2,4,6</sup> JOSÉ SAHEL,<sup>2,4,5</sup>  
MICHEL PAQUES,<sup>2,4,6</sup> AND SERGE MEIMON<sup>1,6,\*</sup>

<sup>1</sup>DOTA, ONERA, Université Paris Saclay, F-91123 Palaiseau, France

<sup>2</sup>Institut de la Vision, Sorbonne Universités, UPMC Univ Paris 06, INSERM, CNRS, 17 rue Moreau, 75012 Paris, France

<sup>3</sup>Quantel Médical, Courmon d'Auvergne, France

<sup>4</sup>CIC 1423, INSERM, Quinze-Vingts Hospital, Paris, France

<sup>5</sup>Department of Ophthalmology, The University of Pittsburgh School of Medicine, Pittsburgh, Pennsylvania 15213, USA

<sup>6</sup>PARIS Group—Paris Adaptive-Optics for Retinal Imaging and Surgery, Paris, France

\*Corresponding author: serge.meimon@onera.fr

Received 3 May 2018; revised 31 May 2018; accepted 2 June 2018; posted 4 June 2018 (Doc. ID 328784); published 2 July 2018

The design and performance of an adaptive optics flood illumination ophthalmoscope (AO-FIO) platform, based on eye motion and dynamic aberrations experimental analysis, are described. The system incorporates a custom-built real-time controller, enabling up to 70 Hz loop rate without jitter, and an AO-corrected illumination capable of projecting high-resolution features in the retina. Wide-field ( $2.7^\circ \times 5.4^\circ$ ) and distortionless images from vessel walls, capillaries, and the lamina cribrosa are obtained with an enhanced contrast and signal-to-noise ratio, thanks to careful control of AO parameters. The high spatial and temporal resolution (image acquisition up to 200 Hz) performance achieved by this platform enables the visualization of vessel deformation and blood flow. This system opens up the prospect of a return to favor of flood illumination adaptive optics systems provided that its high pixel rate and structured illumination capabilities are exploited. © 2018 Optical Society of America

**OCIS codes:** (170.4470) Ophthalmology; (330.4460) Ophthalmic optics and devices; (110.1080) Active or adaptive optics; (170.3880) Medical and biological imaging; (170.2655) Functional monitoring and imaging.

<https://doi.org/10.1364/AO.57.005635>

## 1. INTRODUCTION

Adaptive optics (AO) can provide real-time correction of the wavefront aberrations introduced by the human eye, thus enabling retinal imaging with enhanced contrast and resolution [1–5]. The first AO-corrected retinal images were obtained in 1997 [1] using a flood illumination technique (AO-FIO) recording *en face* images with a camera. This seminal work gave rise to several similar systems, leading to Imagine Eyes' launch of its commercial version of AO-FIO (RTX1 [6]) based on the most popular technology at the time. Since then, AO-FIO has been replaced by AO scanning laser ophthalmoscope (AO-SLO) [5], i.e., the adaptation of the confocal scanning microscope to AO-corrected retinal imaging, due to improved optical sectioning and resolution. Evolutions proposed in the scanning microscopy field [7] (dark field imaging, multiphotonic imaging, fiber optics components) have consequently been translated to ophthalmology on AO-SLO setups.

On the other hand, only a few research teams (see for instance recent research on neurovascular coupling [8,9]) developed custom-made AO-FIO systems, and most of published AO-FIO results are obtained with a commercial system. Although AO-FIO holds the inherent advantage of distortionless high-speed imaging (while AO-SLO systems suffer from distortion artifacts in the presence of retinal motion, which hinders reliable topography of retinal structures, e.g., small caliber vessels), it has not evolved significantly nor found inspiration in breakthroughs from full-field microscopy variants, such as structured illumination [10]. This technique, which requires the projection of high spatial frequency structures onto the retina, could bridge the gap between AO-FIO and AO-SLO in terms of optical sectioning and lateral and axial resolution [11,12]. Moreover, increasing the adaptive optics loop rate, which has been shown to bring image quality enhancement in a scanning ophthalmoscope [13], has never been tried in

AO-FIO, even though we have evidence that getting the AO loop rate from 10 to 50 Hz is highly beneficial [14]. We present here details on an original AO-FIO platform featuring an AO loop rate reaching 50–70 Hz (depending on the configuration) and able to project AO-corrected illumination patterns in the retina.

## 2. METHODS

The system consists of two optical subsystems: the wavefront (WF) sensing and control subsystem and the illumination and detection subsystem (see Fig. 1), which are detailed hereafter.

### A. Wavefront Sensing and Control

The wavefront sensing and control subsystem comprises three light sources, a wavefront sensor (WFS), and a deformable mirror (DM). The system is operated via a real-time controller (RTC).

Wavefront sensing is performed using a custom-built Hartmann–Shack sensor consisting of a  $30 \times 30$  microlens array. Relay optics conjugate the focal plane of the microlens array onto a complementary metal oxide semiconductor (CMOS) camera (PCO.Edge 4.2, Germany), where  $14 \times 14$  pixels are allocated to each lenslet [15]. The microlens array pitch corresponds to  $381 \mu\text{m}$  in the eye pupil plane.

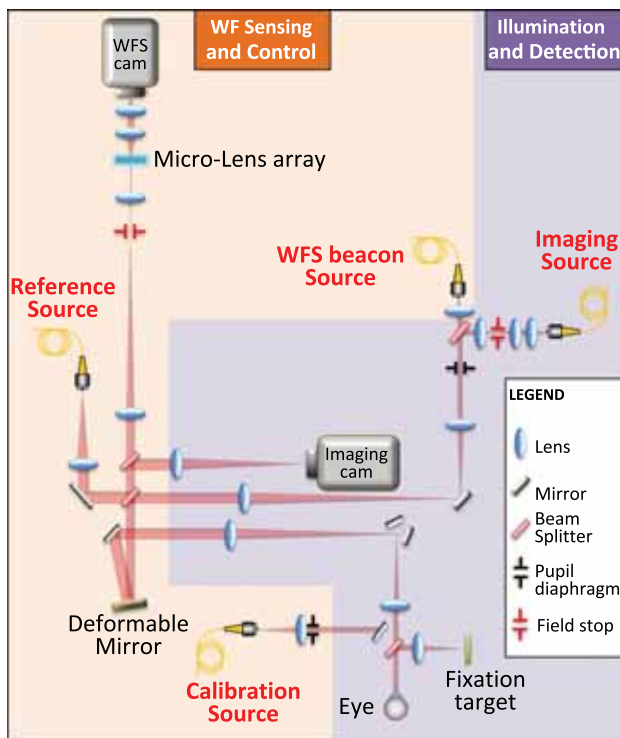


**Fig. 1.** Schematic drawing of the experimental setup. The system can be divided into two subsystems. The wavefront (WF) sensing and control, in yellow, is composed of a reference source (Ref Source), a wavefront sensor (WFS) (microlens array, relay optics, and WFS camera), a WFS beacon source, and a deformable mirror (DM). An additional calibration source can be inserted in place of the eye to calibrate the adaptive optics loop. The other subsystem, in purple, is illumination and detection and is composed of the retinal imaging camera and the corresponding wide-field imaging source.

Wavefront correction is performed by a magnetic deformable mirror (ALPAO, France) with 97 actuators. A diaphragm limits the pupil size to a 10 mm diameter, corresponding to 5 mm in the eye pupil plane.

A fibered super luminescent diode (SLD) (Omicron, Germany) with a nominal center wavelength of 750 nm can be connected to three fiber mounts on the bench, corresponding to a reference source, on which reference wavefront sensor slopes are recorded; a calibration source, used to acquire the interaction matrix between the deformable mirror actuator voltages and the wavefront sensor slope measurements; and a wavefront sensing beacon source, used to project a point source beacon on the retina. The size of the beacon at the eye pupil is 4.5 mm, with a 3 mm central obscuration to prevent stray light. The wavefront-sensing beacon source is positioned upstream of the deformable mirror so that it benefits from adaptive optics correction. This layout also enables us to use the image of the wavefront sensor beacon as an *in situ* point spread function measurement. This point spread function is not the same as the imaging one because the pupil size is not the same (4.5 mm with a 3 mm central obscuration, whereas in the imaging pathway the pupil is set by the deformable mirror to a 5 mm diameter at the eye) but still allows a real-time assessment of the adaptive optics loop performance.

A custom-built RTC comprising core libraries written in IDL (Interactive Data Language, Exelis Visual Information Solutions, Inc., Boulder, Colorado) within a LabVIEW (National Instruments, Texas) framework controls the adaptive optics. This solution enables us to tune control parameters and wavefront sensing methods with an interpreted coding language while enabling up to 70 Hz loop rate without jitter. Control law is an integrator with a 0.5 gain (ensuring a  $45^\circ$  stability margin [16]), assuming a two-frame delay (see chronogram in Fig. 2).

### B. Illumination and Detection

The retinal imaging source is a collimated SLD (Omicron, Germany) with a central wavelength of 860 nm ( $\pm 50$  nm). The 2 mm diameter fiber tip of the illumination source is conjugated to the retina, resulting in a  $3.6^\circ$  diameter illumination field of view. The illumination beam passes through the deformable mirror before reaching the eye. This aberration compensation on the forward path enables projection of high spatial frequency illumination patterns such as fringes onto the retina.

This light is then backscattered by the retina toward a fast scientific CMOS camera (retinal imaging camera in Fig. 1). The camera is an ORCA flash4-V2 (Hamamatsu, Japan), enabling  $2048 \times 1024$  pixel frame acquisition at 200 Hz,

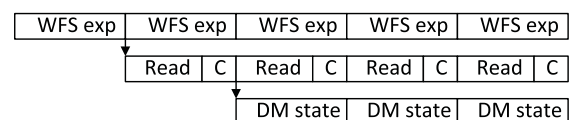


**Fig. 2.** Chronogram of the adaptive optics loop. Two frames (i.e., wavefront sensor camera exposure time) separate a wavefront sensor exposure and the corresponding deformable mirror (DM) state (2-frame delay loop). WFS, WFS camera exposure; Read, WFS camera read out; C, actuator voltages computation.

corresponding to more than  $1.5 \text{ mm} \times 0.75 \text{ mm}$  field-of-view (approximately  $5.4^\circ \times 2.7^\circ$ ). The magnification between the camera and the retina is such that each  $6.5 \text{ }\mu\text{m}$  pixel corresponds to  $0.73 \text{ }\mu\text{m}$  in the retina.

The camera is mounted on a motorized stage (Thorlabs, Germany). By moving the stage, we can focus on various layers of the retina.

### C. Subjects

Acquisitions on three healthy subjects (two men, SM, MP; one woman, EG), have been performed on the AO-FIO. Every participant followed institutional guidelines and adhered to the tenets of the declaration of Helsinki. Informed consent was obtained from subjects after the natural and possible outcomes of the study were explained. Subjects were seated in front of the FIO and stabilized with a chin and forehead rest. They were asked to stare at the fixation target, which is an image of a blue crosshair with a moving dot, enabling us to guide the subject's line of sight and explore various areas of the retina. Image acquisition sessions were performed in standard conditions with neither pupil dilation nor cycloplegia, in a dark room, leading to the largest accessible natural pupil dilation. The total light energy entering the eye from the illumination source and the WFS source are, respectively, under  $400$  and  $2.8 \text{ }\mu\text{W}$ , which is less than half the power stipulated by the ocular safety limits established by ISO standards for group 1 devices.

### D. Real-Time Processing During Acquisition

During acquisition, a custom-made real-time image-processing software is used to display retinal images with enhanced contrast. Each raw image is corrected for uneven background illumination, as brightness falls off toward the edges of the illumination patch. This correction was performed by subtracting a low-pass filtered version of each image to the raw image, where the low-pass image is obtained by a mean filter (kernel of  $50$  pixels) [17]. Following uneven illumination correction, histogram stretching is realized to enhance image contrast by saturating the  $0.1\%$  brightest and darkest pixels. Raw images are recorded without any preprocessing to allow accurate off-line processing, as described below.

### E. Off-Line Image Processing

A flow diagram of our retinal image processing sequence is shown in Fig. 3. Following the acquisition, each raw image was corrected for uneven background illumination, as described above. The image quality of AO-corrected image sequences varies over time, especially before and during blinks and during fast and large fixational eye movements such as micro-saccades [18]. The spatial variance was used as a reliable image quality metric to select the best images of the sequence [17]. The final selected images were registered using a pairwise maximum

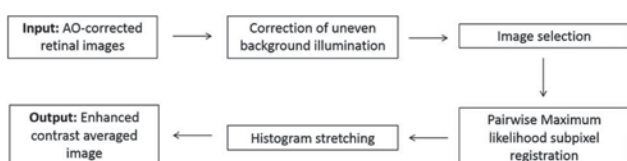


**Fig. 3.** General flow diagram of retinal image processing.

likelihood subpixel approach [19]. We generated an average image on which we perform a histogram stretching to enhance contrast. For some cases, to improve the optical sectioning, we also performed deconvolution [20].

## 3. RESULTS

### A. Wavefront Control Internal Performance

The overall system performance can be assessed and optimized thanks to the calibration source (see Fig. 1). In this configuration, the wavefront sensor beacon source is switched off, and the calibration source, simulating an unresolved point source on the retina, is switched on. In this scenario, only the aberrations introduced by the optics themselves are seen and corrected by the AO loop. This calibration source thus allows us to estimate the ultimate performance of the AO loop, i.e., without external aberrations. This parameter is usually called internal performance. The internal performance is evaluated by two criteria: point spread function (from which the Strehl ratio can be derived) and rejection transfer function (from which a correction cutoff frequency can be derived).

The resulting point spread function (PSF) is observed on the imaging camera with the adaptive optics loop closed on the calibration source. In this configuration, the pupil is limited by the deformable mirror diaphragm ( $5 \text{ mm}$  diameter at the eye pupil plane). The typical internal PSF on the calibration source with AO correction is displayed in Fig. 4. A Strehl ratio can then be derived from the PSF [21]. We have evaluated a Strehl ratio superior to  $90\%$ , demonstrating an excellent correction of the static aberrations, including noncommon path aberrations.

To evaluate the temporal performance of the AO loop, we consider the AO loop rejection transfer function, which describes how different temporal frequencies of the aberrations are attenuated by the AO loop. Assuming a high signal-to-noise ratio on the calibration source, the rejection transfer function is the ratio between the residual phase aberrations temporal power spectrum density  $S(\varphi^{\text{res}})$  and the input phase aberrations temporal power spectrum density  $S(\varphi)$ :

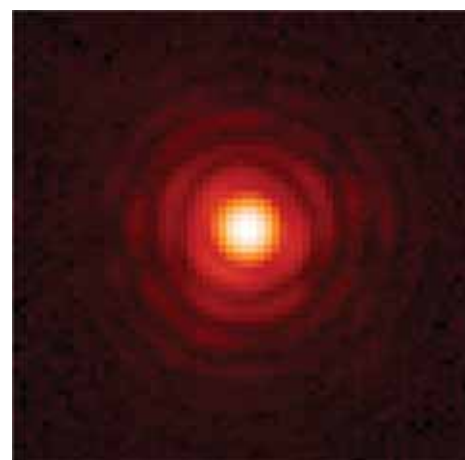


**Fig. 4.** Point spread function in closed loop on the calibration source ( $\lambda = 860 \text{ nm}$ ). The color scale is logarithmic so as to reveal the ripples.

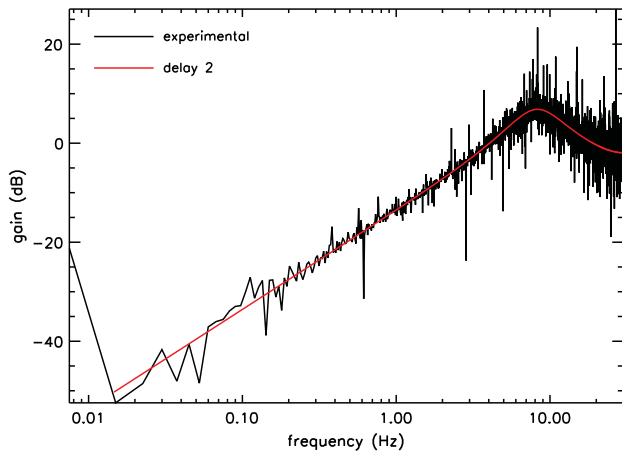


**Fig. 5.** Rejection transfer function. Black: experimental rejection. Red: theoretical rejection with a two-frame delay loop.

$$\text{RTF} = S(\varphi^{\text{res}})/S(\varphi). \quad (1)$$

A standard way to measure this rejection transfer function is to inject known aberrations using the deformable mirror itself to introduce perturbations. A pink noise with a power spectrum density following an  $f^{-1}$  law is generated and applied to each actuator of the deformable mirror (this type of colored noise avoids applying too much energy at high temporal frequencies that could degrade the deformable mirror). Wavefront measurements are recorded with the adaptive optics loop off (i.e., with input phase aberrations) and then with the adaptive optics loop on (i.e., with residual phase aberrations). For each slope measurement, a residual transfer function is obtained. These residual transfer functions are averaged to obtain one overall rejection transfer function, which is shown in Fig. 5. This experimental rejection transfer function is compared with the theoretical one, assuming a two-frame delay and a 0.5 gain (which is the actual setting used during the acquisition). The good match demonstrates that no additional delay or jitter was present during the acquisition and that the temporal performance of the loop is as expected. It has to be noted that, even with a fast adaptive optics loop (60 Hz in this case) and with a high gain (0.5), the loop cutoff frequency, i.e., the highest corrected temporal frequency (associated with 0 dB value), is approximately 4 Hz.

## B. Projection of High-Resolution Features onto the Retina

Projecting high-resolution features onto the retina is required to benefit from the improved resolution and optical sectioning yielded by structured illumination microscopy. In our setup, the illumination source is placed upstream of the deformable mirror, thus benefiting from AO-correction on the way into the retina.

To assess the capability to project image high-resolution features in the retina, we first project a point source pattern using the wavefront sensor beacon, with and without forward aberration compensation by the AO loop, in a real eye (see Fig. 6). A better confinement of the laser beacon is noted with an AO

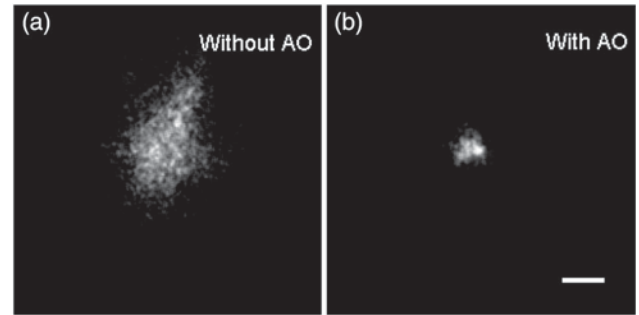


**Fig. 6.** Image of the wavefront sensor laser beacon at subject EG's fovea (a) without adaptive optics correction and (b) with adaptive optics correction (in addition to the sharp dot corresponding to the laser beacon, some multiply-scattered light is present). Scale bar is 50  $\mu\text{m}$ .

correction, although multiply-scattered light makes a reliable size assessment difficult.

We next used a modified field stop on the imaging source, corresponding to an illumination pattern made of two half moons (i.e., a circular field diaphragm, with a cylindrical mask placed vertically in its center). Figure 7 presents the averaged image from a video sequence of the large illumination patch on a phantom eye (OCULAR Model OEMI-7, presenting 3.5 diopters myopia) with and without AO-correction. With AO-correction (on the right), the edges of the illumination patch can be easily identified. On the other hand, without AO-correction (on the left), the field diaphragm is almost imperceptible, and no edges can be identified.

## C. Imaging Performance

A standard way to assess retinal imaging performance is to observe the densely packed mosaic of photoreceptors. In order to illustrate the various steps in retinal image processing (see Fig. 3) and to emphasize the gain of using a 50 Hz AO-loop correction, Fig. 8 presents images of the same cone mosaic and the associated power spectral density with increasing quality: single raw image with a 10 Hz AO-loop correction (a), (b); montaged images (made from 160 short exposure images) with uneven background correction with a 10 Hz AO-loop correction (c), (d); and with a 50 Hz AO-loop correction (e), (f). This last image is then deconvolved to obtain the mosaic presented in (g), (h). At each step, we can observe in the power spectral

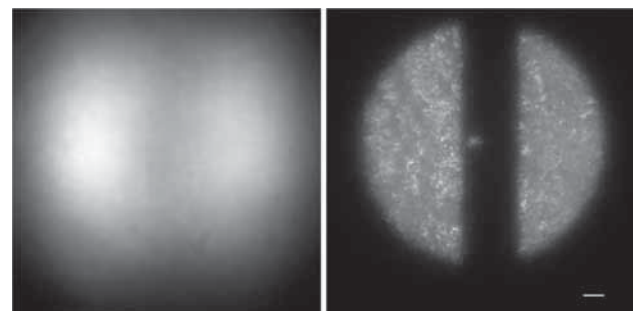


**Fig. 7.** Average image from a video sequence of the large illumination beam on a phantom eye. (Left) without AO correction. (Right) with AO correction. Scale bar is 50  $\mu\text{m}$ .

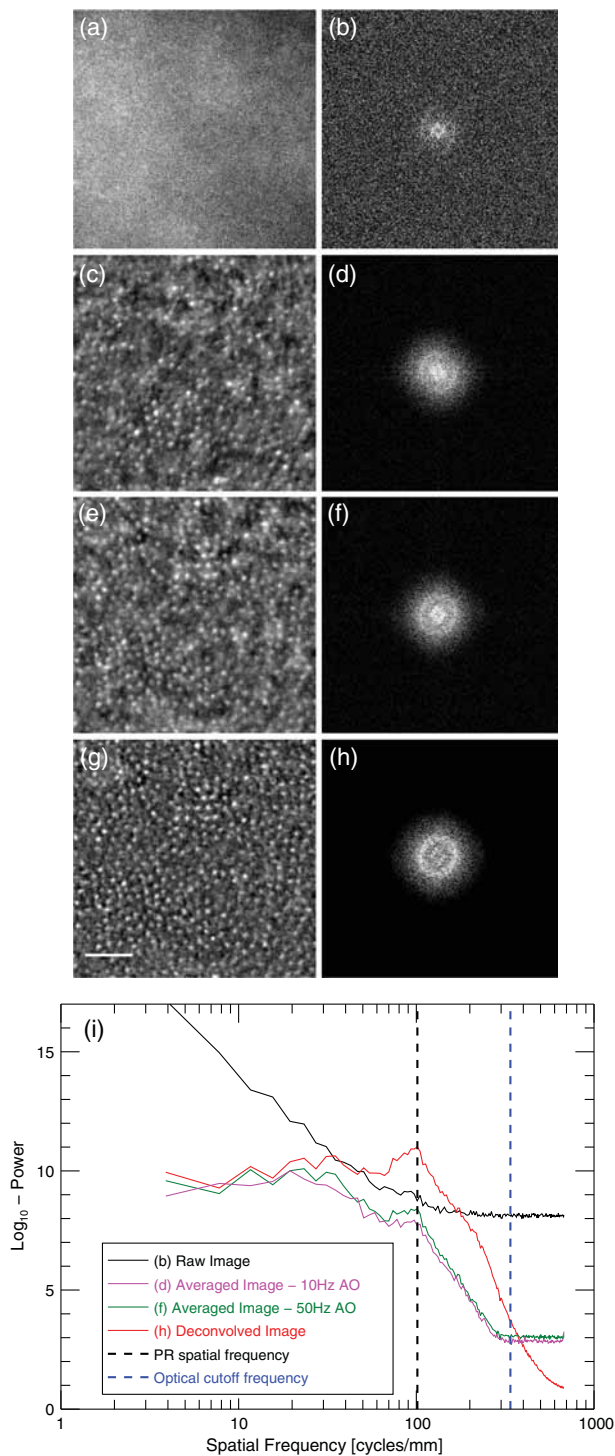


**Fig. 8.** Cone photoreceptor mosaic at  $4^\circ$  temporal (subject EG). (a) Raw image and (b) its power spectral density (PSD) with a 10 Hz AO-loop correction. (c) Corresponding 160 images average, after (d) registration and correction of uneven background illumination and associated PSD. (e), (f) same as (c), (d), but with a 50 Hz AO-loop correction. (g), (h) Image and associated PSD obtained after deconvolution of image (e). Photoreceptor images are represented in linear scale and PSD images represented in logarithm scale. Scale bar is  $50\ \mu\text{m}$ . (i) Radial average of the  $\log_{10}$ -power spectrum densities.

density (PSD) maps that the typical Yellott's ring [22] becomes more highly contrasted at each step.

Further analysis can be done by plotting the radial average of the power spectral density from each of these images [Fig. 8(i)]. The black dashed line highlights the typical photoreceptor spatial frequency peak for this region ( $4^\circ$  temporal), around 100 cycles/mm. It is possible to distinguish the photoreceptor spatial frequency peak in the raw image PSD (black line), but it is still dominated by noise. The signal-to-noise ratio at this frequency is dramatically improved by averaging 160 registered images (which represent 0.8 s image acquisition) and by correcting uneven background illumination (magenta and green lines). A clear signal-to-noise-ratio gain at the photoreceptors' spatial frequency peak is witnessed between a 10 Hz (magenta) and 50 Hz AO-loop correction (green). The frequency content of the averaged images almost reaches the diffraction limit, i.e., the optical cutoff frequency of the system at 323 cycles/mm (blue dashed line), allowing an effective deconvolution yielding an improved image contrast.

#### D. Imaging Various Zones in the Retina

This AO-FIO system is able to resolve microscopic features, as shown previously. In this section, we illustrate the image quality yielded by the resolution and contrast of the instrument on various zones of the retina.

Figure 9 shows representative images of retinal vessels, ranging from  $3\ \mu\text{m}$  capillaries to  $80\ \mu\text{m}$  arteries. The resolution performance and the wide accessible field of view achieved by our platform are particularly suited to image the retinal vascular network, from small vessel structures—vessel walls [see red arrowheads in Figs. 9(a) and 9(d)] and capillaries [see yellow arrowheads in Fig. 9(c)]—to large vessel structures—arterio-venous crossings or bifurcations [see Figs. 9(a) and 9(b)]. The retinal nerve fiber layer is highly contrasted [see Figs. 9(b) and 9(d)]. Such distortionless images of the retinal nerve fiber layer could be valuable to understand and recognize early cases of glaucoma [23]. These images also reveal how nerve fibers and vessels are intertwined: Some vessels are embedded in the nerve fiber layer [yellow arrowhead in Fig. 9(b) and red arrowhead in Fig. 9(d)], and others are partially sitting on top of the fiber layer [red arrowhead in Fig. 9(b) and yellow arrowhead in Fig. 9(d)].

The combination of a large field of view and distortionless and high spatial resolution with the high temporal resolution of the system allows the visualization of large vessel deformations. An example is presented in Visualization 1 corresponding to the image sequence from which Fig. 10 has been averaged (the blur on the vessel bend is actually due to its motion during the sequence). In this video, we observe a  $50\ \mu\text{m}$  diameter vessel, curved with a large bend radius, undergoing a horizontal deformation with the cardiac pulse.

Finally, a high-resolution image sequence of the lamina cribrosa was acquired resulting in the average image in Fig. 11. We are able to resolve collagen fibers from various layers of the mesh-like structure (the yellow arrowhead shows a fiber inside a pore of the lamina cribrosa) and capillaries irrigating the lamina cribrosa (red arrowheads indicate a vessel crossing the laminar mesh). Blood flow in the capillaries is visible

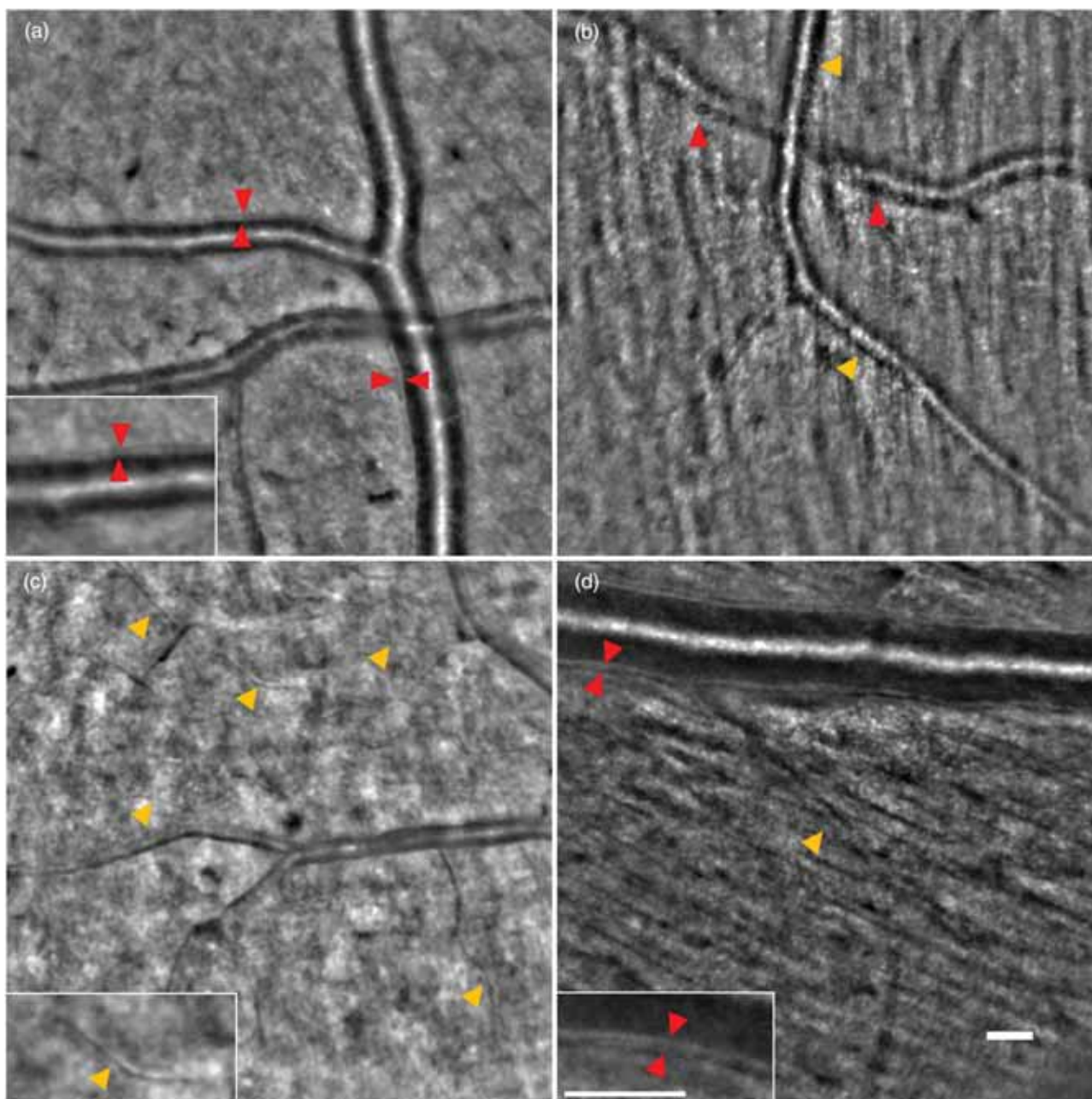


**Fig. 9.** (a) Average image of a bifurcated artery crossing a vein. (b) Average image of vessels crossing embedded in the retinal nerve fiber layer. One of the vessels is above the fiber layer (yellow arrowheads); the other one (red arrowhead) is below the fiber layer. (c) Average image of capillaries (yellow arrowheads) irrigating the retina. (d) Average image of retinal vessels, an 80  $\mu\text{m}$  retinal artery. Red arrowheads indicate vessel wall (thickness around 10  $\mu\text{m}$ ). Scale bar is 50  $\mu\text{m}$ .

in the video sequence (see [Visualization 2](#), the video corresponding to Fig. 11).

#### 4. DISCUSSION

This paper shows the capabilities of a high-performance adaptive optics loop coupled to a flood illumination retinal imager. Imperfect knowledge of the system (e.g., interaction matrix miscalibration, real-time computer jitter, deformable mirror oscillations) can be accommodated by the use of a smaller gain

but at the price of a reduced temporal bandwidth correction. The experimental adaptive optics rejection transfer function shown in Section 3.A proves that our loop is stable at 60 Hz (with two-frame delay, without jitter) with 0.5 loop gain, which is the maximum gain to ensure usual stability margins.

The benefit of a fast AO loop (50 Hz compared with 10 Hz) is demonstrated in Fig. 8. The spectral content of the images reaches the 2.3  $\mu\text{m}$  diffraction limit (optical cutoff frequency) and the signal-to-noise of photoreceptors' spatial frequency is improved by a factor of 4 at 50 Hz compared with 10 Hz.



**Fig. 10.** Average image of a large curved vessel. In the video sequence (see [Visualization 1](#)), the vessel is deformed following cardiac pulses. Scale bar is 50  $\mu\text{m}$ .

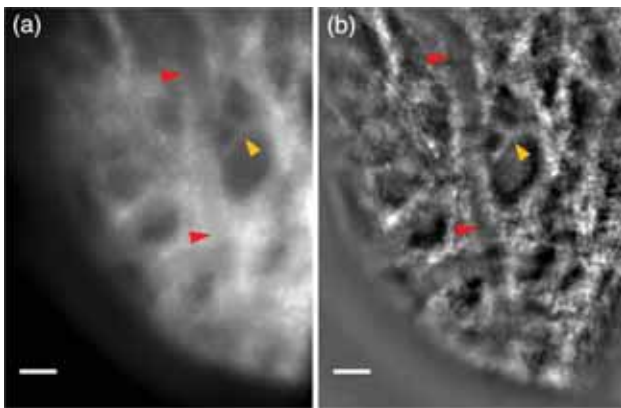


**Fig. 11.** Processed image of the lamina cribrosa (a) before and (b) after uneven illumination correction. Red arrowheads indicate a vessel inside the lamina cribrosa (blood flow is visible in the corresponding sequence, see [Visualization 2](#)). Yellow arrowhead points out fibrous branches from deeper layers of the lamina cribrosa. Scale bar is 50  $\mu\text{m}$ .

Vessel wall structures, capillaries, and lamina cribrosa fibrinogen mesh are revealed on  $3^\circ \times 2^\circ$  video sequences acquired at 200 Hz. This high spatial resolution capability at a high frame rate over a large field of view is undoubtedly underutilized in the retinal imaging community (apart from the commercial apparatus by imagine eyes), probably to an imperfect correction of the aberrations. To our knowledge, flood illumination systems have only been used with slower adaptive optics loops (typically 10 Hz) and lower gains. Also, the importance of a correct conjugation of the eye pupil with the deformable mirror, a key aspect for anisoplanatism mitigation, is probably underestimated.

This is all the more important seeing that flood illumination modality has lower optical sectioning than the scanning laser ophthalmoscope. The only way to beat the photon noise entailed by defocused layers is to have high contrast features at medium to high spatial frequencies. The signal-to-noise ratio at these spatial frequencies is directly linked to adaptive optics

performance. More generally, a flood illumination point spread function is the square root of the confocal scanning laser ophthalmoscope point spread function [24], making aberrations all the more detrimental and a proper adaptive optics correction all the more critical.

The results presented here suggest many investigations to be pursued via our adaptive optics flood illumination ophthalmoscope. For instance, we demonstrate in [25] that a fast adaptive optics loop enables better capacity to separate layers in a flood illumination ophthalmoscope. The wide-field 200 Hz imaging capability could be an extremely valuable tool to assess red blood cell trajectories in vessels from small capillaries to large arteries or veins. Angiography at 593 nm in AO-FIO has been performed by Bedggood and Metha [26], but the capability to obtain similar results at a wavelength that is comfortable for the patient and is neutral in terms of visual stimulation (e.g., the 860 nm imaging wavelength used in the present paper) would be an asset for neurovascular coupling studies in the human eye. The dynamic study of vessel deformation under the systolic wave from video sequences such as in [Visualization 1](#) could be used for local vascular elasticity assessment. Blood flow in capillaries at the surface of the lamina cribrosa (see [Visualization 2](#)) as well as distortionless nerve fiber layer high-contrast images could be used in glaucoma early management. Last but not least, the double-pass correction of aberrations enables us to project high spatial frequency patterns onto the retina. This paves the way toward structured illumination ophthalmoscopy, a technique that could reach AO-SLO optical sectioning and resolution with an AO-FIO setup.

The resolution performance achieved by our setup, thanks to careful control of AO parameters, opens up the prospect of a return to favor of flood illumination adaptive optics systems, particularly in view of their inherent advantages over scanning systems of distortionless, high-speed imaging.

**Funding.** Agence Nationale de la Recherche (ANR) (ANR-14-CE17-0011, ANR-15-RHUS-0001); H2020 European Research Council (ERC) (610110).

<sup>†</sup>These authors contributed equally to this work.

## REFERENCES

1. J. Liang, D. R. Williams, and D. T. Miller, "Supernormal vision and high-resolution retinal imaging through adaptive optics," *J. Opt. Soc. Am. A* **14**, 2884–2892 (1997).
2. A. Roorda and D. R. Williams, "The arrangement of the three cone classes in the living human eye," *Nature* **397**, 520–522 (1999).
3. A. Roorda, "Adaptive optics ophthalmoscopy," *J. Refractive Surg.* **16**, S602–S607 (2000).
4. J.-F. Le Gargasson, M. Glanc, and P. Léna, "Retinal imaging with adaptive optics," *Comptes Rendus de l'Académie des Sciences-Series IV-Physics* **2**, 1131–1138 (2001).
5. A. Roorda, F. Romero-Borja, W. J. Donnelly III, H. Queener, T. J. Hebert, and M. C. Campbell, "Adaptive optics scanning laser ophthalmoscopy," *Opt. Express* **10**, 405–412 (2002).
6. C. Viard, K. Nakashima, B. Lamory, M. Pâques, X. Levecq, and N. Château, "Imaging microscopic structures in pathological retinas using a flood-illumination adaptive optics retinal camera," *Proc. SPIE* **7885**, 788509 (2011).
7. M. Minsky, "Microscopy apparatus," U.S. patent 3,013,467 (19 December 1961).

8. A. Duan, P. A. Bedggood, B. V. Bui, and A. B. Metha, "Evidence of flicker-induced functional hyperaemia in the smallest vessels of the human retinal blood supply," *PLoS ONE* **11**, e0162621 (2016).
9. A. Duan, P. A. Bedggood, A. B. Metha, and B. V. Bui, "Reactivity in the human retinal microvasculature measured during acute gas breathing provocations," *Sci. Rep.* **7**, 2113 (2017).
10. M. G. Gustafsson, "Surpassing the lateral resolution limit by a factor of two using structured illumination microscopy," *J. Microsc.* **198**, 82–87 (2000).
11. M. A. Neil, R. Juškaitis, and T. Wilson, "Method of obtaining optical sectioning by using structured light in a conventional microscope," *Opt. Lett.* **22**, 1905–1907 (1997).
12. S. Gruppeta, "Structured illumination for in-vivo retinal imaging," in *Frontiers in Optics* (Optical Society of America, 2013), paper FW2F.1.
13. J. Lu, B. Gu, X. Wang, and Y. Zhang, "High-speed adaptive optics line scan confocal retinal imaging for human eye," *PLoS ONE* **12**, e0169358 (2017).
14. J. Jarosz, P. Mecê, J.-M. Conan, C. Petit, M. Paques, and S. Meimon, "High temporal resolution aberrometry in a 50-eye population and implications for adaptive optics error budget," *Biomed. Opt. Express* **8**, 2088–2105 (2017).
15. S. Meimon, J. Jarosz, C. Petit, E. G. Salas, K. Grieve, J.-M. Conan, B. Emica, M. Paques, and K. Irsch, "Pupil motion analysis and tracking in ophthalmic systems equipped with wavefront sensing technology," *Appl. Opt.* **56**, D66–D71 (2017).
16. F. Roddier, *Adaptive Optics in Astronomy* (1999).
17. G. Ramaswamy and N. Devaney, "Pre-processing, registration and selection of adaptive optics corrected retinal images," *Ophthalmic Physiol. Opt.* **33**, 527–539 (2013).
18. P. Mecê, J. Jarosz, J.-M. Conan, C. Petit, K. Grieve, M. Paques, and S. Meimon, "Fixational eye movement: a negligible source of dynamic aberration," *Biomed. Opt. Express* **9**, 717–727 (2018).
19. D. Gratadour, L. M. Mugnier, and D. Rouan, "Sub-pixel image registration with a maximum likelihood estimator. Application to the first adaptive optics observations of Arp 220 in the L' band," *Astron. Astrophys.* **443**, 357–365 (2005).
20. L. Blanco and L. Mugnier, "Marginal blind deconvolution of adaptive optics retinal images," *Opt. Express* **19**, 23227–23239 (2011).
21. J.-F. Sauvage, T. Fusco, M. Lamb, J. Girard, M. Brinkmann, A. Guesalaga, P. Wizinowich, J. O'Neal, M. N'Diaye, A. Vigan, and D. Mouillet, "Tackling down the low wind effect on sphere instrument," *Proc. SPIE* **9909**, 990916 (2016).
22. R. F. Cooper, C. S. Langlo, A. Dubra, and J. Carroll, "Automatic detection of modal spacing (Yellott's ring) in adaptive optics scanning light ophthalmoscope images," *Ophthalmic Physiol. Opt.* **33**, 540–549 (2013).
23. G. Ramaswamy, M. Lombardo, and N. Devaney, "Registration of adaptive optics corrected retinal nerve fiber layer (RNFL) images," *Biomed. Opt. Express* **5**, 1941–1951 (2014).
24. K. Venkateswaran, A. Roorda, and F. Romero-Borja, "Theoretical modeling and evaluation of the axial resolution of the adaptive optics scanning laser ophthalmoscope," *J. Biomed. Opt.* **9**, 132–139 (2004).
25. P. Mecê, C. Petit, E. Gofas-Salas, K. Grieve, M. Paques, and S. Meimon, "Enhancing axial resolution in nonconfocal adaptive-optics ophthalmoscopes," *Biomed. Opt. Express* (2018, submitted).
26. P. Bedggood and A. Metha, "Direct visualization and characterization of erythrocyte flow in human retinal capillaries," *Biomed. Opt. Express* **3**, 3264–3277 (2012).

### **4.3 Conclusion**

In this Chapter we have shown the strengths of the the Paris AO-FIO system, such as the resolution performance and the high frame rate, as well as the benefits brought by a careful control of the AO parameters. In particular, we demonstrated the structured illumination capabilities of our set-up, which will be exploited in the following Chapter.

## Chapter 5

# Designing a new illumination for AO-FIO

AO-SLO has benefited from implementations inspired from scanning microscopy, like a confocal pinhole or dark-field imaging (cf.Ch. 2), improving its optical sectioning and contrast and leading to better image quality. Little has been done to AO-FIO since adaptive optics was first implemented, which led us to question ourselves about the possible improvements inspired from the microscopy field that this system could benefit from. The same manipulations conducted on AO-SLO cannot be achieved on AO-FIO because of the optical design of the full field configuration, which makes it quite impossible to separate multiply scattered from ballistic photons at detection. Thus, full field microscopy techniques were explored and proved to be more adapted to our flood system. In particular we identified a few techniques that could be implemented in AO-FIO: First, we were interested in two modalities exploiting the sample scattering, dark-field and phase imaging. Although there are several ways to achieve these modalities, we selected the method that seemed more adapted to our AO-FIO system, oblique back-illumination microscopy. This technique enables the extraction of phase information of a weak scattering thick sample by introducing an asymmetry in the illumination. When setting a particular obliquity all the ballistic photons are discarded leading to dark-field while the acquisition of images with opposed angle of incidence on the sample leads to phase imaging after specific processing. Although optical sectioning and contrast are improved with phase imaging, the spatial resolution remains unchanged and thus lower than the resolution in confocal AO-SLO. To improve the spatial resolution of our system we have contemplated the implementation of another technique from the microscopy field: Structured Illumination Microscopy (SIM). This imaging technique increase the spatial resolution by illuminating the sample with sinusoidally fringe patterns at different orientations and phase shifts. This has the effect of introducing high frequency information of the object into the visible range of the optical instrument by aliasing. The resulting image is processed with specific reconstruction algorithms which allow to recover frequencies beyond the cut-off frequency imposed by the optical transfer function of the optical instrument [75].

The aim of this Chapter is to design a new illumination path leading to an oblique illumination of our sample, the retina. A first Sect. 5.1 describes the principle of oblique back-illumination and how it could be adapted to retinal imaging, and ends with small explanation of structured illumination microscopy. Then, in Sect. 5.2 we derive the illumination geometries that we must be able to achieve with our beam to implement oblique illumination of the retina and summarize the steps of the development of a new illumination path for our AO-FIO incorporating those geometries.

## 5.1 Inspiration from microscopy

### 5.1.1 Oblique back-illumination

In full field microscopy, researchers have improved contrast by manipulating the illumination geometry such as in dark-field or phase contrast imaging [76, 77]. These techniques were implemented by modifying some parts of the standard microscopes, one of the techniques implies the manipulation of the geometry of the illumination beam, which can achieve the detection of phase variation or even the canceling of the background contribution at the camera plane. Most of the samples in microscopy though are illuminated in a trans-illumination configuration and are very thin. In retinal imaging we are confronted with two issues: imaging in an epi-illumination configuration (illumination and detection from one side of the sample), as well as dealing with a thick scattering sample. For this reason, we consider adapting a microscopy technique developed by Ford et al.[78] enabling the phase imaging of thicker scattering samples: the oblique back-illumination.

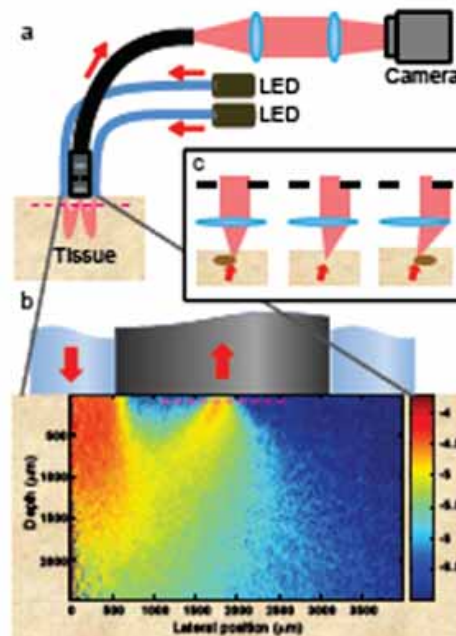


FIGURE 5.1: An Oblique Back-illumination Microscopy (OBM) setup with a contact-mode endomicroscope probe. (a) Illumination from two LEDs is sequentially projected into a thick sample by diametrically opposed optical fibers attached to the probe housing. Multiple scattering in the sample redirects the light so that it trans-illuminates the focal plane of the probe micro-objective (magenta dashed line). An image from the focal plane is then relayed by a flexible fiber bundle and projected onto a digital camera. (b) Close-up of the probe distal end, onto which is superposed a density map obtained by Monte Carlo simulation of the light energy in the sample that was injected by a single fiber (from left) and collected by the micro-objective (Online Methods). Note the obliqueness of the light distribution through the focal plane. (c) Oblique trans-illumination is partially blocked by the micro-objective back aperture. Index of refraction variations at the focal plane refract the light causing changes in the image intensity that are proportional to the slope of the variations, thus leading to phase gradient contrast. [Credits:Ford et al.[78]]

This technique relies on the strong back-scattering of a deep layer of the thick sample to create a secondary source which scatters back through the superior layers illuminating them in a trans-illumination configuration. In particular, this back-scattering reaches the sample, here another layer of the thick sample, with a certain obliquity (see Fig.5.1). The principle of the technique becomes then the same used in more standard oblique illumination microscopy (in a classic trans-illumination configuration microscopy set-up illuminating a thin sample) which is to introduce an asymmetry in the illumination beam of the sample in order to observe phase information in the camera plane. In this asymmetric illumination configuration, the phase contrast derives actually from an asymmetry in the Fourier space which is created by a differential filtering at the pupil plane due to the finite span of the aperture pupil. A quantitative approach of this technique has been presented by Tian et al.[77] whose main aspects are shown here below.

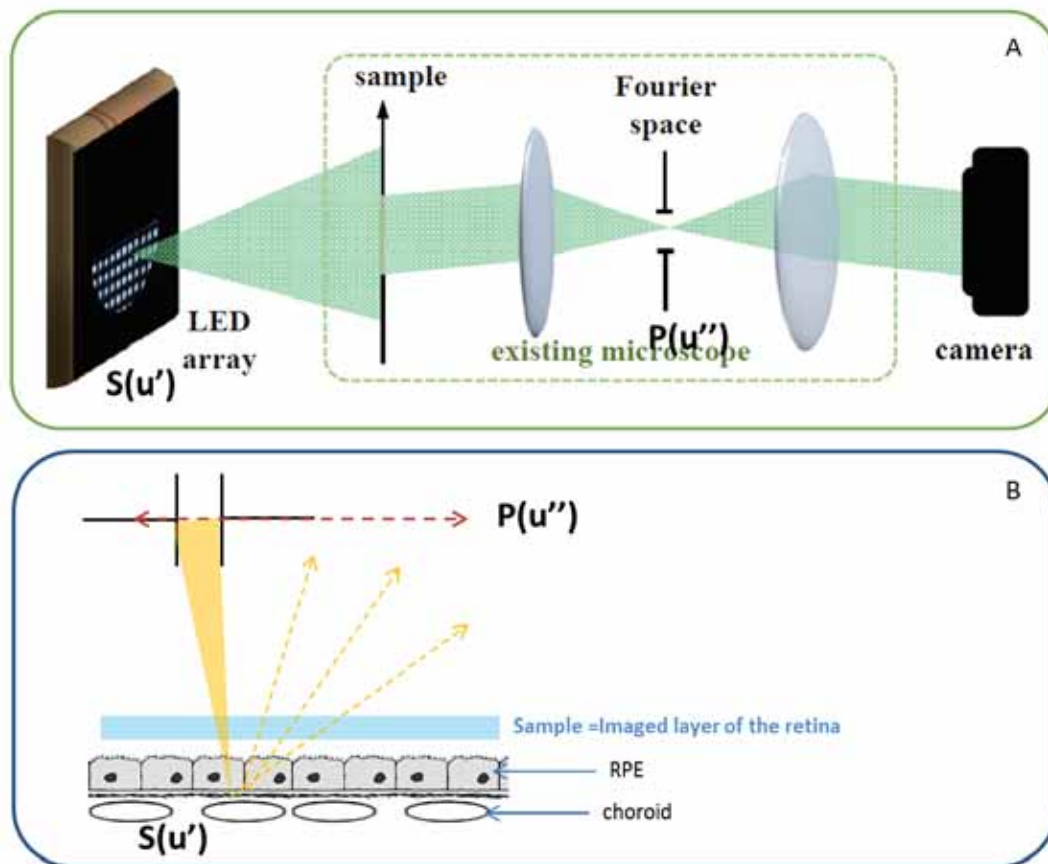


FIGURE 5.2: (A) Imaging set-up from [77] describing oblique illumination differential phase contrast. LED array microscope with a programmable source sufficiently far from the sample to be in Fourier space.  $P(u'')$  is the pupil function with  $u''$  the coordinates at the pupil plane (Fourier space).  $S(u')$  is the illumination distribution function, with  $u'$  the coordinates at the source plane. (B) Schematic drawing of the retina translating of the model from [77] to our optical set-up.  $P(v)$  and  $S(v)$  are the pupil function and illumination distribution function, with  $v$  the coordinates at the eye pupil plane.

When considering a thin sample, in our case the layer of the retina we are imaging, we can write its complex transmission function:  $o(r) = \exp[-\mu(r) + i\phi(r)]$ , where  $\mu$  and

$\phi$  characterizes the sample absorption and phase respectively and  $r$  is the spatial coordinates at the sample plane. If we adopt the weak phase approximation, the complex transmission function of the sample can be linearized and neglecting the cross terms between  $\mu$  and  $\phi$  is given by:  $o(r) \approx 1 - \mu(r) + i\phi(r)$ . This approximation can be used when the object is weak (with low absolute phase or amplitude)[79–81]. The sample is illuminated by an incoherent illumination source with an intensity distribution  $S(u')$ , with  $u'$  the coordinates on the source plane and the system pupil is described by the pupil function  $P(u'')$  (on the Fourier space). Figure 5.2 shows the optical system of this model where the oblique illumination is achieved by illuminating half a circle of LED array.

Using this model we can write the intensity spectrum at the camera plane as the sum of multiplications between optical transfer functions for absorption ( $h_{abs}$ ) and phase ( $h_{phase}$ ) and the Fourier transform of the physical quantities absorption  $\mu$  and phase  $\phi$ [77, 82]:

$$\tilde{I}(u) = B\delta(u) + H_{abs}(u) \cdot \tilde{\mu}(u) + H_{phase}(u) \cdot \tilde{\phi}(u) \quad (5.1)$$

Where  $B$  represents the background term measuring the total energy passing through the optical system, and the terms  $H_{abs}$  and  $H_{phase}$  are the transfer functions for absorption and phase, respectively. The Weak-Object Transfer Functions (WOTF) for both amplitude and phase can be derived[77, 82–84]:

$$B = \iint S(u')|P(u')|^2 d^2 u' \quad (5.2)$$

$$H_{abs}(u) = -\left(\iint S(u')P^*(u')P(u'+u)d^2 u' + \iint S(u')P^*(u')P(u'-u)d^2 u'\right) \quad (5.3)$$

$$H_{phase}(u) = i\left(\iint S(u')P^*(u')P(u'+u)d^2 u' - \iint S(u')P^*(u')P(u'-u)d^2 u'\right) \quad (5.4)$$

Equations 5.3 and 5.4 provide general expressions for WOTF of absorption and phase since it can be applied to any illumination patterns and pupil functions. In Differential Phase Contrast (DPC) method, the acquisition of two images for each axis direction enables us to calculate the phase contrast image of the sample[85, 86], here a layer of the retina. For one direction the phase contrast image  $I_{DPC}$  is given by:

$$I_{DPC} = \frac{I_{\theta} - I_{-\theta}}{I_{\theta} + I_{-\theta}} \quad (5.5)$$

where  $I_{\theta}$  and  $I_{-\theta}$  represent images illuminated with opposite angle of incidence.

We can consider that when using the strong back-scattering from the RPE, we approximate the conditions from [77] leading to the same optical effect that can be described with the theoretical model presented above. Figure 5.2 (B) shows a schematic drawing showing how the obliquity is also obtain by shifting the illumination with respect to the system pupil. In [77] they achieve this shift by illuminating half of a circle LED array (shown in Fig. 5.2 (A)) while in our case we use an aperture stop at a pupil plane. Additionally, our system can be considered aberration-free where our pupil function is a circular function with a radius set by the numerical aperture of the system, and is thus real and symmetrical. With these hypotheses, we can derive the following conclusions. The absorption transfer function  $H_{abs}$  is symmetric while the phase transfer function  $H_{phase}$ , on the other hand, is asymmetric [77, 82]. We derive the specific transfer functions for the DPC image[77]. Given that the effective illumination source of the DPC image is anti-symmetric: 1) The

background term  $B$  and the DPC absorption transfer function  $H_{abs}^{DPC}$  are cancelled. 2) The DPC phase transfer function  $H_{phase}^{DPC}$  is also anti-symmetric and non zero except along the axis of asymmetry. It is interesting to note that in the case of well aligned system the two terms from the transfer function  $H_{phase}$  from Eq. 5.4 cancel out while the subtraction becomes non zero when there is an asymmetry of the illumination distribution with respect to the system pupil. The interest of doing a differential contrast image is to suppress the term of background and absorption that can reduce the contrast of the final image.

In conclusion, when imaging a transparent and weak phase sample the intensity at the camera can be separated in three terms, a background intensity, an absorption intensity and a phase intensity. This last one, which is canceled out in the case of well aligned detection and illumination pupils of the system, becomes visible by the camera when we introduce the asymmetry between pupils (or obliquity of illumination) while the other two remain unchanged by the asymmetry. Therefore, if we acquired two images of the same structure illuminated through two opposite angles we should obtain at the camera two images with opposite phase information and the same absorption and background information.

An adaptation of the oblique back-illumination technique has been implemented for retinal imaging using transcleral illumination [87]. Indeed, the retina is a thick sample which seems well suited for this oblique microscopy technique. The retina has a deep layer, the retinal pigment epithelium, which strongly back-scatters and therefore could be used as the deeper layer serving as secondary source. Additionally, the retina is a transparent organ with several layers which imply that if we only consider the layer or structures of interest to be our sample, we can hypothesize these structures phase to be sufficiently small to use the weak phase approximation adopted for this technique. In the following Part.III we will describe how to implement this phase imaging in our AO-FIO by changing the angle of incidence of the illumination beam of the AO-FIO onto the retina.

### 5.1.2 Structured Illumination Microscopy

Another full-field microscopy technique that could be adapted in the AO-FIO system is Structured Illumination Microscopy (SIM). This method has been developed in microscopy to improve resolution and optical sectioning of the image and consists in manipulating the illumination of the sample by superimposing a grid pattern and shifting or rotating it while acquiring the images. Computational techniques are applied to the images in order to remove the effect of the structure and to extract high frequency spatial information leading to a reconstructed final image with a lateral resolution improved with respect to the one obtain with diffraction-limited instruments.

Indeed, the spatial resolution in a diffraction-limited incoherent optical system can be described by the point spread function (PSF), which is obtained from the square of the Fourier transform of the aperture. The corresponding Optical Transfer Function (OTF), the autocorrelation of the aperture, is equal to zero beyond the cut-off frequency  $f_c$  which implies that all spatial information beyond that limit is lost. The idea of SIM is to inject high frequency information inside the support of the OTF by means of amplitude modulation before the convolution, i.e., SIM introduces aliasing through modulation to gain information beyond  $f_c$ . Indeed, multiplying a signal by a sinusoid consists simply in modulating in amplitude such signal. Therefore, spatial frequencies of the modulated signal will appear symmetrically on either side of the frequency scale around the modulation frequency specified by the sinusoid (which translates in three deltas of Dirac in the Fourier domain

shown in Fig. 5.3 for one direction  $x$ ). This leads to the transfer of spatial frequencies beyond the cut-off of the optical transfer function (OTF) to the observable frequency region that can be reassigned to their correct position through specific post-processing.

The illumination modulation pattern in both spatial and frequency coordinates is expressed as:

$$m(x, y) = I_0 \left( 1 + \alpha \cos(2\pi(k_x x + k_y y + \phi)) \right), \quad (5.6)$$

$$M(f_x, f_y) = I_0 \left( \delta(f_x, f_y) + \frac{\alpha}{2} \delta(f_x - k_x, f_y - k_y) e^{+2i\pi\phi} + \frac{\alpha}{2} \delta(f_x + k_x, f_y + k_y) e^{-2i\pi\phi} \right), \quad (5.7)$$

where  $(x, y)$  and  $(f_x, f_y)$  are, respectively, spatial and frequency coordinates. Parameter  $\alpha$  is the modulation depth and  $\phi$  is the phase shift of the sinusoid. With this modulation, three deltas in the Fourier domain are introduced by the pattern and placed on the frequencies  $(0, 0)$ ,  $(k_x, k_y)$  and  $(-k_x, -k_y)$ .

The spectrum  $G(f_x, f_y)$  of an image observed on a microscope characterized by an OTF  $H(f_x, f_y)$  of an object  $f(x, y)$  (with continuous Fourier transform  $F(f_x, f_y)$ ) multiplied by the pattern defined by Eq. 5.6 is given by:

$$G(f_x, f_y) = I_0 H(f_x, f_y) \left( F(f_x, f_y) + \frac{\alpha}{2} F(f_x - k_x, f_y - k_y) e^{+2i\pi\phi} + \frac{\alpha}{2} F(f_x + k_x, f_y + k_y) e^{-2i\pi\phi} \right). \quad (5.8)$$

This equation can be rewritten as:

$$G(f_x, f_y) = D_0(f_x, f_y) + D_-(f_x, f_y) + D_+(f_x, f_y), \quad (5.9)$$

where  $D_0(f_x, f_y) = I_0 H(f_x, f_y) F(f_x, f_y)$  is the conventional wide-field image and  $D_-(f_x, f_y)$  and  $D_+(f_x, f_y)$  are the terms which translate portions of the object's Fourier transform that usually lie outside the pass-band of the system and are inaccessible in a conventional image into the pass-band of the system [88].

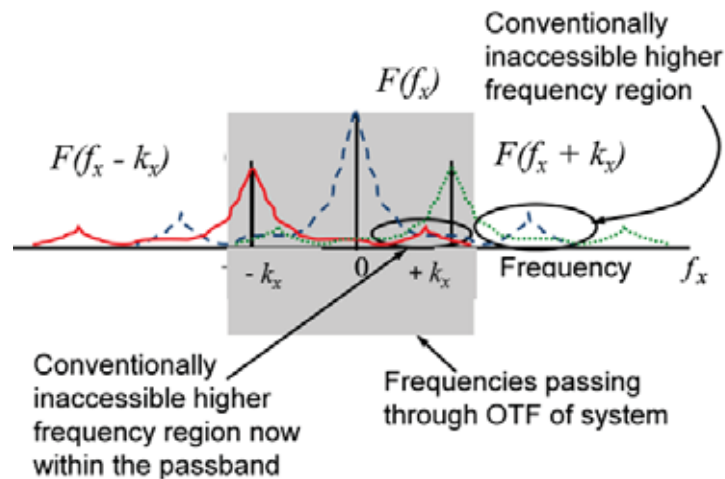


FIGURE 5.3: Visualization of the Fourier transform of a structured illumination image [88].

Since in the expression for  $G(f_x, f_y)$  (Eq. 5.9) there are three unknowns corresponding to the three different components  $D_0(f_x, f_y)$ ,  $D_-(f_x, f_y)$  and  $D_+(f_x, f_y)$ , at least three

images need to be acquired with different phase information to derive them. In the original method [89] this is solved taking three images corresponding to different modulation phase shifts of  $\phi = 0$ ,  $\phi = 2\pi/3$  and  $\phi = -2\pi/3$ . Finally, the same procedure must be repeated with the orientation of the sinusoidal pattern rotated of  $60^\circ$  and  $120^\circ$  in order to cover all possible directions in the Fourier space.

Both of these microscopy techniques can potentially be translated to wide field imaging with an ophthalmoscope using adaptive optics. In both cases it implies the manipulation of the illumination geometry. The next section explores the two illumination geometries required in our AO-FIO to achieve those modalities.

## 5.2 Building a new illumination path

In the previous section we described the microscopy configurations that could be adapted to AO-FIO and which are based on the manipulation of the illumination geometry of the sample. We discussed the possibility of readjusting these modalities to the case of a thick sample such as the retina which is imaged in a epi-illumination configuration. In this section we explore the potential illumination geometries to implement in our AO-FIO system that would include those readjustments before we detail the development of a new illumination path.

### 5.2.1 Deriving two illumination geometries

The principle of the oblique microscopy described above is to generate phase information of the sample in the imaging camera plane by introducing an asymmetry in the illumination. In Subsect. 5.1.1, we defined how this obliquity could be applied to a thicker and scattering sample like the retina leading us to the conclusion that the illumination beam should either irradiate next to the region of interest or reach the retina with various angles of incidence. Additionally, in order to achieve structure illumination in the retina we need to be able to project fringes of different sizes and in different directions on the retina. We have deduced that to exploit the phase contrast we need to modify our imaging system so as to control the shape of the illumination at the retinal plane (or sample plane) and to control the angle of incidence of the beam to the retinal plane.

Indeed, our whole optical system is the AO-FIO including the retina as a sample, meaning that the lens of the eye serves as the last lens in the optical system. As it was described in Ch. 4 the illumination of the retina in our AO-FIO is achieved by imaging a Superluminescent Diode (SLD) onto the retina. In Fig. 5.4 we show two schematic drawings with the two illumination geometries we wish to obtain and the planes of the eye in which the illumination must be manipulated. Figure 5.4(A) corresponds to the control of the shape of the illumination. This modulation of the illumination takes place at the sample plane, i.e. the retina, which in our system is conjugated with the focal planes, including the imaging camera plane. Therefore, manipulating the illumination at the retina implies a modulation of the illumination at a focal plane in our AO-FIO system. On the other hand, Fig. 5.4(B) shows the variation of the incident angle of the illumination beam. To control this angle  $\Theta'$  we must be able to apply a shift to the position of the illumination beam at the pupil plane of the eye: the eye lens. The AO-FIO has been designed in order to have the eye lens plane conjugated with all the pupil planes of the system. Thus, a shift in

the eye pupil plane implies a modulation of the illumination at a pupil plane of the system.

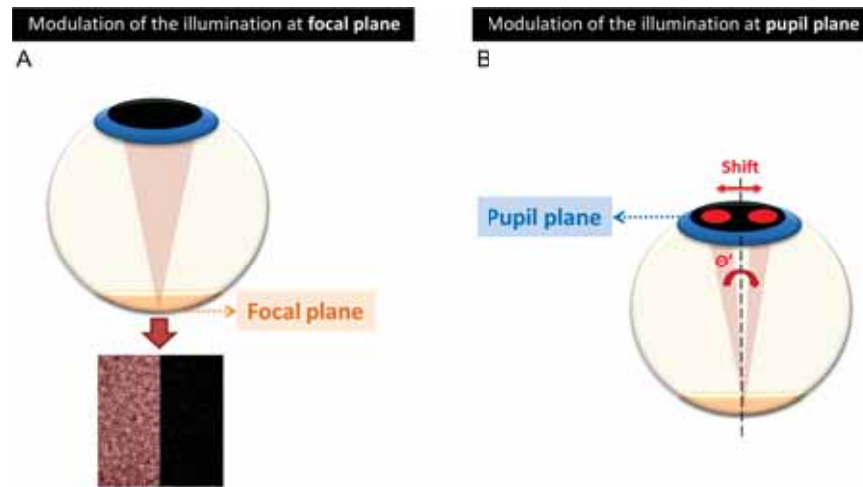


FIGURE 5.4: Schematic drawings of two manipulations (or modulations) of the illumination of the retina. (A) Modulation of the illumination at the focal plane of the eye, i.e. the retina or sample plane. The modulation consists in changing the shape of the illumination at the focal plane, in the schematic drawing an example of illumination shape is presented where the field of view on the photoreceptors is partially illuminated by the near-infrared light. (B) Modulation of the illumination at the pupil plane of the eye, i.e. the eye lens or eye pupil. The modulation consists in shifting the illumination beam size and position at the pupil plane, which leads to different incidences onto the retina.

We have determined two illumination geometries inspired from full field microscopy along with the planes in the eye, focal or pupil, where the beam need to be manipulated. From these definitions we have then derived the optical design of a new illumination for our system allowing both geometries.

### 5.2.2 Optical design

Two possible methods to achieve the illumination modulations shown in Fig. 5.4 are presented in Fig. 5.5 in the form of two schematic layouts. First, in order to achieve a modulation of the illumination at a focal plane, we have selected a Spatial Light Modulator (SLM) working in a reflection configuration as shown in Fig. 5.5(A). When the illumination is focused on the device, we can apply a shape to the SLM that is projected to all the following focal planes, including the retina. Figure 5.5(B) presents the manipulation of the illumination at a pupil plane to vary the angle of incidence of the illumination on the retina. The modulation is conducted by introducing a stop aperture at a pupil plane followed by tip-tilt mirror which can shift the position of the illumination beam at the next pupil planes, including the eye lens.

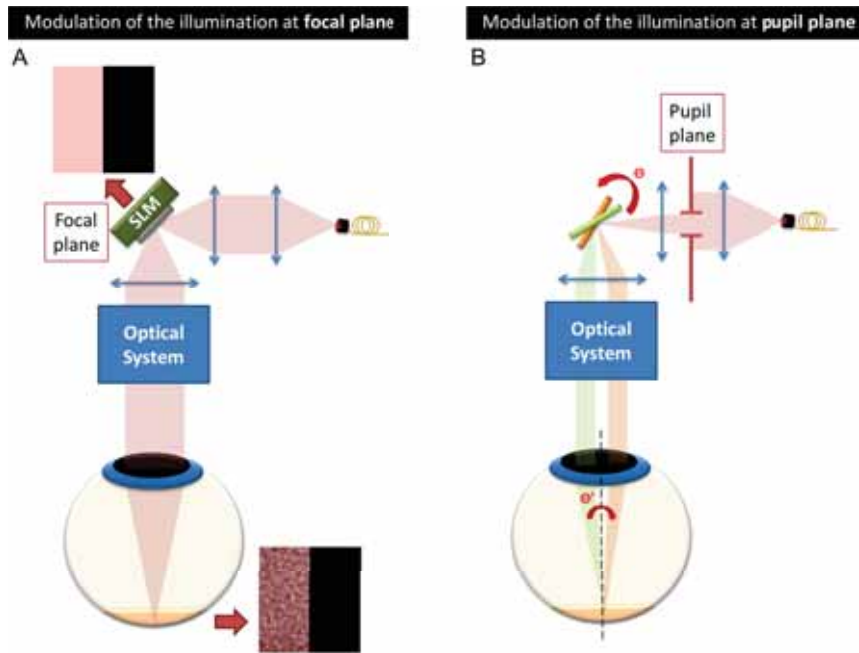


FIGURE 5.5: Schematic layouts of two optical manipulations on the AO-FIO system allowing the illumination modulation at the focal and pupil planes described in Fig. 5.4. (A) corresponds to the focal plane modulation, meaning the projection of patterns on the retina. An SLM is placed at the focal plane conjugated to the retina. This SLM is an array of micro-mirrors that can take ON positions, reflecting the light towards the retina and OFF positions, discarding the rest of the photons out of the optical system. The illumination pattern is then formed at the SLM plane and is then projected by the whole optical system (including the lens of the eye) onto the retina. (B) corresponds to the pupil plane modulation, meaning the shift of the illumination beam at the eye pupil leading to varying incidence on the retina. The shift at the pupil plane is achieved by introducing an aperture stop at a pupil plane, which reduces the size of the beam, before a tip-tilt mirror placed at the next focal plane. The mirror is depicted in green at the first position and orange after a rotation of an angle  $\Theta$ . The rotation leads to a variation in the angle of incidence of the illumination (the two different incident beams are depicted in green and orange in association with their respective mirror positions).

An optical design of a unique illumination path including both modulations from Fig. 5.5 has been conceived and is presented in Fig. 5.6. The new illumination path is highlighted in yellow in Fig. 5.6(A) inside the AO-FIO layout and a zoom of this subsystem is shown in Fig. 5.6(B). We can identify all the key elements described in Fig. 5.5 enabling the two illumination geometries: an SLM is placed in a focal plane after a 2F system D18-D17 imaging the light source. This SLM reflects a selected pattern towards the D16 lens, the next element in the optical path, in a  $24^\circ$  angle. After the D16 lens, an aperture stop is placed in the next pupil plane limiting the pupil of the system. The light is then focused by D15 onto a tip-tilt mirror placed in a focal plane. The rotation of this mirror will shift the image of the pupil created by the aperture stop by the 2F system D15-D14 in any direction of the following pupil plane.

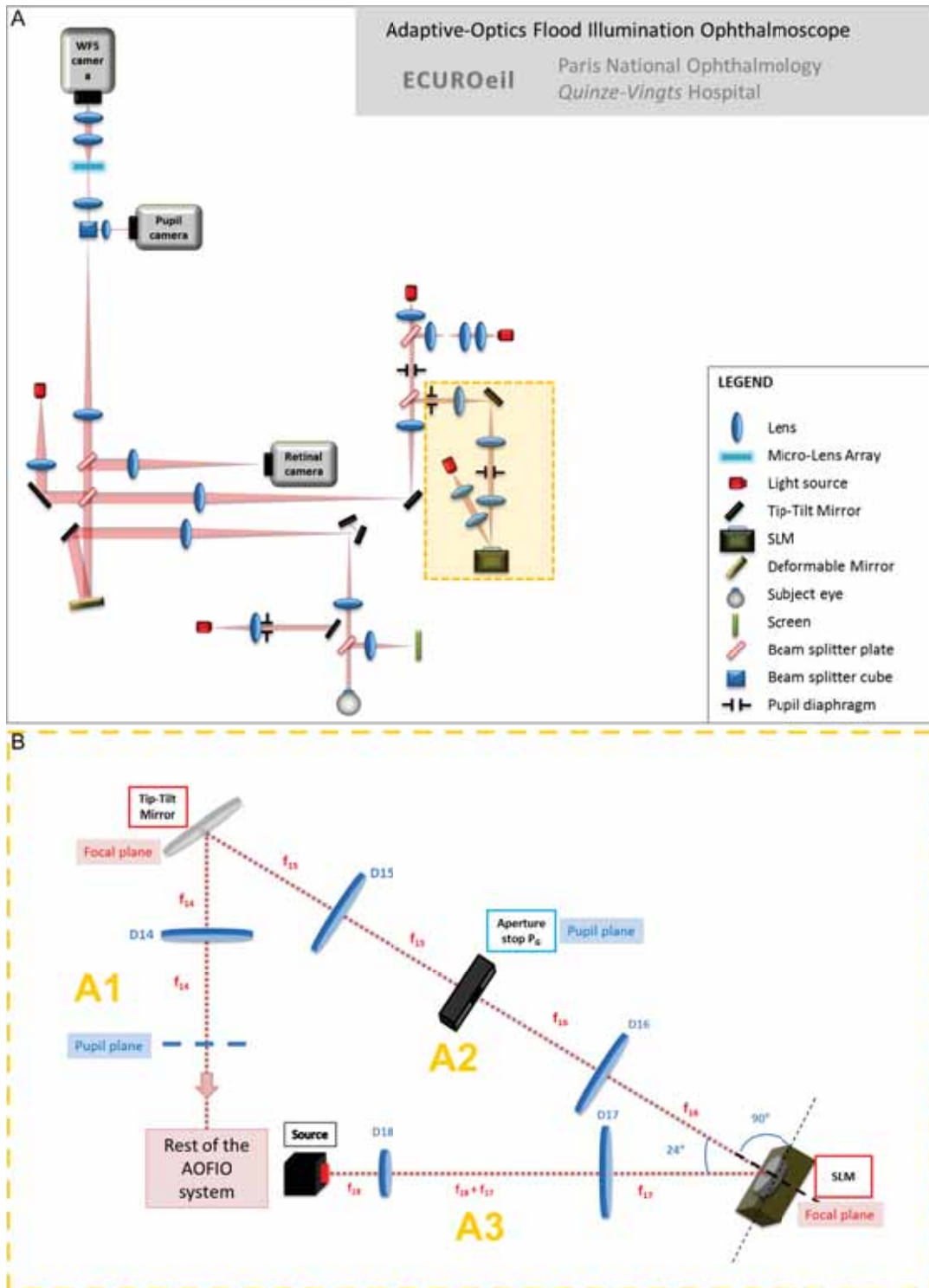


FIGURE 5.6: (A) Schematic layout of the PARIS AO-FIO system with the new illumination path. (B) Zoom of the new illumination path. {A1, A2, A3} three optical axis of the illumination subsystem. {D14 – D18} Optic lens of different focal distances:  $f_{18} = 20\text{mm}$ ,  $f_{17} = 50\text{mm}$ ,  $f_{16} = 75\text{mm}$ ,  $f_{15} = 75\text{mm}$ ,  $f_{14} = 50\text{mm}$ .

When doing the modulation in the focal plane, the aperture stop  $P_G$ , is selected to have the size of the current pupil system, i.e. 5mm at the eye pupil plane, and the tip-tilt mirror is in resting mode with a  $45^\circ$  angle. When the modulation in pupil plane is being

conducted, the SLM reflects all the beam like a flat mirror, a smaller aperture diameter is selected for the  $P_G$  aperture stop and the tip-tilt mirror is being powered to achieve rotation.

The implementation of this subsystem is detailed in the following subsection.

### 5.2.3 Implementation

The new illumination path designed in the previous subsection is composed of the optical elements shown in Tab. 5.1.

#### Optical elements of the path

Optical element	Symbol	Description
Lens	D18	f18=20mm
Lens	D17	f17=50mm
Lens	D16	f16=75mm
Lens	D15	f15=75mm
Lens	D14	f14=50mm
SuperLuminescent Diode	Source	$\lambda=860\text{nm}$
Spatial Light Modulator	SLM	Digital Micromirror Device array
Aperture block	PG	Manufactured piece
Tip-tilt mirror		Physik Instrument piezo-electric mirror

TABLE 5.1: Optical elements of the new illumination path.

The aperture block is a manufactured piece allowing the screwing of different aperture sizes. The light source selected here is the same SuperLuminescent Diode than our current AO-FIO system described in Ch. 4. A more exhaustive description of the two last elements of this table, the SLM and the tip-tilt mirror is given below.

#### Digital Micromirror Device as SLM

We have chosen as SLM an array of mirror known as Digital Micromirror Device (Keynotes, USA). The micromirrors are diamond shaped and can be set into two positions by a rotation of a  $\pm 12^\circ$  tilt angle: mirrors in the ON position or  $+12^\circ$  reflects the light towards the rest of the system while mirrors in  $-12^\circ$  discard the light outside of the optical system. The micromirror array is controlled through a computer using a specific software, from which we can set the shapes to project onto the retina. Binary images with black pixels correspond to mirrors in OFF state and white pixels to those in ON state.

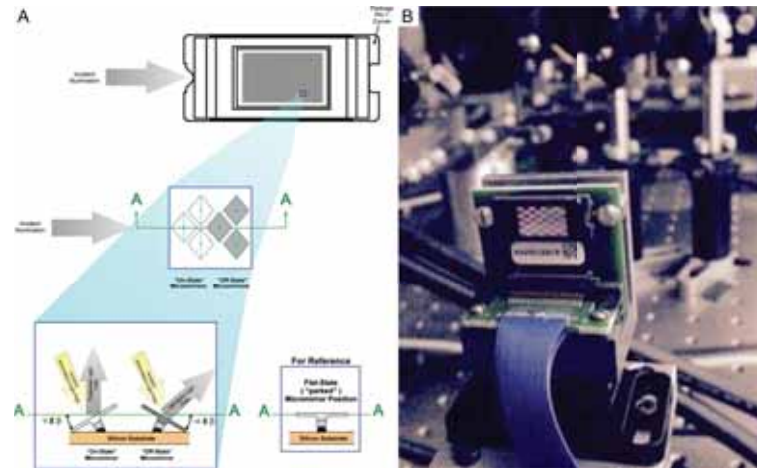


FIGURE 5.7: (A) Schematic drawing of the SLM selected to project pattern in the retina: a Digital Micromirror Device. A zoom shows a few of the micro-mirrors from the SLM array. These diamond-shaped mirrors can be set into two positions, as shown in the bottom of the layout, corresponding to OFF state and ON state. The mirror stays in a Flat state when not powered. [Credits: <http://www.ti.com/lit/ds/symlink/dlp4500.pdf>] (B) Picture of the SLM in our experimental set-up. A checkered board appears in the mirrors array where dark regions correspond to OFF states and bright regions to mirror in ON state.

### S-334 Piezo tip-tilt Mirror

Finally the tip-tilt mirror acquired is Physik Instrument piezo-electric mirror (see Fig. 5.8), powered by an electrical supplier and controlled through a computer using a custom made LabVIEW software (National Instruments, USA).



FIGURE 5.8: Picture of the piezo-electric tip-tilt mirror selected

The tip-tilt mirror has been chosen so as the maximum angle of incidence we can achieve with our system be limited by the diameter of the system pupil. We have computed this maximum value which corresponds to a position of the illumination pupil as close to the edge of the eye pupil as possible. The maximum shift that the mirror must achieve in order to shift the illumination beam up to the edges of the eye pupil is 2.5mm in every direction, corresponding to a mechanical rotation of the tip tilt mirror of  $\pm 15\text{mrad}$ , which falls inside its specifications (cf. Tab. 5.2 for the details of the requirements and specifications of the tip-tilt mirror).

	<b>Requirements Tip-tilt mirror</b>	<b>S-334.2SL Characteristics</b>
<b>Shift of the illumination pupil at the eye lens plane</b>	$\pm 2.5$ mm	$\pm 4.2$ mm
<b>Optical tilt angle of mirror</b>	$\pm 30$ mrad	$\pm 50$ mrad
<b>Mechanical tilt angle of mirror</b>	$\pm 15$ mrad	$\pm 25$ mrad
<b>Tilt frequency</b>	200Hz	1kHz
<b>Tilt accuracy</b>	$\sim 200 \mu\text{rad}$ (taking $\sim 10 \mu\text{m}$ illumination pupil position tolerance at eye lens plane)	$5 \mu\text{rad}$

TABLE 5.2: Table showing the requirements in tilt angle, frequency and position accuracy necessary to the piezo electric mirror for our application and the selected mirror characteristics. The S-334.2SL mirror largely verifies all the mechanical requirements.

### Alignment procedure

Accurately placing the optical elements in position is essential to the correct functioning of this new illumination subsystem. The new light source, SLM and tip-tilt mirror must be placed at planes conjugated with the focal planes of the system, as well as the pupil planes of this new path being well conjugated to and aligned with the pupil planes of the existing AO-FIO system. A summary of the implementation procedure undertaken to place, align and calibrate the elements of this new illumination path is presented in this subsection.

Each optical element has first been placed at its approximated position using a millimeter ruler for distances and a protractor for angles, then has been more accurately aligned using optical alignment tools such as afocal telescopes or viewfinders.

As shown in Fig. 5.6(B) the new illumination path has three optical axes  $\{A1, A2, A3\}$ . The elements of the A1 axis have been sequentially aligned one after the other until the tip-tilt mirror while the elements of axis A2 and A3 excepting the SLM have been aligned separately. Then, each aligned ensemble A2 and A3 has been placed in the optical bench and aligned with respect to the tip-tilt mirror and SLM.

The optical elements of this subsystem are placed either in a pupil plane or a focal plane of the system separated by an optical lens placed in a 2F configuration.

#### *Alignment of elements in pupil planes*

In this new subsystem, elements placed in a pupil plane are all aperture stops with three degrees of freedom. The alignment procedure for the two elements in pupil planes consists in finding the longitudinal position of the pupil plane in the optical axis and then achieving a transverse alignment of the plane in order to be centered with as well as parallel to the rest of the pupil planes of the system.

The longitudinal alignment is achieved by first illuminating an element of the AO-FIO system in a pupil plane using a pocket lamp, for instance at the deformable mirror. Then we have placed the viewfinder in the new illumination path close to the pupil position and

have fixed it when seeing the image of the deformable mirror illuminated by the lamp. The optical element in the pupil plane, for instance an aperture stop in A1 Pupil plane, is placed using a millimetre ruler at its position. The aperture was then slid while illuminating it with a lamp until a sharp image of the aperture can be seen in the viewfinder. Both the image of a pupil plane of the current AO-FIO system and the aperture we want to place appear in the same plane through the viewfinder. The transverse alignment of the pupil has been achieved after having placed all the elements of the new path. Then we turned on the light source of this subsystem with a visible light and used the pupil camera of the AO-FIO. The Diagnostic path of the AO-FIO was used. We placed a paper in front of its light source and slid the path so the beam is reflected towards this diagnostic path and then reflected back towards the camera. We have used the aperture at the diagnostic pupil position whose size can be modified to center and align the pupils of the new path.

### *Alignment of optic lenses*

Optical lens are placed in a 2F configuration, meaning that pupil and focal planes in the subsystem are successively at the focal planes of the lenses or to infinity. After placing the lenses in their positions using the millimeter ruler we achieve a more precise alignment thanks to the afocal telescope. For instance, for the case of D14 we have illuminated with a lamp close behind the previously aligned aperture stop in A1. We have slid D14 until the image of the aperture looked sharp through the afocal telescope and fixed the longitudinal position. The transverse alignment of the lens is achieved through autocollimation. A mirror is stuck to the side of the lens looking towards the AO-FIO system where a visible beam is shot from the diagnostic illumination path. Using a paper in front of the Pupil plane in A1 we verify that the incoming and reflected beam are confounded.

### *Alignment of the elements at focal planes*

Three important elements are placed at focal planes of the system in this new illumination path: the new light source, the tip-tilt mirror and the SLM. The source as mentioned before is aligned separately when aligning the A3 axis. The two remaining elements are aligned in the following way.

The **tip-tilt mirror** has six degrees of freedom and has been aligned without being power supplied. The longitudinal position has been identified by first placing the viewfinder where the image of the diagnostic source looks like the sharpest point spread function. Then the mirror is slid until the residual dust on the middle of its surface looks sharp as well through the viewfinder. Then the mirror has been rotated with respect to the vertical and horizontal axes until the reflected beam is parallel to the table (i.e. it is not deviated) at a  $45^\circ$  angle with respect to axis A1. The correct position of the beam has been verified using a millimetered grid paper affixed to a bracket. An iteration of successive longitudinal and transverse alignment was necessary to achieve an accurate alignment of the mirror.

The **SLM** has been aligned after placing axis A2, which was aligned separately using the methods explained in the previous paragraph for lenses and aperture stop alignments. Using the diagnostic beam with visible light, the whole axis has been positioned so the elements are aligned with the optical axis drawn by the beam thanks to alignment apertures of half a millimeter placed on each lens as well as the aperture stop. Then, using the afocal telescope the image of the diagnostic source should be at the infinity of the D15 lens. The whole A2 axis is slid until the image of the point source looks sharp through the telescope.

The SLM is placed using a millimeter ruler at the focal plane of D16. Similarly to the alignment of the tip-tilt mirror we have used the viewfinder to accurately slide the SLM into its precise longitudinal position. The SLM has five degrees of liberty that we use to align the beam with the optical axis of A3. As mentioned before, the SLM is an array of micromirrors set into two positions of  $12^\circ$  with respect to the optical axis perpendicular to the array, and therefore when the SLM is placed orthogonal to the optical axis of A2, the optical reflection angles are  $24^\circ$  on each side depending if the mirrors are on ON or OFF state. We first have aligned the SLM by autocollimation orthogonal to the optical axis of A2 using the mirrors in resting state (without power supply of the SLM). Then when turning ON the SLM and setting all the mirrors in ON positions the beam is reflected with an angle of  $24^\circ$ . The A3 axis, which has been separately aligned as well, is then placed by centering its axis with the beam using alignment apertures. Using the afocal telescope, A3 axis is slid until the SLM is placed at the focal plane of D17.

#### 5.2.4 Difficulties and limitations

The first difficulty this alignment presented was the restriction in space. Since all the elements of this subsystem are confined in approximately a  $20 \times 50 \text{ cm}^2$  area, positioning the alignment tools was a challenge in such a reduced space. The second challenge was the alignment of the SLM. The array of micromirrors acts as a grating splitting the beam into various diffraction orders when using the visible point source. This effect led to several alignment and imaging limitations. The first consequence of this effect is related to the energy of the orders. Because of the micromirrors tilt, the grating is blazed and depending on the wavelength used and the angle of incidence on the grating the energy can be shifted from the higher orders towards the first order. Indeed, when rotating the SLM with respect to the vertical axis we have observed that the energy goes from being almost completely equally distributed between four orders to being almost fully concentrated in the first order. Since the four orders are separated by a few millimeters when reaching the next pupil plane after the SLM, the system pupil would filter out a large part of the energy. Therefore, we have to rotate the SLM so a maximum of the energy of the diffracted beam is concentrated in the first order. Additionally, there is an issue with the wavelength. We want to use the visible wavelength for this alignment, but the optimal angle in order to have the maximum energy in the first order varies with the wavelength, and is therefore going to change when using the near-infrared wavelength of our system. To solve this we have found an optimal angle in the visible light and then optimize it in the infrared using a watt-meter to identify the angle of the SLM giving the maximum energy.

Finally, even when finding this optimal angle for the diffraction, the pupil of the system filters out some of the diffracted light. This leads to a reduction of the quality of the pattern projection in the borders of the field of view and needs to be optimized in future work.

### 5.3 Structured Illumination Imaging

The implementation of the SLM in the new illumination path enables us to project patterns onto the retina, and can be used in particular to project the sinusoidal pattern necessary to develop structured illumination in our system. Adding to this the fact that the illumination is corrected for eye aberrations (cf.Ch. 4), the projection of such patterns was achieved on a human retina *in-vivo* and is presented in Fig. 5.9 (A).

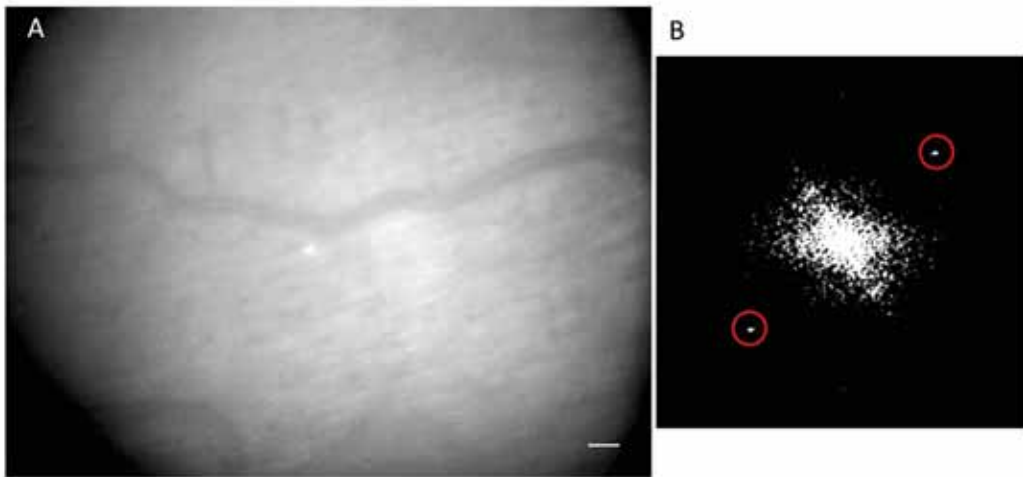


FIGURE 5.9: (A) Raw image of retinal vessels acquired with the new illumination path using a stripes pattern for structured illumination imaging. (B) Fourier Transform of the raw image showing the frequency signature of the pattern in the form of two peaks (red circles).

Figure 5.9 (B) shows the Fourier transform of the average image (A) of the object illuminated with a sinusoidal pattern. In this Fourier transform we can see the two peaks identified with the red circles which are the spectral signature of the fringes pattern. Therefore the new illumination path achieve the desired structuration of the illumination necessary for the development of this technique.

The work in this thesis concerning the SIM was limited to the manipulation of the illumination of the AO-FIO in order to be able to project the necessary structured illumination. The development of specific image processing was started by [90] and is the subject of another thesis currently in progress at ONERA and INSERM.

## 5.4 Conclusion

In this Chapter we have summarized the principal modalities from the field of microscopy that have inspired two new illumination geometries as well as the details of the implementation of the a new illumination path in our AO-FIO allowing such geometries. These two manipulations of the illumination allow the projection of patterns whose size, shape and position in the field of view can be easily modified. These illumination projections have been used to develop modalities improving the contrast and optical sectioning of the retina which are described in Chs. 6, 7. The second developed illumination geometry, i.e. the variation of angle of the incident beam on the retina, has led to two different imaging modalities. On the one hand, inspired from oblique microscopy, we have implemented phase imaging of the retina described in Ch. 8. On the other hand, this illumination incidence variation can be an instrument allowing a functional analysis of the photoreceptors: the derivation of their orientation. The details of this functional application are summarized in Ch. 9.

## **Part III**

# **Imaging instruments: Design, integration & testing**



The optimization of our experimental setup led to high quality brightfield images of very reflective structures such as photoreceptors and large vessels. However, the less contrasted and transparent structures were still hard or even impossible to see and required further development. The two modulations of the beam at the focal and pupil planes of the AO-FIO illumination path achieved in the previous Part II are exploited here together with specific image processing to develop more advanced imaging modalities. In the following two chapters composing this part, two imaging modalities are implemented with the modulation of the illumination at the focal plane: dark-field and pseudo-confocal imaging. A third instrument is developed in the last chapter of this part, which modulates the illumination at the pupil plane achieves the variation of the angle of the incidence of the beam and is adopted here to perform phase imaging. Another application for this last instrument is explained further in this thesis manuscript. In each of these chapters the details of the implementation steps as well as the resulting enhancement in image quality such as the improvement of contrast or optical sectioning are presented.



## Chapter 6

# Developing a dark-field modality in full field ophthalmoscope

### 6.1 Introduction to the article

In Ch. 5 we described oblique back-illumination microscopy as the method from a range of imaging modalities that would be best suited to be translated into our AO-FIO setup in order to visualize fairly transparent and hypo-reflective retinal structures. The idea of using modalities exploiting multiply scattered light came first from studies carrying out these kind of axis techniques in AO-SLO set-ups. In particular, Chui et al. hypothesized that such exploitation should be possible in wide field setup corrected with adaptive optics [9]. This hypothesis was validated by images obtained with our AO-FIO system near the lamina cribrosa region. Figure 6.1 (B) shows a vessel above the lamina cribrosa next to an average image of a vessel from the peripheral retina (Fig. 6.1(A)). The aspect of these vessels are completely different, with the peripheral vessel showing a standard bright-field contrast while more features, such as wall structure, can be visualized on the other vessel localized near the lamina cribrosa.

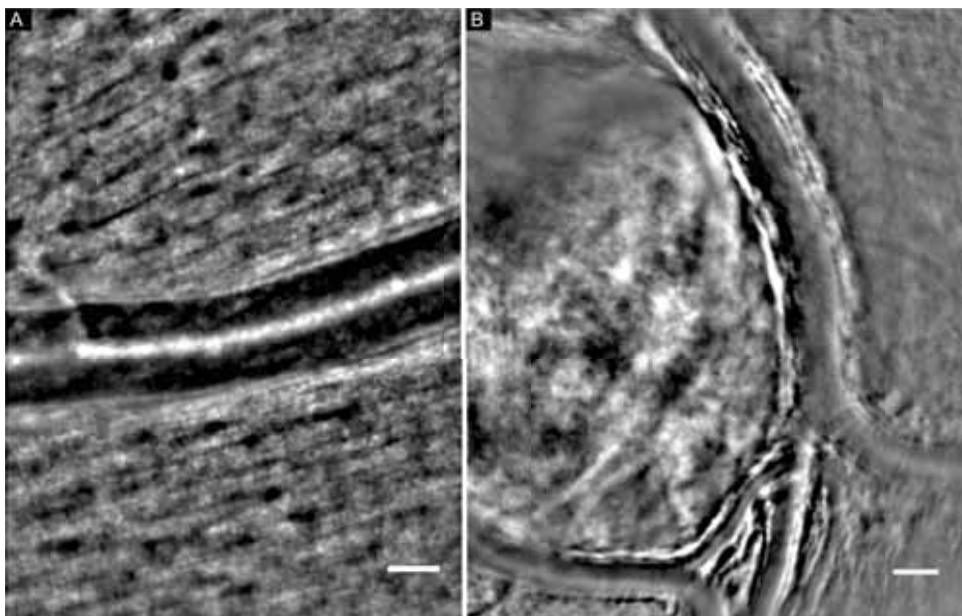


FIGURE 6.1: (A) Average image of a peripheral retinal vessel lying on the nerve fiber layer. (B) Average image of an artery above the lamina cribrosa. Scale bars are  $50\mu\text{m}$ .

Indeed, Fig. 6.1 (B) displays a contrast typical of dark-field imaging in AO-SLO. We interpreted this contrast as an effect of the strong back-scattering coming from the lamina

cribrosa that illuminates the vessel from below in a trans-illumination configuration. As observed in Fig. 6.1 (B), the lamina is not exactly below the vessel but has a slight off-set thus achieving an oblique illumination of the vessel. This dark-field contrast was then observed at the border of the illumination field of the AO-FIO (see Fig. 6.2) implying that the contrast typical from dark-field could be generated.

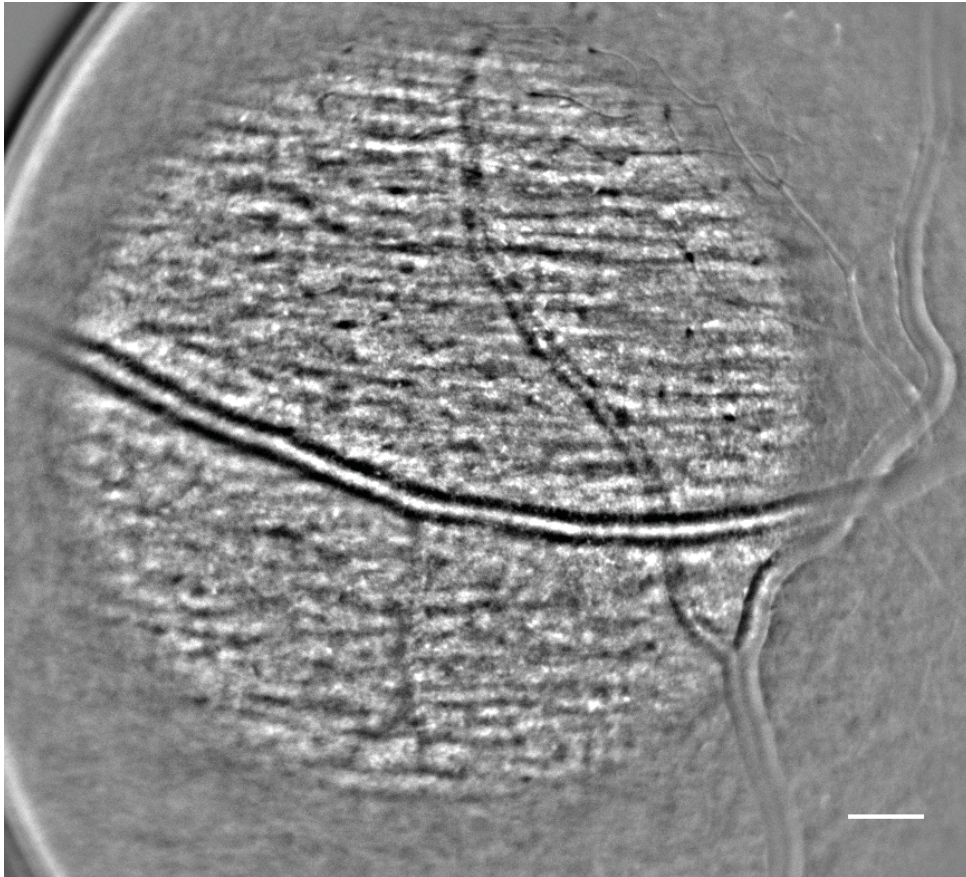


FIGURE 6.2: Average image of retinal vessels on a nerve fiber layer. Inside the circular illumination field of the AO-FIO we observe a standard bright-field contrast. On the right side of the image, outside the illumination field, the vessels show a contrast similar to the one observed in dark-field where capillaries appear visible and the nerve fibers signal is filtered out. Scale bar is  $100\mu\text{m}$ .

The aim of this Chapter is to show how such contrast can be generated through the manipulation of the illumination. In particular it describes the implementation of the dark-field modality in our AO-FIO using the projection of patterns onto the retina and the retinal structures revealed by the enhancement in contrast. The results of this work have been summarized in a scientific paper to be submitted to *Biomedical Express* and presented in the following section.

## 6.2 *Article in Progress*: Dark-field imaging using an Adaptive Optics Flood Illumination Ophthalmoscope

# Dark-field imaging using an Adaptive Optics Flood Illumination Ophthalmoscope

**ELENA GOFAS-SALAS,<sup>1,2,6</sup> PEDRO MECÊ,<sup>1,3,6</sup> FRÉDÉRIC CASSAING,<sup>1</sup> KATE GRIEVE,<sup>2,4,6</sup> CYRIL PETIT,<sup>1,6</sup> MICHEL PAQUES,<sup>4,6</sup> JOSÉ ALAIN SAHEL,<sup>2,5</sup> AND SERGE MEIMON<sup>1,6,\*</sup>**

<sup>1</sup>*DOTA, ONERA, Université Paris Saclay F-91123 Palaiseau - France*

<sup>2</sup>*Institut de la Vision, 17 rue Moreau, Sorbonne Universités, UPMC Univ Paris 06, INSERM, CNRS, 75012 Paris, France*

<sup>3</sup>*Quantel Medical, Cournon d'Auvergne, France*

<sup>4</sup>*CIC 1423, INSERM, Quinze-Vingts Hospital, Paris, France*

<sup>5</sup>*Department of Ophthalmology, The University of Pittsburgh School of Medicine, Pittsburgh, PA, United States*

<sup>6</sup>*PARIS group - Paris Adaptive-optics for Retinal Imaging and Surgery*

\*[serge.meimon@onera.fr](mailto:serge.meimon@onera.fr)

**Abstract:** Off-axis detection, only implemented on AO-Scanner Laser Ophthalmoscope(SLO), led to the detection of previously invisible structures like smaller capillaries blood flow, retinal pigmented epithelium and even retinal ganglion cells. Although this modality has an outstanding resolution, it suffers from SLO limitations, namely low pixel rate and distortion. We implemented a structured illumination on a high pixel rate FIO to obtain dark field images in order to detect these structures on a larger field at higher temporal resolution.

© 2018 Optical Society of America under the terms of the [OSA Open Access Publishing Agreement](#)

**OCIS codes:** (110.1080) Active or adaptive optics; (110.1220) Apertures; (110.2970) Image detection systems; (230.6120) Spatial light modulators; (330.4300) Vision system - noninvasive assessment.

## References and links

1. A. Roorda and D. R. Williams, "Optical fiber properties of individual human cones," *Journal of vision* **2**, 4–4 (2002).
2. N. M. Putnam, H. J. Hofer, N. Doble, L. Chen, J. Carroll, and D. R. Williams, "The locus of fixation and the foveal cone mosaic," *Journal of Vision* **5**, 3–3 (2005).
3. D. Merino, J. L. Duncan, P. Tiruveedhula, and A. Roorda, "Observation of cone and rod photoreceptors in normal subjects and patients using a new generation adaptive optics scanning laser ophthalmoscope," *Biomedical optics express* **2**, 2189–2201 (2011).
4. A. Dubra, Y. Sulai, J. L. Norris, R. F. Cooper, A. M. Dubis, D. R. Williams, and J. Carroll, "Noninvasive imaging of the human rod photoreceptor mosaic using a confocal adaptive optics scanning ophthalmoscope," *Biomedical optics express* **2**, 1864–1876 (2011).
5. D. Scoles, Y. N. Sulai, and A. Dubra, "In vivo dark-field imaging of the retinal pigment epithelium cell mosaic," *Biomedical optics express* **4**, 1710–1723 (2013).
6. T. Y. Chui, D. A. VanNasdale, and S. A. Burns, "The use of forward scatter to improve retinal vascular imaging with an adaptive optics scanning laser ophthalmoscope," *Biomedical optics express* **3**, 2537–2549 (2012).
7. T. Y. Chui, S. Mo, B. Krawitz, N. R. Menon, N. Choudhury, A. Gan, M. Razeen, N. Shah, A. Pinhas, and R. B. Rosen, "Human retinal microvascular imaging using adaptive optics scanning light ophthalmoscopy," *International journal of retina and vitreous* **2**, 11 (2016).
8. D. Scoles, Y. N. Sulai, C. S. Langlo, G. A. Fishman, C. A. Curcio, J. Carroll, and A. Dubra, "In vivo imaging of human cone photoreceptor inner segments," *Investigative ophthalmology & visual science* **55**, 4244–4251 (2014).
9. E. A. Rossi, C. E. Granger, R. Sharma, Q. Yang, K. Saito, C. Schwarz, S. Walters, K. Nozato, J. Zhang, T. Kawakami *et al.*, "Imaging individual neurons in the retinal ganglion cell layer of the living eye," *Proceedings of the National Academy of Sciences* **114**, 586–591 (2017).
10. T. N. Ford, K. K. Chu, and J. Mertz, "Phase-gradient microscopy in thick tissue with oblique back-illumination," *Nature Methods* **9**, 1195 (2012).
11. T. Laforest, D. Carpentras, C. Moser, and M. Künzi, "System, method and apparatus for retinal absorption phase and dark field imaging with oblique illumination," *Tech. rep.* (2017).
12. D. Carpentras, T. Laforest, M. Künzi, and C. Moser, "Effect of backscattering in phase contrast imaging of the retina," *Optics express* **26**, 6785–6795 (2018).

13. E. Gofas-Salas, P. Mecê, C. Petit, J. Jarosz, L. M. Mugnier, A. M. Bonnefois, K. Grieve, J. Sahel, M. Paques, and S. Meimon, "High loop rate adaptive optics flood illumination ophthalmoscope with structured illumination capability," *Applied optics* **57**, 5635–5642 (2018).
14. D. Gratadour, L. Mugnier, and D. Rouan, "Sub-pixel image registration with a maximum likelihood estimator-application to the first adaptive optics observations of arp 220 in the L' band," *Astronomy & Astrophysics* **443**, 357–365 (2005).
15. I. Standard, "15004," *Ophthalmic optics and instruments* (2007).
16. A. E. Elsner, S. A. Burns, J. J. Weiter, and F. C. Delori, "Infrared imaging of sub-retinal structures in the human ocular fundus," *Vision research* **36**, 191–205 (1996).
17. A. Roorda, Y. Zhang, and J. L. Duncan, "High-resolution in vivo imaging of the rpe mosaic in eyes with retinal disease," *Investigative Ophthalmology & Visual Science* **48**, 2297–2303 (2007).
18. J. I. Morgan, J. J. Hunter, B. Masella, R. Wolfe, D. C. Gray, W. H. Merigan, F. C. Delori, and D. R. Williams, "Light-induced retinal changes observed with high-resolution autofluorescence imaging of the retinal pigment epithelium," *Investigative ophthalmology & visual science* **49**, 3715–3729 (2008).
19. E. A. Rossi, P. Rangel-Fonseca, K. Parkins, W. Fischer, L. R. Latchney, M. A. Folwell, D. R. Williams, A. Dubra, and M. M. Chung, "In vivo imaging of retinal pigment epithelium cells in age related macular degeneration," *Biomedical optics express* **4**, 2527–2539 (2013).
20. C. E. Granger, D. R. Williams, and E. A. Rossi, "Near-infrared autofluorescence imaging reveals the retinal pigment epithelial mosaic in the living human eye," *Investigative Ophthalmology & Visual Science* **58**, 3429–3429 (2017).
21. T. Liu, H. Jung, J. Liu, M. Droettboom, and J. Tam, "Noninvasive near infrared autofluorescence imaging of retinal pigment epithelial cells in the human retina using adaptive optics," *Biomedical optics express* **8**, 4348–4360 (2017).
22. Z. Liu, O. P. Kocaoglu, and D. T. Miller, "3d imaging of retinal pigment epithelial cells in the living human retina," *Investigative ophthalmology & visual science* **57**, OCT533–OCT543 (2016).
23. L. Tian and L. Waller, "Quantitative differential phase contrast imaging in an led array microscope," *Optics express* **23**, 11394–11403 (2015).
24. C. E. Granger, Q. Yang, H. Song, K. Saito, K. Nozato, L. R. Latchney, M. M. Chung, B. T. Leonard, , D. R. Williams, and E. A. Rossi, "Human retinal pigment epithelium: in vivo cell morphometry, multi-spectral autofluorescence, and relationship to cone mosaic," *Investigative Ophthalmology & Visual Science* (2018).

---

## 1. Introduction

The introduction of Adaptive optics (AO) into ophthalmic systems supplied diffraction-limited retinal images enabling the visualization of individual retinal cells such as photoreceptors [1, 2]. In particular thanks to the enhancement of contrast in AO Scanning laser ophthalmoscopy (AO-SLO) brought by the implementation of a confocal pinhole, filtering out the out of focus light, more details were revealed such as the smaller cones and even sometimes the rod mosaic [3, 4].

However, some retinal features still remained invisible, such as retinal pigment epithelium (RPE) or capillaries. This is due to their low reflectivity compared to the nerve fibers or photoreceptor mosaic whose strong back-scattering masks these structures' signal in standard bright-field images. The development of off axis techniques exploiting the multiply scattered light led to the visualization of these microscopic transparent retinal structures. RPE imaging [5] as well as microvascular mapping [6, 7] was achieved thanks to dark-field implementation in AO-SLO, which consists in shifting the confocal AO-SLO pinhole in order to filter out the strong back-scattered signal as well as to detect forward scattered photons from the hypo-reflective structures of interest. Another off-axis technique, known as split-detection, which is based on the subtraction of the detected light from two opposite shifted pinholes with respect to the confocal pinhole position, also enhances AO-SLO image contrast enabling the imaging of photoreceptors inner segments [8]. Finally, multi-offset imaging, a more complex configuration of the split technique, led to the in vivo visualization of very transparent ganglion neurons with AO-SLO [9]. Even though only implemented in AO-SLO, Chui et al. hypothesized [6] that dark-field could be achieved in AO Flood Illumination Ophthalmoscope (AO-FIO) too since multiply scattered photons were also detected by the full field camera. Indeed, AO-FIO, though less used than its scanning version because of its lower contrast, has the advantage of benefiting from a potential large field and high acquisition rate as well as being free of distortion. These implementations inspired from microscopy methods that led to unprecedented high-contrast in vivo imaging of the retina with AO-SLO could be implemented in AO-FIO. However, unlike AO-SLO, multiply

scattered photons cannot be isolated at the detection plane in the full field configuration, making it necessary to explore a different approach.

In full field microscopy, Ford et al. [10] developed a technique known as phase imaging with oblique back-illumination. This imaging technique developed to image thick transparent objects, which cannot be imaged in classical bright-field epi- or trans- illumination configuration. The obliquity is achieved in the thick sample by illuminating on the side of the region of interest, where in the deeper layers of this sample the light is back-scattered towards every direction. This strongly scattering layer becomes a secondary source and the region of interest is therefore trans-illuminated in this configuration by an oblique beam. This obliquity introduces an asymmetry between the illumination and detection pupils of the system which alters the Fourier spectrum of the imaged sample leading to an intensity variation at the camera plane related to phase gradient variations generated by the sample. In particular, the more shifted the pupils, the more the ballistic photons, not affected by the sample, are filtered out. We reach dark-field configuration when all the ballistic photons have been filtered out. Oblique illumination in retinal imaging in vivo has been explored by La Forest et al. [11, 12]. This team used transcleral illumination of the RPE, which is a strongly scattering layer, in order to create a secondary illumination source that illuminates the rest of the layers in a trans-illumination configuration. Indeed, the retina is a thick sample where most of the layers are weak scattering transparent tissues and can therefore in this configuration lead to phase contrast. Even though this technique achieved the imaging of very low contrasted retinal features, it requires a high power light source being a potential hazard to the subject. A similar configuration to the one achieved by Ford et al. [10] could be implemented in AO-FIO by partially illuminating the imaged field of view. To do so, we have used the PARIS AO-FIO system [13] where the illumination is corrected by the deformable mirror ensuring the control of the illumination reaching the retina.

## **2. Methods**

### *2.1. Adaptive optics instrumentation*

This experiment has been carried out using the PARIS AO-FIO previously described in detail in [13]. In short, our system wavefront and imaging light sources are Superluminescent Diodes (Omicron) with nominal centre wavelengths of 750 and 860 nm, respectively. The system pupil size, defined by the deformable mirror (DM) diaphragm, is 5 mm at the eye pupil plane, which implies a theoretical lateral resolution of approximately  $2.9 \mu\text{m}$ . Images were acquired at a frame rate of 200 Hz with a field of view of  $5.4^\circ \times 2.7^\circ$ .

### *2.2. Generating dark fields using a field stop*

In order to generate a dark-field image on the AO-FIO we first modified the illumination geometry by adding a field stop at a conjugated plane of the retina (plane D on the layout in Fig.1)). The shape of the diaphragm is then imaged onto the retina creating dark areas in the imaging field of view. The field stop used was square shaped with a diagonal length of 5 mm and with a 2 mm separation in between (see Fig.3(a)). Images acquired with this set-up had simultaneously bright and dark fields.

### *2.3. Generating dark fields using a pattern projector*

In order to be able to generate dark-field images anywhere on the field of view and easily adapt the geometry of these dark fields, a new illumination path was built including a Spatial Light Modulator (SLM) at a focal plane conjugated of the retina. The SLM is a Digital Micromirror Device (DLP4500, Keynotes, USA) consisting in a  $912 \times 1140$  micromirrors array each diamond-shaped with a diagonal pitch of  $7.6 \mu\text{m}$ , which corresponds to around  $2 \mu\text{m}$  in the retinal plane.

Mirrors can be set into two positions, "ON" and "OFF" states, by tilting them of  $\pm 12^\circ$  with respect to the parked state ( $0^\circ$ ). This leads in this set-up to bright or dark fields respectively on the retina. The axis of rotation of the micromirrors of the SLM was set vertically in order to be orthogonal to the optical axis of our system. The nominal SLM total optical efficiency results essentially from the diffraction efficiency (89%) and the fill factor (92%). The same imaging source as the one of the old illumination path of the PARIS AO-FIO was used. The details of this subsystem providing structured illumination are shown in the schematic drawing in Fig.1.

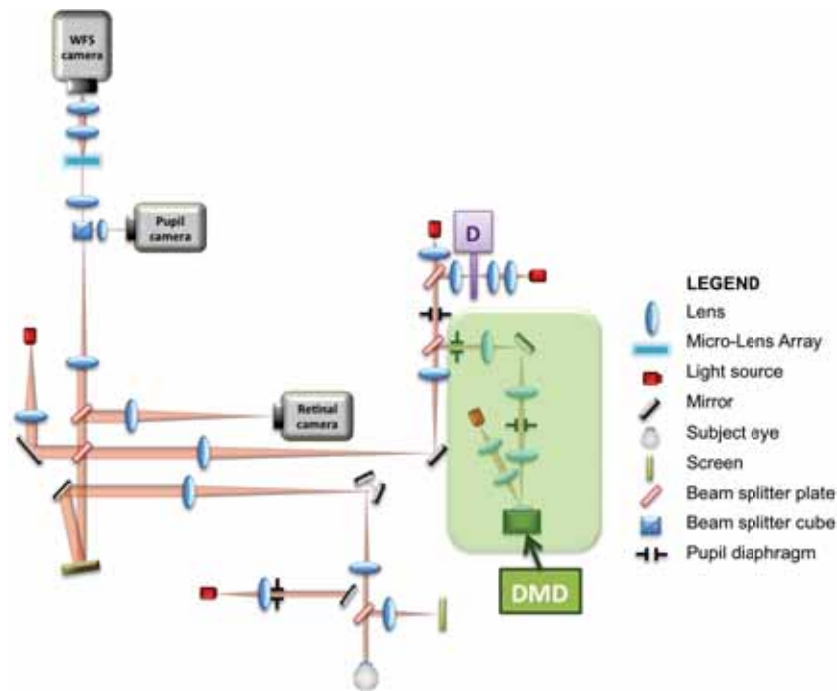


Fig. 1: Schematic drawing of the AOFIO. D marks the field diaphragm plane used in the first Dark Field set-up. Shaded in green is the new illumination path including a projector (DMD) a plane conjugated with the retina enabling to image different pattern shapes to generate dark fields.

#### 2.4. Image acquisition

Video frames of typically 1000 images were acquired on every subject with standard and modified illumination. The regions of interest in this study were the fovea and the peripheral retina. The imaging camera was focused on the photoreceptor layer and a layer containing vessels respectively.

#### 2.5. Image processing

All images were corrected for the inhomogeneity in illumination created by the multiscattering of the light beam in the retina by subtracting from each frame the low-passed filtered image from the image itself [13]. For each sequence, images were aligned using custom-built registration algorithms [13]. These algorithms compute correlation maps between each frame and then derive the shifts in horizontal and vertical directions necessary to align it to the reference frame using *Maximum A Priori* theory [14].

For video frames with dark areas generated with the field stop, binary masks adapted to the

shapes of the illumination were used to limit the image areas on which registration algorithms realize the computations only to the bright zones. For sequences generated while using the pattern projector, each frame was divided by an average of the non aligned image sequence before applying registration. This ensures the alignment is based on the retinal structures and not the shapes of the patterns. Average images were computed from all aligned image sequences.

## 2.6. Subjects

A chin and head rest was used to stabilize the subject's head. Acquisition on several healthy subjects was carried out during this experiment. They were asked to fixate the image of a blue target with a moving dot, which enables us to guide the patient sight and to explore various areas of the retina. Every participation followed institutional guidelines and adheres to the tenets of the Declaration of Helsinki. Informed consent was obtained from subjects after the nature and possible outcomes of the study were explained. The total light energy entering the eye from the illumination source and the WFS source are respectively under  $400 \mu\text{W}$  and  $2.8 \mu\text{W}$ , which is less than half the power stipulated by the ocular safety limits established by ISO standards for group 1 devices [15].

## 3. Results

### 3.1. Dark-field contrast at the boundaries of standard AO-FIO illumination

Average images obtained using standard AO-FIO leads to the usual bright-field contrast inside the illuminated area. We noticed though a typical dark-field contrast close to the illumination boundaries.

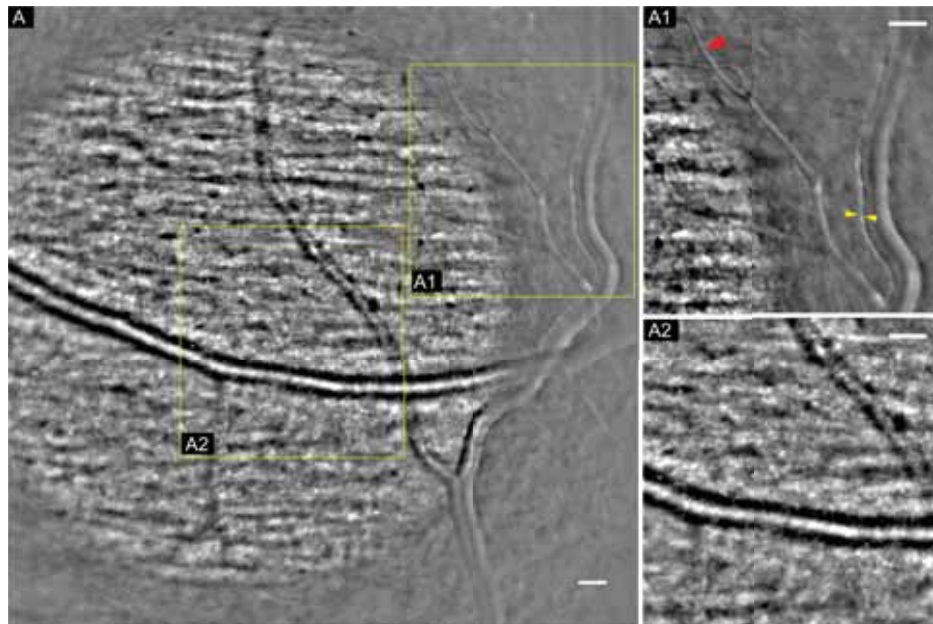


Fig. 2: (A) Average image of a vessel bifurcation obtained from an image sequence acquired in standard bright-field configuration using the old illumination path of the AO-FIO. (A1,A2) Zooms of two regions of (A) with bright-field and dark-field contrast respectively. Scale bars are  $50 \mu\text{m}$ .

Figure 2 shows an example from an image sequence using the standard configuration. Two

different contrasts can be appreciated in the two branches of the vessel in the bright and the dark region respectively. The border between bright and dark fields is visible in Fig.2 (A1), where, nerve fibers are clearly resolved on the left part of the image while invisible on the right. This image displays a zoom of a dark area of the field of view where capillaries (red arrowhead) are revealed while the strongly reflective signal of nerve fibers is filtered out. Additionally, vessel walls (yellow arrowheads) are also revealed in the dark-field area unlike in the vessels situated in the bright field in Fig.2(A2) where the specular reflection from the upper part of the vessel wall dominates the contrast. The light beam is focused on the retina and reaches its various layers. One portion of the photons entering the retina is single back-scattered by strongly reflective features like nerve fibers and vessel walls (Fig.2(A2)), the other portion is multiply scattered through the deeper layers, such as the RPE or the choroid [5, 16]. Multiply scattered photons are then scattered back through the retina and back to the detector generating the dark-field like images of Fig.2(A1).

### 3.2. Dark-field contrast using a field stop

A field stop was used to create a dark field in the middle of the field of view. Figure 3 (B) shows an example of an image of retinal vasculature obtained with the square shaped field stop. In this set-up a dark area is generated between two bright areas, increasing the number of edges between bright and dark fields. Admittedly, multiple scattering implies a loss of energy which means that the multiply scattered photons cannot be detected far off the illuminated areas. In this case the increase of contrast does not appear on the dark area but close to the border of the illumination.

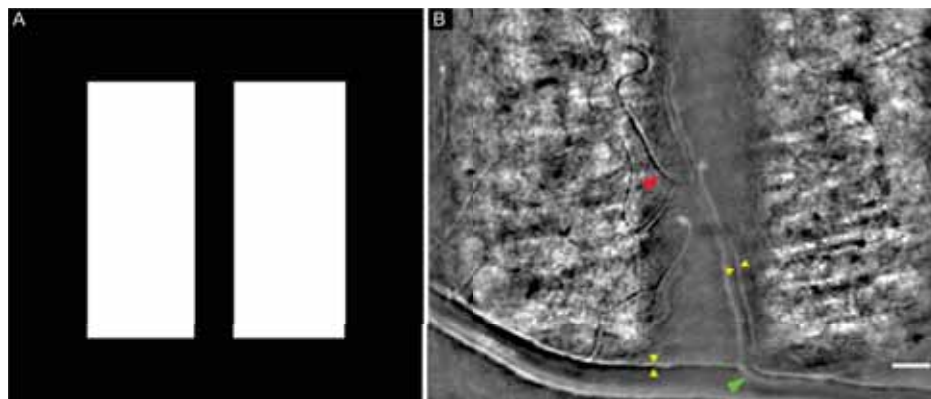


Fig. 3: (A) Schematic drawing of the square field stop used. White areas corresponding to the illumination region of the field of view and black to the dark fields. (B) Average image of retinal vasculature obtained with the square field stop shown in (A). Red arrowhead shows the confluence between a vein and a venule. Scale bar is 50  $\mu\text{m}$ .

Observations similar to the images acquired with standard illumination can be made on images obtained using a field stop. The nerve fibers are clearly visible in the two bright fields of image Fig.3 (B) while they are filtered out in the dark areas generated by the field stop. Capillaries, hardly visible in the illuminated areas, appear contrasted at the boundaries of the illumination too (red arrowhead). Finally, vessel wall contrast is enhanced in dark-field areas (yellow arrowheads). An interesting detail revealed in dark-field is the confluence of a venule with a vein. A white trace (green arrowhead in Fig. 3 (B)) appears where both flows of the venule and the vein meet, suggesting they do not mix. This type of observation cannot be made in bright-field contrast,

where the image is dominated by the specular reflection of vessels wall.

### 3.3. Dark-field contrast using an SLM for pattern projection on the retina

The field stop enabled us to generate dark field images of features of interest by asking the subject to follow the target. However, this set-up only allows us to use part of the field of view, losing one of the principal advantages of the AO-FIO, which is a larger field. The new illumination path includes an SLM that projects patterns onto the retina allowing us to choose the shape and size of the dark fields and eventually obtain the dark-field contrast over the whole field of view.

Figure 4 shows two averaged images of the same region of the peripheral retina with standard illumination (A) and projecting a pattern onto the retina (B) respectively. We were able to observe the same enhancement in contrast noticed in the two experimental set-ups described above. Capillaries (red arrowheads) are revealed in the dark fields, such as in the yellow and green zoom of Fig.4, and vessels appear more contrasted, including a better definition of their walls (yellow arrowheads), like in the red and green zoom of Fig.4. Finally we notice that the SNR of dark-field areas is very low, leading to a good contrast only close to the boundary of the illumination.

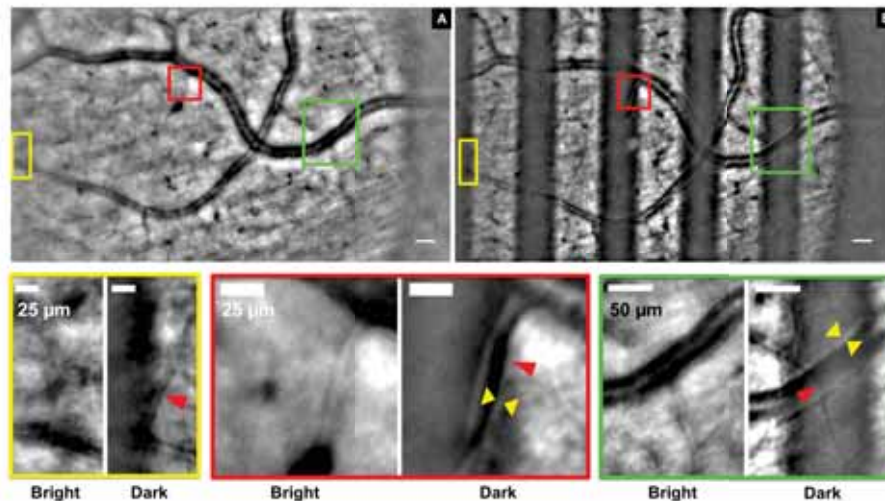


Fig. 4: Two average images of the peripheral retina showing a vessels crossing with (A) standard AO-FIO illumination and with (B) a stripes pattern illumination using the SLM. Three areas are zoomed to show the differences in contrast between bright-field (left images marked "Bright") and dark-field (right images marked "Dark") configuration. The yellow zooms show how a vessel invisible in bright-field appears in dark-field (red arrowhead). The red zooms show an improvement in contrast of a small capillary (red arrowhead) and how its walls appear more defined in the dark-field (yellow arrowheads). Finally the green zooms show again a difference in contrast which allows in the dark-field to observe on the one hand the walls (yellow arrowheads) of one of the vessels crossing, and on the other hand to image a small capillary (red arrowhead) underneath this same vessel.

Image sequences at the foveal region were also acquired. Figure 5 shows an average image from a video acquired on this region while illuminating the retina with a striped pattern. In this image photoreceptors appear contrasted in the bright stripes, i.e. the illuminated areas of the field of view, while other structures with lower contrast are visible in the dark stripes. These structures are particularly defined in the region of interest inside the yellow boxes of Fig.5. A zoom of this

mosaic presented in Fig. 5 (B) shows the details of the mosaic where a red arrow identifies one cell. This image also shows an adjacent bright field where lies the photoreceptors mosaic, which enables us to qualitatively appreciate the larger size and spacing of the cell mosaic on the left compared to the photoreceptor mosaic. Using Image J (National Institutes of Health, USA), we manually measured their size and spacing in each of the yellow boxes finding average values of  $10 \pm 2 \mu\text{m}$  and  $14.5 \pm 2 \mu\text{m}$  respectively. Those values match the dimensions of the RPE cells in this foveal region suggesting that what we are observing may be RPE cells thanks to the filtering out of the strong back-scattering from the photoreceptor layer in dark-field.

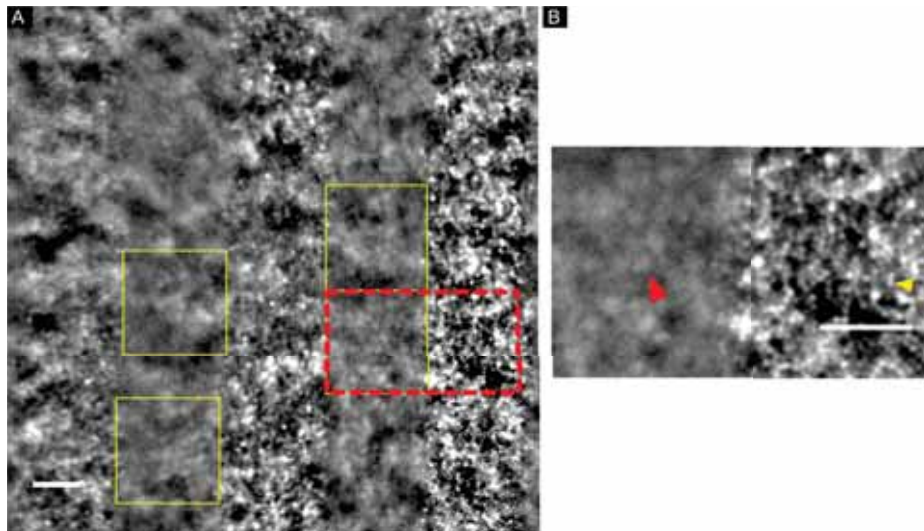


Fig. 5: Average image of an image sequence acquired near the foveal region using a striped pattern illumination. A zoom (red rectangle in dashed line) showing a zoom of both dark and bright fields. Yellow boxes show the areas where the density of this large cell mosaic have been computed. (B) Zoom from (A) (highlighted in a red dashed line) showing on the right photoreceptor cells and on the left cells in a mosaic larger than the photoreceptor mosaic and having a spacing and size corresponding to Retinal Pigmented Epithelium (RPE) cells in this region of the retina. Scale bars are  $50 \mu\text{m}$ .

#### 4. Discussion

Although our PARIS AO-FIO has a high temporal and spatial resolution and many retinal structures can be resolved with it [13], the contrast of some transparent layers of the retina remained too low to be visualized. The aim of this work was to develop dark-field imaging on our AO-FIO system in order to improve the contrast of these weakly transparent structures by exploiting their strong scattering. The obtained results have revealed in dark-field regions previously invisible retinal features with a contrast similar for most cases to the one observed in AO-SLO images acquired with off-axis techniques.

Average images of vasculature shown in the Results section display a contrast typical of dark-field imaging revealing previously invisible vascular features. Figure 2 shows how the strong back-scattered signal from the fibers dominating the image (A2) is filtered out in the dark area of the field of view (A1) enabling us to visualize capillaries and the vessels lumen, and like in AO-SLO dark-field we are able to identify the vessels wall too. These vascular features appear also very clearly in Fig. 3 (B) at the boundaries between the dark and the bright fields. The lumen and wall of the large vessel in the bottom of the average image can be easily identified due to

the fact that this multiply scattered signal is not masked here by the back-scattered light from the crest of the vessel. Likewise, capillaries appear highly contrasted at the boundaries of the field stop illumination where there is no strong signal from nerve fibers. Figure 6 details our interpretation of the generated phase-like contrast. Fig.6(B) shows a schematic drawing of a cross-section of the retina where for simplification purposes we have only drawn the RPE, the retinal nerve fiber layer (RNFL) and a few vessels in between. This schematic layout shows the illumination configuration of our system where only part of the field of view is illuminated. The RPE is a scattering tissue and therefore photons are multiply scattered towards adjacent tissues. This light reaches, for instance, the vessel drawn next to the illumination boundary (in Fig. 6 (B)) in an oblique trans-illumination configuration. Fig.6(A1-A3) shows three ray tracing when the trans-illumination light from the RPE reaches the vessel at three different points. The vessel has different tissues with different refractive index that induce different phase shifts and therefore the scattering angle varies too. Because the system has a finite pupil and an asymmetry of the illumination, the amount of light filtered at the pupil plane generates intensity variations at the camera plane. This is indeed what we observe in the dark regions as shown in Fig.6(C) where the vessel walls appear visible and highly contrasted. In particular ballistic photons from the background are highly filtered out which leads to a partial optical sectioning previously nonexistent in AO-FIO imaging.

However, we noticed a difference between the dark-field contrast generated at the boundaries of the standard illumination (Fig. 2) and at the boundaries of the field stop (Fig. 3) or SLM illumination (Fig. 4). In the first case, we were able to image retinal structures quite distant to the illuminated field (up to 200  $\mu\text{m}$ ) in the second case the contrast seems to decrease within a fairly short distance (50  $\mu\text{m}$  to 100  $\mu\text{m}$ ). The main difference between the dark regions in Fig. 2 and Fig. 3, 4 is that in the first case we are illuminating only from one side while on the other two cases there are bright fields on both sides of the dark field. Indeed, in accordance with the phase gradient imaging theory, if we illuminate a sample, here retinal vessels, from two opposite incident angles then the phase gradient variations obtained would be opposed. When analyzing the images from Fig. 3 and Fig. 4 we notice that high contrast is obtained near the borders of the illumination but in the center of the dark region the contrast is lower, which could be due to an illumination of this central area by two opposite incident beams and leading to complementary phase variations. In particular in Fig. 3(B) we have the two configurations, where in the dark central region of the image we observe this contrast restriction while the large vessel at the bottom seems highly contrasted for a longer distance.

Near the foveal region we were able to visualize another previously invisible structure. Figure 5 shows an average image of this region where we identify cells that could be RPE cells as they display the same size and spacing. Imaging RPE is challenging since their back-scattered signal is very weak and is therefore masked by the photoreceptor layer. En-face images of these cells were first realized on AO-SLO on subjects suffering from pathologies where the photoreceptor layer is degenerated enabling the detection of photons from the RPE layer [17]. The development of modalities that increase image contrast by either increasing the signal coming from the RPE layer or by filtering out strong surrounding signals on AO-SLO led to RPE en-face images on healthy subjects. For instance, auto-fluorescence imaging reveals RPE cells by only detecting the excited photons from fluorophores inside these cells [18–21]. Off-axis techniques like dark-field or multi offset imaging in AO-SLO have exploited the scattering properties of the RPE by removing the single back-scattered signal coming from the retina and only detecting the multiply scattered light, increasing this way the contrast of the RPE layer [5]. Finally, Miller et al. achieved RPE imaging using AO-OCT [22]. Their contrast is due to intracellular organelle movements and long duration averaging, requiring long imaging session making it hard to exploit the technique in a clinical setting. Figure 5 shows a cell mosaic larger than the photoreceptor mosaic whose characteristics suggest they could be RPE cells. It is interesting to note that the aspect of these

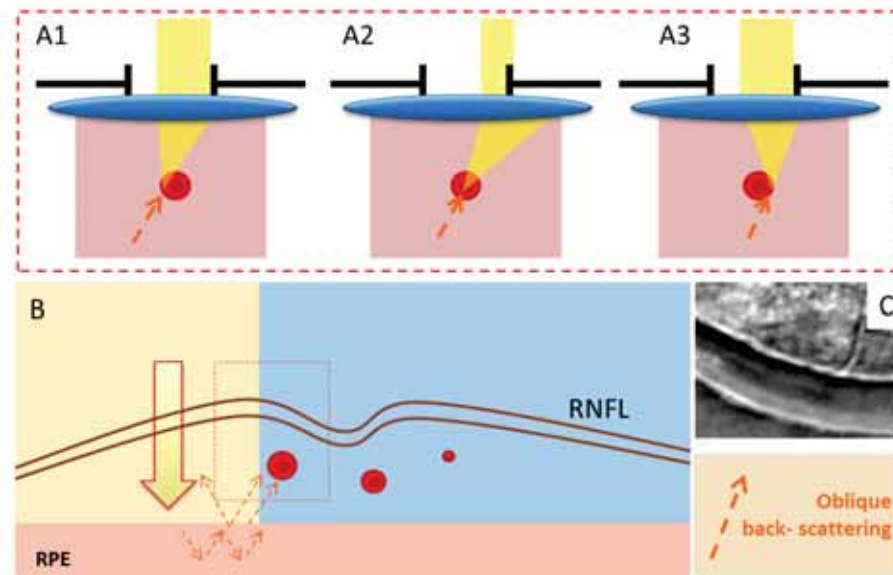


Fig. 6: (A1,A2,A3) Schematic drawings inspired from Ford et al. [10] of oblique trans-illumination of a vessel where the scattered light is partially blocked by the system aperture (the image of this aperture is drawn in black on the eye pupil). The variations of the index of refraction at different points of the focal plane (here the vessel) lead to different angles of refraction, which generates intensity changes at the image plane related to the phase of the sample. (A1,A2) show the refraction of the light reaching the sides of the vessel where the index of refraction leads to refracted angles allowing more light through the system aperture. (A2) shows the light reaching the center of the vessel where the refraction angle is lower and a higher amount of the refracted light is filtered out by the system pupil. (B) Schematic drawing of the cross-section of the retina where the field of view is partially illuminated. Light is multiply scattered by the RPE leading to oblique illumination of the closest vessel. (C) Cropped area of Fig.3 in dark-field illumination, it illustrates the effect explained in (A1,A2,A3) where the borders of the vessels are brighter than the center. This phase-like contrast typical in AO-SLO dark-field enables the visualization of the vessel walls and lumen.

cells is very different to what is typically seen in the other modalities of RPE images. While other techniques have revealed a mosaic of large cells with a dark nucleus surrounded by a bright body, here we observe the inverse contrast with cells displaying a bright nucleus and dark body. We interpret this observation as an effect induced by our illumination configuration. Indeed, the cells mosaic in Fig. 5 is trans-illuminated by two oblique back-scattered beams on each side. The illumination beam from one of the side would lead to a particular phase variation different from the one generated by the illumination on the other side of the dark region. If the asymmetry of each illumination beam is complementary, i.e. it has opposite angles of incidence, then the superimposed phase variations would cancel, or at least be strongly reduced if the incident angles were not the exact opposite. This would lead to a darker body as its signal has been suppressed and a brighter nucleus as the absorption is doubled. On the contrary in techniques, like split-detection [8] or differential phase imaging [10, 23], the subtraction of images with opposite illumination doubles the phase related intensity variations while canceling the absorption contributions, leading in RPE images to the inverse contrast to that observed in our images. Although this mosaic has been observed on various regions of Fig. 5(A) field of view (yellow boxes), we have so far observed these cells on a single subject increasing the uncertainty on the results. Other hypothesis on the nature of these cells could be suggested such as being

averaged cone or rod mosaic or features from the choroid. Indeed the rod mosaic can have similar form and density to RPE at some far eccentricities [24], though not at the eccentricity imaged here, close to the fovea. The regularity and dimensions of the mosaic makes us incline towards the hypothesis of RPE imaging. This last hypothesis will be further investigated by achieving autofluorescence imaging of the RPE at the same region in order to compare the mosaic from both AO-FIO dark-field and autofluorescence.

#### *4.1. Limitations and future work*

The results shown in this study support the concept of imaging weakly reflective retinal structures using off axis techniques. Nonetheless, there are still a few limitations to the current technique. On the one hand the contrast of these weakly reflective features, although increased, remains quite low. This is partly due to the low signal to noise ratio of our images. Indeed, a new light source is soon going to be acquired as we are limited by the maximum power reached by the current light source. We believe this contrast can also be further increased by optimizing the illumination pattern and avoiding the canceling of the intensity variations related to the phase by averaging regions surrounded by bright fields.

On the other hand we face the limitations of our SLM. First, this device, which is an array of mirrors generates a diffraction in the reflected beam. This diffraction effect has a strong impact on our image quality which we believe is linked to the fact that we filter out some of the diffraction orders. A more optimized optical design of the illumination path with the SLM capturing all the orders would mitigate the observed deterioration of the image quality. Finally, the SLM is limited by high frequency noise due to a cyclic memory refreshment of the mirrors which has for the moment prevented us to achieve this off axis imaging in real-time. Nevertheless, this SLM is a great tool to look for the optimal illumination pattern as it is easy to vary its shape and size. A different SLM could be considered in the future if a particular pattern has proven the most efficient to achieve high contrast of transparent structures.

## **5. Conclusion**

This study demonstrated dark-field imaging in AO-FIO in healthy subjects. The results revealed weakly reflective retinal structures previously invisible such as capillaries or vessel walls, and a cell mosaic that could be RPE cells. This phase-like contrast has been achieved by implementing an asymmetric illumination inspired from oblique back-illumination [10]. Thanks to the strong back-scattering from deeper layers like the choroid and RPE adjacent dark regions have been trans-illuminated with tilted beams leading to intensity variations related to the phase gradients. The implementation of this technique in AO-FIO can be also used to further understand the origin of the off axis contrast in the retina as well as leading to a complementary imaging tool of these transparent layers.

### **Funding**

The research leading to these results has received funding from the European Research Council SYNERGY Grant scheme (HELMHOLTZ, ERC Grant Agreement # 610110), the Agence Nationale de la Recherche under grants CLOVIS3D (grant number ANR-14-CE17-0011) and the RHU LIGHT4DEAF (grant number ANR-15-RHUS-0001).

### **Disclosures**

The authors declare that there are no conflicts of interest related to this article.

### 6.3 Conclusion

The new illumination path implemented in our AO-FIO system, and described in Ch. 5, has led to the first development of dark-field modality in AO-FIO for retinal imaging in this Chapter. This modality, like in AO-SLO systems, relies in the selection of multiply scattered photons from all the back-scattered photons from the retina. Indeed, when we partially illuminate the retina, only the illuminated field of view scatters light back towards the camera, while the surrounding dark areas are back-illuminated by multiply scattering from deeper retinal layers leading to a better contrast. However, if we look at this illumination manipulation from a different point of view we notice another effect. The non-illuminated fields are not (or barely) scattering back any photons, single or multiply scattered, from any retinal layer. The surrounding illuminated fields are therefore receiving almost none of the multiply scattered light that they would if the whole field of view was illuminated. Thus, the illuminated fields have less light pollution from other parts of the retina which leads to a better optical sectioning and contrast. We have indeed noticed this effect on image sequences acquired using dark-field modality in our AO-FIO system, where the contrast was not only enhanced at the boundaries between dark and bright fields, but also on the bright fields themselves. We explore the exploitation of this effect of near confocality in the following Ch. 7.

## Chapter 7

# Developing pseudo-confocal modality in an Adaptive Optics Flood Illumination Ophthalmoscope

As mentioned in the previous Chapter, when projecting a checkerboard pattern we have noticed an improvement in contrast inside the illuminated regions. This we hypothesize to be an effect of improved optical sectioning approaching what is observed in confocal configuration. The idea derived from this observation is that, similarly to line scanning presented in Ch. 2, we are going to use a Digital Micromirror Device (DMD) to project specific patterns. However, instead of scanning a line we aim to project multiplexed spots that would be detected on digital apertures composed by groups of pixels in the high speed imaging camera. Then, as shown in Fig. 7.1, these spots are moved until the whole field of view is acquired.

The aim of this Chapter is to show the first steps of this study where we implement this modality in our AO-FIO and we show how it improves the contrast of our retinal images. In particular, even though the first projected spots and detection apertures are large due to the low signal to noise ratio, an optical sectioning is still achieved. This Chapter is divided in two sections. First, Sect. 7.1 describes the confocal principle and the implementation of this near confocal technique on the AO-FIO. In particular, we detail the imaging protocol conducted on the photoreceptors layer which has been selected for this proof of concept because of its high frequency content. Then, in Sect. 7.2 we analyze the results and show the enhancement in optical sectioning and contrast obtained with this new modality and the perspectives to improve it.

## 7.1 Description of pseudo-confocal imaging technique

### 7.1.1 Principle of confocality and near-confocality

#### Confocal scanning systems

The principle of the confocal instrument, in either microscopes or ophthalmoscopes, is to render the instrument only sensitive to back-scattered light from the focus plane. The technique is based on spatial gating, which is achieved by scanning an illumination spot and detecting the signal through a pinhole conjugated with the focus plane which rejects the out-of-focus light. Another key property of the confocal system is that its resolution is higher than the conventional instrument[91].

The spatial resolution of the confocal ophthalmoscope is determined by the focus of the incident beam [57] and can be calculated as the full width at half maximum (FWHM)

of the intensity point-spread function (PSF) at the focal plane[92]. The PSF of a confocal instrument free of wavefront aberrations  $H_{conf}$  is given by Eq. 7.1[92, 93]:

$$H_{conf} = (|h_{illumination}|^2 \otimes D_{source}) \cdot (|h_{imaging}|^2 \otimes D_{pinhole}) \quad (7.1)$$

where  $h_{illumination}$  and  $h_{imaging}$  denote the amplitude point-spread functions of the illumination and the imaging arms respectively,  $D_{pinhole}$  are the spatial sensitivity function of the light detector which translates the effects of pinhole size,  $D_{source}$  accounting for the source size (point source, usually negligible) and  $\otimes$  is the convolution symbol.

The spatial resolution has been estimated to be roughly  $\sqrt{2}$  times better that conventional instrument in aberration free systems and with an infinitely small pinhole aperture [93]. When the pinhole size increases, the enhancement in resolution decreases towards the conventional system resolution, which is defined by the pixel sampling.

On the other hand, the optical sectioning is controlled by the focus of the return beam at the confocal pinhole and its strength is defined by the variation of the value of the transfer function of the system at zero frequency as a function of defocus [93]. The thickness of the optical section is the half width of this curve and is given by [93]:

$$FWHM_{conf} = 0.67 \frac{\lambda}{n - \sqrt{n^2 - NA^2}} \sqrt{1 + AU^2} \quad (7.2)$$

where  $\lambda$  is the illumination wavelength,  $n$  the refractive index of the eye (here approximated by 1.33),  $NA$  the numerical aperture of the system and  $AU$  stands for Airy Unit ( $AU = \frac{\text{diameter of pinhole}}{\text{diameter of Airy disk}}$ ). We consider here  $D_{source}$  small enough so its impact can be neglected.

Although there is an effective improvement of spatial resolution in the confocal setup, it has been admitted that both conventional and confocal produces similar high resolution images. It is indeed due to the substantial improvement in optical sectioning that the confocal ophthalmoscope reaches higher contrast images.

The equations described above are defined in the case of instruments free from aberrations, which can be considered the case of the Adaptive Optics ophthalmoscopes after the wavefront correction.

### Near-confocal line scanning systems

The line scanning ophthalmoscope uses a light line (usually generated by a cylindrical lens) projected onto the retina, and the back-scattered light is detected with a line camera or a fast camera with rolling shutter synchronization [60, 61, 94]. As mentioned in Ch. 2, multiple lines can be projected simultaneously improving the acquisition speed [62]. Fig. 7.1 shows two schematic illustrations of the principle of this instrument.

Although Eq. 7.1 describes the resolution of AO-SLO systems, a similar equation can be extended to non confocal systems.

$$H_{conv} = (|h_{illumination}|^2 \otimes D_{source}) \cdot (|h_{imaging}|^2 \otimes D_{pixel}) \quad (7.3)$$

where we replaced  $D_{pinhole}$  by  $D_{pixel}$ . Indeed, the resolution of non confocal and aberration free systems is defined by the sampling of the detector and therefore the size of the pixels on the retina plane. If we analyze Eq. 7.3 in the case of standard AO-FIO imaging,  $D_{source}$  is very large and therefore  $(|h_{illumination}|^2 \otimes D_{source}) \sim \text{constant}$  leading to  $H_{conv} \sim (|h_{imaging}|^2 \otimes D_{pixel})$ .

The optical resolution of the AO-LSO systems (when free of optical aberration) is described by Eq. 7.1 on one direction only, orthogonal to the light line. The resolution of the other direction is defined by the camera pixel sampling described in Eq. 7.3. Additionally, the confocality is lost along the light line direction, with optical sectioning only realized in one direction too.

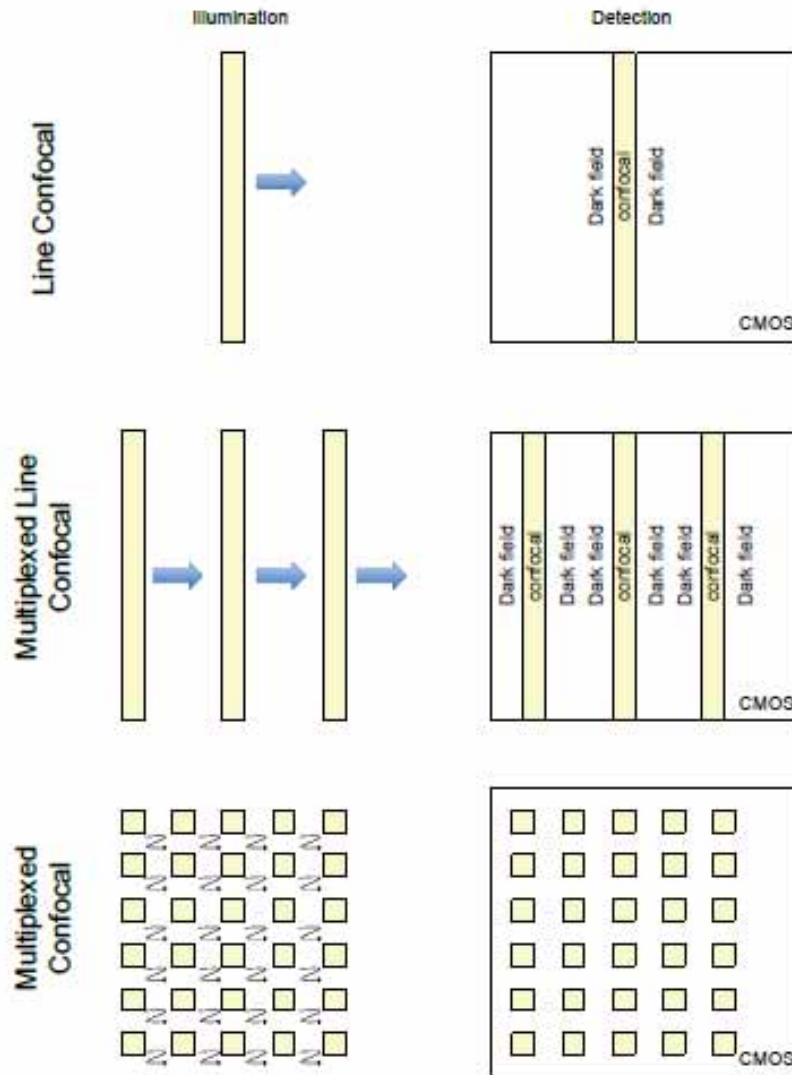


FIGURE 7.1: Schematic illustration of the principle of the line scanning (top), the parallel line scanning (middle) and our pseudo-confocal instrument (bottom). [Credit: Serge Meimon [95]]

Figure 7.1 shows at the bottom a schematic illustration of the principle of our pseudo-confocal instrument. Multiplexed illumination voxels are projected onto the retina and successively shift to cover the whole field of view. The spatial resolution of our pseudo-confocal system can be described using Eq. 7.3. If our light voxels are too large, the resolution will be defined by the pixel sampling like in our current AO-FIO system. However, as

we are reducing the size of our multiplexed spots, whose impact on resolution is described by  $D_{source}$ , we may approach the improved resolution of confocal systems.

### 7.1.2 Implementation in the PARIS AO-FIO

The experimental setup is the modified AO-FIO system with the new illumination path described in Ch. 5. In short, a new illumination path enabling the projection of patterns thanks to a spatial light modulator has been built on an AO-FIO system. Like in dark-field imaging, described in previous Ch. 6, we use the spatial light modulator from this path to manipulate the illumination geometry of the system. A pattern, leading to illuminated (bright fields) and non illuminated areas (dark fields) of the retina, and its inverse have been uploaded to the controller of the spatial light modulator manipulated through a computer. These patterns, created with Interactive Data Language (Exelis, USA) or Photoshop (Adobe Systems, USA), are consecutively projected to a subject retina. Pattern shapes are selected so as to surround as many pixels of interest as possible with dark fields, reducing as much as we can the out of focus parasite light. We chose squares large enough so not to restrict too much the signal-to-noise ratio. Even though here we use the same spatial light modulator to project the illumination patterns on the retina, there are two main differences from the imaging protocol from the dark-field modality described in Ch. 6. First, the patterns we have used here are adapted to the pseudo-confocal configuration. In order to completely surround the pixels of interest with dark areas we have used checkerboard patterns instead of the stripes used in dark-field. Secondly, in pseudo-confocal imaging we are interested in the information inside bright areas, unlike dark-field where the information lies in the dark fields close the illumination boundaries. This implies the development of image processing retrieving information solely from illuminated pixels. Finally, image sequences go through the same image processing already described in Ch. 4 of correction from inhomogeneous background, registration, and lucky averaging (image averaging after discarding blurred images due for instance to eye motion).

Once we have implemented the pseudo-confocal illumination, our goal is to show that imaging the retina with this specific illumination improves the contrast of our videos and processed images. To achieve this purpose, we compare standard illuminated images of our AO-FIO system to the whole field of view obtained with the pseudo-confocal illumination after processing. In the next section we describe the imaging protocol followed and demonstrate this improvement in image quality.

## 7.2 Proof of concept in the photoreceptor layer

We mean to prove that the pseudo-confocal technique improves AO-FIO optical sectioning partially overcoming in this way one of its most bothersome limitations.

In order to assess the improvement in contrast with this new technique, three image sequences have been acquired on the photoreceptor layer at 10° Temporal. One receives the standard AO-FIO illumination, and two others opposite patterns projected onto the retina whose sum corresponds to the whole illuminated field of view. The patterns created for this proof of concept are a checkerboard, with squares of 50  $\mu\text{m}$  in the retina plane, and its inverse. The acquisitions have been made in the same imaging session to minimize the variations in the retina between sequences. Indeed, this layer contains high spatial frequency features and is therefore often used to test image quality.

Improvement in contrast is analyzed over two time scales: 1) **First time scale**: a real-time (at 20Hz since averaging 10 frames at a time) improvement of contrast and 2) **Second**

**time scale:** the enhancement obtained in averaged image (using all the frames in the image sequence) after the usual imaging processing.

**First time scale: Contrast in averaged images from 10 frames for real-time visualization**

We start by evaluating if we notice an enhancement in contrast in the first time scale, meaning in the videos frames or just a sum of a few frames without any processing. To do so, we have generated averages from a few successive images for each illumination configuration, shown in Fig.7.2. We notice that photoreceptors appear more contrasted on the pseudo-confocal image (B) than on the standard one (A).

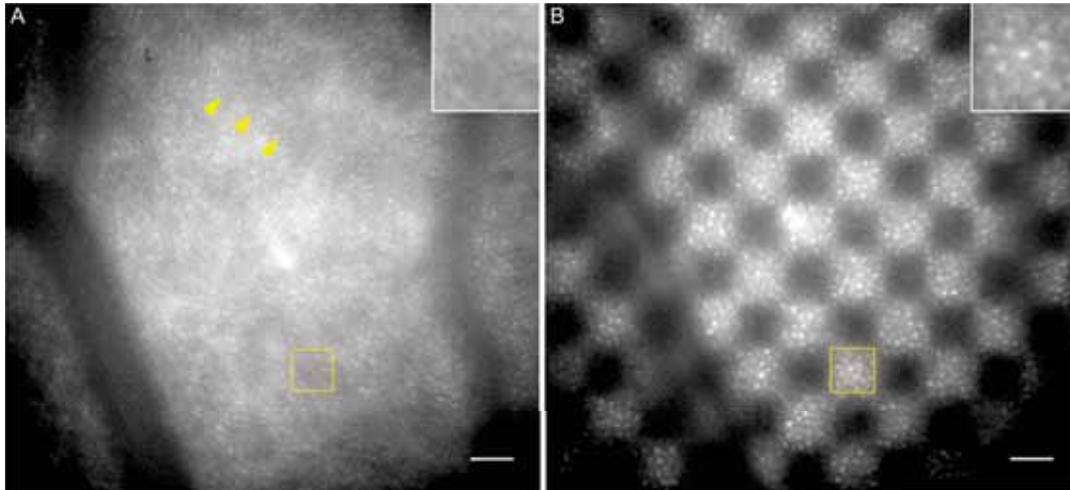


FIGURE 7.2: Two average (10 frames) images from a raw image sequence obtained with AO FIO, with (A) acquired with a standard flood illumination and (B) with a checkerboard pattern illumination. The contrast is enhanced in (B) where we do not see the out of focus spots visible in (A). Scale bars are  $50 \mu\text{m}$ .

To quantify this contrast enhancement we first computed the Michelson contrast on both average images. The contrast value (where 1 is the maximum value) for the pseudo-confocal illumination was 0.09 higher than the contrast obtained with standard illumination. Since the uncertainty computed for both contrasts was 0.06, the difference does not seem to reflect the qualitative improvement observed when comparing both images implying that Michelson contrast might not be adapted to this particular feature.

Another appropriate analysis tool to evaluate the contrast of photoreceptors images is the Fourier Transform. Indeed, photoreceptors form a mosaic that has a characteristic spacing and shows a frequency signature in the Fourier domain known as Yellot's ring. So, we have computed the Fourier Transform of both averages in order to observe if there is a difference between the Yellot's rings of each image. Figure 7.3 shows the Fourier Transform images corresponding to the standard illuminated image (A) and to the pseudo-confocal one (B). The stronger the signal of the Yellot's ring, the higher the contrast of features with this spatial frequency, i.e. the photoreceptors mosaic. The ring in (B) appears brighter than the ring in (A) implying a better contrast of the photoreceptors in the images acquired with pseudo-confocal illumination.

An improvement in image quality that can be noticed is that the cloudy aspect given by out of focus large patches appearing on (A) have been filtered out in (B), leaving only the high spatial resolution content corresponding to photoreceptors inside the illuminated areas. The yellow arrowheads identify a dark shade corresponding to an out of focus feature. This observation supports the idea that this pseudo-confocal modality improves the

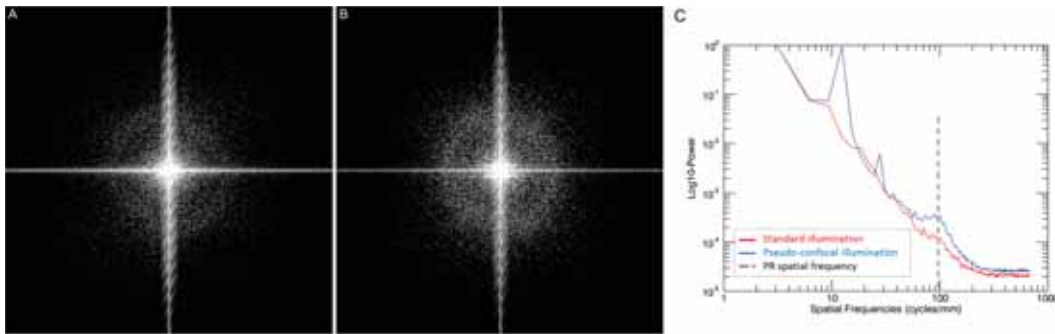


FIGURE 7.3: Fourier transforms of averaged raw images (10 frames) presented in Fig.7.2. (A) corresponding to standard illumination and (B) corresponding to the pseudo-confocal illumination. Both (A,B) show Yellot's rings at photoreceptors spatial frequencies, with (A) a slightly less contrasted Yellot's ring than (B). The bright crosses in (A,B) are due to fixed pattern noise. (C) Plots of the power spectrum from both (A) in red and (B) in blue. A dashed line show the spatial frequency of the photoreceptors. The blue line corresponding to the pseudo-confocal image shows another peak corresponding to the frequency of the checkerboard pattern. We notice that the pseudo-confocal displays a higher peak at the photoreceptors frequency than the standard illumination profile.

optical sectioning of the full field ophthalmoscope.

This analysis has been carried out on images obtained by the averaging of just a few (10) frames. Not only the improvement in image quality is visible, but it is supported by the computation of the contrast and Fourier analysis on both images. Noticing better contrast in the video sequences or the sum of just a few images before any image processing implies an improvement in real-time, the first time scale, of the image quality. We could have a full field system continuously displaying a high contrasted video, which would facilitate the exploration of the retina, by switching very fast between the opposite checkerboard patterns and averaging just a few successive images. Therefore we could obtain an enhanced contrast full field imaging system, displaying a higher optical sectioning than the classic AO-FIO but without the limitations of distortion and with the possibility of a large field of view.

### Second time scale: Contrast in average images using all the frames of the image sequence

We then analyze the effect of this technique on the contrast of processed average images. This image processing consists in a correction of the inhomogeneous background by filtering out the low frequencies, then registration of frames (cf. Ch. 4) and lucky averaging (i.e. previously discarding blurry images). Average images illuminated with standard configuration and with one of the patterns are shown in Fig. 7.4. In this case, the combination of the subtractions of the background illumination and the averaging of the frames improved the contrast of the photoreceptors in both illumination configurations. However, we are able to spot some differences. Like in the previous images from Fig.7.2, large dark patches, which are out of focus structures from other layers of the retina, noticed in the images from the standard configuration (dark shade is again identified with yellow arrowheads in Fig.7.4) disappear in the pseudo-confocal illuminated images. Indeed, these patches, giving images a cloudy aspect, have

a low spatial frequency but too high to be filtered out with the correction of the inhomogeneous illumination. So, they cannot be filtered out through image processing. In the pseudo-confocal technique, most of this out of focus light is canceled out by surrounding the illuminated fields with dark regions. Thus, these dark regions do not receive ballistic photons from the source that can be multiply scattered towards the illuminated region of interest (illuminated squares in this case) and therefore the amount of multiply scattered light from out of focus layers is severely reduced leading to the imaging of a photoreceptor mosaic without dark patches. This effect is the same we observe in AO-SLO where the confocal hole filters out the out of focus light and also leads to a photoreceptor mosaic without the out of focus spots.

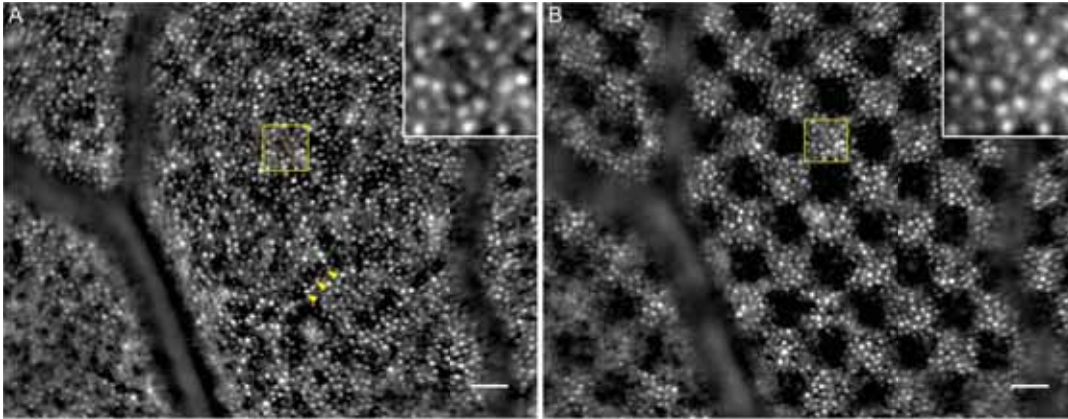


FIGURE 7.4: Two average ( $\sim 700$  frames) images from processed image sequences obtained with AO FIO, with (A) acquired with a standard flood illumination and (B) with a checkerboard pattern illumination. Scale bars are  $50 \mu\text{m}$ .

In order to assess more accurately the potential improvement in final processed images we carry out a Fourier analysis of average images in both illumination configurations from Fig. 7.4. Figure 7.5 shows the two Fourier transform (A,B) corresponding to both averages. We observe that the difference between the Yellot's ring is much harder to appreciate here, if there is one. In order to conduct a better comparison we compute circular means of the power spectrum density of both (A,B) leading to the plots in image (C). The pseudo-confocal plot, in blue, shows just a slightly higher peak at the photoreceptor frequency. The difference between the two peaks is much lower here than in the real-time case. Nonetheless, a difference is observed, which leads us to believe that with optimization of the parameters, like pattern size or shape, of these pseudo-confocal technique we could obtain a better improvement in contrast. For instance, a smaller pattern could further lead to the rejection of out of focus light and therefore to a more contrasted photoreceptors layer.

Although to a much lower extent than in the case of the average of raw frames, we have also noticed an improvement in image quality in averages of processed image sequences. Observing an upgrade of contrast in average images, i.e. over a larger time scale, implies that the pseudo-confocal technique provides an upgrade in image quality in addition to the one provided by image processing.

### 7.2.1 Optical sectioning

The voxels from the checkerboard pattern sent during this first test have a width of  $50 \mu\text{m}$  long at the retina plane. We can approximate the optical section thickness by considering

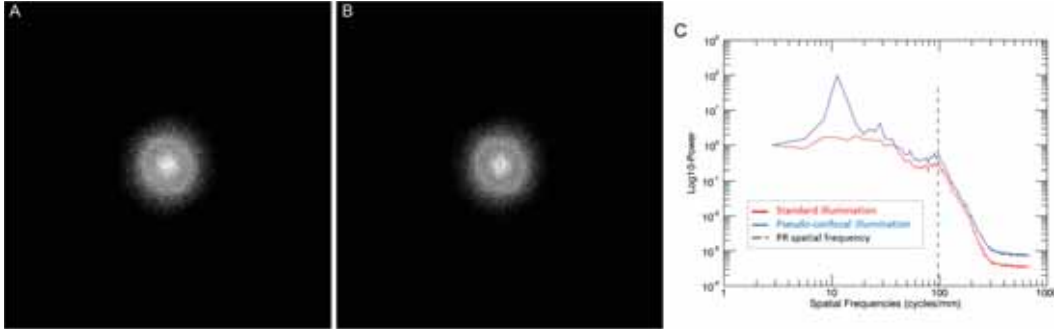


FIGURE 7.5: Fourier analysis of average images (700 frames) from Fig. 7.4. (A,B) correspond to the Fourier Transforms and show both a Yellot's ring at photoreceptors spatial frequency. (A) Fourier Transform of the average image acquired with standard illumination, which shows a slight less contrasted Yellot's ring than (B) corresponding to the pseudo-confocal average image Fourier Transform. (C) Plots of the power spectrum from both (A) in red and (B) in blue. A dashed line shows the spatial frequency of the photoreceptors. The blue line corresponding to the pseudo-confocal image shows another peak corresponding to the frequency of the checkerboard pattern. We notice that the pseudo-confocal display a higher peak at the photoreceptors frequency than the standard illumination profile.

this width to be the diameter of our detection pinhole, which here would physically be the conjugated pixels of the camera. Using Eq. 7.2 with Airy disk =  $\frac{2.44\lambda f_{eye}}{D_{pupil}} = 7.13 \mu\text{m}$  and  $AU = \frac{50 \mu\text{m}}{7.13 \mu\text{m}} = 7$  we obtain an optical section of  $500 \mu\text{m}$ . However, we must note that this computation of optical sectioning thickness concerns the lower frequencies which have the slowest variations. Middle frequencies from other layers would probably present a smaller optical section thickness, which is why we could previously appreciate the filtering of the cloudy aspect which was typical in wide field images from AO-FIO. To further improve the contrast we aim to reduce the size of the illumination and detection voxels. If we multiplexed voxels with  $10 \mu\text{m}$  width, the optical section thickness approximated by Eq. 7.2 would be  $120 \mu\text{m}$ . The theoretical optical section thickness derived on the MAORI PSI AO-SLO is  $60 \mu\text{m}$  but considering the system perfectly aligned, and is therefore relatively larger when it is not the case. The gain in optical sectioning with the reduction of the voxels size to  $10 \mu\text{m}$  would enable us to approach the scanning system optical sectioning capacities.

## 7.2.2 Limitations

The limitations of this technique are similar to those described in the previous Ch. 6. There are two limitations in particular that have had a larger detrimental impact on this technique. On the one hand, since we do not achieve field stabilization in real time, the patterns move with the eye's fixational movements. This has complicated the generation of a whole field of view by combining the images acquired with a pattern and its inverse. For this reason, the analysis in this Chapter has been carried out on images with one of two patterns. This limitation does not affect the conclusions derived in this Chapter but incites us to improve our setup or imaging protocol to achieve a whole field image in this modality. On the other hand, we suffer from the same limitations arising from the Spatial Light Modulator (SLM) which projects the patterns. In particular, this regards the high frequency noise caused by the memory refreshment of the micromirrors position stopping us to perform real-time visualization. Indeed, since we have a high frame rate of 200Hz, if we compute for instance every 10 frames a complete field of view by combining frames

with a pattern and its inverse, we could achieve a real-time visualization at 20Hz. This could facilitate the exploration of the retina.

### 7.3 Conclusion

This Chapter introduces a new modality implemented in AO-FIO, the pseudo-confocal technique. Similar to the line scanning, the principle of this technique is to reduce the amount of out of focus multiply scattered light and is achieved by projecting an illumination pattern on the retina. However, instead of parallel lines we project multiplexed voxels that are shifted in order to cover the whole field of view. In the first test of this technique presented in this Chapter, large voxels of  $50\ \mu\text{m}$  width were projected. These illuminated areas display a higher contrast since in this configuration they receive less out of focus light from other regions of the retina. We have noticed a minor improvement of the contrast with this technique in average images compared to the considerable enhancement observed in raw images. Indeed, a lot of the out of focus light detected by the camera presents low frequencies and are therefore filtered out by the image processing described in Ch. 4, likewise the averaging lowers the noise and improves the contrast. However, we notice in both raw images and averages that the large dark patches visible in images from the standard illumination configuration disappear in images from the pseudo-confocal configuration. These dark spots result from out of focus light but seem to have a spatial frequency too large to be filtered out by the processing. The pseudo-confocal technique enables us to get rid of these medium frequencies patches leading to a better contrasted photoreceptor mosaic close to the one obtained with AO-SLO.

The first test of this new modality on the photoreceptor layer encourages us to pursue the study of the various parameters of this configuration affecting the image quality, in particular the pattern projected onto the retina, in order to optimize the upgrade in contrast in the resulting processed images. In particular, by projecting very small voxels the term  $D_{source}$  could be reduced so as to gain in resolution compared to conventional AO-FIO resolution and reduce the optical section thickness of the system.

Finally, future work should be oriented towards overcoming the SLM limitations in order to fully exploit the benefits of this modality and to stabilize the AO-FIO field of view to achieve a better control of the position of the pattern projection in order to image the whole field of view of the system in pseudo-confocal imaging.

Chapter 6 and this Ch. 7 describe the two imaging modalities that derive from the use of the SLM described in Ch. 5. The use of this device has enabled us to select photons from the combination of back-scattered and multiply scattered light in AO-FIO for the first time. Although this SLM suffers from technological limitations that must be overcome, we have proved in these two Chapters the prospective enhancement in contrast and therefore image quality of the two modalities developed.

The next Ch. 8 addresses the other instrument implemented in the new illumination path described in Chapter 5. While the SLM manipulated the shape of the illumination beam, this next instrument enables us to vary the angle of incidence of the illumination beam on the retina.



## Chapter 8

# Developing a Retinal Goniometer in an Adaptive Optics Flood Illumination Ophthalmoscope

The previous Chs. 6, 7 described the manipulation of the illumination through a Spatial Light Modulator (SLM) allowing to "switch off" the illumination on selected areas of the field of view. In particular, Ch. 6 describes the use of this SLM for the development of dark-field in AO-FIO generated by the oblique illumination of a secondary source in the retinal pigment layer created next to the region of interest thanks to the strong backscattering of this layer. However, the obliquity of this secondary illumination probably depends on the illuminated structures and subject, and is almost impossible to control with this previously described technique. Therefore, to gain control of this obliquity a different manipulation of the illumination source must be carried out. We cannot control the angle of incidence of the light which is back-scattered by the retinal pigment epithelium layer to reach the structures we want to observe, but we can control the angle of incidence of the beam onto this retinal pigment epithelium layer that must serve as a secondary source. Indeed, it has been suggested, based on Monte-Carlo simulations, that the retinal pigment epithelium layer displays a non symmetrical back-scattered light, increasing its intensity in the direction of the incoming beam, when illuminated with a large angle of incidence[96]. Therefore, by changing the angle of incidence on the retina we should change the angle of the secondary source that is generated at the retinal epithelium layer. This variation in incidence is achieved by using the tip tilt mirror and diaphragm implemented in the new illumination path of the system described in Ch. 5. As mentioned in this previous Ch. 5, the angle of incidence of the beam is modified by varying the position of the illumination pupil which when focused by the eye lens on the retina leads to a angle of incidence dependent on the pupil position at the eye pupil plane. Furthermore, if we consider the retina like in Ch. 6 to be a phase object and we place ourselves in the weak object phase approximation, this experimental setup could enable us to detect phase information at the camera plane in AO-FIO. Although the intended application of this incidence varying instrument in this Chapter is the phase imaging, it was first designed with the perspective of achieving a functional measurement of the photoreceptors orientation. This other application is explored in Ch. 9 using the same implementation described in this Chapter. For both applications we name this varying illumination incidence angle instrument **Retinal Goniometer**.

The aim of this Chapter is to show the development of the Retinal Goniometer for phase imaging using AO-FIO thanks to the obliquity of the illumination. In Sect. 8.1 we explain how to use this instrument to achieve phase-imaging in our system and the steps undertaken for the implementation of the technique on the AO-FIO system. Then a proof of concept is conducted on an artificial eye in Sect. 8.2 before testing the new instrument then on a human retina *in vivo* and discussing the results in Sect. 8.3.

## 8.1 Description of the technique

In Ch. 4 we have described the principle of phase imaging through oblique illumination developed by Mertz and his team [78], and justified its approach in our case of the imaging of the retina. In Ch. 5 we have shown the instrument implemented on our AO-FIO that enables us to modify the angle of incidence of the illumination beam on the retina. In short, changing the angle of incidence is achieved by changing the illumination beam position at the eye pupil plane. When the optical pupil of the illumination beam is at the center of the eye pupil, it reaches the retina perpendicularly when focused by the lens of the eye. In this configuration, the beam is coincident with the system's optical axis. On the other hand, the closer the optical pupil of the beam is to the edge of the eye pupil, the larger the incident angle of the beam is with respect to the optical axis of the system. In this section we detail how this modality from microscopy is actually translated to our system, the principle of the technique in the case of the retina imaged with an AO-FIO and finally how this implementation was carried out, in particular the choices of angle of incidence, illumination pupil size, etc.

### 8.1.1 Phase imaging in the retina by oblique illumination

The principle of phase imaging in our AO-FIO resembles the principle described by Ford et al. in [78]. We illuminate the retinal structure of interest with an illumination beam with an angle  $\theta$  and then with the opposite angle  $-\theta$ . The light is strongly back-scattered by the retinal pigment epithelium, principally in the direction of the illumination beam [96], in the two previous illumination incidence towards the upper layer of the retina. These layers are then in a trans-illumination configuration and receive an illumination beam from two opposite angles from the deeper layer. The intensity from images obtained at the imaging camera with each illumination configuration ( $\theta$  and  $-\theta$ ) contains a phase and its opposite phase information. By subtracting these two images we retrieve the phase information while removing the background and absorption information that remains unchanged when varying the illumination incidence. This theory has been experimentally tested by Carpentas et al. [96] leading to the imaging of transparent features using transcleral illumination. In our case we aim to exploit the same effect but achieving the illumination through the eye pupil.

In practice we have implemented this imaging technique in the following way. Four positions for the illumination pupil inside the detection pupil have been selected, leading to four angles of incidence onto the retina, opposed two by two. Then an image sequence consecutively varying the position of the illumination pupil is acquired. Finally, the frames acquired with opposed incidence are subtracted in order to observe the phase of the imaged structure.

### 8.1.2 Implementation in the PARIS AO-FIO

Chapter 5 described the optical design and alignment of a new illumination path of the system allowing the manipulation of the illumination geometry. Among the two instruments composing this path, this section details the one which enables us to vary the angle of incidence of our illumination. It also describes the implementation of the phase imaging technique achieved with it.

Figure 8.1 shows the optical design of our system with the new illumination path, as described in Ch. 5, where we have underlined the two elements of our instrument: an aperture stop and a tip-tilt mirror. Indicated with a green arrow is the aperture stop at a pupil plane, noted as  $P_G$ , that will determine the size of the illumination pupil at the eye pupil plane. The piezo tip-tilt mirror (Physik Instruments, Germany) placed in a focal plane is identified with a red arrow and, as explained in Ch. 5, shifts the image of the aperture stop allowing us to illuminate the retina with a range of different incident angles. The tip/tilt mirror is connected to a computer by a USB connection and is controlled through a custom-made algorithm using Labview programming language (Labview, USA). This algorithm allows the user to vary the angle of the mirror by sending a voltage between [-1V,10V]. Additionally, it enables the user to set a cycle with various positions of the mirror at a given frequency. This implies that we can automatically change the positions of the illumination beam at the eye pupil plane during an acquisition instead of having to do it manually.

A calibration of the tip-tilt mirror control algorithm described above has been performed to determine the conversion factor between the voltage commands and the mirror's tilt. We have started by deriving the voltage corresponding to the zero position. Indeed, the tilt position in which we have aligned the mirror in previous Chapter 5 is randomly shifted when the mirror is supplied in power for the first time. To replace the mirror in that zero state while power is supplied we have first marked the zero position with the power OFF using a graph paper placed at the pupil plane  $P_i$  (cf.Fig8.1). Then, we have applied power to the tip-tilt mirror which has made the beam shift. We have sent various voltage commands until we have found a set of voltages that shifted the beam back to the zero position marked on the graph paper. This voltage set corresponded to [4.5V,4.5V]. Then, from this position we have applied 1V command to the tip-tilt mirror on its x axis and measured 0.42 mm on the graph paper. We have carried out the same protocol on the y axis, obtaining 0.42 mm. We have derived a conversion factor between voltage command and pupil shift in the eye pupil plane of  $cf = \frac{\text{Pupil shift at eye lens plane}}{\text{voltage command}} = 0.7 \text{ mm/V}$  for both of the axes of the tip-tilt mirror.

Next, we define the two following parameters of the instrument:

- 1) The size of the aperture stop  $P_G$ , which is defined by the desired size of the illumination pupil
- 2) The rotation angle of the tip-tilt mirror, which is defined by the desired angle of incidence of the illumination beam on the retina.

The first parameter, the aperture stop diameter, is set so as to have its image at the eye pupil plane smaller than both the pupil of the eye and the pupil of the AO-FIO imaging system, as well as to provide a correct signal to noise ratio. Two aperture stops have been selected, with diameters of 1.8mm and 2.25mm. These correspond to 2mm and 2.5mm pupil diameter of the illumination beam respectively at the eye pupil plane. The eye pupil is centered in our system with the detection pupil which is set to 5mm diameter. Both illumination pupil sizes obtained with these diaphragm have half the size of the pupil of the system or less, enabling us to shift them inside this detection pupil. Unlike AO-SLO we do not use the same pupil for illumination as for the collection [97] and thus our detection pupil has still 5 mm diameter ensuring a high resolution.

The second parameter, the angle of incidence, is determined by the distance from the center of the pupil of the eye to the center of the illumination pupil. We need the illumination pupil position to stay inside of the system pupil in order to limit

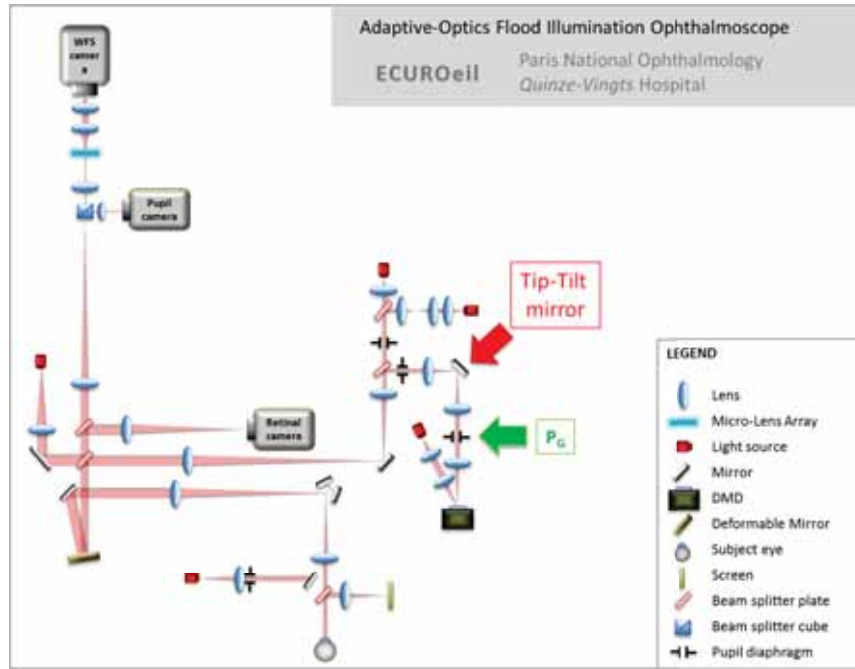


FIGURE 8.1: Optical layout of the system including the new illumination path where the retinal goniometer was implemented.

any potential vignetting. Since the radius of the system pupil is 2.5mm, we set the illumination pupil shifts to 1mm from the center of the eye pupil, which represent a rotation of the mirror of 10mrad in the chosen direction of shift. This leads to an angle of incidence of 20mrad in the chosen direction.

Thus, the four positions of the illumination pupil at the eye pupil plane necessary for the phase imaging have been defined accordingly and are shown in a schematic drawing in Fig.8.2. (A) summarizes the selected dimensions of the pupil size ( $s$ ) and the four positions of the pupil ( $d$ ) with respect to the pupil of the eye, which is centered with the system pupil. (B) shows the four selected positions of the illumination pupil for phase imaging, with two set of images with opposed illumination.

Once all the parameters have been derived from the specifications imposed by the system pupil, we have introduced them into the controller software commanding the tip-tilt mirror. Using the previously computed calibration factor, we have derived the voltage values that must be sent to the mirror in order to shift the illumination pupil to the four selected positions. These values are summarized in Tab. 8.1 here below.

Position	1	2	3	4
Voltage (V)	[3.5,5.5]	[3.5,3.5]	[5.5,3.5]	[5.5,5.5]

TABLE 8.1: Set of voltages sent to the tip-tilt mirror controller in order to shift the illumination to the four positions described in Fig.8.2 B.

The voltage values can then be introduced in the algorithm described in Ch. 5 enabling us to automatically change the position of the illumination pupil at a selected frequency during an image sequence acquisition.

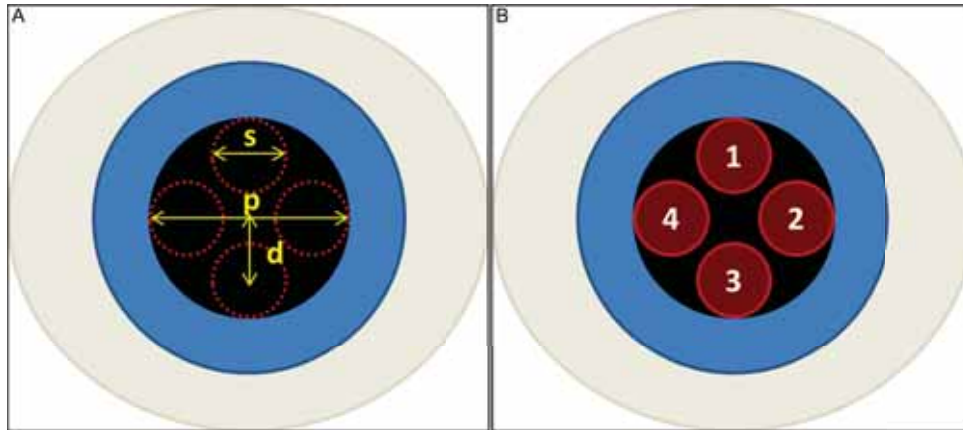


FIGURE 8.2: Schematic drawing showing the positions of the illumination beam pupil at the eye pupil plane and the dimensions set.  $s$  is diameter of the image of the aperture stop  $P_G$  at the eye pupil plane and has been set to two values: 2mm and 2.5mm.  $p$  is the diameter of the eye pupil, which is approximately 5mm.  $d$  is the distance between the center of the eye pupil and the center of the sub-aperture generated by the aperture stop shifted by the tip-tilt mirror. It is set to 1mm at the eye pupil plane.

The instrument being defined to perform phase imaging was first tested on an artificial eye. The description of the imaging protocol and the analysis of the results are presented in the following section.

## 8.2 Proof of concept in artificial eye

We have performed a test on artificial eye of this new instrument. The proof of concept described here below aims, firstly to demonstrate that we are able to vary the angle of incidence of the illumination beam and secondly that images with oblique illumination lead to phase information at the camera and that the acquisition of images with opposite illumination leads to the generation of an image with phase contrast.

The artificial eye chosen for this test consist in an sphere filled with viscous liquid and has a rough paper stuck to one side of the sphere opposite to the pupil, i.e. an aperture with a small lens. We have found this artificial eye well adapted to a first proof of concept since we have freed ourselves from the fixational eye movements while having a lens in the pupil which can focus the illumination beam at different angles depending on its position in the pupil. Finally, the back of the artificial eye is a rough paper which has strong scattering properties and can therefore be used to test if our instrument can achieve phase imaging though back oblique illumination.

### Imaging protocol

To do so, we have acquired an image sequence on an artificial eye fundus while shifting the pupil of the illumination beam to the four positions, away from the center of the pupil of the artificial eye, as described in Fig.8.2 (B) in the previous section. In order to avoid vignetting we have started by selecting the aperture stop of 1.8mm diameter, which leads to an illumination pupil diameter at the artificial eye pupil plane of 2mm. Then, we have

applied the set of four voltages, shown in Tab. 8.1, corresponding to the four positions derived in the previous section for phase imaging. Finally, we have set the frequency of the cycle changing the position of the illumination pupil to 10Hz, which led to the acquisition of 20 frames at each of the four pupil positions of the illumination beam. Since this first test has been performed on artificial eye, which remains still, we have only acquired an image sequence of 100 frames in the conditions previously described.

### Image processing

We have averaged every 20 frames for each pupil position in order to have a higher signal to noise ratio of the generated images. At least one averaged image for each of the four illumination pupil positions shown in Fig. 8.2 (B) has been obtained.

In order to achieve differential phase contrast we have conducted the computation described by Eq. 8.1 [77] and presented in the previous Ch. 5, where  $I_\theta$  and  $I_{-\theta}$  represent images illuminated with opposite angles of incidence. Since we have acquired images with two sets of opposite illuminations we can compute two phase contrast images  $I_{DPC}$ : a first one between top and bottom illumination pupil positions 2,4 and a second between left and right illumination pupil positions 1,3.

$$I_{DPC} = \frac{I_\theta - I_{-\theta}}{I_\theta + I_{-\theta}} \quad (8.1)$$

The subtraction between two images from opposite asymmetric illumination ideally cancels the background absorption contribution while the sum of the two images is close to the bright-field image. The obtained image  $I_{DPC}$  is related to the sample's phase gradient (here the artificial eye paper) [77].

### Results: Achieving phase gradient contrast

Figure 8.3 shows the four average images corresponding to the four positions of the pupil of the illumination beam. We notice a variation in the aspect of the paper fundus from the artificial eye. When visualizing this image sequence we notice a 3D rendering brought by change of illumination incidence. However the contribution of the background is considerable and the aspect of the fundus does not seem to vary substantially from the standard bright-field image. The two phase contrast images previously computed are presented in Fig. 8.4. The first phase image corresponds to the subtraction of the average images Fig. 8.3(A) and Fig. 8.3(B) corresponding to the illumination resulting from illumination pupil position 1 and 3 respectively. The second phase image results from the same computation this time between images Fig. 8.3(C) and Fig. 8.3(D), corresponding to pupil position 2 and 4. Both resulting phase images generated thanks to Eq. 8.1 are shown in Fig. 8.4. These two images in Fig. 8.4 display a shadowing that gives this classic 3D rendering typical of phase gradient images [78, 98]. Additionally, the images show positive and negative phase gradient values in the form of bright and dark pixels standing out from a grey background corresponding to a zero phase gradient value. The paper being a fairly scattering material has generated a back oblique illumination that has illuminated with a given obliquity the superior layer of the paper. In image Fig. 8.4(A) a small area has been zoomed in order to appreciate the granularity of this paper layer visible thanks to conversion of the phase gradient variations to intensity variations.

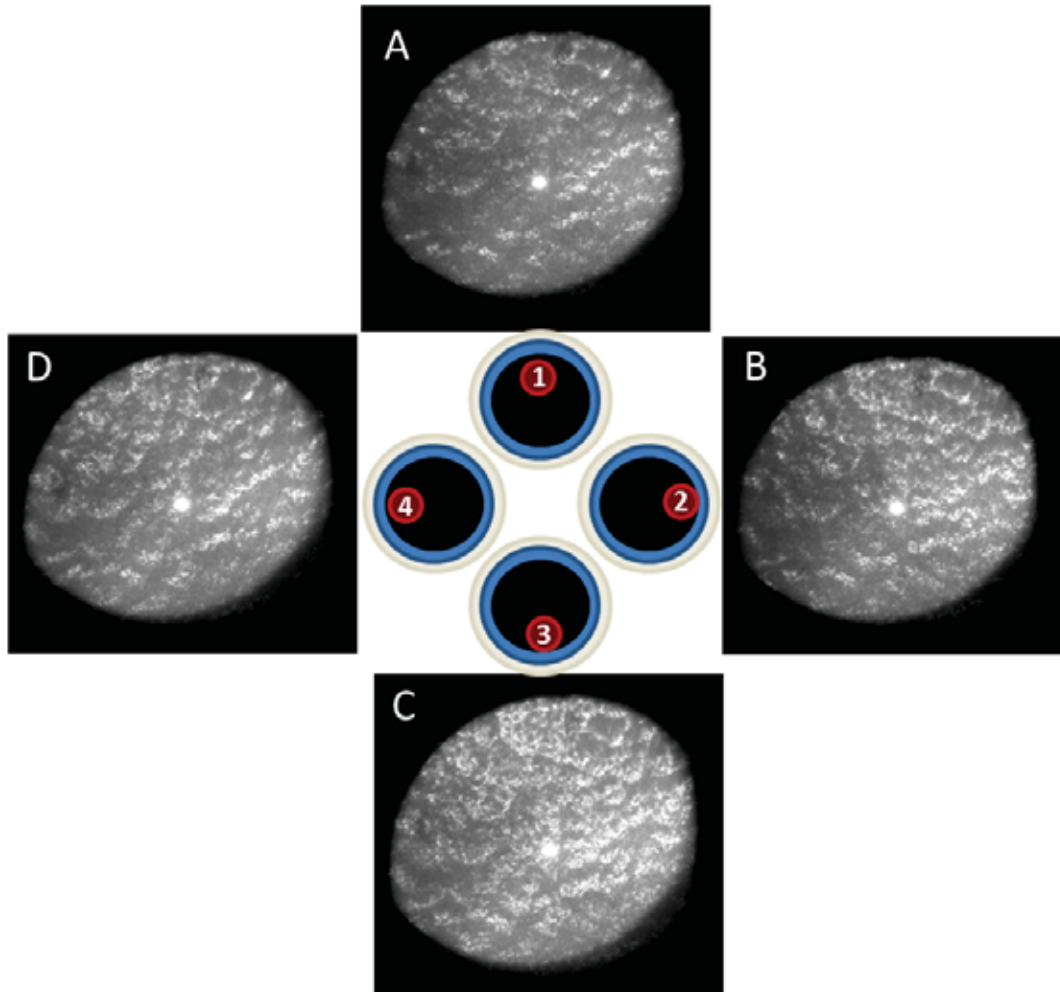


FIGURE 8.3: Four average images from the image sequence acquired on the artificial eye illuminated and corresponding to the four different angles of incidence.

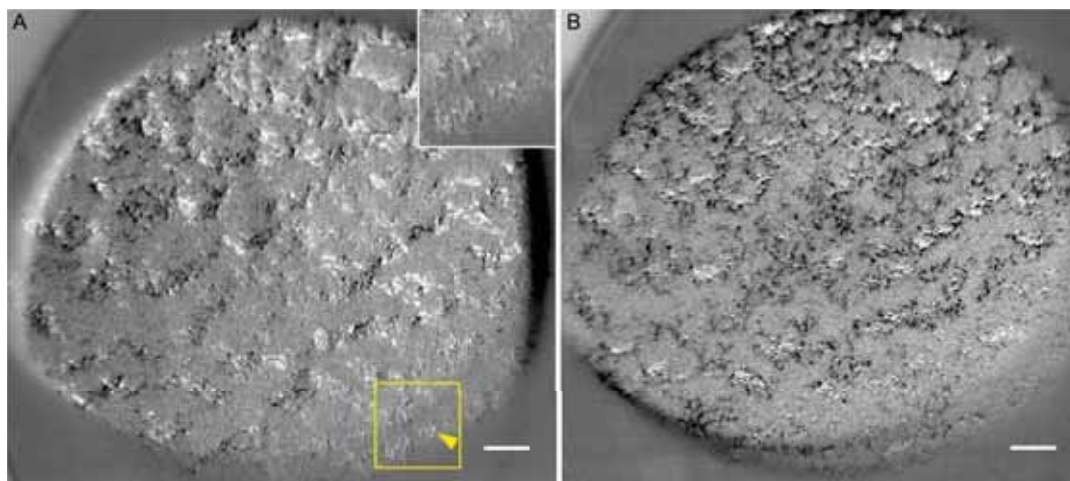


FIGURE 8.4: Differential phase contrast images of the artificial eye generated using Eq. 8.1. (A) results from the subtraction between images Fig. 8.3(A) and Fig. 8.3(D) acquired with illumination angles derived from position 1 and 3 (cf. Fig. 8.2) while (B) results from subtraction of Fig. 8.3(C) to Fig. 8.3(D), acquired with illumination angles derived from position 2 and 4

## Conclusion

This first test on an artificial eye has proven that the introduction of an asymmetry in the illumination of our system leads to phase gradient imaging. Indeed, this obliquity in the illumination introduces an asymmetry in the Fourier plane of our sample due to a partial filtering by the finite pupil of the system. Thus, a recombination of this asymmetric diffracted light in the Fourier plane by the next optic lens leads to an intensity variation related to the phase gradient of the sample, in our case the artificial eye. The phase contrast is increased by computing differential phase images which subtracts two images with opposite phase gradients and similar background contributions.

The use of an artificial eye enabled us to achieve a first proof of concept of this instrument without the additional difficulties that we meet when realizing *in-vivo* human retina imaging such as eye fixation movements, temporal aberrations or higher complexity of the sample to name a few. These challenging issues, along with others, are met in the following section which address the first test of this instrument on an *in-vivo* human retina of a healthy subject.

## 8.3 Test in humans

The test performed on artificial eye has shown that varying the pupil position of the illumination in the eye pupil plane effectively changes the angle of incidence of illumination of the sample, in the previous case the artificial eye. The generation of intensity variations at the camera plane observed in the computed phase contrast image and which seemed related to the phase gradient have proved that the paper at the back of the artificial eye has back-scattered the light with two different angles when illuminated through two opposed incidences. We have then tested if the same protocol works in a healthy human eye *in-vivo*. As mentioned before, this test presents new difficulties: Firstly, the eye moves even when in fixation, leading to a movement of the illumination pupil to another position in the eye pupil plane than the one planned by the user. Since we do not have currently a pupil stabilization in our system, the accuracy of the illumination pupil position is lower than in test on the artificial eye. Secondly, we are limited in power. Since we use a small diaphragm at the pupil plane, it implies an important restriction of the power of the light source, which is already used at its maximum power. With the low amount of back scattered light from the retina, the signal to noise ratio of the images is very low in this configuration.

To reduce the impact of both of these limitations in order to achieve a first test in humans *in-vivo* we have acquired short image sequences (a few seconds) on a subject with good fixation to limit the variation of the positions of the illumination beam at the eye pupil plane and we have doubled the time of exposure (10ms instead of 5ms) to increase the signal to noise ratio.

The same protocol and distances computed for the artificial eye test has been selected. An image sequence has been acquired at 10°T focused on the photoreceptors layer. However we have set a larger exposure time for each image sequence corresponding to each of the four different angles of incidence. Since the illumination pupil is here 1mm at the eye pupil plane instead of the standard 5mm, the light power reaching the retina is strongly reduced, and therefore we need longer exposure times and to average a few frames per

angle of incidence. However, we must take into account the eye stability. Because we do not have a pupil stabilization, averaging several images over a large period of time can lead to a shift of the planned positions of the illumination pupil and end up with an unwanted variation in the angle of incidence. We have set the exposure time at 10ms, only the double of our standard 5ms which seemed experimentally the minimum to reach a acceptable signal to noise ratio. We have kept the same 10Hz illumination pupil variation rate used in the artificial eye test.

### Results: Directional back-scattering of photoreceptors

Figure 8.5 shows four average images (averaging 10 frames each) corresponding to each of the four angles of incidence of the illumination beam on the photoreceptor layer. A few differences can be observed between those four images of the same region.

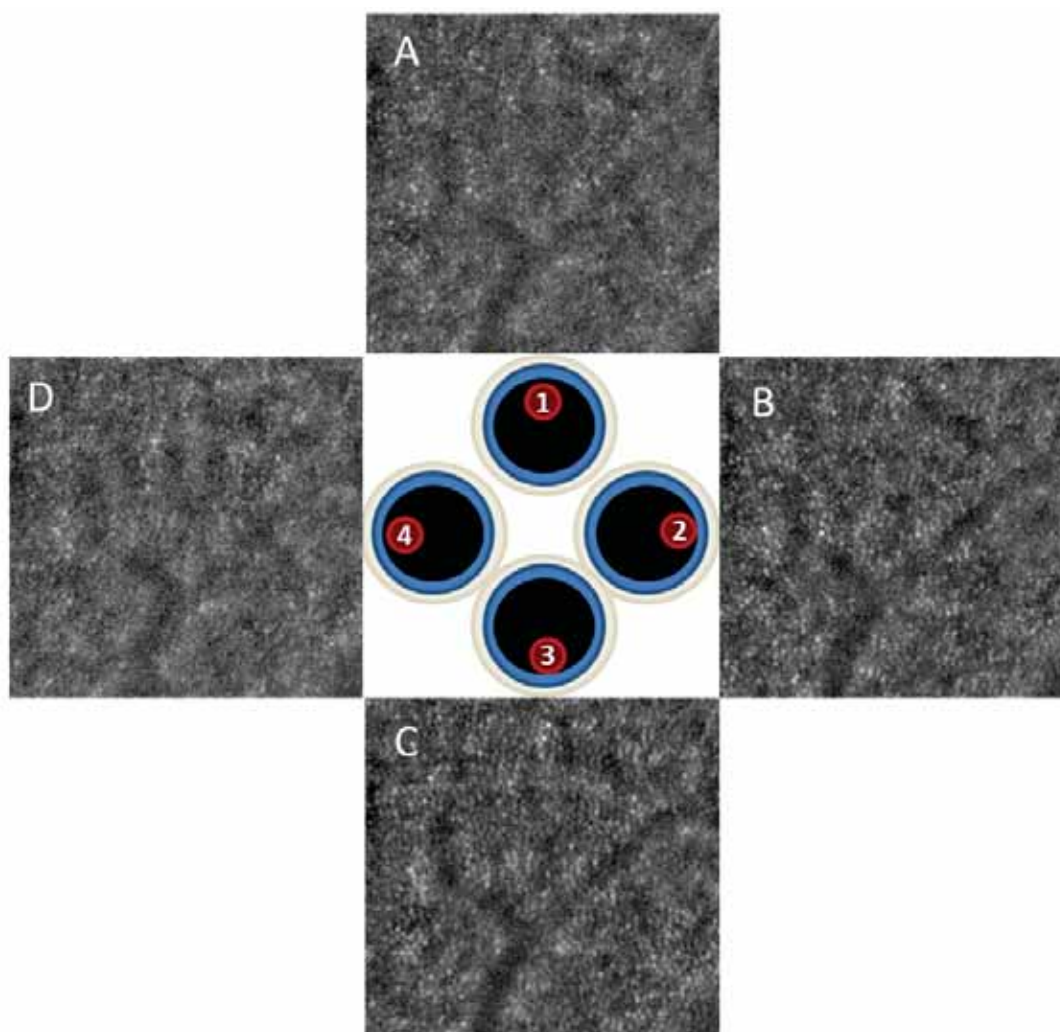


FIGURE 8.5: Four average images from the image sequence acquired on a healthy human subject and corresponding to the four different angles of incidence.

Firstly, we have noticed that the photoreceptors intensity varies with the angle of incidence. In particular, images (A) and (D) seem blurry as almost every photoreceptor seems dark, particularly when comparing it to images (B) and (C). We interpret this phenomenon

to be a consequence of the Stiles Crawford Effect described in Ch. 1. Indeed, photoreceptors behave like wave-guides, meaning the photoreceptors acceptance angle of light presents a Gaussian distribution, with its peak corresponding to the light coming from the center of the pupil in healthy subjects. So a position of the illumination beam at the eye pupil plane too far from the center of the eye pupil in (A) and (D) can explain a photoreceptors response significantly lower. Even though we have planned the four positions for the illumination beam at the eye pupil to be around the center of the pupil of the eye, the limitations of our system make it difficult to precisely control their exact position. Indeed, the subject, even with good fixation, may have moved before the acquisition, shifting the four position towards one edge which would explain the darkness of the photoreceptors in (A) and (D), most likely close to the edge, and the bright photoreceptors in (B) and (C), most likely close to the center of the pupil. This shift of the four illumination pupil positions of could also be explained by an error of the imaging protocol. Indeed, since we are imaging at  $10^\circ$  T, we have asked our subject to follow the fixation target (cf.Ch. 4 for details on the fixation target) and he has therefore moved the center of his pupil towards that direction. If the system has not been correctly realigned the four positions of our illumination beam might have reached the eye pupil slightly shifted towards one edge.

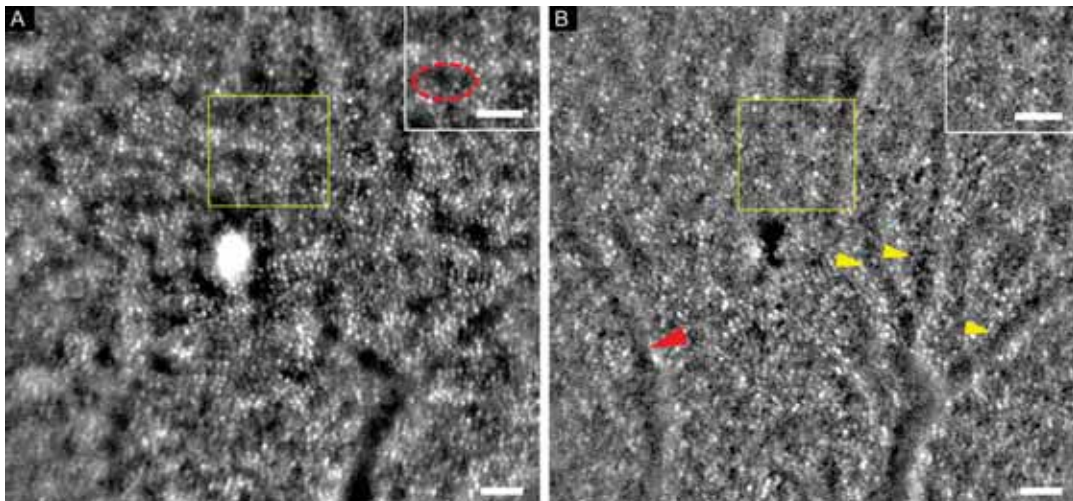


FIGURE 8.6: (A) Average image generated from the sum of Fig 8.5 (A) and Fig 8.5(C). A zoom of the area marked in a yellow box is shown in the top right side of the image, where a circle in dashed line identifies a shade from out of focus features. (B) Differential phase image computed from Fig 8.5 (A) and Fig 8.5(C) with a zoom of the same area than the zoom in (A). Red and yellow arrowheads identify a vessel on the left and branches of a vessel on the right respectively, which are invisible in the averaged image (A). Scale bars are  $50\mu\text{m}$ .

Similarly to the test on artificial eye we have computed here the differential phase contrast image using Eq. 8.1 with images (A) and (C) in Fig.8.5 which have been illuminated with opposite incidence angles. Figure 8.6 shows the resulting phase contrast image (B) next to the average image generated from the sum of images (A) and (C). The bright spot in the middle of Fig. 8.6 (A) corresponds to the wavefront sensor punctual light source and appears as a dark spot in the center of the phase contrast image. This kind of artifact, since the spot masks information from the retina, will be avoided in the future by introducing a dichroic filter in front of the imaging camera. Concerning the rest of the information in both images, the first observation we can make is the lack of out of focus dark patches present in the average image (A) compared to (B). A zoom on the same region

of each image is shown in Fig. 8.6 where a red ellipse with a dashed line identifies in (A) a dark shade corresponding to out of focus features which does not appear in the phase contrast image (B). Indeed, phase imaging has the advantage of improving optical sectioning since the out of focus light is contained in the background contribution and does not depend on the angle of incidence. Therefore, when subtracting the two differently illuminated images we cancel these out of focus terms. We can also notice a difference in the aspect of the vessels. In the averaged reflectance image they appear dark and belonging to the same plane, while in the phase image they display a shadowing that gives a relief making them look as belonging to a different layer. Additionally, we seem to better visualize the vessels in the phase contrast image than in the average image (A), where for instance the left vessel observed in (B) (identified with a red arrowhead) is completely invisible in (A). The same can be said of the branches of the vessel of the right (identified with yellow arrowhead).

Nonetheless, even though these observations relate to phase imaging we also observe a strong back scattering of the photoreceptors that is not related to the phase gradient. Indeed, as mentioned before, photoreceptors have a directional acceptance angle because of the Stiles Crawford effect. Because of this same effect they back-scattered the light primarily towards the direction they are oriented, which is in the case of healthy subjects the center of the pupil. Our phase contrast image in Fig. 8.6(B) is the subtraction of two images which have been illuminated with two angles of incidence and thus the same photoreceptors in each image display different intensity because of this Stiles Crawford effect. When subtracting the image obtained is therefore dominated by a non-zero term corresponding to the difference in intensity of photoreceptors in each image. This strong signal may be masking other signals originating in phase gradient differences of other retinal structures.

Finally some limitations concerning the experimental set-up must be addressed. First, the low signal to noise ratio due to the low power of the source has made us increase in exposure time which has led to a slower acquisition frequency. Adding to this fact that even with the increase the exposure time, the contrast remains lower than with standard illumination, a more powerful light source is necessary to achieve a suitable exploitation of this instrument. Second, this instrument, allowing us to vary the angle of incidence of the illumination of the retina, has been implemented in the same illumination path as the dark-field imaging described in Chs. 5, 6. Therefore, the diffraction effect generated by this SLM has also an impact on the quality of the images acquired with this instrument. A separated illumination path for the implementation described in this Chapter could improve the image quality while solutions for the limitations of the SLM are being studied.

## 8.4 Conclusion

The computation of a phase contrast image using the method from [77] and [78] on a human retina *in-vivo* with this instrument developed in AO-FIO has led to a less conclusive image than in the previous test on artificial eye. The 3D rendering clearly observed on the paper in previous section typical of phase gradient contrast is not observed here. Additionally the directional back-scattering of photoreceptors prevents us from canceling their signal as part of the background contribution which dominates the contrast of the image.

From these conclusions, future lines of work have been drawn. On the one hand, since we have observed in images (A) and (B) almost a complete extinction of photoreceptors, most likely due to an illumination incidence far from the center of the pupil, we could hypothesize that two acquisitions with two angles of incidence as close to opposite edges of the eye pupil as possible could lead to two images with dark photoreceptors. The absence of photoreceptors signal could enable the detection of the phase gradient term from other retinal structures. Another option could be to change the focus of the camera to other layers, making the photoreceptors signal so out of focus that it would be cancelled out as part as the background contribution as shown before. On the other hand, instead of using this instrument to exploit phase contrast we could use it to exploit the directionality of the photoreceptors back-scattering. Indeed, since the maximum amount of back-scattered light by these retinal structures is achieved in the direction in which they are oriented, we could use the variation of illumination of photoreceptors as a tool to derive their orientation. This functional analysis is described in following Ch. 9 in Part. IV where the clinical applications of the instruments are addressed.

## **Part IV**

# **Clinical application: From structure to function**



The three implementations described in the previous Part III turn the AO-FIO into a valuable tool for microvasculature analysis as it enables us to observe microscopic structures like vessel walls or capillaries. It has also enabled us to observe structures that might be retinal pigment epithelium, in which case it would mean that we are able to image structures that are usually masked by photoreceptors strong back-scattered signal. This enhancement is complemented in this part with the computation of biomarkers useful in a clinical setting. This part is divided into three chapters concerning each a particular retinal network or structure. The neural network still remains globally invisible aside from the nerve fibers layer and photoreceptors. A structural and functional analysis of the latter is explored in Ch.9. Chapter10 describes the biomarkers that can be computed on dark-field image sequences obtained with our AO-FIO as we are able to follow erythrocytes in capillaries or vessel deformation. In particular, it describes functional analysis of the perfusion function achieved thanks to the development of specific image processing. Finally the last chapter introduces an alternative imaging technique to image retinal pigment epithelium and draws a comparison with the dark-field imaging in AO-FIO.



## Chapter 9

# Extracting neural retinal biomarkers

Parts II and III described the manipulation of the illumination geometry on an AO-FIO and the implementation of three instruments. This manipulation aimed to improve the contrast by either selecting multiply scattered light (Chapter 6), filtering out the out of focus light (Chapter 7) or by selecting directional scatterers (Chapter 8). In these following two Chapters we aim to show the various applications that an AO-FIO with an optimized adaptive optics and the improved contrast can carry out in a clinical setting.

In this Chapter we describe the two neural structures, photoreceptors and nerve fibers, that can be imaged with a high contrast using our optical system and the biomarkers that can be derived informing on the pathological state of these structures. Finally we describe how the orientation of photoreceptors can be derived, which has been proposed as an indirect functional biomarker in the sense that it might provide an information on the healthy or pathological functioning of this retinal structure.

### 9.1 Structural biomarkers

In order to achieve functional imaging you must first be able to resolve the retinal structures concerned by those functions. In Chapter 6 we have developed dark-field in full field which enabled us to resolve cells with the same dimensions and spacing as the Retinal Pigment Epithelium (RPE). In Chapter 7, the improvement in optical sectioning brought by the pseudo-confocal technique leads to a more sensitive detection of photoreceptor intensity and variation in intensity. Improving the contrast of the retinal structures carrying out the functions implies that we are more sensitive to any variation, spatial or temporal, of said structures.

#### 9.1.1 Photoreceptors

##### Clinical interest

Photoreceptors are intensively studied in the retinal imaging community for two main reasons. Firstly, they participate in the transduction function (see Ch. 1) which converts the light stimulus into a neural stimulus, leading to vision. Pathologies degenerating the photoreceptor mosaic lead rapidly to blindness and are irreversible. A good understanding of these structures as well as an early diagnosis are critical.

A biomarker often used to evaluate the degeneration of this mosaic is the **cone density** [99, 100]. This density computation can be done automatically, using methods which have been developed by a few teams [101, 102], or semi-automatically as sometimes the contrast of images does not always allows an exhaustive automatic computation [103]. In both cases a very well resolved and highly contrasted mosaic is necessary. As mentioned above, Chapter 7 describes the implementation of an imaging technique allowing us to partially filter out the out of focus light in an AO-FIO, leading to an enhancement in contrast of the

photoreceptor mosaic. Here we show how this technique improves the computation of the photoreceptor density, a biomarker evaluating the degeneration of the mosaic.

### Biomarker

Two image sequences of the photoreceptor layer have been acquired, one using the AO-FIO with the standard illumination, the other using the pseudo-confocal technique described in Chapter 7. Both sequences were acquired at 10° temporal and in the same imaging session for comparison purposes.

Average images have been computed for both sequences and the same region displaying a photoreceptors mosaic has been cropped in both averages. Then, both cropped areas (see Fig.9.1) corresponding to each modality have been processed using Li et al. [101] cone counting algorithm. The algorithm binarize the cropped images with respect to a size in pixels of the structure of interest as well as a threshold value that we introduce. Results are shown in Table 9.1. We notice that the cropped area acquired with standard illumination is less contrasted and leading to missing cones in the counting. We can conclude that the enhancement in contrast brought by the pseudo-confocal technique leads to a more accurate computation of this metric.

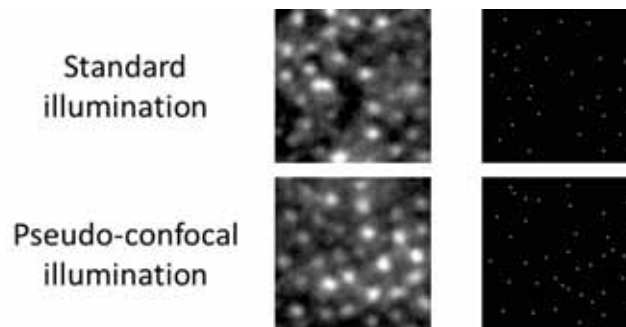


FIGURE 9.1: Positions of the cones computed by the algorithm of Li et al on two cropped areas of the same region of interest of two average images illuminated in a standard and pseudo-confocal configuration respectively.

Illumination configuration	Number of cones in region #1	# of regions analyzed	Cone density (cones/mm <sup>2</sup> )
Standard illumination	29	9	8324
Pseudo-confocal illumination	38		9469

TABLE 9.1: Table showing the number of cones in both cropped areas displayed in Fig.9.1 and computed by Li et al algorithm.[101], the number(#) of regions from images in Fig. 7.4 (illuminated squares in the pseudo-confocal images and their corresponding regions in the standard illumination average), and the computed cone density.

### 9.1.2 Nerve fibers

#### Clinical interest

Another neural structure that can be very clearly visualized in our system is the nerve fiber layer. When focusing on this layer we are able to resolve the nerve fiber bundles and even

identify vessels interlaced in between.

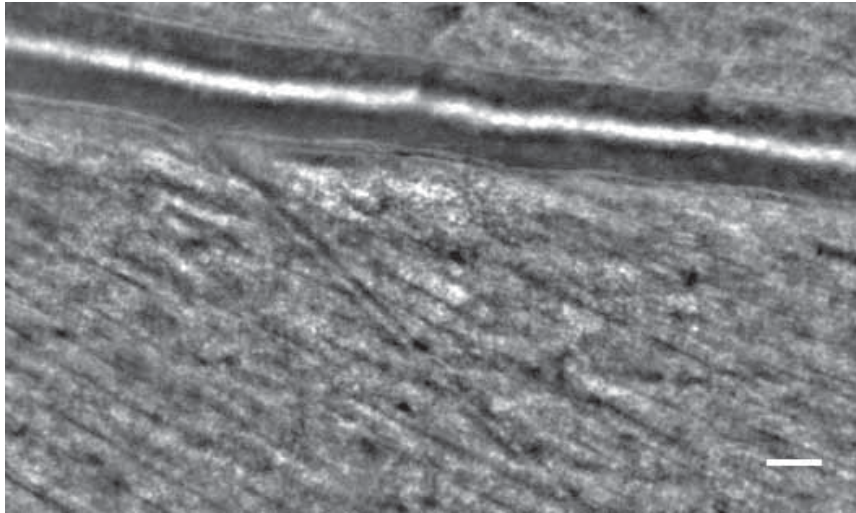


FIGURE 9.2: Average image showing a vessel lying in the nerve fiber layer, which appears highly contrasted. The fiber bundles are resolved and we can derive the direction of alignment of the fibers. Scale bar is 50  $\mu\text{m}$ .

### Biomarker

A very useful biomarker concerning the nerve fibers is the thickness of the nerve fiber layer, which is usually carried out by Optical Coherence Tomography (OCT) [104, 105]. In our system we do not have the axial resolution of the OCT but we have a high spatial resolution and good contrast. Thanks to these performances we are able to obtain highly contrasted images of the nerve fibers like the one shown in Fig.9.2. Several characteristics of the fibers can be closely studied thanks to these images such as the direction of the fibers, which appears very clearly on the images of this layer as well as their position relatively to vessels and the way they are interlaced.

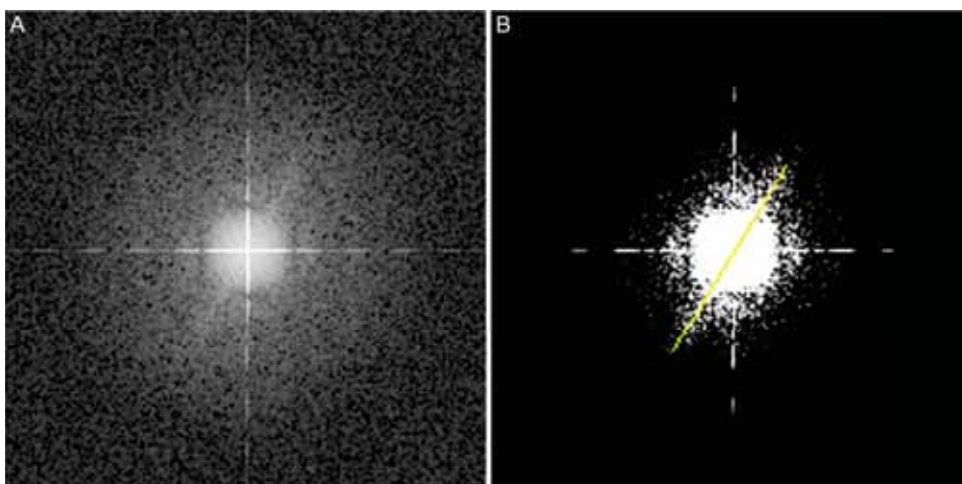


FIGURE 9.3: (A) Fourier Transform of the nerve fibers image in Fig. 9.2. (B) Binary image generated by applying a threshold to (A), which enables us to better visualize the frequency signature of the fibers regular spacing: a diagonal segment marked with a yellow segment.

Finally, we could imagine computing the spacing between the fiber bundles in order to analyze if the spacing increases in subjects with neural degenerative diseases. Indeed, when we compute the Fourier transform, shown in Fig. 9.3 (A), of a region of Fig. 9.2 containing only fiber bundles, we observe a frequency signature of the fibers in the form of a diagonal segment (identified with a yellow segment on the binarized image). By measuring the size of this segment we can derive the spacing between the fibers. Using ImageJ software (National Institutes of Health, USA) we measured  $45 \pm 2$  pixels leading to spatial frequency of 120 cycles/mm, i.e. a spatial period of  $8 \mu\text{m}$  between fiber bundles which is consistent with the literature (which indicates the spacing is a few microns) [106].

### 9.1.3 Comparison with AO-SLO

AO-SLO enables us to acquire very highly contrasted images of the photoreceptor mosaic as a confocal pinhole is often implemented allowing the filtering of out of focus light, leading to a high optical sectioning and a very clear cone mosaic. However, the implementation of a technique allowing the filtering of out of focus light in full field implies a contrast close to AO-SLO but without distortion artifacts. Indeed, as mentioned in Chapter 1, AO-SLO may need an AO-FIO template for distortion correction as in some image sequences all of the frames are distorted. If the same great contrast could be achieved in AO-FIO, a single instrument could be used, instead of the two suggested in Chapter 1. This is particularly true for pathological eyes, being the cases which interest us in the clinical setting since we are looking to evaluate retinal degeneration. Furthermore, AO-FIO also benefits from a large field of view, which implies faster total image processing time when studying large regions of the retina. Both of these advantages are also valid for nerve fiber imaging where distortion can mislead diagnosis and a large field of view is interesting since they are long structures visible in large areas of the retina.

## 9.2 Functional biomarkers

In this section we explore the second application of the instrument implemented in Ch. 8 that enables the variation of the incident angle of the illumination beam. As it was mentioned, this instrument was first designed to derive the photoreceptors orientation, which is the neural functional biomarker presented in this Chapter. The following paragraphs describe the clinical interest and the interest of this particular biomarker as well as the details on its computation, the first results and perspectives. We use the name "retinal goniometer" for the instrument implemented in Ch. 8 throughout this section as its application is measuring the photoreceptors orientation.

### 9.2.1 Clinical interest

Photoreceptors takes part in transduction, i.e. the conversion of the optical signal to electrical signal. In some pathologies photoreceptors are still visible on retinal images although the patient's vision is impaired and therefore their function is clearly failing. A clue to the failure of photoreceptors can be the loss of their normal orientation, which is towards the eye pupil.

In the following paragraph we have shown how the retinal goniometer could represent a valuable tool to assess the orientation of photoreceptors. Although it remains unclear what is the relationship between the reflectivity in AO retinal imaging and the cone function [107], this instrument could be used to further investigate the functional application of this biomarker (orientation of photoreceptors).

### 9.2.2 Biomarker: Photoreceptor brightness at various illumination incidences

A biomarker indicating the orientation of the photoreceptors could be derived by exploiting the optical effect known as the optical Stiles Craford effect. This effect, related to the directional sensitivity of the photoreceptors, consists in the variation of the amount of light acceptance and back-scattered photons of the photoreceptors with the incidence of the illumination beam. The maximum of both acceptance and back-scattering happens when photoreceptors are illuminated in the same direction they are oriented. Light reaches the photoreceptors when the direction of the illumination beam is coincident with the orientation of the photoreceptors.

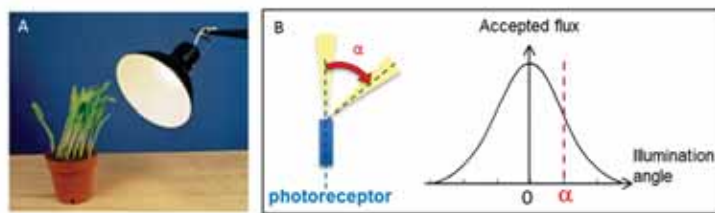


FIGURE 9.4: (A) Picture illustrating the Stiles Craford effect of photoreceptors. Here the plants represent photoreceptors that are oriented in the direction of the illumination. The isolated sprout represents a pathological photoreceptor whose orientation is opposed to the light. (B) A schematic illustration of a photoreceptor with two illumination beams, one in the axis of its orientation and another with an angle of incidence  $\alpha$  with respect to its orientation axis. A graph shows the acceptance flux as a function of the illumination angle of incidence. The maximum acceptance flux corresponds to the illumination beam at a  $0^\circ$  while the beam at  $\alpha$  shows a reduced acceptance.

The computation of this biomarker has previously been attempted by Miloudi et al. [108] using the RTX1 system (Imagine eyes, France), a commercial AO-FIO. The method implemented in this study was to manually vary the illumination pupil and analyze the photoreceptor brightness over the same region for each incidence which led to the visualization of the optical Stiles Craford effect in the form of a negative cone mosaic. However, the precision in the control over the illumination pupil position was limited as it was achieved manually and the time between acquisitions with different incidences was quite long which increases the uncertainty on photoreceptor brightness variations.

We propose here a similar approach but with an instrument enabling an automatic and fast variation of the illumination incidence in order to overcome those limitations. The principle of the computation of this biomarker is the following. Retinal images in our AO-FIO system are acquired by asking the subject to fixate a target. An illumination beam is focused into the retina forming an illuminated field of view in the back of the eye. We have acquired images with different illumination incidence. The acquisition protocol is the same as described in Ch. 8. We have acquired an image sequence where the illumination incidence is sequentially and automatically modified at a 10Hz rate by a custom-made Labview software to four pupil positions of the illumination beam at the eye pupil plane (see Fig.9.5 (B)). This leads to four different incidence angles of illumination of the retina. We have selected a 1.8mm diameter of the aperture stop, which corresponds to 2mm at the eye pupil plane. Dimensions have been computed to keep the pupil of the

beam inside the pupil of the eye, which is set in our system to 5mm. All the selected dimensions are summarized in Fig.9.5(A). Then, an average image for each incidence was computed.

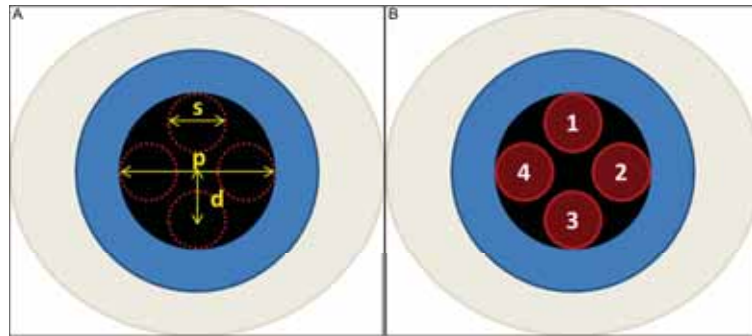


FIGURE 9.5: Schematic drawing showing the positions of the illumination beam pupil at the eye pupil plane and the dimensions set.  $s$  is 2 mm,  $p$  is 5 mm and  $d$  is set to 1mm at the eye pupil plane.

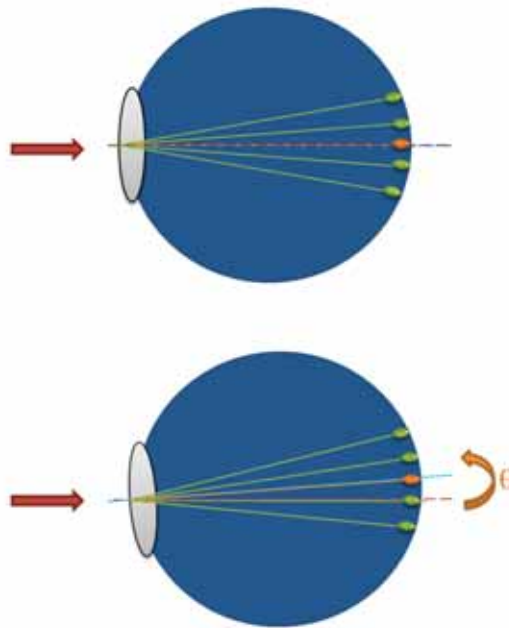


FIGURE 9.6: Schematic drawing showing photoreceptors alignment. The small green ellipsoids at the back of the eye represent photoreceptors at different eccentricities. The orange ellipsoid represent the photoreceptors at  $0^\circ$  eccentricity. The green segments going from the photoreceptors to the center of the pupil show their orientations axis. Red and blue segments represent the illumination and visual axis (see Ch. 1 for the definition of visual axis) respectively of the eye. Two configurations are represented. The upper drawing shows the visual axis of the eye confounded with the illumination axis. The lower drawing shows a rotation with respect to the upper configuration where the visual axis differs from the illumination axis. Here the illumination axis is confounded with the photoreceptors orientation axis from another eccentricity. The red arrow represents the light coming into the eye.

The photoreceptors of every eccentricity can be evaluated by asking the subject to follow a visual target leading to the imaging of various regions of the retina. In Fig. 9.6 there is a schematic drawing showing a subject eye fixated so as to image the photoreceptor mosaic. Photoreceptors are represented as an orange ellipsoid, for  $0^\circ$  eccentricity, and green ellipsoids, for the rest of the eccentricities. Wherever the subject is fixating, the illumination axis (red axis) should always be parallel to the photoreceptors orientation we are imaging given our small field of view, and therefore their orientation would correspond to the illumination incidence of the image showing their maximum brightness.

The results shown in Fig. 9.7 are the same presented in Ch. 8.5 analyzed here for a different application. We have used the same image sequence described in Ch. 8. The image sequences were processed using the same custom-made algorithms described in Ch. 4. In short, we have corrected images for inhomogeneous illumination, registered the sequence and averaged the frames corresponding to the each pupil position.

These first images enable us to assess if our system is sensitive enough to the change of photoreceptors brightness with varying illumination incidence. We have noticed that some of the positions (Fig. 9.7 (B) and (C)) back-scatter much more light than others (Fig. 9.7 (A) and (D)). However these are images averaged over a time period of half a second, which is quite long if we take into account other potential effects with an impact on photoreceptor brightness, such as photoreceptor bleaching. So, a more accurate comparison has been achieved using this image sequence.

Figure 9.8 shows the variation in brightness of a small region with a photoreceptor mosaic, where each cropped image corresponds to the average of 10 successive frames. Indeed, in our imaging protocol the illumination beam is sequentially changed between four positions. The time on each averaged image marked in yellow corresponds to the moments when the pupil position changes, which is every 100 ms or 10 frames. We notice that for each pupil position, even at different times in the sequence, the photoreceptors mosaic aspect is very similar. Positions 1 and 4 back-scatters very little while 2 and 3 display a bright mosaic. These observations show that the system is sensitive to a variation in pupil position and that the variation in brightness is not due to eye fixational movements or other physiological reasons but the angle of incidence of the illumination.

However we also notice subtle differences between the images for the same pupil position. For instance when looking in Fig. 9.8 to images of position 2, a red arrowhead identifies a cone in each image whose brightness slightly varies from one moment to the next. These variations, which could have a physiological origin, incite us to analyze the Stiles-Crawford effect on a short temporal period in order to have more accurate measurements by reducing the potential impact of other effects, such as intrinsic signal variations of the cones.

Since the images have been acquired on a healthy subject we have expected to observe four similar brightness levels considering that we shifted the illumination pupil of the same distance which should lead to the same angle of incidence in four different directions. However, the brightness levels highly vary between positions {1,4} and {2,3}. This difference, as it has been quickly explained in Ch. 8, is probably due to a misplacement of the four positions which instead of being centered around the center of the eye pupil could all have been slightly shifted to the edge of the pupil. In our case, the four positions have probably been shifted towards the edge in positions 4 and 1 which would lead pupils 2 and 3 in a more central position. Additionally, the difference between positions 2 and 3 is more difficult to evaluate as the signal to noise ratio is low.

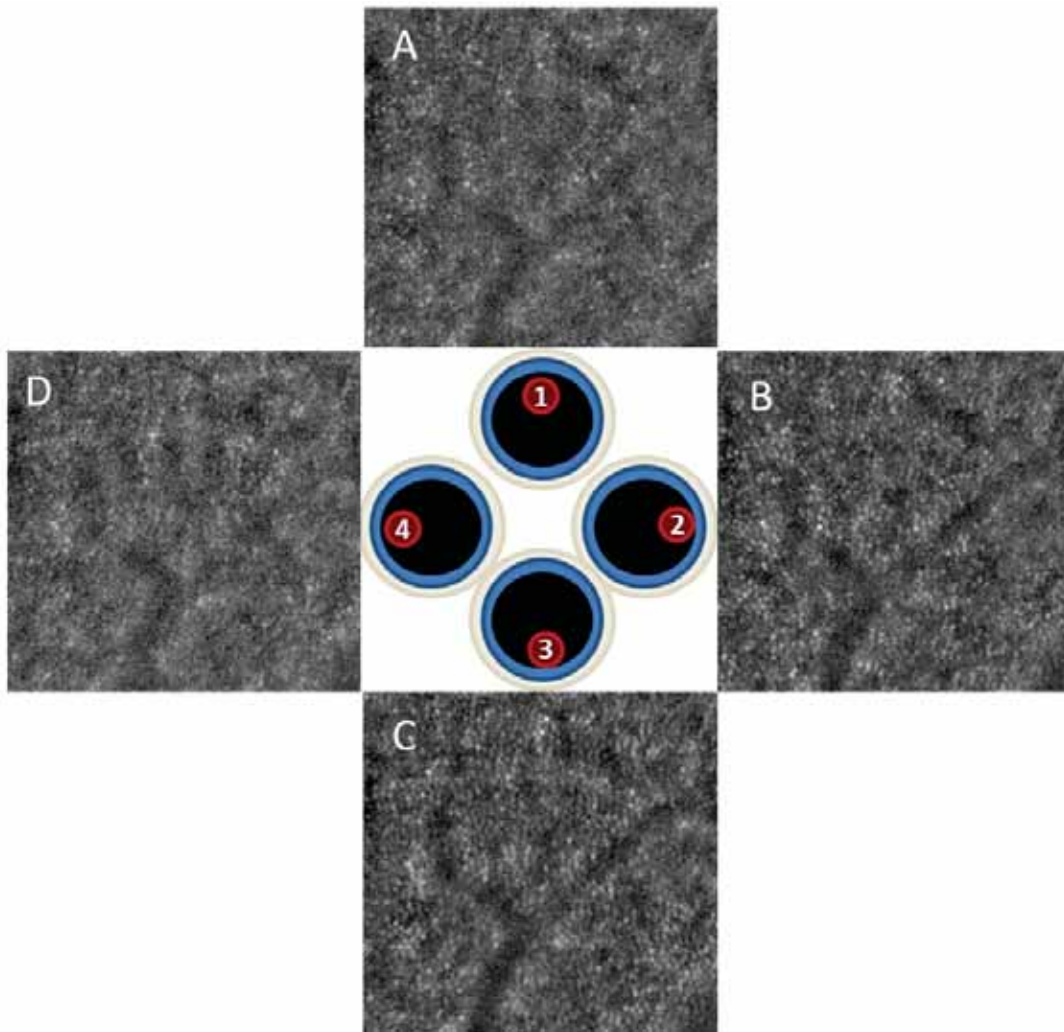


FIGURE 9.7: Four averaged images from the image sequence acquired on a healthy human subject and corresponding to the four different angles of incidence.

Nonetheless we observe a sensitivity of the retinal goniometer to the angle of incidence which delivers a functional information about the orientation of photoreceptors. In this first test we derive that photoreceptors are oriented towards the incidence given by the pupil position 2 or 3. The accuracy of this analysis could be increased by enhancing the signal to noise ratio. These conclusions encourage us to further improve this system for this application, in particular by implementing a pupil stabilization which would enable a fine control and knowledge of the pupil position and therefore illumination beam incidence.

In order to study the directionality of the back-scattered light by photoreceptors we can subtract two images acquired with complementary illuminations (two opposite pupil positions). Such an image has been obtained in previous Ch. 8, where we have computed the Differential Phase Contrast ( $I_{DPC} = \frac{I_{\theta} - I_{-\theta}}{I_{\theta} + I_{-\theta}}$ ) using images with complementary illuminations 1 and 3 (cf. Fig. 9.5). In Fig. 9.9 the absolute value of the DPC image is presented next to the average image of the same region. We have noticed when comparing these images that some photoreceptors appear dark in the DPC image (red arrowheads in Fig. 9.9) implying that they back-scattered with the same brightness intensity when illuminated at different incident angles. Indeed, if the intensity of a photoreceptor varied substantially

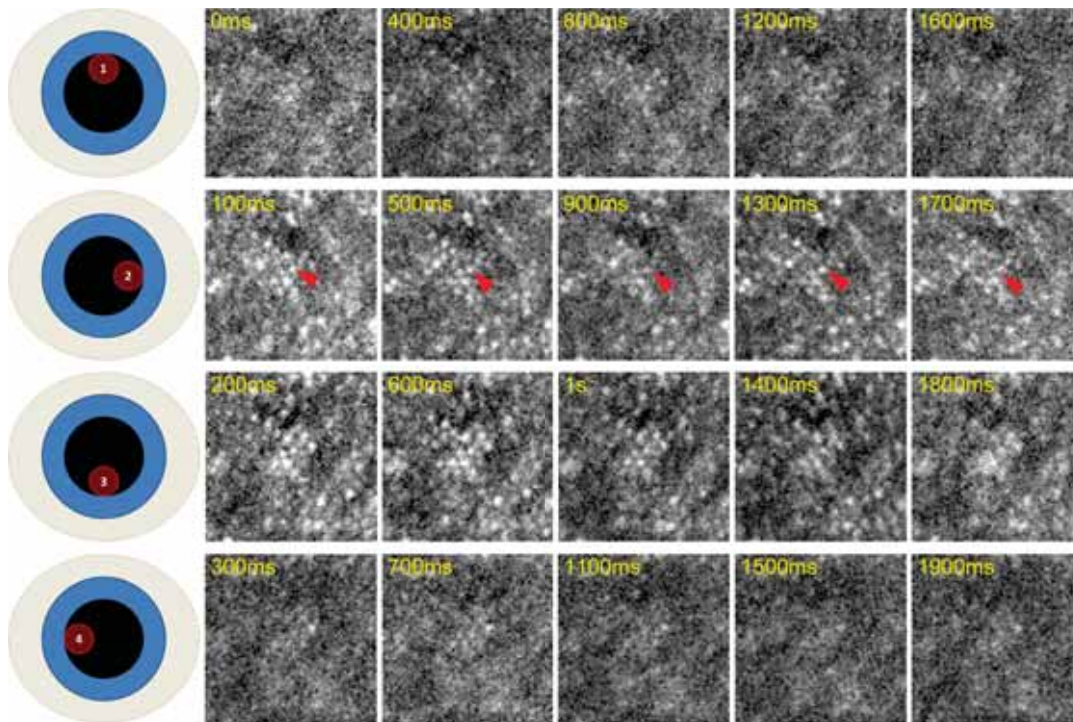


FIGURE 9.8: Cropped images showing the same photoreceptor mosaic illuminated through four different angles of incidence. The four incidence are represented on the left by four schematic drawings showing the illumination pupil at the eye lens. For each incidence five averages of 10 frames are displayed. In yellow is marked on each average image the acquisition time of the image sequence where the first raw image of the 10 averaged frames is captured. Averages of pupil positions 2 and 3 show higher reflectance than 1 and 4.

the subtraction between two images of this photoreceptors would lead to either a bright spot or a dark spot in the DPC image. By taking the absolute value of the DPC image, the dark spots become the pixels with an intensity close to zero. A first interpretation was that we are observing rods which have not the same wave guiding properties of the cones and therefore would keep the same brightness when varying the angle of the incident illumination beam. Indeed, even though we do not have the resolution to image rods, it could be an unresolved image of a rod or a group of rods. However, it might also be a cone whose back-scattered light remained constant between the two illuminations. Although the subject tested was healthy, it could be hypothesized that the orientation of the cones identified as dark in the DPC images is different to the orientation of the surrounding cones. Indeed, as mentioned before, if our illumination shifts were perfectly centered with the center of the eye pupil, the photoreceptors brightness should be the same on images with complementary incidences. Here we are probably not perfectly centered and therefore the majority of the photoreceptors show an intensity difference between the two complementary images, with the exception of the identified dark cones. Finally, another hypothesis is that the wave-guiding properties assigned to the cones might not be verified for these particular cone photoreceptors because of a physiological difference in the cell (e.g. they are at a different stage in the disk renewal or pathological deterioration) with respect to the other cones. Further investigation needs to be done to answer these questions.

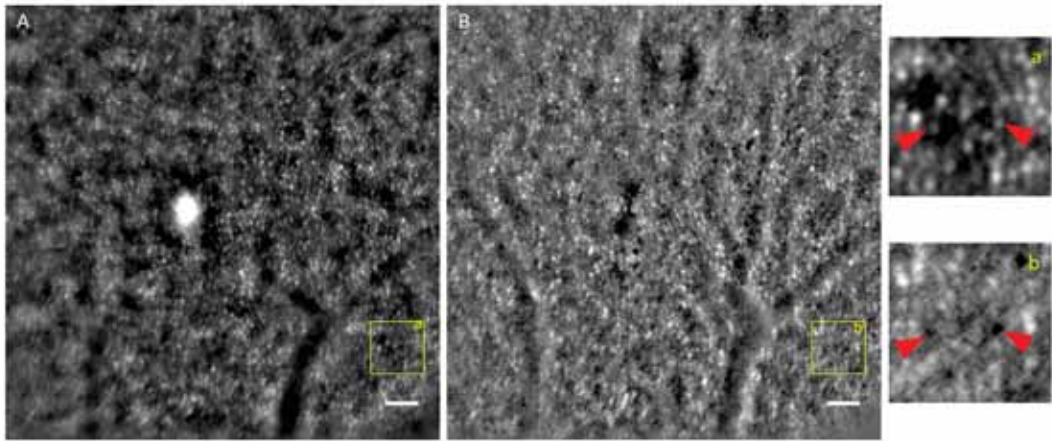


FIGURE 9.9: (A) Average image generated from the sum of Fig 8.5 (A) and (D). (B) Differential phase contrast image between positions 1 and 4. (a,b) Zooms on the same area of images (A,B) respectively. Red arrowheads show two photoreceptors appearing black in the differential image, implying that the photoreceptors brightness has not vary significantly between the two positions. Scale bars are  $50\mu\text{m}$ .

### 9.3 Conclusion

In this section we have shown the clinical applications of the implementations in Part III for the evaluation of neural cells, and in particular photoreceptors. The enhancement of contrast achieved in Ch.7 leads to the clearer visualization of the photoreceptor mosaic and therefore a more accurate computation of structural biomarkers. Finally, the instrument described in Ch. 8 is used here as a retinal goniometer, i.e. as an instrument measuring the orientation of photoreceptors. We have shown that our system is sensitive enough to detect a difference in photoreceptor brightness when varying the angle, and future work should therefore be oriented towards building a protocol and image processing leading to a measurement of the orientation, as well as improving the measurement accuracy.

## Chapter 10

# Extracting vascular retinal biomarkers

In previous Ch.9, we discussed the clinical applications of the instruments described in Part III for the study of neural structures and in particular on photoreceptors. We showed that quantifying variations of these cells was critical to understanding a range of pathologies affecting photoreceptors and to eventually provide the earliest possible diagnosis. However, the detection of a damaged structure or dysfunction of the photoreceptors might come a little too late indicating already an irreversible deterioration of the retina. Therefore, to prevent this neural damage it is essential to detect the pathology before the appearance of symptoms in the neural cells. This could be achieved by studying the surrounding cells whose deterioration are not always a symptom of the neural pathology but can be its actual cause. An example of such retinal structure is the vascular network, whose function is to provide oxygen and nutrients to the retina. The lack of these supplies leads to this kind of cellular degeneration. Therefore spotting a failure of the vascular function can lead to an early diagnosis avoiding an irreversible deterioration of the retina.

The aim of this Chapter is to show that the implementations achieved in the previous Chapters have also clinical applications in the study of vascular structures. Like Ch.9, this Chapter is divided in two sections: Section 10.1 is focused on the imaging of retinal vessels and quantification of their structural variations, we detail the clinical interest of studying these retinal structures and describe various biomarkers for evaluating their good condition, i.e. quantifying a variation in the structures of interest that could be an indication of a pathology. Then, in Sect. 10.2 we discuss the potential functional imaging of the vascular network that could be achieved thanks to the new implementations. To do so, we show functional biomarkers whose variations could indicate a damage of the vascular structures before this degradation could affect the aspect of the vessels themselves.

## 10.1 Structural biomarkers

In this section we first explain the clinical interest of studying the vascular structure. Then we describe a range of vascular biomarkers, three of which we compute on our data set in order to show the clinical perspectives of our system in structural imaging of the vascular network.

### 10.1.1 Clinical interest

The retinal vascular network, which delivers nutrients and oxygen to the retina (see Ch. 1 for details), is not very well characterized. Although a few models of the geometry of the network have been proposed, much is still unknown.

A range of clinical tests check the state of the retinal vascular network, but often the information they provide concerns only large vessels since they are unable to resolve capillaries. Yet, when the pathologies are detected at the level of the larger vessels, surrounding cells might have already suffered irreversible damage.

The symptoms observed in retinal vessels vary from one pathology to another. Diseases like macular degeneration or diabetes often result in vessel blockage and the appearance of micro aneurysms respectively, both imply the formation of avascular areas lacking the necessary supplies. Additionally, this usually leads to the formation of new capillaries with a very chaotic geometry and which are very fragile, and therefore break easily, leading to blood leakage in the retina. Other pathologies, such as arterial hypertension, show other symptoms like focal contractions of vessel lumen. These are reversible reductions of the vessel lumen size, which indicates a decrease of vasoconstriction and are generally accompanied by a thickening of the wall. This reduction of the lumen size is also often observed in older patients, where a vein has been drawn to an artery, without achieving contact. This could be due to the fact that the amount of fibers surrounding vessels decreases with age. These vasoconstrictions reduce the amount of blood that reach certain areas and can lead to change of pressure as well as a shortcoming in necessary supplies in the affected regions.

All these pathologies show vascular symptoms that, if not treated, can lead to a rapid deterioration of other retinal structures.

The study of vasculature is therefore essential, in particular the study of the microvascular network, since it is the site of exchange between blood and tissue. Detecting disruptions at this level would lead to early diagnosis before consequences at a larger scale, implying a more important retinal deterioration, appear.

### **Vascular biomarkers**

A range of biomarkers have been defined to inform on the state of the retinal vascular structure in order to detect a potential disruption as well as to indicate the progress of a retinal pathology. We describe here a few biomarkers that allow the quantification of the symptoms mentioned in the above paragraph.

On the one hand, structural biomarkers have been defined to detect the presence of blockage by detecting its symptoms, like chaotic vascular geometry or new avascular zones. Since healthy capillaries follow a very regular geometry, biomarkers evaluating the capillaries nominal geometry and quantifying the geometrical irregularities have been defined to help diagnosis. Additionally, the size and shape of the Foveal avascular Zone (FAZ) [109] can be a helpful biomarker to detect pathologies leading to blood blockage. Finally in order to detect symptoms altering the normal vascular contraction and dilation of vessel, three other biomarkers have been defined, quantifying their lumen size, their wall thickness and the ratio between the two. Ideally, when computing these three biomarkers, the values obtained should be compared to a nominal value associated to vessels of a certain caliber from healthy subjects. However, such values have not been found yet. Thus, the current method relies on computing the mean value of the biomarkers along a large path of the vessel and then comparing values from single points along the vessel to this mean. Pathological values stand out from the mean indicating an irregular constriction or dilation of the vessel.

These three last biomarkers have been computed on vessels and capillaries from healthy

subjects imaged with dark-field imaging developed on our AO-FIO (Ch. 6) and the results are presented in the following paragraph.

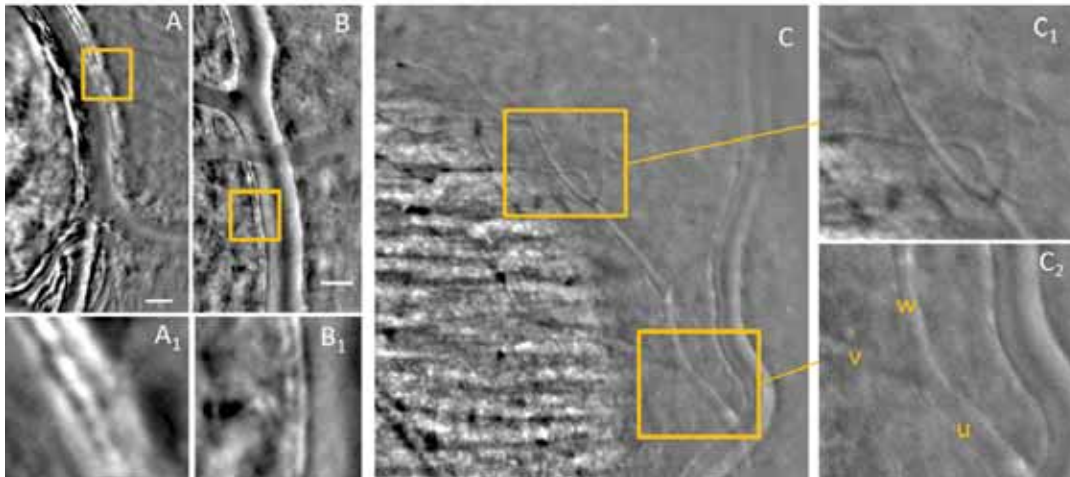


FIGURE 10.1: (A,B,C) Average images of vessels of different calibers imaged in dark-field configuration showing how the contrast enhancement of this modality enable us to derive the lumen size of capillaries (C) and accurate WLR of retinal vessels (A,B). (A1) Zoom of vessel wall in (A), (B1) zoom of vessel wall in (B), (C1) zoom to capillaries of (C) where the lumen is visible, (C2) zoom to vessel lumen of (C).

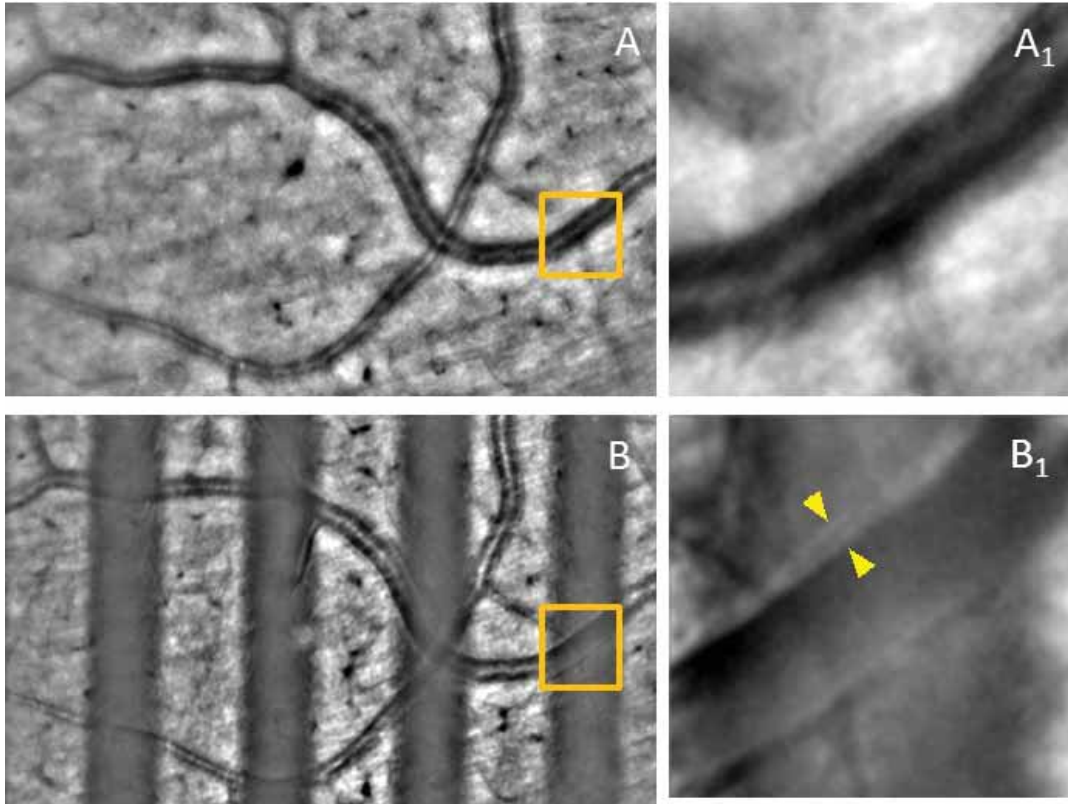


FIGURE 10.2: Two average images of the same peripheral retina vessels with (A) acquired in bright-field configuration and (B) with regions in dark-field configuration using the new illumination path described in Chapter 5. Zooms (A1) and (B1) show the same region of interest from averages (A) and (B). Lumen and wall (yellow arrowheads) are visible in (B1) while harder to visualize in (A1).

#### *Biomarkers on our data: capillaries lumen size, wall thickness and wall-to-lumen ratio*

Thanks to the enhancement of contrast obtained in the dark-field imaging implemented in our system we are able to measure **vessel lumen size**, including capillaries, and **wall thickness**, where we can even detect each one of its layers. With these two measurements we can also compute the **wall-to-lumen ratio**. We show in Fig. 10.1 and Fig. 10.2 examples of vessels and capillaries on which we have computed these three biomarkers. In Fig. 10.1 images were acquired using the standard AO FIO illumination and the dark-field was generated either by the back scattering of the lamina cribrosa (Fig. 10.1 A), the dark regions from the field stop (Fig. 10.1 B) or simply by the boundaries of the standard illumination (Fig. 10.1 C).

The biomarkers have been computed manually in image processing software ImageJ (National Institute of Health, USA) and the results have been summarized in Tab. 10.1. Several measurements have been conducted in order to compute the uncertainty on the values.

A few observations can be made on the results shown in Tab. 10.1. Firstly, as it has been previously mentioned, we did not find a given wall-to-lumen ratio value associated to a healthy vessel. The vessel from Fig. 10.1 (A1) has ratio of 0.68 while the one from (B1) has much lower ratio of 0.19. It is even more interesting when we consider than both those

Figure #	Zoom #	Structure of interest	Biomarker	biomarker's value
10.1.A	A1	Artery near lamina cribrosa	Wall thickness	$26 \mu\text{m} \pm 1 \mu\text{m}$
			Lumen size	$38.7 \mu\text{m} \pm 1 \mu\text{m}$
			WLR	0.68
10.1.B	B1	Peripheral retina artery	Wall thickness	$11 \mu\text{m} \pm 1 \mu\text{m}$
			Lumen size	$58 \mu\text{m} \pm 1 \mu\text{m}$
			WLR	0.19
10.1.C	C1	Peripheral retina capillaries	Lumen size	$3.5 \mu\text{m} \pm 1 \mu\text{m}$
	C2	Peripheral retina vessel u	Lumen size	$29.6 \mu\text{m} \pm 1 \mu\text{m}$
		Peripheral retina vessel v	Lumen size	$10.5 \mu\text{m} \pm 1 \mu\text{m}$
		Peripheral retina vessel w	Lumen size	$14 \mu\text{m} \pm 1 \mu\text{m}$
10.2.B	B1	Peripheral retina vessel	Wall thickness	$7 \mu\text{m} \pm 1 \mu\text{m}$
			Lumen size	$31 \mu\text{m} \pm 1 \mu\text{m}$
			WLR	0.23
		Peripheral retina capillary	Lumen size	$3.2 \mu\text{m} \pm 1 \mu\text{m}$

TABLE 10.1: Table summarizing the computed biomarkers (eg. wall thickness, lumen size and wall-to-lumen (WLR) ratio) on the vascular structures shown in Fig.10.1 and Fig.10.2

vessels have a total outer diameter of  $65\mu\text{m}$  and  $69\mu\text{m}$  respectively, meaning the wall-to-lumen ratio can show a significant difference between two vessels of similar sizes. For this reason the current method consists in comparing the wall-to-lumen ratio values obtained on a given vessel to the mean value of the wall-to-lumen ratio computed along a path of the vessel itself. Secondly, results on Fig.10.1 (C) presented in the third row of Tab.10.1 show that a large range of vessel calibers that can be measured using dark-field imaging in full field, with a precision of half a micron. Finally, the last row of Tab.10.1 show that these results can also be obtained when using the new illumination path described in Chapters 5 and 6. However, these last computations have been carried out on an average image (Fig.10.2) where the field of view has only been partially illuminated in dark-field configuration. In order to be able to compute these biomarkers anywhere in the whole field of view we need to improve our dark-field configuration. Indeed, we need to identify the size of the dark fields that are best adapted to the structures we are imaging and increase the signal to noise ratio so as to obtain the necessary high contrast in the whole field of view.

### Comparison with AO-SLO

Several studies on vasculature, particularly on the microvascular network, has been carried out using AO-SLO. This technique is indeed a valuable tool to study this structure as it has an outstanding resolution and contrast and the biomarkers presented in this section have been computed with AO-SLO systems. Similarly, vascular pathologies have been studied using the commercial adaptive optics camera RTX-1 (Imagine Eyes, Orsay, France), where biomarkers such as those presented in this section have been exploited [5, 110–112]. However, in AO corrected cameras, some features remain masked by strong back-scattered signal, such as the smaller capillaries. The aim of this work was to reach a contrast with these new developments enabling us to image the vascular features that were previously invisible in AO-FIO systems and therefore improve the visibility of structures like the vessel walls or the microvasculature. The possibility of achieving these accurate measurements on full field implies getting rid of distortion and the potential gain of a larger field of view when imaging vessels. These two advantages that come with the full

field technology are essential when thinking about the clinical applications. A distortion free image ensures that observed deformation comes from a physiological origin and a large field of view provides a faster analysis of the various regions of retina.

Section 10.1 described a few examples of biomarkers that can be computed using our modified AO-FIO to evaluate the state of the vascular structure structures. In the next section we explore the potential functional biomarkers of the vascular network that can be computed with our system.

## 10.2 Functional biomarkers

Before a retinal pathology causes damages to the vascular structures, it will impair their function [6]. Therefore, detecting a dysfunction in the vascular network can allow the diagnosis and treatment of the pathology before it affects the structure itself, avoiding a wider deterioration of the retina. The vascular network carries out the function of supplying retinal cells with nutrients and oxygen, which are delivered by the blood. An exchange between blood and tissue takes place at the capillaries level before the blood flows back to replenish new supplies. Spotting an irregular delivery of these supplies, meaning noticing an alteration of the blood flow or vessels reaction, implies a failure in this supplying function. These alterations, which could be an unusual blood flow speed or a slow vasoconstriction reaction of the vessels for instance, represent small spatial and temporal variations in the vascular structure. Therefore, a system with high spatial and temporal resolution is required to be able to capture them. When visualizing the image sequences presented in Ch. 4 that were acquired with our AO-FIO system, we notice that the blood flow was visible suggesting we had at least the necessary spatial lateral and temporal resolution to detect such variations. Moreover, unlike scanning instruments, all pixels in each frame of our full field system are acquired at the same time. This simultaneity in acquisition has two implications. First, that a motion in the field of view observed in a video sequence can be traced in time, making this system very suitable for temporal analysis of spatial variations. Secondly, that we have a high temporal resolution which keeps improving with the fast development of camera technology. Finally, we have been able to conduct the functional analysis of the blood flow in both the standard bright-field and the dark-field modalities thanks to the implementations presented in Ch. 6.

In this section we explore the extraction of vascular functional biomarkers, i.e. values evaluating the normality of vascular variations that inform on the good condition of the vascular function. If we compare the computed values of these biomarkers to what have been established as nominal values, from healthy subjects, we could detect irregularities which would indicate the presence of a pathology affecting the vascular function.

The results of the functional analysis carried out on the retinal vasculature using our system is presented in the form of an article currently in peer review, which is introduced by the reading guide in Section 10.2.1 and is presented in Sect. 10.2.2.

### 10.2.1 Reading guide

A range of techniques are used to characterize the blood flow in the retina by extracting features of the blood flow like its speed, levels of oxygenation or spatial localization in the retina. For instance, speed analysis of the blood flow in retinal large vessels can be achieved using Doppler flowmetry, however the precision decreases when studying the smaller vessels such as capillaries. Another well adapted technique to characterize retinal

vascular flow is the image based angiography. This technique consists in computing perfusion maps which localize the flow in the retina. The computation of these maps, also known as motion contrast maps, is based on the computation of the temporal variance of an image sequence. This variance quantifies the variation in brightness generated by the absorption of the light by the passing erythrocytes and therefore shows a high pixel value where there is blood flow. This spatial characterization of perfusion can be carried out with systems like OCT or AOSLO but these techniques lack the spatial resolution to detect the capillary flow or the temporal resolution to detect the faster flow in large vessels respectively. Therefore, vascular function remains poorly characterized in spite of this variety of instruments.

In this section we introduce the AO-FIO as a new instrument within the framework of retinal angiography. The purpose is to map the blood using the same temporal variance computation used on the data from the other systems. Nevertheless, because the contrast of flood systems is lower, the development of an specific image processing routine specific to our system was necessary. The results are summarized in a scientific paper accepted in January 2019 by *Biomedical Optics Express*. I participated in the data acquisition, processing and analysis, as well as in the development of the specific processing for blood mapping and speed extraction and the writing of the article.

The reader should start by the first section ("Introduction") to understand the challenges of this functional analysis on an AO-FIO. Then, section 2 ("Methods") describes first the experimental set-up, which consists in the AO-FIO system described in Ch. 4 and its illumination manipulation to obtain dark-field imaging, described in Ch. 6. Secondly, section 2 describes the studied population and image processing, in particular the specific processing, consisting in a spatio-temporal filter, developed to achieve high contrasted blood mapping. Finally, the second section ends in introducing the temporal fraction of the image sequences using a temporal filter to isolate in different perfusion maps blood varying at different speeds. Finally, all results are summarized in section 3 ("Results") and discussed in section 4 ("Discussion") leading to the conclusion of the prospective clinical use of this system for angiographic studies.

### **10.2.2 Peer reviewed Article: Near Infrared Adaptive Optics Flood Illumination Angiography**

# Near infrared adaptive optics flood illumination retinal angiography

ELENA GOFAS-SALAS,<sup>1,2,3</sup> PEDRO MECÊ,<sup>1,3,4</sup> LAURENT MUGNIER,<sup>1</sup> AURÉLIE MONTMERLE BONNEFOIS,<sup>1</sup> CYRIL PETIT,<sup>1,3</sup> KATE GRIEVE,<sup>2,3,5</sup> JOSÉ SAHEL,<sup>2,4,5</sup> MICHEL PAQUES,<sup>2,3,5</sup> AND SERGE MEIMON<sup>1,3,\*</sup>

<sup>1</sup>DOTA, ONERA, Université Paris Saclay, F-91123 Palaiseau, France

<sup>2</sup>Institut de la Vision, 17 rue Moreau, Sorbonne Universités, UPMC Univ Paris 06, INSERM, CNRS, 75012 Paris, France

<sup>3</sup>PARIS Group - Paris Adaptive-Optics for Retinal Imaging and Surgery, Paris, France

<sup>4</sup>Quantel Medical, Cournon d'Auvergne, France

<sup>5</sup>CIC 1423, INSERM, Quinze-Vingts Hospital, Paris, France

<sup>6</sup>Department of Ophthalmology, The University of Pittsburgh School of Medicine, Pittsburgh, PA, USA

\*serge.meimon@onera.fr

**Abstract:** Image-based angiography is a well-adapted technique to characterize vasculature, and has been used in retinal neurovascular studies. Because the microvasculature is of particular interest, being the site of exchange between blood and tissue, a high spatio-temporal resolution is required, implying the use of adaptive optics ophthalmoscopes with a high frame rate. Creating the opportunity for decoupled stimulation and imaging of the retina makes the use of near infrared (NIR) imaging light desirable, while the need for a large field of view and a lack of distortion implies the use of a flood illumination-based setup. However, flood-illumination NIR video sequences of erythrocytes, or red blood cells (RBC), have a limited contrast compared to scanning systems and visible light. As a result, they cannot be processed via existing image-based angiography methods. We have therefore developed a new computational method relying on a spatio-temporal filtering of the sequence to isolate blood flow from noise in low-contrast sequences. Applying this computational approach enabled us to perform angiography with an adaptive optics flood illumination ophthalmoscope (AO-FIO) using NIR light, both in bright-field and dark-field modalities. Finally, we demonstrate the capabilities of our system to differentiate blood flow velocity on a retinal capillary network in vivo.

© 2019 Optical Society of America under the terms of the [OSA Open Access Publishing Agreement](#)

## 1. Introduction

The accurate mapping and quantification of retinal blood flow has become a major goal in vision research since several of the most common retinal pathologies show vascular abnormalities as early symptoms, in particular at the microvascular level [1]. Different approaches have been explored to characterize the retinal blood flow. Doppler flowmetry, which uses speckle interferometry, was successfully used to generate maps displaying retinal perfusion and to extract the blood flow velocity, but with limited resolution [2, 3]. Other approaches such as image based angiography techniques, involving instruments such as Optical Coherence Tomography (OCT) or adaptive optics ophthalmoscopes, have been developed to achieve noninvasive visualization and characterization of retinal blood flow [4–6].

For all these systems, the computation of angiographic maps, known as motion contrast maps or perfusion maps, is based on the same principle. The blood is mapped by computing the temporal variance of an image sequence. This variance quantifies the variation in brightness generated by the absorption of the light by the passing erythrocytes. Through this computation a high signal appears where the blood passes. Among these non invasive technologies, OCT Angiography

(OCTA) competes in the clinical setting with the current gold standards of Fluorescein and Indocyanine Green angiography [7], both of these tests being invasive and requiring intravenous administration of a dye and long imaging sessions lasting from 10 to 30 minutes. OCTA has proven to be a fast and robust technique providing a 3D mapping of both the retinal and choroidal vascular network within a few seconds, showing both structural and blood flow information [8]. However, even though OCTA enables accurate mapping of large vessels, it has been shown that lumen sizes of smaller capillaries are generally overestimated [9,10], which makes this technique less suitable to study the microvascular network than others with higher lateral resolution, such as ophthalmoscopes combined with adaptive optics (AO).

AO technology corrects the eye's aberrations in real time to capture images with diffraction-limited resolution [11]. Some teams have developed image processing to generate retinal perfusion maps adapted to image sequences obtained with AO corrected ophthalmoscopes, in both full field [5] and scanning configurations [12,13]. Multiple studies have been carried out to study the retinal microvascular network, in particular in AO corrected scanning laser ophthalmoscopy (AO-SLO). Indeed, retinal perfusion maps where capillaries are accurately mapped [4,14] were obtained thanks to the superior contrast and optical sectioning of AO-SLO compared to AO flood illumination ophthalmoscope (AO-FIO), and its combination with off axis techniques (eg dark-field, offset aperture, split detection). However, the scanning nature of the acquisition process in AO-SLO poses two problems when attempting quantitative angiography with this technique. Firstly, the presence of image distortion due to eye motion, even after post processing [15], generates artifacts in the contrast maps, and implies an uncertainty as to whether a movement observed between two frames is due to physiological reasons or due to scan distortion. Secondly, the AO-SLO acquisition rate is limited by the raster scan speed, which restricts the temporal resolution, making it difficult to accurately measure erythrocyte speed. Nevertheless some teams have been able to overcome this limitation through the manipulation of the scanning such as the multiple beam illumination carried out by DeCastro et al. [16], where the acquisition rate is increased over the scanning raster limit, enabling them to measure the speed of single erythrocytes in human retina in vivo. Other implementations such as the near confocal line scanning from Gu et al. [17] accelerates the scanning process as it is only carried out in one direction leading to images of blood flow in human parafoveal capillaries. Finally, another technique developed by Zhong et al. [18] achieves erythrocyte velocity by stopping the slow scanner leaving only a single line projected by the fast scanner on a blood vessel leading to spatiotemporal traces of erythrocytes. Although these solutions solve the temporal resolution limitations, they come with restrictions such as small field of view [18], an uneven contrast in capillaries [17] or a limitation concerning the direction and plane of the vessels whose blood flow can be analyzed [16].

In order to obtain the necessary spatial and temporal resolution, Metha's group developed an AO-FIO working at a wavelength centered at 593 nm and using a fast sCMOS camera (see Bedggood et al., [19]). The choice of this wavelength provides a near optimal erythrocyte contrast, leading to enhanced motion contrast maps. They studied neurovascular coupling at microvascular level with no distortion and an accurate quantification of capillaries size as small as 3  $\mu\text{m}$ . They measured the size of capillaries in reaction to stimulation and were able to detect less than a micron in variation [19]. However, the contrast maps obtained have a small field of view ( $0.8^\circ \times 0.2^\circ$ ) which, for a larger analysis of the retina, would mean long imaging sessions. In addition, the use of a wavelength in the visible spectrum is not only uncomfortable for the subject, but for safety reasons, it restricts the amount of power that can be sent into the eye, which limits the size of the field of view. Finally, at this visible wavelength, the imaging light also stimulates the retina, so that stimulation and imaging cannot be decoupled.

It appears that there is an unanswered need for angiography maps produced from a flood illumination setup (providing distortion-free, large field-of-view, high frame rate sequences)

using Near Infrared (NIR) illumination (creating the opportunity for decoupled stimulation and imaging). However, flood-illumination NIR video sequences of erythrocytes, or red blood cells (RBC), have a limited contrast compared to scanning systems and visible light. As a result, although blood flow is visible in image sequences from our NIR AO-FIO [20], conventional image processing developed by the teams previously mentioned tends to fail in our image sequences due to a low signal-to-noise ratio (SNR). In this paper, we provide the methodology to produce NIR wide field undistorted angiography maps : we use a finely tuned NIR AO-FIO (previously described in [20]) to produce image sequences; we then use a temporal filter to isolate pixels which vary in contrast at a rate falling in the physiological range of erythrocyte velocity, and a spatial filter to reduce the noise variation; last, we compute perfusion maps from the filtered image sequences. This method is used on a few healthy subjects to test the method *in vivo*. Then, in order to validate our results we verified that the obtained angiography results are in line with previous works of the characterization of retinal blood flow. Finally, by temporally filtering the image sequence in various temporal bands, we demonstrate the capabilities of our system to map the blood flow velocity, opening the way to more elaborate and accurate velocity analysis of our data set.

## 2. Methods

### 2.1. Adaptive optics imaging

The imaging system used here is the PARIS AO-FIO which has been described in detail in a previous work [20]. The system consists of two optical subsystems, the Wavefront (WF) Sensing and Control subsystem and the Illumination and Detection subsystem (see schematic layout in Fig. 1). The dynamic and static aberrations of the eye are measured with a custom made Shack-Hartmann wavefront sensor and corrected using a 97 actuator deformable mirror (ALPAO, France). The adaptive optics loop rate is 50Hz. A fibered Super Luminescent Diode (SLD) (Omicron, Germany) with nominal center wavelength of 750 nm is used to measure the aberrations and an 860nm SLD (Omicron, Germany) coupled with a liquid fiber illuminates the retina with a 3.6° diameter field of view. The light is then back-scattered by the retina towards a fast Scientific CMOS ORCA flash4-V2 camera (Hamamatsu, Japan), enabling 2048 × 1024 pixel frame acquisition at 200Hz, which corresponds to 1.5 mm × 0.75 mm field-of-view. The exposure time being set at 5 ms, acquired retinal images can be considered as distortionless, as eye movement can be considered negligible [21]. The magnification between the camera and the retina is such that each 6.5 μm pixel corresponds to 0.73 μm in the retina.

The camera is mounted on a motorized stage (Thorlabs, Germany) enabling us to focus on various layers of the retina by moving the stage.

### 2.2. Subjects

Healthy subjects were selected in order to compare our results to normal erythrocyte speeds in the literature. Acquisitions were made on two men (ages 28,39) and one woman (age 25). The project followed the tenets of the Declaration of Helsinki. Informed consent was obtained from subjects after the nature and possible outcomes of the study were explained. The subject's head was stabilized with a chin and forehead rest. They were asked to stare at the fixation target which enabled us to guide the subject's line of sight and explore various areas of the retina. The subjects pupil was not dilated. The total light energy entering the eye from the illumination source and the WFS source are respectively under 400 μW and 2.8 μW, which is less than half the power stipulated by the ocular safety limits established by ISO standards for group 1 devices.

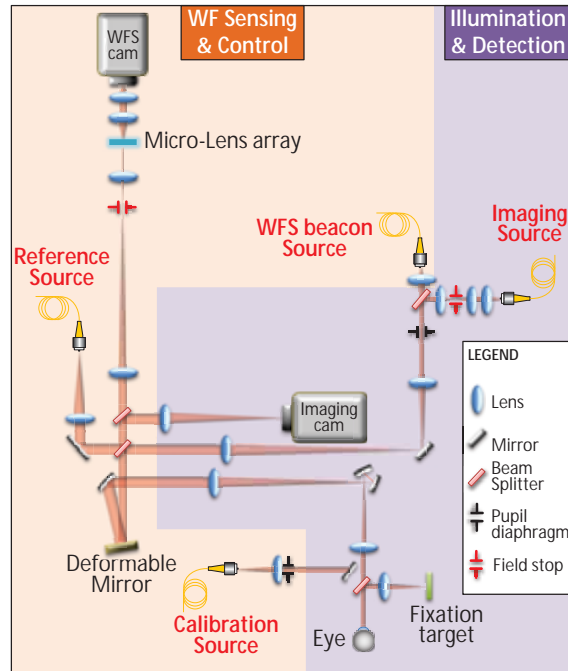


Fig. 1. Schematic drawing of the PARIS adaptive optics flood illumination ophthalmoscope. The system can be divided into two subsystems. Wavefront (WF) Sensing & Control, in yellow, is composed of a Reference Source (Ref Source), a Wavefront Sensor (WFS) (Micro-lens array, relay optics, and WFS camera), a WFS beacon source and a Deformable Mirror (DM). An additional calibration source can be inserted in place of the eye to calibrate the adaptive optics loop. The other subsystem, in purple, is Illumination & Detection and is composed of the retinal imaging camera and the corresponding wide field imaging source.

### 2.3. Image acquisition

AO-FIO image sequences of typically 1000 frames were acquired at 200Hz (total acquisition time of 4s) with a  $2.7^\circ \times 5.4^\circ$  field of view.

For each subject we acquired image sequences near the lamina cribrosa ( $10^\circ$ - $12^\circ$ ) and the peripheral retina ( $5^\circ$ - $10^\circ$ ). In order to obtain optimal perfusion maps, the focus of the camera was placed on the nerve fiber layer. Images were acquired using standard bright-field AO-FIO illumination and dark-field AO-FIO illumination [22].

### 2.4. Image processing

#### 2.4.1. Background subtraction and image registration

Following the acquisition, the low spatial frequency components of the retinal image, corresponding to scattered light from out of focus layers of the retina, were removed [20]. This correction was performed by subtracting a low-pass filtered version of each image from the raw image, where the low-pass image is obtained by a mean filter (kernel of 50 pixels) [23]. Then, the spatial variance was used as an image quality metric to get rid of images blurred [23] by fast and large fixational eye movements such as microsaccades or blinking. For each image sequence, about 1% of images were discarded, which represents so few frames that the temporal variance computation

leading to the perfusion maps is not affected. The final selected images were registered using a pairwise maximum likelihood sub-pixel approach [24]. An advantage of our method is that thanks to the high acquisition speed of our flood illuminated AO fundus camera, a single native image acts as template for stabilization of the acquired movies, without having to resort to an externally acquired template image as scanning techniques do [15] due to the distortion intrinsic to the scanning modality. The averages of the registered image sequences were computed.

#### 2.4.2. Computation of perfusion maps

In order to isolate the signal variation produced by the absorption of erythrocytes flowing in vessels and capillaries, we developed a spatio-temporal filter with frequency bands centered on the theoretical spatial and temporal frequencies corresponding respectively to the size and speed of erythrocytes in retinal vessels. These filters were applied to the video frames before computing the temporal variance leading to enhanced contrast angiography maps of retinal vessels.

*Temporal filtering* - We start by applying a temporal filter to the image sequences. This enables us to get rid of signal variations slower than blood flow (e.g. deformation of the retina during the cardiac cycle) or faster than blood flow (high temporal frequency component of the noise).

We select a large frequency interval for the temporal filtering which goes from 10Hz to 80Hz, i.e. from 10% to 80% of the Nyquist temporal frequency of our instrument. The tuning of the frequency bandwidth was set to be as large as possible in order to avoid filtering erythrocyte motion while leading to the highest possible signal to noise ratio in perfusion maps. Processing was carried out in IDL programming language (IDL, Exelis, USA).

*Spatial filtering* - A spatial low-pass filter was then necessary to filter out the features, essentially noise, in the images whose variations fall in the same temporal frequency interval as the erythrocytes and therefore decrease the contrast of the motion contrast maps.

For the spatial filtering we used a Gaussian filter with a cutoff frequency (normalized by the Nyquist frequency) of 0.14, which corresponds to a spatial frequency of 47.6 cycles/mm. The boundary of the filter is chosen to filter structures smaller than 21  $\mu\text{m}$ , which correspond to a few erythrocytes. As well as the temporal filtering the spatial cut-off frequency of the low pass filter was selected to increase the signal to noise ratio of the perfusion maps without filtering out blood cells.

[Visualization 1](#) and [Visualization 2](#) in Supplementary data are the registered image sequence (corresponding to the image presented in Fig. 2(C)) before and after the application of the spatio-temporal filtering. After this processing we obtain an image sequence containing only features around the size of a few erythrocytes moving at speeds close to the values of the blood flow speed.

Finally we compute the temporal variance of the sequence to obtain the motion contrast maps.

#### 2.4.3. Perfusion color map generation based on blood flow speed

The high temporal resolution of the system allows us to subdivide the frequency band of the temporal filter in order to spatially analyze the different speeds of the retinal vessels. To achieve this, we apply various filters with different bandwidths to the video sequence and generate various contrast maps corresponding to each filter in order to be able to identify the capillaries and vessels with different blood flow speeds.

### 3. Results

#### 3.1. Perfusion maps in bright-field AO-FIO illumination

Nonmoving structures are filtered out leading to enhanced contrast perfusion maps. Figure 2 shows two examples of typical perfusion maps obtained with NIR AO-FIO after spatio-temporal filtering in bright-field configuration. (A,C) are the average images of peripheral retinal vessels, (B,D) their corresponding perfusion maps. In all the images, large vessels lie in a nerve fiber bed where one can barely detect a hint of some capillaries. In the intensity images the capillaries are barely detectable, but appear with relatively high contrast in the perfusion maps. This ability to remove stationary features, such as the fibers signal, and enhance motion is shown in a magnified view (Fig. 2(A) and 2(B), yellow box). The red arrowheads in Fig. 2(C) and 2(D) indicate longitudinal capillaries going deep into the retina, these black spots in the average images appear as bright spots in the perfusion maps. Finally larger vessels remain visible in the perfusion maps (Fig. 2(B)). A magnified view (yellow box) in Fig. 2(D) shows the confluence of a venule with this vein. We observe multiple bands as if the flow remains unmixed after the confluence. See [Visualization 2](#) and [Visualization 3](#) in Supplementary in data to watch the videos corresponding to Fig. 2.

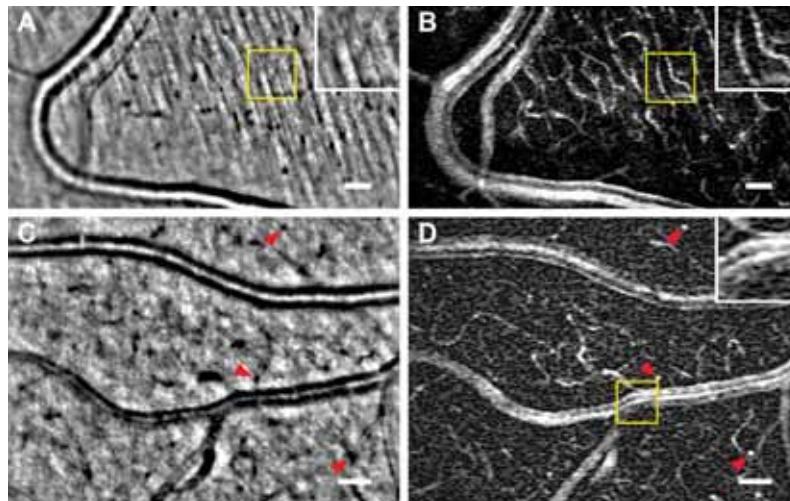


Fig. 2. (A,C) Average images of peripheral retinal vessels on the nerve fiber layer bed.(B,D) Motion contrast maps of the same areas displayed on the average images (see [Visualization 1](#), [Visualization 2](#) and [Visualization 3](#) in Supplementary data). (C,D) show both an artery and a vein. In (A,B) A magnified view (yellow box) on the nerve fiber bed shows how the capillaries, invisible in the average image (A), appear contrasted on the perfusion map (B). In (C,D) Longitudinal capillaries, indicated with red arrowheads, in black in the average image (C) appear as bright white spots on the perfusion map (D). A magnified view (yellow box) in (D) shows in detail the confluence of the vein with a venule. The large vessel display several parallel bright bands, with the central band being the brightest. Scale bars are 50  $\mu\text{m}$

### 3.2. Perfusion maps in dark-field configuration

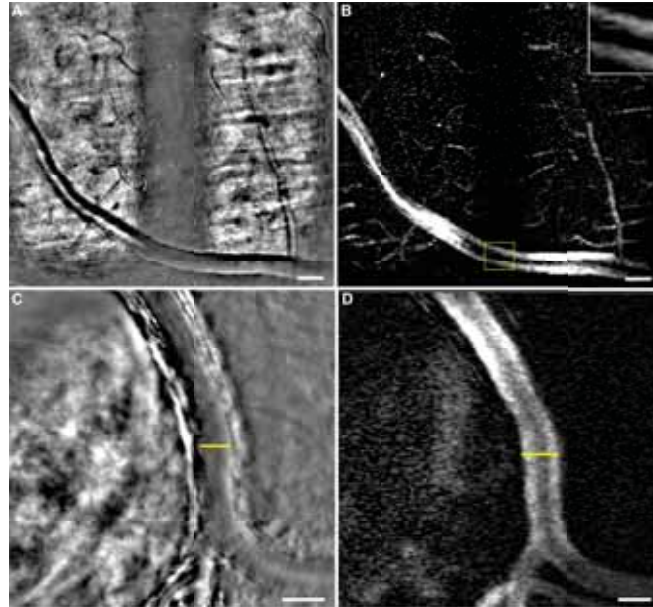


Fig. 3. (A,C) Average images including vessels with a contrast typical of dark-field modality and (B,D) their respective perfusion maps (see [Visualization 4](#) and [Visualization 5](#) in Supplementary data). (A) Large vessel of peripheral retina lying on the nerve fiber layer alternatively illuminated in bright-field and dark-field configuration. A magnified view (yellow box) in (B) shows the aspect of the perfusion map on a large vessel when illuminated in dark-field. The large vessel shows two parallel bands, with a darker aspect in the center of the vessel, instead of the typical several bands observed in bright-field configuration (cf. Fig 2(D)). Again, capillaries hardly visible in (A) appear contrasted in (B). (C) Artery from the optic nerve head region. The artery is lying over the lamina cribrosa which illuminates it from behind leading to forward scattering which gives this contrast to the vessel, characteristic of dark-field illumination. In (D) the large vessel lumen is easier to measure than in (C) where it is hard to determine the beginning of the wall (yellow lines). Scale bars are 50  $\mu\text{m}$

Since the use of the dark-field modality has enhanced perfusion maps in AO-SLO, we also acquired images in this illumination configuration and generated their respective perfusion maps. Figure 3 shows two average images of vessels with a typical dark-field configuration contrast Fig. 3(A) and 3(C). The dark-field illumination has been induced in Fig. 3(A) by introducing a field diaphragm in the illumination path while in Fig. 3(C) it is due to the presence of the lamina cribrosa located under the vessel [22]. Videos corresponding to these average images can be seen in Supplementary data [Visualization 4](#) and [Visualization 5](#). Figures 3(B) and 3(D) correspond to their respective perfusion maps. We observe in both of these maps that large vessels display two bands, with a darker aspect at the center of the vessel, instead of the several previously described in bright-field illumination, with a brighter signal in the center. A magnified view showing the aspect of the vessel on the dark-field area is displayed in Fig. 3(B) (yellow box). Another difference between perfusion maps in bright-field and dark-field configuration is the contrast of the capillaries. Indeed, the smaller capillaries seem to be less contrasted in the center of both bright and dark fields, while their contrast seems enhanced when they lie on the border between

the two different illumination fields.

### 3.3. Differentiation of vessels by blood flow speed

The high temporal resolution of the system enables a fine temporal sampling of the erythrocyte motion. The temporal filter, firstly designed to isolate the signal of red blood cell moving, is used here to separate this signal into three separate temporal bands going respectively from a frequency of 1Hz to 10Hz, 10Hz to 25Hz and 25Hz to 40Hz. This fractioned temporal filter was applied to an image sequence (corresponding to [Visualization 6](#) in Supplementary data) acquired on a region with a capillary network to be able to compare blood speeds between several retinal vessels. Figure 4 shows, at the top, the average image of this region (Fig. 4(A)) and its corresponding perfusion map (Fig. 4(D)). At the bottom is presented the speed analysis with the three perfusion maps corresponding to these temporal bands Fig. 4(C), 4(D), 4(E). By assigning an RGB channel to each temporal frequency band, we generate a perfusion color map in which each color is associated to certain frequencies. In Fig. 4(F), blue represents the slower motions (1Hz to 10Hz), red the fastest (25Hz to 40Hz), while green is used to display features moving at medium speeds (10Hz,25Hz). We notice that although the three perfusion maps share many similar features, some capillaries appear more clearly in one particular map than another. Indeed this difference is highlighted in color map Fig. 4(F). For instance, capillaries appearing contrasted in Fig. 4(C) while invisible in 4(D) and 4(E) are blue in image 4(F).

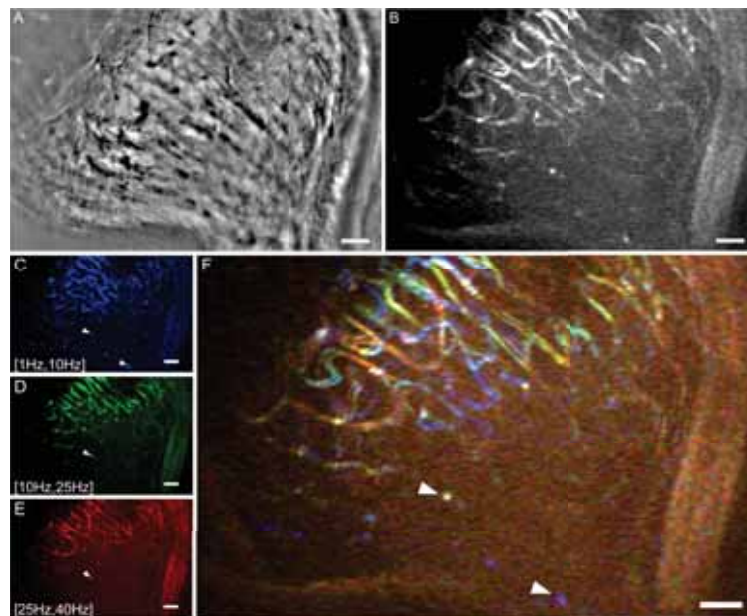


Fig. 4. (A) Average image of a capillary bed near the lamina cribrosa region and (B) its respective perfusion map after a temporal filtering with a frequency bandwidth of [1Hz,40Hz] (see [Visualization 6](#) in Supplementary data). (C,D,E) Perfusion maps of that same region after three different temporal filtering, with respectively frequency bandwidths of [1Hz,10Hz] (blue map),[10Hz,25Hz] (green map) and [25Hz,40Hz] (red map). (E) Perfusion color map generated by assigning to each perfusion map from a temporal frequency band (A,B,C) an RGB color. Slow temporal frequencies are in blue, medium in green and the faster frequencies corresponds to red. White arrowheads indicate two examples of longitudinal capillaries. Scale bars are 50  $\mu\text{m}$ .

In each channel sub-image Fig. 4(C), 4(D) and 4(E), the pixels appearing bright are pixels temporally varying with frequencies between [1Hz,10Hz], [10Hz,25Hz] and [25Hz,40Hz] respectively.

## 4. Discussion

### 4.1. Distortionless high resolution perfusion maps in the near infrared

Distortionless high resolution perfusion maps in near infrared could be a highly valuable tool for assessing the state of the retinal vascular network, and particularly for neurovascular studies of the retina, as near infrared wavelength range is more comfortable for the subject, safer in terms of thermo-chemical damage, and does not stimulate the retina (thus enabling decorrelation of stimulation and imaging channels to carry out functional imaging). Distortionless maps would enable extraction of reliable biomarkers, such as foveal avascular zones (FAZ) [12]. Such maps can only be obtained using adaptive optics (for spatial resolution) near-infrared imaging, in a full-field modality (to prevent distortion artifacts entailed by scanning), such as the PARIS AO-FIO [20]. Indeed, there are two main difficulties generated by the distortion artifacts, which are produced in an image obtained with a retinal scan when the eye moves during the acquisition of a frame. On the one hand, when there is a deformation in a retinal structure, there is an uncertainty regarding whether it comes from distortion or has physiological origin. On the other hand, to correct distortion on all the frames in an image sequence, the user must select a reference frame. However, there may not be a working reference in every acquisition [15]. Although some teams have found solutions to increase the acquisition rate of scanning systems and therefore minimize the impact of eye movement [18], choice of template remains subjective, meaning that the metrics extracted from processed images could be confounded by significant local distortions, caused for instance by disease. In consequence, some teams resort to using an image acquired sequentially with an AO fundus camera as a ground truth template for distortion correction [15]. Our images, acquired with a high speed AO fundus camera, are inherently ground truth templates and thus distortion free allowing reliable metric extraction. However, the existing perfusion map processing methods, which produced either high contrast maps in near-infrared contrast maps with distortion [12, 13], or without distortion but in another wavelength (wavebands centered on 593nm to maximize erythrocyte absorption contrast [5, 19]), fail in full-field NIR due to a poorer SNR in the image sequences. Using a spatial and temporal filtering of our image sequences, we were able to obtain large field-of-view ( $2.7^\circ \times 5.4^\circ$ ) distortion-free enhanced contrast perfusion maps of the retina using AO-FIO image sequences in near infrared. The spatial resolution (down to capillaries of  $5 \mu\text{m} \pm 1 \mu\text{m}$  diameter) and contrast (0.6-0.8 range) of the obtained perfusion maps is similar to confocal AO-SLO results [14].

A thorough analysis of the image sequences was carried out in order to confirm that the perfusion maps were not a result of introduced artifacts by the filter: when looking at bright-field perfusion maps we notice that large vessels display parallel bands with, in several cases, a brighter central band. We first thought that this brighter central band could be due to the temporal variation of the specular reflection along the crest of the vessel wall instead of erythrocyte motion. However, when closely looking at the videos ([Visualization 1](#), image sequence corresponding to average Fig. 2(C)) we observe a flow motion at the center of the vessel with a speed and direction close to the blood flow characteristics, leading us to the conclusion that the bright band at the center of the large vessel in the perfusion map is generated by a temporal variation of erythrocytes motion.

Finally, to validate our results we verified that the obtained perfusion maps are in line with previous works of the characterization of retinal blood flow: Fig. 2(D) shows a vein on the lower part of the image with several ramifications. The flux seems to remain unmixed after the confluence as we observe these various bands in the perfusion map. Indeed, this phenomenon has been previously described in [14] using AO-SLO where they show perfusion maps of several

branch venules entering a vein with various illumination configurations.

#### 4.2. Comparing dark-field and bright-field perfusion maps

Our system enables us to acquire dark-field and bright-field images in AO-FIO of the same regions [22]. We wanted to verify if the dark-field modality in flood imaging could increase the contrast of the perfusion maps the same way it has been shown in AO-SLO [14].

With regards to capillaries in perfusion maps, Chui et al report enhanced contrast in dark-field imaging with AO-SLO [14]. In our case, for instance in Fig. 3(B), capillary contrast is higher in the bright-field zone than in the dark-field zone, except at the edge of the central obscuration. This zone, which corresponds to the maximal illumination gradient in the image, is precisely the region where the sensitivity to the phase of the sample is the highest [25] and where the dark-field full-field configuration most closely resembles the standard scanning configuration [14].

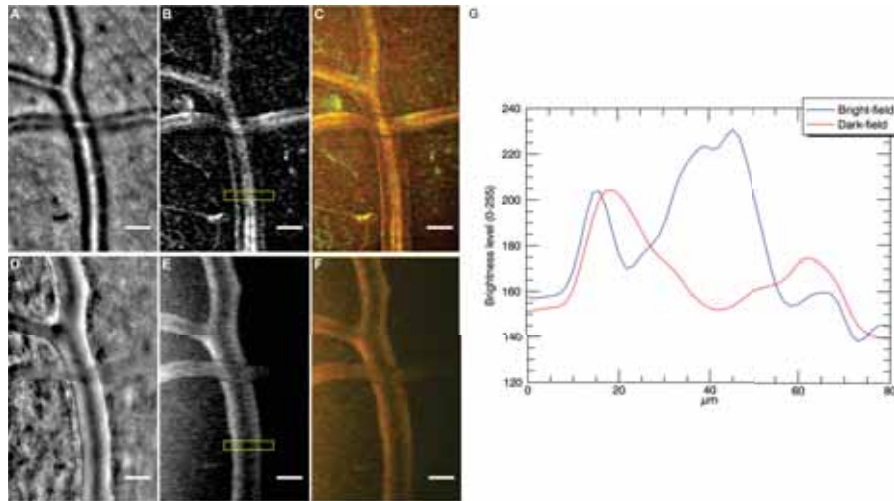


Fig. 5. Images generated from image sequences of the same region showing an artery crossing with a vein in bright-field (A,B,C) and dark-field (D,E,F) illumination configuration respectively (see [Visualization 7](#) in Supplementary data). (A,D) are average images, (B,E) perfusion maps and (C,F) color generated maps showing in green slow variations and in red fast variations. (G) displays two horizontal intensity profile plots (vertically averaged) from yellow boxes in images (B) and (E) corresponding to bright-field and dark-field perfusion maps respectively. The x-axis indicates the horizontal position in microns inside the yellow box and the y-axis indicates the brightness level of the vertical average for each of these horizontal positions.

With regards to larger vessels, we acquired image sequences of the same region, showing an artery crossing with a vein, in bright-field and dark-field (see [Visualization 7](#) in Supplementary data). In addition to the fact that average images in bright-field and dark-field show differences in contrast (Fig. 5 (A), 5(D)), we also noticed that perfusion maps in both configurations show significant differences. In Fig. 3, we noticed that large vessels display only two parallel bands in dark-field perfusion maps, whereas several bands are visible in our bright-field configuration. The same effect is shown in Figs. 5(B) and 5(E), where we show the perfusion maps of the same region for comparison purposes. The corresponding intensity profiles are plotted in Fig. 5(G): the blue plot, corresponding to the bright-field map, has three maxima (three bands), with the

central maximum higher than the ones on the sides; the red plot, corresponding to the dark-field map, has only two maxima, with a darker region in the center of the vessel.

It is interesting to note that this two line shape observed in dark-field modality in full field is not observed in the dark-field modalities perfusion maps shown in [14]. This could be due to the fact that AO-SLO offset aperture dark-field modality does not completely filter the single back-scattered light, leading to images with a slight back-scattered reflection on top of the lumen of the larger vessels.

The flow shape observed in our system dark-field illumination seemed to imply that erythrocytes have two preferred paths that lie on each side of the lumen, which was in contradiction with the observations made on bright-field perfusion maps (showing several bands). However, when studying the flow in image sequences with dark-field configuration, we are able to detect at times the blood flow motion in the center of the vessel (see [Visualization 4](#) corresponding to the video from Fig. 3(A)) which goes against this hypothesis of two preferred paths. Our interpretation of this discrepancy is illustrated in Fig. 6. Let us consider first the bright-field case. In the same way in which the specular reflection will be greater at the top of the vessel where the wall is orthogonal to the direction of illumination, the back-scattering generated by the inside of the lumen of the vessel will also be greater on the wall that is orthogonal to the direction of the illumination, leading to more photons returning in this direction to the camera (see left image in Fig. 6). Thus, the variation in intensity would be greater along the crest of the vessel wall orthogonal to illumination than in other areas of the vessels which back-scatter relatively less light. The variance signal would therefore be higher at the center than the borders, and thus the variance image would be brighter.

In dark-field, the light detected by the camera comes from forward scattering (scattered by layers below the artery) and goes through the vessel, where it is partially absorbed by red blood cells flowing inside the vessel. The absorption is then stronger at the center, where the vessel (and red blood cell flow) is the thickest. In dark-field, this effect is not counterbalanced by a stronger specular reflection at the bottom of the vessel, so that no bright central band is visible.

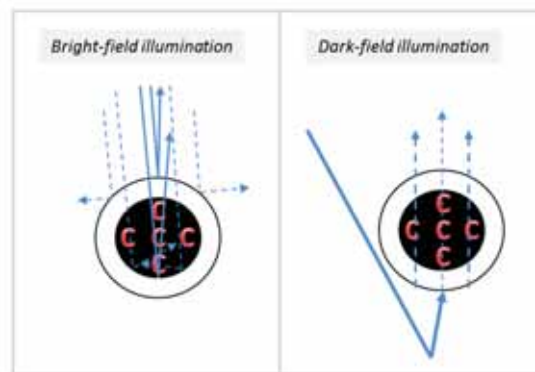


Fig. 6. Schematic drawings showing a cross-section of a vessel scattering light in bright-field (left) and dark-field (right). The red C letters represent red blood cells (or erythrocytes) and blue arrows represent light rays, dashed lines representing lower amount of photons while the solid lines show larger amounts.

#### 4.3. Wall-to-lumen ratio

Aside from studying perfusion itself, a better estimation of the size of the lumen can be reached with perfusion maps, leading to more accurate retinal biomarkers such as wall-to-lumen ratio [26]

or quantification of vessel lumen expansion or contraction [19]. Indeed, perfusion maps of vessels enable us to determine their lumen size better than in averaged reflectance images, because they mark the passage of the blood, and therefore display the lumen size of capillaries and veins more distinctively. For instance, Figs. 3(C) and 3(D) show how the limit between lumen and wall is hardly distinguishable in 3(C) while the perfusion map 3(D) displays a sharp border between the high bright signal coming from the blood flow motion and the dark background coming from the motionless vessel wall.

#### 4.4. Velocity color maps

Figure 4 shows how by applying a temporal filter to the image sequence with various cut off frequencies we can identify capillaries with different blood flow speeds. Indeed when we assign a color to each temporal band and we merge them in one image (Fig. 4(F)), we observe that the capillary network displays a mixture of these three colors. This means that two pixels with different colors vary at different speeds. In particular we observe that the longitudinal vessels (indicated with white arrowheads in Fig. 4), which are not visible in AO-SLO [14], display a slower signal variation than other capillaries whose flow moves laterally. By using simplistic assumptions, it is possible to link the pixel temporal variation with an order of magnitude of the blood velocity. We assimilate the red blood cells as particles with a typical size  $\phi_{RBC}$ , and we suppose that these particles have a periodic flow with a spatial period equal to  $2\phi_{RBC}$ , so that the blood flow speed  $v_{RBC}$  is linked to the pixel temporal frequency  $\nu$  as:

$$v_{RBC} = 2\phi_{RBC} \cdot \nu \quad (1)$$

It is difficult to assign an accurate value to  $\phi_{RBC}$ : red blood cells can get as small as  $5 \mu\text{m}$  when they fold to travel in small capillaries [27, 28]; on the other hand, the particles we visualize in video sequences often correspond to a cluster of red blood cells rather than individual ones, with a typical size around  $20 \mu\text{m}$ . We will consider here an  $8 \mu\text{m}$  typical value [5]. With this simplistic model, the three inferred velocity ranges corresponding to Fig.4(F) frequency bands are [0.02 mm/s, 0.2 mm/s], [0.2 mm/s, 0.5 mm/s] and [0.5 mm/s, 0.8 mm/s]. These orders of magnitude are in agreement with the literature [5]. Although this approach only provides an order of magnitude of the absolute blood velocity, it does provide insight on the relative blood velocity in the vascular network. For instance, capillary velocity maps such as Fig.4(F) could be used to monitor blood flow abnormalities at a microvascular level.

#### 4.5. Limitations and future work

A limitation from this temporal analysis appears in Figs. 5(C) and 5(F). This cropped area of a color map displays in the same red color a vein and an artery crossing, even though arterial flow is faster than the blood flow in veins. This could be caused by the fact that we analyzed the intensity variation caused by the RBC passage over a large temporal interval (a few seconds), which is longer than a diastole and systole (less than a second), leading to the averaging of the artery speed variations. We would need to increase the temporal resolution to reach a rate higher than the current rate of our system (200Hz) and analyze over a smaller interval, which requires a more powerful light source so as not to limit the SNR, and a faster camera. Also, some small artifacts appear in the form of white lines parallel to the vessel walls, which we interpret as the temporal variation of the vessels vibrating when the blood is flowing.

Despite these limitations, the technique presented here opens up exciting prospects, such as producing 3D dark-field angiography maps. In Fig. 2 three examples of this vessel going into deeper retina layers are indicated with red arrowheads in both the average image Fig. 2(C) and its perfusion map Fig. 2(D). These longitudinal vessels and capillaries do not seem to appear to our knowledge in AO-SLO images, and belong to the vascular plexus linking the various vascular

beds. The detection and mapping of these vessels could lead to the possibility of 3D mapping the microvascular network the same way OCT does for the larger vascular network. Indeed, we have recently shown that the axial resolution capabilities of our AO-FIO system are better than usually accounted for in the literature, and that cross sectional images (analogous to OCT B-scans) can be produced to identify the various retinal layers [29]. The combination of this tool with the undistorted widefield angiography maps (in dark-field or bright-field) presented here could lead to the 3D mapping of the microvascular network.

Future work will be oriented towards improving the spatial dynamic study of the perfusion and increasing the accuracy of the blood flow speeds in capillaries by increasing the acquisition rate and/or developing more sophisticated processing to derive the erythrocytes' speeds in a similar way to particle image velocimetry [30].

## 5. Conclusion

The high spatial and temporal resolution of the NIR AO-FIO combined with the specific image processing presented in this paper enables us to compute retinal perfusion maps with enhanced contrast, no distortion and a large field of view. In particular, we are able to resolve capillaries as small as 5  $\mu\text{m}$  in various regions of the retina. These angiography maps obtained on healthy subjects are in line with the characteristic described in previous work of the field validating this image processing method. The implementation of the dark-field illumination in full field led to an increase of contrast at the boundary between the illuminated and dark areas in perfusion maps. This observation encourages us to compute motion contrast maps with different structures of the illumination in order to further improve the contrast of these maps. Another valuable feature of our system, possible because of the high acquisition rate, is the spatial analysis of the temporal dynamic of the blood flow. By temporally filtering the image sequence we can generate several perfusion maps, each one showing capillaries with blood flowing at a different speed range.

## Funding

The European Research Council SYNERGY Grant scheme (HELMHOLTZ, ERC 610110); the Agence Nationale de la Recherche under grants CLOVIS3D (ANR-14-CE17-0011); the RHU LIGHT4DEAF (ANR-15-RHUS-0001).

## Disclosures

The authors declare that there are no conflicts of interest related to this article.

## References

1. T. Bek, "Regional morphology and pathophysiology of retinal vascular disease," *Prog. Retin. Eye Res.* **36**, 247–259 (2013).
2. G. Michelson, J. Welzenbach, I. Pal, and J. Harazny, "Automatic full field analysis of perfusion images gained by scanning laser doppler flowmetry," *Br. J. Ophthalmol.* **82**, 1294–1300 (1998).
3. R. D. Ferguson, D. X. Hammer, A. E. Elsner, R. H. Webb, S. A. Burns, and J. J. Weiter, "Wide-field retinal hemodynamic imaging with the tracking scanning laser ophthalmoscope," *Opt. Express* **12**, 5198–5208 (2004).
4. T. Y. Chui, S. Mo, B. Krawitz, N. R. Menon, N. Choudhury, A. Gan, M. Razeen, N. Shah, A. Pinhas, and R. B. Rosen, "Human retinal microvascular imaging using adaptive optics scanning light ophthalmoscopy," *Int. J. Retin. Vitreous* **2**, 11 (2016).
5. P. Bedggood and A. Metha, "Direct visualization and characterization of erythrocyte flow in human retinal capillaries," *Biomed. Opt. Express* **3**, 3264–3277 (2012).
6. Z. Mammo, C. Balaratnasingam, P. Yu, J. Xu, M. Heisler, P. Mackenzie, A. Merkur, A. Kirker, D. Albiani, K. B. Freund, M. V. Sarunic, and D.-Y. Yu, "Quantitative noninvasive angiography of the fovea centralis using speckle variance optical coherence tomography," *Investig. Ophthalmol. & Vis. Sci.* **56**, 5074 (2015).
7. R. F. Spaide, J. M. Klancnik, and M. J. Cooney, "Retinal vascular layers imaged by fluorescein angiography and optical coherence tomography angiography," *JAMA Ophthalmol.* **133**, 45–50 (2015).
8. Y. Jia, J. C. Morrison, J. Tokayer, O. Tan, L. Lombardi, B. Baumann, C. D. Lu, W. Choi, J. G. Fujimoto, and D. Huang, "Quantitative oct angiography of optic nerve head blood flow," *Biomed. Opt. Express* **3**, 3127–3137 (2012).

9. T. S. Hwang, S. S. Gao, L. Liu, A. K. Lauer, S. T. Bailey, C. J. Flaxel, D. J. Wilson, D. Huang, and Y. Jia, "Automated quantification of capillary nonperfusion using optical coherence tomography angiography in diabetic retinopathy," *JAMA Ophthalmol.* **134**, 367–373 (2016).
10. A. M. Hagag, S. S. Gao, Y. Jia, and D. Huang, "Optical coherence tomography angiography: technical principles and clinical applications in ophthalmology," *Taiwan J. Ophthalmol.* **7**, 115 (2017).
11. J. Liang, D. R. Williams, and D. T. Miller, "Supernormal vision and high-resolution retinal imaging through adaptive optics," *JOSA A* **14**, 2884–2892 (1997).
12. T. Y. Chui, Z. Zhong, H. Song, and S. A. Burns, "Foveal avascular zone and its relationship to foveal pit shape," *Optom. Vis. Sci.* **89**, 602 (2012).
13. J. Tam and A. Roorda, "Speed quantification and tracking of moving objects in adaptive optics scanning laser ophthalmoscopy," *J. Biomed. Opt.* **16**, 036002 (2011).
14. T. Y. Chui, D. A. VanNasdale, and S. A. Burns, "The use of forward scatter to improve retinal vascular imaging with an adaptive optics scanning laser ophthalmoscope," *Biomed. Opt. Express* **3**, 2537–2549 (2012).
15. A. E. Salmon, R. F. Cooper, C. S. Langlo, A. Baghaie, A. Dubra, and J. Carroll, "An automated reference frame selection (arfs) algorithm for cone imaging with adaptive optics scanning light ophthalmoscopy," *Transl. Vis. Sci. & Technol.* **6**, 9 (2017).
16. A. de Castro, G. Huang, L. Sawides, T. Luo, and S. A. Burns, "Rapid high resolution imaging with a dual-channel scanning technique," *Opt. Lett.* **41**, 1881–1884 (2016).
17. B. Gu, X. Wang, M. D. Twa, J. Tam, C. A. Girkin, and Y. Zhang, "Noninvasive in vivo characterization of erythrocyte motion in human retinal capillaries using high-speed adaptive optics near-confocal imaging," *Biomed. Opt. Express* **9**, 3653–3677 (2018).
18. Z. Zhong, B. L. Petrig, X. Qi, and S. A. Burns, "In vivo measurement of erythrocyte velocity and retinal blood flow using adaptive optics scanning laser ophthalmoscopy," *Opt. Express* **16**, 12746–12756 (2008).
19. P. Bedggood and A. Metha, "Analysis of contrast and motion signals generated by human blood constituents in capillary flow," *Opt. Lett.* **39**, 610–613 (2014).
20. E. Gofas-Salas, P. Mecê, C. Petit, J. Jarosz, L. M. Mugnier, A. M. Bonnefois, K. Grieve, J. Sahel, M. Paques, and S. Meimon, "High loop rate adaptive optics flood illumination ophthalmoscope with structured illumination capability," *Appl. Opt.* **57**, 5635–5642 (2018).
21. J. Lu, B. Gu, X. Wang, and Y. Zhang, "High-speed adaptive optics line scan confocal retinal imaging for human eye," *PloS one* **12**, e0169358 (2017).
22. S. Meimon, E. G. Salas, P. Mecê, K. Grieve, J. A. Sahel, and M. Paques, "Manipulation of the illumination geometry on adaptive optics (ao) flood illumination ophthalmoscope (fio) for dark field imaging of the retina," *Investig. Ophthalmol. & Vis. Sci.* **59**, 4641 (2018).
23. G. Ramaswamy and N. Devaney, "Pre-processing, registration and selection of adaptive optics corrected retinal images," *Ophthalmic Physiol. Opt.* **33**, 527–539 (2013).
24. D. Gratadour, L. Mugnier, and D. Rouan, "Sub-pixel image registration with a maximum likelihood estimator-application to the first adaptive optics observations of arp 220 in the L' band," *Astron. & Astrophys.* **443**, 357–365 (2005).
25. L. Tian and L. Waller, "Quantitative differential phase contrast imaging in an led array microscope," *Opt. Express* **23**, 11394–11403 (2015).
26. E. Meixner and G. Michelson, "Measurement of retinal wall-to-lumen ratio by adaptive optics retinal camera: a clinical research," *Graefes's Arch. for Clin. Exp. Ophthalmol.* **253**, 1985–1995 (2015).
27. R. Skalak and P. Branemark, "Deformation of red blood cells in capillaries," *Science* **164**, 717–719 (1969).
28. A. Guevara-Torres, A. Joseph, and J. Schallek, "Label free measurement of retinal blood cell flux, velocity, hematocrit and capillary width in the living mouse eye," *Biomed. Opt. Express* **7**, 4228–4249 (2016).
29. P. Mecê, E. Gofas-Salas, C. Petit, K. Grieve, C. Chabrier, M. Paques, and S. Meimon, "High ao-loop rate improves axial resolution in ao ophthalmoscopes," *ARVO Imaging Eye Conf.* (2018).
30. A. Nakano, Y. Sugii, M. Minamiyama, and H. Niimi, "Measurement of red cell velocity in microvessels using particle image velocimetry (piv)," *Clin. Hemorheol. Microcirc.* **29**, 445–455 (2003).

### 10.3 Conclusion

This Chapter shows how the instruments described in Part.III enable us to extract biomarkers informing both on the state of the vascular structure and function. On the one hand we can use our dark-field configuration to help the diagnosis of pathologies such as arterial hypertension affecting the contraction and dilation of vessels. On the other hand, the processing tool developed in Sect. 10.2.2 not only enables us to localize the vascular network up to a capillary level in the retina, it can also be used to characterize the speed of the blood flow up to that same microvascular level. Even though future work should be carried to achieve higher precision in the extracted speeds and the contrast of the perfusion maps obtained, this Chapter showed the potential of the manipulated AO-FIO for vascular study, and particularly the microvascular study.

The next Chapter addresses the last retinal structure studies with our system, the retinal pigment epithelium. This structure is very hard to visualize as it is hypo-reflective. We showed how the dark-field configuration allowed us to image these cells and compare it to another imaging technique that allows the visualization of retinal pigment epithelium layer. Finally, since the contrast of these cells is quite low in our images we have limited ourselves to structural imaging, concluding with suggestions on the necessary next steps to achieve functional imaging of retinal pigment epithelium cells.

## Chapter 11

# Clinical analysis of the retinal pigment epithelium cells with two complementary imaging techniques

Chapters 9 and 10 explored the clinical applications of the AO-FIO with its new implementations described in Part III, and in particular the functional analysis that could be carried out on the acquired image sequences of neural and vascular retinal structures. This functional analysis implied the extraction of a biomarker evaluating the correct function of photoreceptors and vessels and it was possible because of the high contrast of the obtained images. In Ch. 6 other features were revealed whose dimensions suggested that we could be imaging retinal pigment epithelium cells (RPE). The RPE layer absorbs light in order to protect the retina from radiation and avoid image blur by excessive reflected light, but it also continually provides to the photoreceptors a molecule, the retinal, which is vital for the achievement of transduction. Damage in the RPE layer inevitably leads to the failure of visual function and possibly to the photoreceptors deterioration due to radiation.

This layer of the retina is, in conventional bright-field images, masked by the photoreceptor signal and the cells are difficult to visualize on en-face images with any system. A cross section of the retina generated with OCT shows a bright stripe at the depth of the RPE layer and can be used to evaluate its degeneration. En-face images using techniques exploiting multiply scattered light in AO-SLO [12] or exploiting the motion of the intracellular organelles in AO-OCT [113] have been developed to visualize the structures. However, the contrast of such images is either quite low or either requires long imaging sessions, making it unsuitable for clinical application. Finally, autofluorescence imaging has been used to image RPE cells thanks to the excitation of fluorophores like lipofuscin [114] or melanin [115–117] present in these cells leading to decent contrast, but commonly using visible light which is uncomfortable for the subject and can be unsafe [114]. The obtained contrast of these cells with our system was also fairly low when compared to the other retinal structures previously described and like the other existing imaging techniques, clinical analysis of this layer in humans *in-vivo* remains a considerable challenge.

While we have shown in Ch. 6 that the enhancement in contrast reached with full field dark-field imaging enables us to image retinal structures which we interpreted as retinal pigment cells, in this Chapter we aim to further investigate the potential of RPE images with our dark-field imaging for clinical exploitation. To do so, Sect. 11.1 details the extraction of a structural biomarker evaluating the normality of the RPE mosaic from images acquired with AO-FIO dark-field imaging. Then, a complementary method developed in AO-SLO for RPE imaging in NIR autofluorescence is described in Sect. 11.2 and compared to our dark-field imaging with respect to clinical applications in Sect. 11.3. Finally, a conclusion of the results of this Chapter is presented in Sect. 11.4 where we discuss the next steps to achieve functional imaging of the RPE cells.

## 11.1 Clinical application of the AO-FIO dark-field images

### 11.1.1 Clinical interest

Retinal pigmented epithelium is a layer which ensures light-scattering protection of the retina and supplies a vital molecule for transduction to photoreceptors (see Ch. 1 for more detailed description of its structure and functions). Because of the crucial role of RPE in the visual cycle, a failure to achieve its functions could not only affect the cycle itself but it could also rapidly lead to a degeneration of the photoreceptors and thus a permanent deterioration of vision. Therefore the importance of identifying early signs of damage of this structure.

### 11.1.2 Retinal pigment epithelium biomarkers

A range of biomarkers can be computed to evaluate the state of the pigment epithelium structure. Like the photoreceptors, the pigment epithelium cells form a mosaic, whose density can be computed. A loss in density would indicate a degeneration of this layer and therefore be a sign of retinal pathology. If the degeneration is more localized, meaning that there is an area containing several consecutive dead cells, another quantification of the damage is to compute the size of the wound corresponding to the total area missing the epithelium cells. Finally more sophisticated analysis could be carried out by verifying the position of the epithelium cells with respect to photoreceptors, i.e. the number of photoreceptors per pigment epithelium cell.

The following paragraph describes the computation of the density biomarker on the cell mosaic in our dark-field images, which we interpret as RPE cells. The computation has been on an area (yellow box) of the average image shown in Fig. 11.1 (A).

### 11.1.3 Extraction of density biomarker of the retinal pigment epithelium mosaic

Figure 11.1 shows the average image previously presented in Ch. 6 of a large cell mosaic acquired near the fovea whose characteristics suggest they could be RPE cells. The zoom indicated by a yellow box in this image shows the cells (red arrow head identifying one) in detail to better appreciate the mosaic.

Cell density is computed using the same algorithm employed in the previous Ch. 9 and developed by Li et al.[101] Indeed, pigment epithelium cells form also a mosaic but with a different size and spacing from photoreceptors. By simply changing those parameters in the algorithm we can apply the same procedure to compute the number of cells in the selected area.

Since the contrast of this mosaic is lower, the numbers of cells obtained through the automatic computation has been corrected by manually counting the cells to find the final value presented in Tab.11.1. Several measurements have been carried out on the regions marked in yellow (Fig. 11.1) using the previous algorithm in order to obtain an uncertainty (standard deviation error) of the result. This value is consistent with the literature as it matches the value obtained at 2° Temporal eccentricity shown in Fig.11.1(B) and is close in general to the density obtained by other teams in this region of the retina in humans *in-vivo*[118] and *ex-vivo* [119].

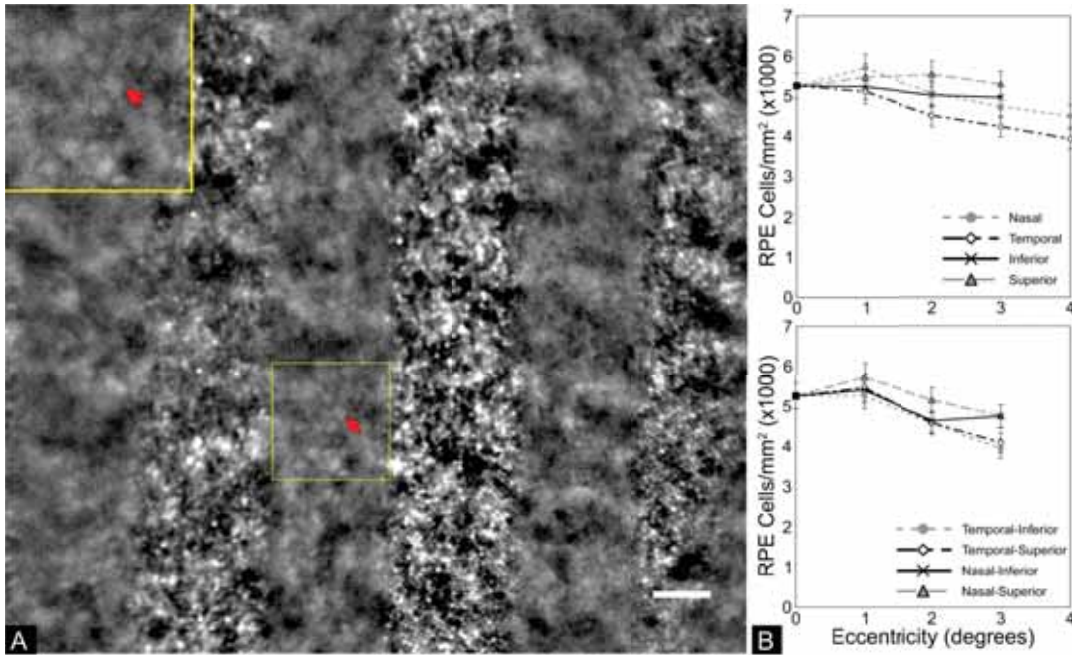


FIGURE 11.1: (A) Average image of an image sequence acquired on the Paris AO-FIO near the fovea. The illumination geometry was manipulated to obtain dark fields in the field of view. RPE cells are visible in some of the dark regions. A yellow box indicates an area that has been zoomed to show the details. A red arrowhead identifies one epithelium cell inside the mosaic. (B) Two plots describing the density of RPE cells in the human retina (image from Morgan et al.[118])

Area analyzed ( $\mu\text{m}^2$ )	Number of cells	Density (cells/ $\text{mm}^2$ )
92 x 100	41 $\pm$ 2	4500 $\pm$ 250

TABLE 11.1: Table showing the computed biomarker of density of the mosaic which could be RPE cells in the area shown in Fig.11.1(A) (yellow box).

The density shown here has been computed on a fairly small area. Ideally this computation should be done on a larger region of the retina with a very accurate knowledge of the eccentricity of said region. Even though we have only one image on one subject, the aim of this section was not to give a new information on the density of these cells but rather to show that, if these cells are proven to be RPE cells, the computation of its density his possible in AO-FIO thanks to an enhancement in contrast brought by dark-field imaging. Future work will be oriented towards achieving a higher signal-to-noise ratio in order to obtain a better contrasted mosaic of these cells in full field dark-field as well as increasing the analyzed area and the number of subjects tested.

#### 11.1.4 Comparison with AO SLO

First reflectance images of in vivo human RPE cells were obtained by Scoles et al. [12] using dark-field imaging in AO-SLO. We showed here that this could also be achieved using dark-field imaging in AO-FIO. The contrast on our system is currently lower than the one achieved in AO-SLO, whether it is in autofluorescence or dark-field imaging. Nevertheless, we are able to visualize and even quantify this structure using a technique free from distortion and with the potential to acquire large fields of view. Therefore, we are

encouraged to work in improving the SNR of our images in order to provide an alternative to AO-SLO dark-field imaging by reaching the same contrast and to offer complementary information to autofluorescence images. Finally, the analysis on the relative position of photoreceptors with respect to RPE mentioned in Sect. 11.1 is trivial on the AO-SLO due to RPE and photoreceptor mosaic simultaneous coincident capture.

### 11.1.5 Conclusion

The imaging of RPE cells has been made possible in our AO-FIO thanks to the development of dark-field imaging (see Ch. 6), and so has the computation of biomarkers evaluating its structure. Nevertheless, some concerns about the aspect of these cells in our images, which is quite different from the usual in other imaging systems, along with a low contrast which increases the uncertainty of measurement leads us to look for another way to verify our results. The next section describes the development of a near-infrared autofluorescence imaging technique for the study of the RPE at 757nm. This wavelength better adapted to the absorption spectrum of the melanin fluorophore is used to increase the contrast of the cells images. This imaging technique, which has been realized in a completely separate study, is interesting to me as it was an opportunity to learn more about RPE.

## 11.2 Autofluorescence imaging of the retinal pigment epithelium with AO-SLO

### 11.2.1 Reading guide

This section describes the exploitation of an AO-SLO for autofluorescence imaging of RPE at 757nm, which resulted in a paper in press in *Biomedical Express* (accepted in October 2018). The aim of this study was to improve the contrast of near-infrared autofluorescence of retinal pigmented epithelium imaging with AO-SLO by exciting fluorophores with a more optimal wavelength. Indeed, near infrared autofluorescence has been developed and described in previous works, but using a 790 nm wavelength which is not optimal for excitation of melanin due to the fact that the absorption spectrum of melanin is relatively low at this wavelength. This study aims to increase the detected autofluorescence signal by using a 757nm excitation wavelength, thus also shifting the emission band to shorter wavelength where detector sensitivity is higher. This increase in signal strength leads to improved image quality and robustness bringing this technique closer to become a reliable tool in the clinical evaluation of retinal pigmented epithelium and in the following of therapies evaluating diseases affecting this retinal structure. Moreover, optimizing the near infrared autofluorescence imaging also leads to an alternative technique to the current golden standard of autofluorescence imaging of RPE: short-wavelength autofluorescence. This technique is based on the excitation of a different fluorophore, lipofuscin, using short wavelength (blue or green) visible light which can present a potential harm for the retina. Finally, since the contrast of both short-wave and near-infrared techniques arises from different excitation fluorophores, they can be used to extract complementary information of the same retinal structure.

The MAORI AO-SLO of the Quinze-Vingts Hospital was modified by changing the illumination wavelength with the optimal wavelength of 757nm mentioned above. Filters

were added before the camera to limit the detection to the excited photons. I participated in the data acquisition and the discussion of the imaging protocols and resulting images, as well as in the writing of the article. The development of an imaging technique of RPE in the same laboratory was interesting to me, in particular because I could participate in the exploitation of an instrument leading to images that could be compared to our dark-field images of large cell mosaic in order to further investigate the hypothesis of being RPE cells.

**11.2.2 *Peer-reviewed Article: In vivo near-infrared autofluorescence imaging of retinal pigment epithelial cells with 757nm excitation***

# **In vivo near-infrared autofluorescence imaging of retinal pigment epithelial cells with 757 nm excitation**

**KATE GRIEVE<sup>1</sup>, ELENA GOFAS-SALAS<sup>1,2</sup>, R. DANIEL FERGUSON<sup>3</sup>,  
JOSÉ ALAIN SAHEL<sup>1,4</sup>, MICHEL PAQUES<sup>1</sup>, AND ETHAN A. ROSSI<sup>4,5,\*</sup>**

<sup>1</sup>Vision Institute and Quinze Vingts National Ophthalmology Hospital, PARIS group, 28 rue de Charenton, 75712, Paris, France

<sup>2</sup>DOTA, ONERA, Université Paris Saclay F-91123 Palaiseau - France

<sup>3</sup>Physical Sciences Inc., Andover, MA, USA 01810

<sup>4</sup>Department of Ophthalmology, University of Pittsburgh School of Medicine, Pittsburgh, PA, USA 15213

<sup>5</sup>Department of Bioengineering, University of Pittsburgh Swanson School of Engineering, Pittsburgh, PA, USA 15213

[\\*rossiea@pitt.edu](mailto:*rossiea@pitt.edu)

**Abstract:** We demonstrate near-infrared autofluorescence (NIRAF) imaging of retinal pigment epithelial (RPE) cells *in vivo* in healthy volunteers and patients using a 757 nm excitation source in adaptive optics scanning laser ophthalmoscopy (AOSLO). NIRAF excited at 757 nm and collected in an emission band from 778–810 nm produced a robust NIRAF signal, presumably arising from melanin, and revealed the typical hexagonal mosaic of RPE cells at most eccentricities imaged within the macula of normal eyes. Several patterns of altered NIRAF structure were seen in patients, including disruption of the NIRAF over a drusen, diffuse hyper NIRAF signal with loss of individual cell delineation in a case of non-neovascular AMD, and increased visibility of the RPE mosaic under an area showing loss of photoreceptors. In some participants, a superposed cone mosaic was clearly visible in the fluorescence channel at eccentricities between 2–6° from the fovea. This was reproducible in these participants and existed despite the use of emission filters with an optical attenuation density of 12 at the excitation wavelength, minimizing the possibility that this was due to bleed through of the excitation light. This cone signal may be a consequence of cone waveguiding on either the ingoing excitation light and/or the outgoing NIRAF emitted by fluorophores within the RPE and/or choroid and warrants further investigation. NIRAF imaging at 757nm offers efficient signal excitation and detection, revealing structural alterations in retinal disease with good contrast and shows promise as a tool for monitoring future therapies at the level of single RPE cells.

© 2018 Optical Society of America under the terms of the [OSA Open Access Publishing Agreement](#)

**OCIS codes:** (110.1080) Active or adaptive optics; (170.0110) Imaging systems; (170.2520) Fluorescence microscopy; (170.4460) Ophthalmic optics and devices; (170.4470) Ophthalmology

## **References and links**

1. A. von Rückmann, F. W. Fitzke, A. C. Bird, "Fundus autofluorescence in age-related macular disease imaged with a laser scanning ophthalmoscope," *Invest. Ophthalmol. Vis. Sci.* 38(2):478-86 (1997).
2. J. I. Morgan, J. J. Hunter, B. Masella, R. Wolfe, D. C. Gray, W. H. Merigan, F. C. Delori, D. R. Williams, "Light-induced retinal changes observed with high-resolution autofluorescence imaging of the retinal pigment epithelium," *Invest Ophthalmol Vis Sci.* 49(8):3715-29 (2008).
3. J. R. Sparrow and T. Duncker, "Fundus Autofluorescence and RPE Lipofuscin in Age-Related Macular Degeneration" *J Clin. Med.* 3(4), 1302-1321 (2014).
4. C. N. Keilhauer and F. C. Delori, "Near-Infrared Autofluorescence Imaging of the Fundus: Visualization of Ocular Melanin," *Invest. Ophthalmol. Vis. Sci.* 47(8), 3556–3564 (2006).
5. U. Kellner, S. Kellner, and S. Weinitz, "Fundus autofluorescence (488 nm) and near-infrared autofluorescence (787 nm) visualize different retinal pigment epithelium alterations in patients with age-related macular degeneration," *Retina* 30(1), 6–15 (2010).

6. S. Schmitz-Valckenberg, D. Lara, S. Nizari, E. M. Normando, L. Guo, A. R. Wegener, A. Tufail, F. W. Fitzke, F. G. Holz, and M. F. Cordeiro, "Localisation and significance of in vivo near-infrared autofluorescent signal in retinal imaging," *Br. J. Ophthalmol.* 95(8), 1134–1139 (2011).
7. L. Feeney-Burns, E. Hilderbrand, S. Eldridge, "Aging human RPE: morphometric analysis of macular, equatorial, and peripheral cells," *Invest. Ophthalmol. Vis. Sci.*, 25, 195-200 (1984).
8. J.J. Weiter, F.C. Delori, G.L. Wing, K.A. Fitch, "Retinal pigment epithelial lipofuscin and melanin and choroidal melanin in human eyes," *Invest. Ophthalmol. Vis. Sci.*, 27, 145-152(1986).
9. A. Pollreis, J. D. Messinger, K. R. Sloan, T. J. Mittermueller, A. S. Weinhandl, E. K. Benson, G. J. Kidd, U. Schmidt-Erfurth, and C. A. Curcio, "Visualizing melanosomes, lipofuscin, and melanolipofuscin in human retinal pigment epithelium using serial block face scanning electron microscopy," *Exp Eye Res.* 166,131-139 (2018).
10. J. R. Sparrow, E. Gregory-Roberts, K. Yamamoto, A. Blonska, S. K. Ghosh, K. Ueda, and J. Zhou, "The bisretinoids of retinal pigment epithelium," *Prog Retin Eye Res.* 31(2), 121-35 (2012).
11. J. R. Sparrow, D. Hicks, and C. P. Hamel, "The retinal pigment epithelium in health and disease," *Curr Mol Med.* 10(9), 802-23 (2010). Review.
12. J. Liang, D. R. Williams, and D. T. Miller, "Supernormal vision and high-resolution retinal imaging through adaptive optics," *J. Opt. Soc. Am. A* 14(11), 2884–2892 (1997).
13. D. X. Hammer, R. D. Ferguson, M. Mujat, A. Patel, E. Plumb, N. Iftimia, T. Y. P. Chui, J. D. Akula, A. B. Fulton, "Multimodal adaptive optics retinal imager: design and performance," *J Opt Soc Am A Opt Image Sci Vis.* 29, 2598–2607 (2012).
14. P. Xiao, V. Mazlin, K. Grieve, J. A. Sahel, M. Fink, A. C. Boccara, "In vivo high-resolution human retinal imaging with wavefront-correctionless full-field OCT," *Optica* 5, 409-412 (2018).
15. A. Roorda, Y. Zhang, and J. L. Duncan, "High-Resolution In Vivo Imaging of the RPE Mosaic in Eyes with Retinal Disease," *Invest. Ophthalmol. Vis. Sci.* 48(5), 2297–2303 (2007).
16. T. Liu, H. Jung, J. Liu, M. Droettboom, J. Tam, "Noninvasive near infrared autofluorescence imaging of retinal pigment epithelial cells in the human retina using adaptive optics," *Biomed. Opt. Expr.* 8(10), 4348-4360 (2017).
17. D. Scoles, Y. N. Sulai, A. Dubra, "In vivo dark-field imaging of the retinal pigment epithelium cell mosaic," *Biomed. Opt. Express* 4(9), 1710–1723 (2013).
18. Z. Liu, O. P. Kocaoglu, and D. T. Miller, "3D Imaging of Retinal Pigment Epithelial Cells in the Living Human Retina," *Invest. Ophthalmol. Vis. Sci.* 57(9), OCT533 (2016).
19. C. Torti, B. Považay, B. Hofer, et al, "Adaptive optics optical coherence tomography at 120,000 depth scans/s for non-invasive cellular phenotyping of the living human retina," *Opt Express.* 17(22), 19382-19400 (2009).
20. A. Roorda, F. Romero-Borja, W. Donnelly, III, H. Queener, T. Hebert, and M. Campbell, "Adaptive optics scanning laser ophthalmoscopy," *Opt. Express* 10, 405-412 (2002).
21. J. I. W. Morgan, A. Dubra, R. Wolfe, W. H. Merigan, and D. R. Williams, "In Vivo Autofluorescence Imaging of the Human and Macaque Retinal Pigment Epithelial Cell Mosaic," *Invest. Ophthalmol. Vis. Sci.* 50(3), 1350–1359 (2009).
22. E. A. Rossi, P. Rangel-Fonseca, K. Parkins, W. Fischer, L. R. Latchney, M. A. Folwell, D. R. Williams, A. Dubra, M. M. Chung, "In vivo imaging of retinal pigment epithelium cells in age related macular degeneration," *Biomed. Opt. Expr.* 4(11), 2527-2539 (2013).
23. C. E. Granger, D. R. Williams, and E. A. Rossi, "Near-infrared autofluorescence imaging reveals the retinal pigment epithelial mosaic in the living human eye," *Invest. Ophthalmol. Vis. Sci.* 58, 3429 (2017).
24. C. E. Granger, Q. Yang, H. Song, K. Saito, K. Nozato, L. R. Latchney, B. T. Leonard, M. M. Chung, D. R. Williams, and E. A. Rossi, "Human retinal pigment epithelium: in vivo cell morphometry, multi-spectral autofluorescence, and relationship to cone mosaic," *Invest. Ophthalmol. Vis. Sci.*, In Press (2018).
25. J. Tam, J. Liu, A. Dubra, and R. Fariss, "In Vivo Imaging of the Human Retinal Pigment Epithelial Mosaic Using Adaptive Optics Enhanced Indocyanine Green Ophthalmoscopy," *Invest. Ophthalmol. Vis. Sci.* 57(10), 4376-4384 (2016).
26. Q. Yang, J. Zhang, K. Nozato, K. Saito, D. R. Williams, A. Roorda, E. A. Rossi, "Closed-loop optical stabilization and digital image registration in adaptive optics scanning light ophthalmoscopy," *Biomed. Opt. Express* 5, 3174-3191 (2014).
27. K. Venkateswaran, F. Romero-Borja, A. Roorda, "Theoretical Modeling and Evaluation of the Axial Resolution of the Adaptive Optics Scanning Laser Ophthalmoscope" *J. Biomed. Opt.* 9(1): 132-138 (2004).
28. Laser Institute of America. ANSI Z136.1 - 2014, American National Standard for Safe Use of Lasers. Orlando, FL: Laser Institute of America; (2014).
29. B. D. Masella, D. R. Williams, W. S. Fischer, E. A. Rossi, J. J. Hunter, "Long-term reduction in infrared autofluorescence caused by infrared light below the maximum permissible exposure," *Invest Ophthalmol Vis Sci.* 55(6), 3929–3938 (2014).
30. D. C. Gray, W. Merigan, J. I. Wolfing, B. P. Gee, J. Porter, A. Dubra, T. H. Twietmeyer, K. Ahmad, R. Tumber, F. Reinholz, D. R. Williams, "In vivo fluorescence imaging of primate retinal ganglion cells and retinal pigment epithelial cells," *Opt. Express* 14, 7144-7158 (2006).
31. K. Y. Li, A. Roorda, "Automated identification of cone photoreceptors in adaptive optics retinal images," *J Opt Soc Am A Opt Image Sci Vis.* 24(5), 1358-63 (2007).

32. Q. X. Zhang, R. W. Lu, J. D. Messinger, C. A. Curcio, V. Guarcello, X. C. Yao, "In vivo optical coherence tomography of light-driven melanosome translocation in retinal pigment epithelium," *Sci Rep* 3, 2644 (2013).
33. R. F. Cooper, C. S. Langlo, A. Dubra, J. Carroll, "Automatic detection of modal spacing (Yellott's ring) in adaptive optics scanning light ophthalmoscope images," *Ophthalmic Physiol Opt*, 33, 540–549 (2013).
34. J. I. Yellott Jr, "Spectral analysis of spatial sampling by photoreceptors: topological disorder prevents aliasing," *Vision Res* 22, 1205–1210 (1982).
35. O. Strauss, "The Retinal Pigment Epithelium," 2011. In: Kolb H, Fernandez E, Nelson R, editors. *Webvision: The Organization of the Retina and Visual System* [Internet]. Salt Lake City (UT): University of Utah Health Sciences Center; 1995-. Figure 2. [Transmission electron micrograph of the...]. Available from: <https://www.ncbi.nlm.nih.gov/books/NBK54392/figure/StraussRPE.F2/>, Accessed 12 October 2018.
36. S. Panda-Jonas, J. B. Jonas, M. Jakobczyk-Zmija, "Retinal pigment epithelial cell count, distribution, and correlations in normal human eyes," *Am J Ophthalmol*. 121(2), 181-189 (1996).
37. P. M. Prieto, J. S. McLellan, S. A. Burns, "Investigating the light absorption in a single pass through the photoreceptor layer by means of the lipofuscin fluorescence," *Vision Res*. 45(15), 1957-1965 (2005).
38. G. J. V. Blokland, D. V. Norren, "Intensity and polarization of light scattered at small angles from the human fovea," *Vision Res*. 26, 485-494 (1986).
39. J.-M. Gorrard, F. C. Delori, "A reflectometric technique for assessing photoreceptor alignment," *Vision Res*. 35, 999-1010, (1995).
40. S. A. Burns, J. C. He, F. C. Delori, "Do the cones see light scattered from the deep retinal layers?," <http://www.opt.indiana.edu/people/faculty/burns/navs97steve.htm>, Accessed 23 July 2018
41. E. C. Zanzottera, J. D. Messinger, T. Ach, R. T. Smith, C. A. Curcio, "Subducted and melanotic cells in advanced age-related macular degeneration are derived from retinal pigment epithelium," *Invest. Ophthalmol. Vis. Sci*. 56, 3269–3278 (2015).
42. K. Gocho, V. Sarda, S. Falah, J. A. Sahel, F. Sennlaub, M. Benchaboune, M. Ullern, M. Paques, "Adaptive optics imaging of geographic atrophy," *Invest Ophthalmol Vis Sci*. 54, 3673–3680 (2013).
43. M. Paques, S. Meimon, F. Rossant, D. Rosenbaum, S. Mrejen, F. Sennlaub, K. Grieve, "Adaptive optics ophthalmoscopy: application to age-related macular degeneration and vascular diseases," *Prog Ret Eye Res*, online 17 July 2018 (2018).

---

## 1. Introduction

Fundus autofluorescence imaging is routinely performed in clinical ophthalmology with scanning laser ophthalmoscopy (SLO) [1] and is an important tool for evaluating disease status and monitoring progression in pathologies affecting the retinal pigment epithelium (RPE) and photoreceptors (PRs), hence applicable in various retinal degenerations such as age-related macular degeneration (AMD). The RPE may be affected early on in disease, before damage to photoreceptors and vision loss has occurred, so precise imaging of the RPE is desirable to detect pathology at an early stage where treatment and management techniques may be most effective. SLO, with its lateral resolution of 10  $\mu\text{m}$ , can view a large field of the fundus but cannot resolve individual cells.

Short wavelength autofluorescence (SWAF) and fluorescein for retinal vasculature angiography are excited at visible wavelengths, usually using blue (488 nm) or green (532 nm) light. A drawback of using these wavelengths is that they are uncomfortably bright, even at light levels considered to be safe, and may potentially be harmful to diseased retinas that may be at greater risk for light induced damage [2]. Near-infrared autofluorescence (NIRAF) has typically been excited at  $\sim 790$  nm. This wavelength has been utilized for NIRAF due to its convenience as it has been built into commercial SLO systems for reflectance imaging and to excite indocyanine green (ICG). The intrinsic NIRAF signal is thought to be approximately 60 times lower than SWAF [4], so detecting NIRAF is challenging. In addition, SWAF and NIRAF do not reveal the same fluorophore [3-6].

The principle fluorophore responsible for the autofluorescence (AF) signal at short wavelengths is lipofuscin, a material that accumulates in RPE cells as a consequence of the visual cycle [3-6]. Lipofuscin accumulates over a person's lifetime [7, 8] and thus is expected to correlate with age. At near-infrared (NIR) wavelengths, melanin in RPE cells is thought to be the principle contributor to the AF signal, along with some choroidal melanin, and possibly some lipofuscin [4]. Melanin is expected to decrease with age [7]. Concentrations of intrinsic RPE fluorophores follow an inverse relation across the macula with melanin peaking in the fovea and lipofuscin in the periphery. In addition, melanolipofuscin forms with age [9] in

quantities closer to that of lipofuscin than that of melanin. This means that both SWAF and NIRAF may potentially be generated from the same structures, containing both fluorophores. Lipofuscin itself is not a single fluorophore with narrow excitation and emission bands but is rather an array of fluorophores of overlapping broad excitation and emission bands, stretching from blue-green excitation producing green-red emission, to green-red excitation emitting with a red shifted peak [10]. As a unique broadband absorber, the excitation and emission spectra of ocular melanin and its sub-types (eumelanin, pheomelanin) are not well characterized, particularly in the near-infrared. For the purposes of monitoring pathology, lipofuscin has been the fluorophore of most interest as regional autofluorescence thought to be generated by lipofuscin has been shown to often be correlated with areas of photoreceptor death [11]. However, NIRAF has garnered increased interest recently as it is comfortable for patients and provides complementary information [5]. In addition, considering recent findings regarding the high proportion of melanolipofuscin in aging eyes [9], the NIRAF signal may serve as a surrogate for SWAF and biomarker of RPE status in diseased eyes.

Cellular level resolution imaging of the living retina has typically required the use of adaptive optics (AO) [12]. AO ophthalmoscopy (AOO) usually uses a closed-loop wavefront control to produce near diffraction-limited images ( $\sim 2\mu\text{m}$  lateral resolution) using the full 6-9 mm pupil size available in the dilated human eye [13]. This allows individual photoreceptor cells to be resolved in the living retina, along with other microscopic structures such as the microvasculature and individual nerve fiber bundles. Imaging the other cell layers such as the RPE is more challenging as their weak contrast is masked by the bright reflections from the nerve fiber, vascular and photoreceptor layers. However, several imaging techniques have met this challenge in order to successfully reveal the RPE layer. Optical coherence tomography (OCT) is routinely used to reveal all the retinal layers in cross-section, including a particularly bright signal at the RPE layer due to the absorption/scattering properties of melanin in the cells of the RPE. However, despite exquisite axial resolution, commercially available OCT without AO lacks sufficient lateral resolution to resolve individual cells [14].

Individual RPE cells can be revealed in patients with reflectance AOO when the overlying photoreceptors are lost, but this is rare and is indicative of extensive, lasting damage, at a stage too late for many types of therapy [15]. RPE cells can be imaged using detection techniques such as dark-field AO, but only in some subjects and usually only near the fovea [17]; the reason for this remains unclear but it may be related to differences in the scattering properties of the photoreceptor layer outside of the cone-dominated macula [17]. Individual RPE cells have also been detected using AO-OCT [18,19]. The most recent report using this technique suggests that dynamic imaging is required and that RPE contrast may be enhanced by the natural movement, over minutes-long timescales, of organelles within individual cells [18]. However, to record this signal *in vivo*, long video sequences (90 minutes) on subjects with excellent fixation are required, so patient imaging is not yet feasible [18].

Adaptive optics scanning laser ophthalmoscopy (AOSLO) [20] has been used to image SWAF [21, 22] and NIRAF [16, 23, 24] in healthy volunteers and reveals the individual cells of the RPE mosaic *in vivo*. NIRAF has also been used to image the RPE mosaic after administration of ICG [25]. These previous NIRAF techniques used wavelengths adopted from ICG imaging ( $\sim 790\text{ nm}$  excitation,  $\sim 800\text{-}850\text{ nm}$  emission). The absorption spectrum of melanin shows a steady decrease from the visible toward the infrared and by  $790\text{ nm}$  absorption is relatively low [4]; this fact, along with a recently published report showing relatively high noise levels and low contrast images when using these wavelengths [16], suggests that these previous implementations may not have been optimized. Here, we set out to improve AOSLO for NIRAF imaging of RPE cells *in vivo*. We implemented NIRAF in AOSLO with excitation at  $757\text{ nm}$ , to seek to improve in signal strength, image quality and robustness over previous studies. This shift allowed us to move the emission band for NIRAF detection to shorter wavelengths where our detectors have slightly improved sensitivity, in addition to providing access to an area of the melanin absorption spectrum where

absorption/excitation should be greater compared to longer wavelengths [4]. We validated this new NIRAF AOSLO implementation by imaging both normal eyes and those of several patients with RPE abnormalities.

## 2. Methods

We modified the multimodal adaptive optics retinal imager (MAORI) (Physical Sciences, Inc., Andover, MA, USA) at the Quinze Vingts Hospital in Paris, to add in a fluorescence detection channel optimized for the weak NIRAF signal (Fig. 1). This modification of the MAORI optical system added a series of dichroic beamsplitters and filters at suitable wavelengths along with a highly sensitive detector, and benefitted from the use of custom-developed image registration software for data processing [26].

### 2.1 Setup

The MAORI system (Fig. 1) has been described in detail elsewhere [13]. Briefly, the system provides simultaneous adaptive optics correction for both an AOSLO and a spectral domain AO-OCT subsystem. An additional simultaneous wide-field SLO channel is used to target the high-resolution imaging to specific regions of interest. The AOSLO system includes a confocal reflectance channel and four offset apertures for non-confocal imaging; optical fibers serve as apertures and relay the light to avalanche photodiode (APD) detectors. A 69-actuator deformable mirror (DM69, Alpao, France) in a 10 Hz closed loop with a Shack-Hartmann wavefront sensor corrects the wavefront aberrations. Images are acquired at 24 frames per second (fps). The three imaging sub-systems each have an independent light source: 940 nm for the wide-field SLO; 757 nm (Exalos SLD; 757 nm center, 20nm full-width at half maximum (FWHM)) for the AOSLO; and 840 nm for the wavefront sensing beacon and OCT. We modified the system to use the 757 nm beam for NIRAF excitation and added appropriate filters (see below; Semrock, USA) and dichroic mirrors to add in a new detection arm with a photomultiplier tube (PMT) (H7422-50, Hamamatsu, Japan). The PMT was chosen for NIRAF, rather than the APD detectors used for the other channels, because the high gain, low noise performance of the PMT is key in this “photon counting regime” low light application, where the AF signal is much weaker than the scattered/reflectance signal from the photoreceptors.

The fluorescence channel detects very low light levels and is therefore highly sensitive to stray light and detector alignment. Scattered light from other sources is minimized by doubling up on bandpass filters in front of the sources (FF01-747/33, Semrock, (excitation path on AOSLO source), FF01-888/131, Semrock, (excitation path on beacon), at 0° incidence, doubled) and the detector (FF01-794/32, Semrock, (emission path in front of PMT), at 0° incidence, doubled), providing an optical attenuation density of 12 at the excitation wavelength to obtain a high rejection rate of stray light. To combine paths, we used dichroic filters/mirrors as follows: on the AO beacon, we used a dichroic filter (Chroma 750dcxr at 17° angle of incidence (AOI)), which acts as a longpass filter cutting at 812nm, which in combination with the beacon excitation filters which cut hard below ~825nm guaranteed that none of the beacon light could bleed through to the NIRAF channel. The SLO/NIRAF beams dichroic (Chroma zt780sp-UF3, at ~45° AOI, shortpass) was a 1” x 3mm ultraflat substrate which reflected the NIRAF signal towards the collimator/multimode fiber and PMT. Detector alignment was fine-tuned by manually adjusting the x-y position of the fluorescence detection channel’s confocal pinhole for each subject, at each imaging position (the confocal pinhole is in fact an optical fiber that collects the light to take it to the PMT, whose core fiber diameter is equal to pinhole size). As the Airy disk (AD) of the system is 48  $\mu\text{m}$ , a confocal pinhole of 50  $\mu\text{m}$  was found to provide the optimal tradeoff between optical sectioning and photon collection [27]. A smaller pinhole of 25 $\mu\text{m}$  produced noisy images, in which any improvement in optical sectioning that the smaller pinhole may provide was

difficult to appreciate due to the increased noise. We typically acquired 800 frames at 24 fps, requiring 30 seconds to record each movie. In comparison to other NIRAF AO imaging [16, 23-25], our excitation wavelength of 757 nm should give higher melanin absorption compared to the longer wavelength excitation light near 790 nm that they used. We also used a shorter wavelength emission band compared to previous studies, 778 nm to 810 nm versus 800 nm to 830 nm in [16, 23-25]. Light levels were 0.75 mW for the  $2^\circ$  long line scan 840 nm beacon and 0.9 mW for the  $2^\circ \times 2^\circ$  field 757 nm AOSLO beam, whose overlapping combination, when considering the fraction of the ANSI maximum permissible exposure (MPE) of each source, represents 80% of the total MPE as defined by ANSI [28]. The 940 nm wide-field SLO was not used simultaneously with the other beams for the experiments in this paper. For the AOSLO channel, our power level is at only 50% of the MPE, though this lies within the range of the levels shown by Masella to cause NIRAF reduction in primate [29].

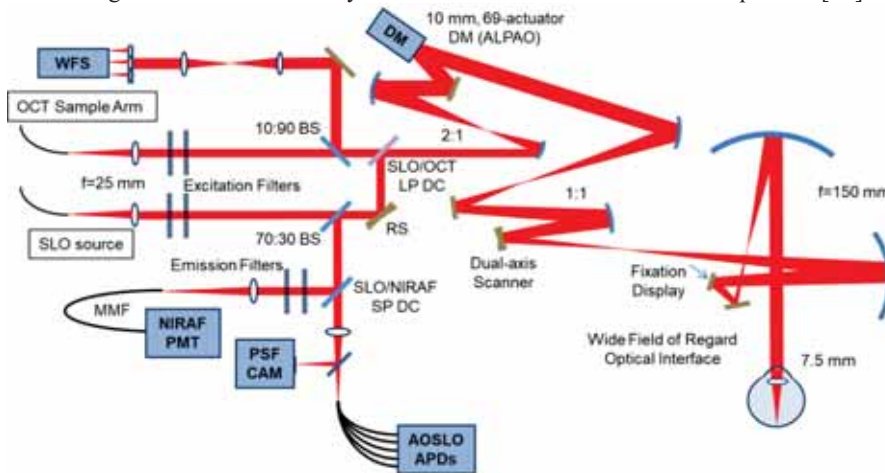


Fig. 1. System diagram. WFS, wavefront sensor, DM, deformable mirror, NIRAF PMT, near infrared photomultiplier tube, PSF CAM, point spread function camera, AOSLO APDs, adaptive optics scanning laser ophthalmoscope avalanche photodiodes, OCT, optical coherence tomography, SLO, scanning laser ophthalmoscope, BS, beamsplitter, SLO/OCT LP DC, scanning laser ophthalmoscope/optical coherence tomography long pass dichroic, SLO/NIRAF SP DC, scanning laser ophthalmoscope near infrared short pass dichroic, RS resonant scanner, MMF, multimode fiber.

## 2.2 Image processing and analysis

Each individual frame captured in the fluorescence channel resembles dark noise, i.e. sparse pixels that appear as white on a black background. Several hundred frames must be averaged to reveal the final image, requiring co-registration of the weak AF signal with the simultaneous, coincident, clear image of the photoreceptors acquired in the confocal channel. We used a strip-based registration algorithm described previously [26] to perform the co-registration, after Gray et al. [30]. Some image analyses, including discrete Fourier transforms, were computed in ImageJ (NIH, Bethesda, MD, USA). Average cell profiles were computed using custom scripts in MATLAB (The MathWorks, Inc., Natick, MA), utilizing elements of the Image Processing Toolbox. Cone positions were semi-automatically determined using previously described methods [31] and average cell profiles were computed by taking the center of each cone position as the center of a new sub-image. All sub-images fully contained within the image were then averaged to generate the average cell profiles.

## 2.3 Subjects

The research was carried out according to the Declaration of Helsinki and approved by our local ethics committee (CPP Ile de France 5 #16145). Informed consent was obtained for each volunteer. We imaged 4 volunteers considered healthy by routine fundus imaging on multiple occasions (subject #1: 25 year old female, subject #2: 24 year old male, subject #3: 38 year old female, subject #4: 53 year old male,), and 3 patients, all with natural lenses: a 58 year old male with drusen in an otherwise normal retina, a 31 year old male with radiation retinopathy, and an 80 year old female with non neovascular or “dry” AMD with geographic atrophy.

### 3. Results

#### 3.1 Imaging in healthy volunteers

The characteristic appearance of the RPE cell mosaic in fluorescence AOSLO, with cells appearing with a hypo-AF center and hyper-AF surround, was revealed with robust signal strength in most locations imaged in normal eyes (Fig. 2). We imaged the RPE mosaic in contiguous overlapping fields in 4 normal subjects from the fovea out to an eccentricity of  $10^\circ$  temporal (Fig. 3). We were able at all locations in young subjects #1 and #2 to obtain clear images of the RPE mosaic, though at lower contrast in subject #2 at the periphery. On older subjects #3 and #4, the RPE mosaic was generally not as highly contrasted as in the younger eyes. In subjects #1 and #3, we obtained a superposition of the RPE mosaic with a mosaic resembling the cone photoreceptors at some locations (Fig. 3, 4). In these cases, the RPE mosaic was clearly visible outside the fovea but became confused with the cone mosaic between  $2^\circ$  and  $6^\circ$ . For subject #4, the RPE mosaic was clearly resolved from the fovea to  $3^\circ$  temporal. This was followed by a reduced NIRAF signal of low contrast in an annular region around the fovea from  $3-5^\circ$ , in agreement with previous findings from SWAF [24]. Interestingly, this area contained a few very bright hyper-AF cells (Fig. 3; middle row; central region). Beyond  $5^\circ$ , NIRAF showed diffuse fluorescence with some RPE cells appearing as the dark centered, bright contoured hexagonal mosaic seen elsewhere in normal eyes, but in other areas resembled bright hexagons with fine dark contours suggesting a different distribution of the fluorophores within the cells.

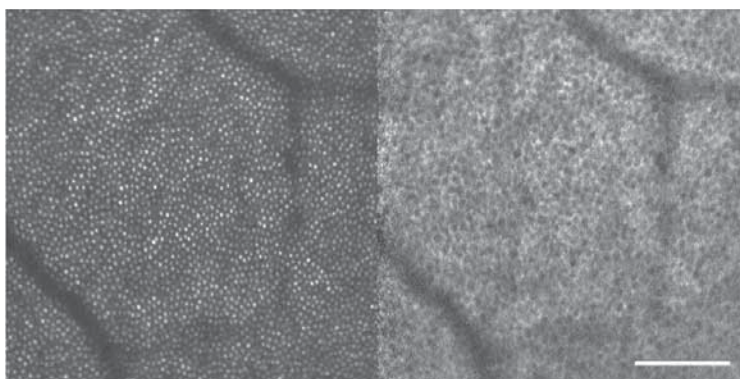


Fig. 2. Photoreceptors in reflectance (left) and RPE cells in NIRAF (right) in healthy volunteer #1; location is  $10^\circ$  temporal; scale bar is  $100 \mu\text{m}$ .

After the method of Masella et al [29], NIRAF reduction was measured by imaging with commercial SD-OCT (Spectralis HRAOCT, Heidelberg Engineering GmbH, Heidelberg, Germany) in ICG acquisition mode (787 nm excitation) in subject #3 and showed approximately 8% reduction in average NIRAF signal intensity in the zones covered by AO imaging compared to those that had not been exposed, 3 weeks after AO imaging. No changes to other retinal features were seen in SLO reflectance mode with the Spectralis. This

is comparable with the 4-12% NIRAF reductions seen in [29], also for exposures well below the MPE.

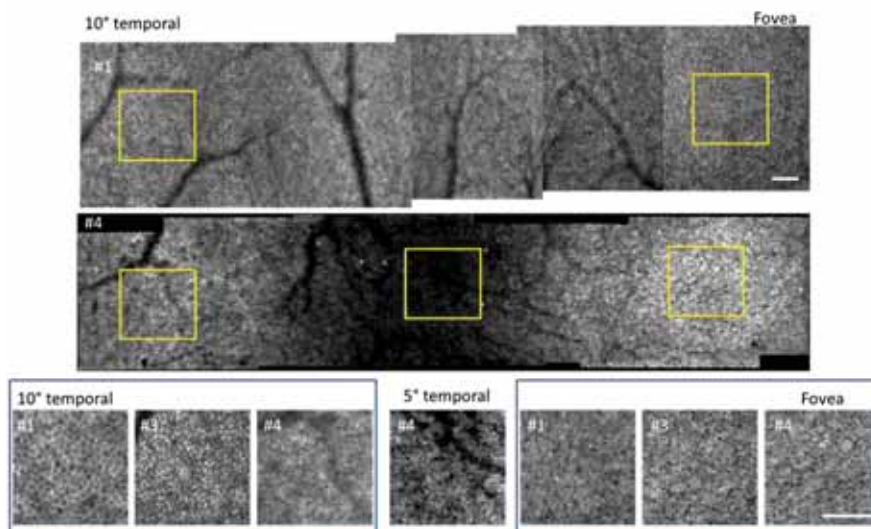


Fig. 3. Variation in appearance of RPE in healthy volunteers. Top and center row: mosaics from 10° temporal to the fovea in subjects #1 and #4. Note the dimmed ring containing a few hyper AF cells from 3-5° in subject #4. Bottom row: zooms on 10° temporal (left box), 5° temporal (center panel) and fovea (right box) of subjects #1, #3 and #4; inset yellow squares in images above denote locations shown for subjects #1 and #4. Contrast and brightness have been altered in the zoomed panel on the 5° temporal location in subject #4 as this region of the retina gave dimmer images than elsewhere. Note the diffuse fluorescence with hyper AF cells in #4 at 10°. Scale bars are 100 $\mu$ m.

### 3.2 Measures taken to remove cones superposed with the RPE mosaic

On noticing an appearance of cones in the NIRAF signal during our pilot testing of this setup (at some locations, on some subjects) we took measures to attempt to optically eliminate it. First, we sought to eliminate any reflectance signal from cones that may be reaching the PMT at the excitation wavelength by adding an extra bandpass filter in front of the NIRAF detector to increase the rejection rate from an initial optical density of 7 in our pilot testing up to 14 (used for all images shown here, as stated in the Methods). This addition produced no noticeable difference to the images.

To determine whether the cone signal varied with focus, through focus image stacks were acquired by adding defocus to the deformable mirror. This was tested with 1 and 0.5 Airy disk diameter detection pinholes. In all subjects, the best subjective RPE image contrast was coincident with subjective best focus on the PR layer, as the optical sectioning of our AOSLO [27] is larger than the RPE to photoreceptor distance [18], so that both are included in the same optical section. The photoreceptors appear “in focus” in the AOSLO over a considerable range due to the relatively wide optical section (with a 1 or 0.5 Airy disk diameter pinhole, we can expect around a 60 $\mu$ m optical section [27] at 757nm wavelength). In order to ensure best RPE focus for routine imaging, we therefore chose to image in the deepest focal plane that still showed bright photoreceptors (i.e. closest to the RPE, as opposed to closest to the ELM). For both pinhole sizes, changing focus did not remove superposed cones in those subjects and locations where they were visible. With the 0.5 Airy disk diameter pinhole, images were noisier and dimmer, with increased contrast of the superposed cones and reduced visibility of the RPE. The 1 Airy disk diameter was selected for all subsequent imaging as it provided the optimal compromise between confocality, signal level and RPE contrast.

Finally, we tested dark versus light adapted retina on subject #1 after both 10 hours (overnight) and 1 hour (prior to imaging) of dark adaptation, and on subject #2 after 1 hour (prior to imaging) dark adaptation, to see if mobility of melanin from RPE cell cytoplasm into apical processes [32] was detectable and could explain the variable appearance of the PR mosaic on the NIRAF images (since the apical processes surround cones and may therefore follow a cone mosaic structure). Dark adaptation was performed using an adherent eye patch doubled over with a dark fabric blindfold. The light adapted condition was set to be the eye's state under ambient conditions (normal daylight), without bleaching. No changes were detected between images obtained after light and dark adaptation under these conditions, though this could merit further exploration under various conditions of strict dark adaptation.

As the optical measures to remove the superposed cone signal were not successful, we also explored a computational approach. On analyzing the modal frequencies [33] (Yellott's rings [34]) present in the reflectance and NIRAF images, we could identify the frequency corresponding to the cone spacing and suppress it with a bandpass filter in the Fourier domain; this improved visibility of the RPE mosaic as shown in Fig. 4.

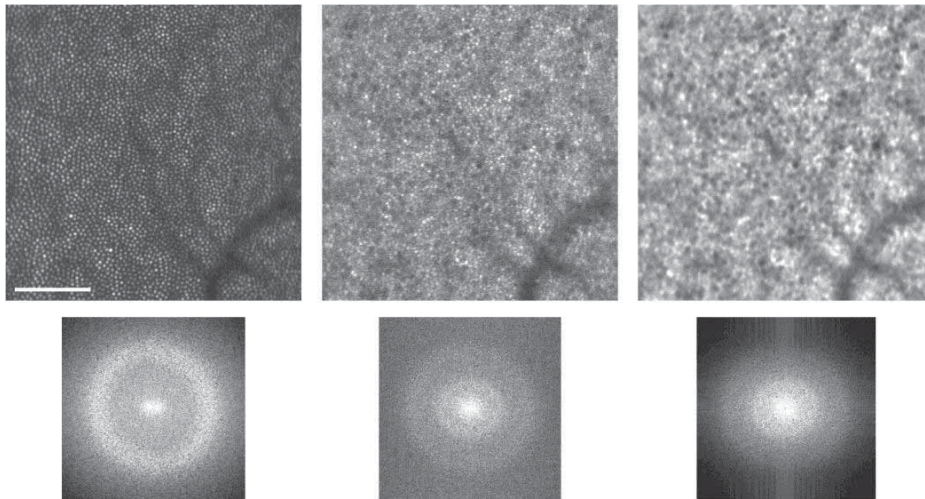


Fig. 4. The discrete Fourier transform of the reflectance (top left) and NIRAF (top center) images produces Yellott's rings in the power spectrum corresponding to the modal frequencies of the photoreceptor and RPE spacing (bottom). The NIRAF power spectrum contains peaks in two frequency bands corresponding to that of the photoreceptors (outer ring) and that of the RPE (inner ring). Applying a bandpass filter can suppress the cone signal to enhance visibility of the RPE mosaic (right). Scale bar is 100  $\mu\text{m}$ .

### 3.3 Retinal diseases affecting the RPE

In a patient with a small drusen in an otherwise normal eye, the regular RPE mosaic was disturbed when observed with NIRAF (Fig. 5). In this area structures larger than normal RPE cells were seen with nonuniform, decreased autofluorescence across their surface. Some darker structures remained within this region but they appeared larger than the dark regions of adjacent RPE cells (which presumably correspond to the melanin-free nucleus of the cells [35]).

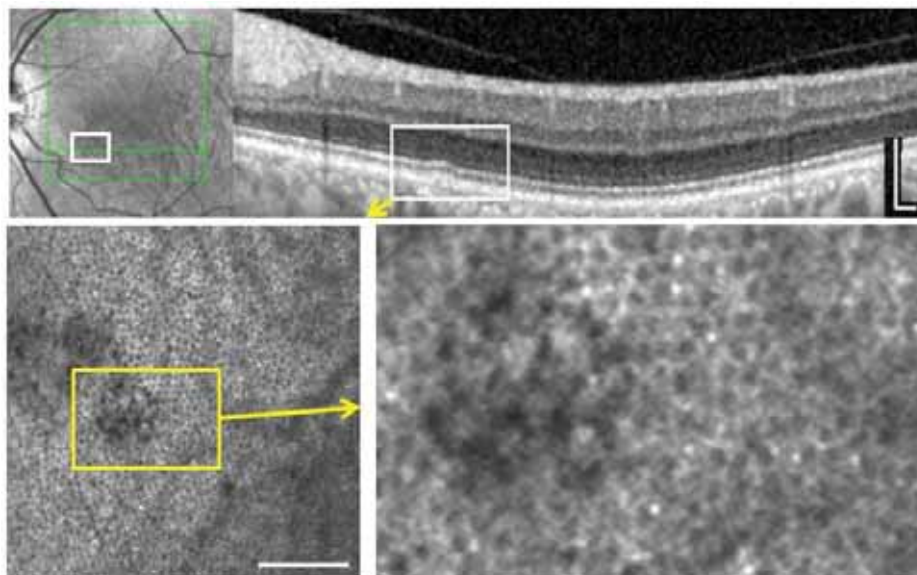


Figure 5. Small drusen. Top, IR SLO and OCT imaging. Bottom, NIRAF which shows local disruption of an otherwise normal RPE mosaic. Scale bars, 200µm.

In a patient with non-neovascular AMD, areas with presumably intact RPE cells as judged from OCT showed a coarse granulation in NIRAF, without the central hypo-AF that is seen in the RPE mosaics on young healthy subjects (Fig. 6). Minute zones of NIRAF were also detected adjacent to atrophic areas. In the fovea, NIRAF was higher contrast in AOSLO than in conventional SLO, but the normal RPE cell mosaic was not visible.

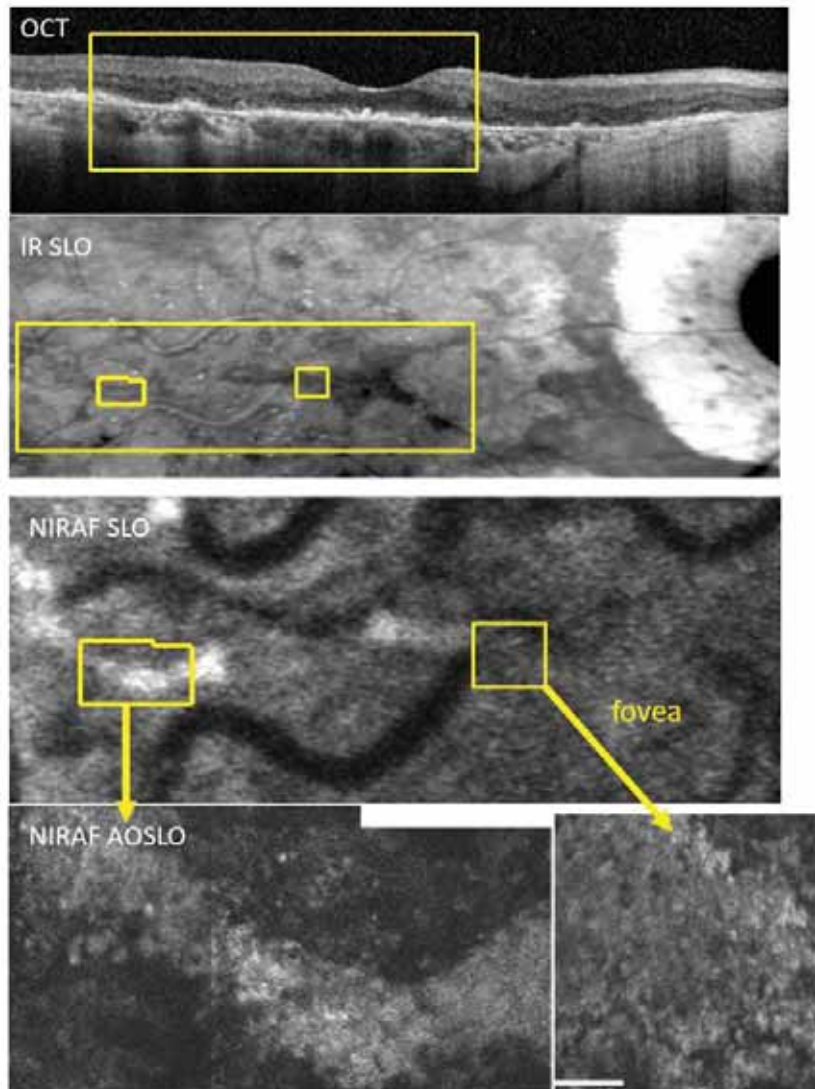


Figure 6. Case of non-neovascular age-related macular degeneration with foveal sparing. From top to bottom, OCT, IR SLO, NIRAF SLO, and NIRAF-AOSLO. In the periphery (lower left) the contrast appears higher in NIRAF AOSLO, across a band of hyper-AF. In the fovea the NIRAF contrast in AOSLO (lower right) is higher than that in the NIRAF SLO image. This area showed no recognizable RPE mosaic but rather a diffuse fluorescence with some granularity. This is similar to what is observed in our oldest control (compare with #4, fig 2 zoom at 10° temporal). Scale bar is 100 $\mu$ m.

A patient with diabetic retinopathy showed hyper AF in the foveal zone underlying PR damage (Fig. 7), in an otherwise normal RPE mosaic. NIRAF contrast was much higher in the fovea, possibly due to increased transmission of light due to the absence of photoreceptor outer segments.

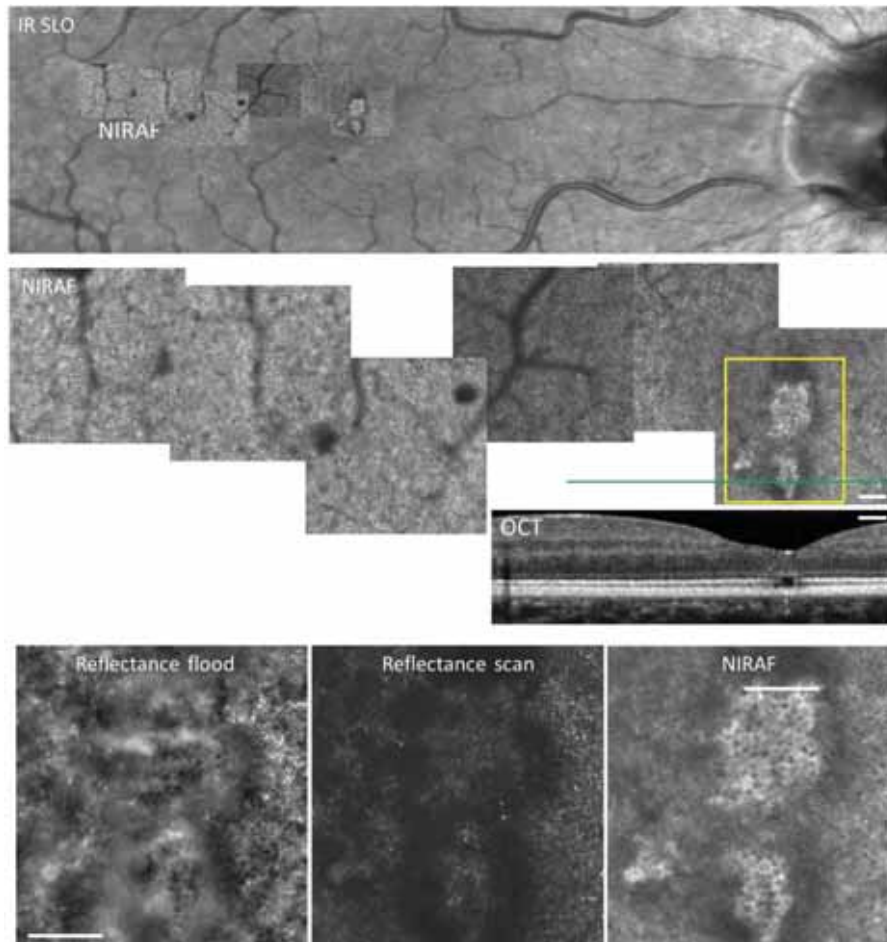


Figure 7. Case of radiation retinopathy with sequelae of macular edema that caused loss of foveal photoreceptors. Top, IR SLO image with overlaid NIRAF mosaic; center shows a zoom on the NIRAF AOSLO mosaic and corresponding OCT; bottom shows magnifications in the fovea in reflectance flood adaptive optics ophthalmoscopy, reflectance scan AOSLO and NIRAF AOSLO. Note by NIRAF AOSLO the visualization of the RPE mosaic within the area lacking outer segments. Note also the shadowing from microaneurysms in the top and center panel views. Scale bar, 200 $\mu$ m.

### 3.4 Indocyanine Green (ICG)

We performed a preliminary attempt to image in a normal subject (#4) after injection of a typical dose of indocyanine green (ICG) fluorophore for angiography. Images were recorded before, immediately following, and 1 hour following, ICG injection. In contrast to the result shown in [25] at 790nm, we observed no change between these three cases, suggesting that at our wavelengths of excitation and detection, we are not sensitive to ICG, likely due to being at a shorter wavelength, too far from the excitation and emission peaks [26]. These preliminary tests should be followed with more detailed exploration.



Figure 8. Average image intensity at cone locations demonstrates that a cone signature persists in the images even when it is not visible by eye. Cone positions in the reflectance images at 4 degrees (a) and 10 degrees (c) were used to compute average cone intensity profiles across a 30 x 30  $\mu\text{m}$  area centered on each cone (e,g). When applied to the corresponding NIRAF images (b, d), signatures of the cones were also visible (f, h). Radial averages of the images shown in (e & f and g & h) are plotted in i and j, respectively (red lines are from the reflectance images and blue dashed lines are from the NIRAF images). These plots demonstrate that the cone signature is nearly identical in both images at 4 degrees but that the NIRAF signature is narrower than the cone intensity profile from the reflectance image at 10 degrees. Control images generated by using the transposed cone positions showed no cellular signatures in any image (k-n).

Radial averages were computed for each image and are compared for the two eccentricities in Fig. 8i,j. At four degrees, the radial averages are nearly identical (Fig. 8i). Not surprisingly, discordance between the radial average of the intensity profile of the two images was observed at 10 degrees (Fig. 8j). The first peak likely arises from cones situated on the margin of RPE cells in the image and may be narrowed somewhat compared to the cone profile from the reflectance image due to the topography of the cones, since at this eccentricity there are 2 or 3 cones across each RPE cell. Interestingly, the second peak in the radial average for the NIRAF image closely corresponds to the radius of the RPE cells, suggesting that many of the cones are centered on an RPE cell. This spatial arrangement would have the tendency to bring down the difference between the amplitude of the first and second peaks in the normalized radial average, which is what was observed. Control images generated by transposing the cone positions showed no cone structure in any of the images (Fig. 8k-n).

The superposed cone mosaic phenomenon is probably related to the waveguiding properties of cones. Cones could modulate the fluorescence signal in two ways, when considering the effects of waveguiding on both the ingoing excitation light and the outgoing fluorescence. As the excitation light is waveguided by the cones to the photopigment discs in the tips of the outer segments, photons that are not absorbed by photopigment will emerge from the tips of the outer segments and be absorbed or scattered by the melanin granules in the RPE. This funneling of light by the cones may cause relatively more fluorescence excitation to occur at those positions beneath the tips of the outer segments of cones than at positions between the outer segment tips, causing an imprint of the cones to be visible in the RPE mosaic. It is also possible that the autofluorescence could be waveguided back through the cones. Though waveguiding in the backward direction appears unlikely for SWAF from lipofuscin [37], and indeed no Yellott's ring at the spatial frequency of the photoreceptors appears in SWAF RPE images, it is possible that NIRAF could be more strongly coupled back into the cones and thus waveguided back out of the eye. It has been assumed that the light guided back out of the eye from the photoreceptors arises from scattering of light by melanin granules in the apical processes of the RPE cells close to the tips of the outer segments [38-40]. Thus, it would not be surprising if the light emerging from these granules from NIRAF might be coupled back into the cones in a similar way. We are pursuing future experiments that could provide further evidence to support this hypothesis.

A second possibility which was briefly explored in our study was the movement of the melanin pigment in light versus dark adapted conditions, which has previously been shown in amphibian [32], though not in mammals. If the pigment migrates from the base of the RPE cell cytoplasm into apical processes that surround cones on light stimulation, then the fluorescing structures might follow a cone pattern. We did not observe differences between light and dark adapted eyes within the limits of our capacity to provide effective dark adaptation and the limited number of subjects in this first exploratory study. This could benefit from more careful investigations in a future study.

Another possible explanation could be that there is an NIRAF signal coming from the cones themselves at 757 nm. NIRAF signal has up till now been presumed to be generated by

melanin, but there may be other fluorophores active at this excitation wavelength, in the RPE but also in other retinal layers including, for example, choroidal melanin or a weak lipofuscin contribution, though these would not be expected to have a cone appearance. This possibility cannot be ruled out at this point but it seems unlikely.

Finally, it is possible that light fluorescing from the RPE/choroid might be acting as an illumination source for imaging the cones in transmission. This could potentially provide a low angle illumination source somewhat analogous to what is seen when the retina is illuminated with an annular illumination in some forms of 'dark field' imaging. In fact, a superposed cone mosaic is often seen when the RPE is imaged using dark field techniques [17]. However, this phenomenon may not be distinct from the effects of cone waveguiding on the outgoing light, as cone waveguiding may modulate the light emerging from the RPE no matter the source.

#### *4.2 Imaging the RPE mosaic with NIRAF in diseased eyes*

We observed that a variety of conditions may alter the visualization of the RPE mosaic with NIRAF in AOSLO, either increasing or decreasing cell contrast or blurring the RPE mosaic altogether. In patient 1, which showed a very small drusen, the appearance of the RPE mosaic was locally disrupted but surrounding RPE cells appeared normal. This is similar to what was observed by Rossi et al. [22] and highlights the capability of NIRAF for revealing subtle abnormalities in the appearance of the RPE mosaic. These findings may suggest that drusen may develop in an otherwise normal RPE mosaic, or conversely that the presence of drusen may distort the view of the RPE beneath. In either case, a local disruption of the RPE mosaic appearance may be an early indicator of the development of a drusen, which may hence be considered as a biomarker of interest for investigations on retinal aging.

In patient 2 who had late-stage non-neovascular AMD, NIRAF structure could be detected over areas with severely damaged RPE as seen in the OCT and SLO views with higher contrast than by NIRAF in conventional SLO, however, no mosaic could be clearly evidenced. Instead, a diffuse hyper AF was present. This may be related to the superimposition of RPE cells [41]. However, a similar appearance was seen in peripheral zones in our oldest healthy subject (#4, fig 3 zoom at 10° temporal), so this may perhaps reflect an age-related aspect of fluorophore distribution [9] rather than an indication of retinal pathology. Future work is needed to better characterize and distinguish the changes that occur from normal aging from those that occur on the pathway to age related diseases such as AMD.

We failed to detect NIRAF signals corresponding to the hyporeflective clumps (HRCs) [42, 43], presumed to contain melanin, that are widely detected and highly visible in AMD patients and other retinal disease with flood-illumination fundus camera AO. Though image contrast was low in NIRAF, we did not observe HRCs co-localized with hyper-AF in the non-neovascular AMD patient we examined here using both imaging modalities (data not shown). However, it is possible that the HRCs include aggregates of material including both melanin and lipofuscin (i.e. melanolipofuscin) and that we may see heterogeneity in the fluorescence spectra of such aggregates. Future studies should be directed to more carefully investigate this in a systematic manner. In patient 3, the absence of outer segments in the fovea was likely the cause of the improved visibility of the RPE mosaic. This may provide additional evidence supporting the contention that NIRAF is modulated by the overlying cones, however, it cannot be excluded that changes within RPE cells secondary to the absence of outer segments caused the increased NIRAF signal.

## **5. Conclusions**

This small-scale pilot study demonstrates the feasibility for shifting the spectrum for NIRAF to shorter wavelength bands. It is likely that due to the overlapping spectra of lipofuscin and melanin that the RPE is broadly excitable across the visible and NIR and future efforts should

be made to continue to optimize the spectra for cellular level imaging of the RPE. Considering the NIRAF reduction we observed, similar to previous reports [29], future studies are needed to better understand this phenomenon. NIRAF in AOSLO can help to elucidate the cellular level origin of RPE alterations. As new therapies for diseases affecting the RPE, such as AMD, look towards repairing or replacing RPE cells, NIRAF in AOSLO offers promise for evaluating the efficacy of such treatments at the level of single cells.

### **Funding**

This work was supported by a European Research Council SYNERGY Grant scheme (HELMHOLTZ, ERC Grant Agreement # 610110), a grant from the Edward N. & Della L. Thome Memorial Foundation to José Alain Sahel and by departmental startup funds from the University of Pittsburgh to Ethan A. Rossi. This work was also supported by NIH CORE Grant P30 EY08098 to the University of Pittsburgh Department of Ophthalmology, the Eye and Ear Foundation of Pittsburgh, and from an unrestricted grant from Research to Prevent Blindness, New York, N.Y., USA.

### **Acknowledgements**

We would like to thank orthoptist Céline Chaumette, ophthalmologist Chiara Eandi MD and intern Natalie Norberg at the Quinze Vingts National Ophthalmology Hospital, Paris, France, for their assistance with medical exams and patient imaging. We would also like to thank Charles E. Granger of the University of Rochester, for helpful comments and discussions, intern Ahmer Shaikh at the University of Pittsburgh, for his assistance with image analysis, and Qiang Yang and David R. Williams for sharing their image registration software with us, under license from the University of Rochester.

### **Disclosures**

RDF: PSI(E). All other authors declare that there are no conflicts of interest related to this work.

### 11.3 Comparing two complementary imaging techniques of retinal pigment epithelium

The RPE usually shows a low contrast in most *in-vivo* en-face imaging techniques that have achieved its visualization. Additionally, even when imaged, its signal is often mixed with other structures. One example is the previously described autofluorescence technique where overlaid to the RPE mosaic was another mosaic strongly resembling the photoreceptors. Another example is the images acquired with AO-FIO dark-field imaging. Indeed, although the characteristics of the large cell mosaic lead us to think that we are observing RPE, an uncertainty lies on the result as only one test was achieved on one subject. For these reasons, being able to visualize this retinal structure with various modalities can help remove some uncertainties about the origin of the signal, if it is the RPE that we are imaging, or simply double the information about its structure and optical properties.

In the previous sections of this Chapter we have shown two imaging techniques at our disposal used to visualize the RPE cells to a level allowing the extraction of clinical biomarkers such as density. However, after the exploitation of images from both modalities we have noticed the difference in aspect. In this section we adopt the interpretation that this mosaic in our dark-field images are RPE cells and pursue the analysis by comparing them the autofluorescence images.

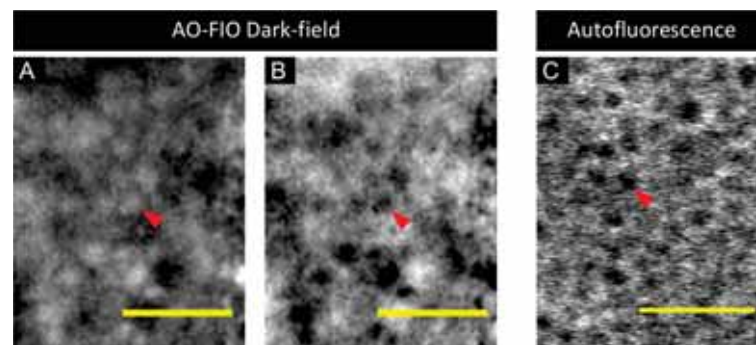


FIGURE 11.2: Images of a cropped area generated from RPE average images obtained with (A,B) AO-FIO dark-field imaging and (C) NIR autofluorescence using AO-SLO. (A) shows a few cells from the retinal pigment mosaic of the average image in Fig.11.1 and (B) corresponds to image (A) inverted brightness. (C) corresponds to a few cells of a mosaic from the average image of subject #4 at the Fovea shown in Fig.2 from the article presented in Sect. 11.2. Scale bars are  $50\mu\text{m}$ .

The first observation we have made when comparing RPE cells from dark-field (Fig. 11.2(A)) and autofluorescence (Fig. 11.2(B)) images is the inversion in brightness that seems to exist between the cells in the average images from each modality. The cells display a more standard structure in autofluorescence images, with a dark nucleus surrounded by a bright body. On the contrary, retinal pigment cells in dark-field imaging with our system are bright at their center, or nucleus, which is surrounded by a dark body. In order to assess if the contrast was really inverted we have computed the inverse of the dark-field image Fig. 11.2(A) and presented side by side in (B). This inverted image shows cells with shapes and contrast that look more like we were expecting from results obtained in previous studies as well as like the autofluorescence image (C), meaning the nucleus of the cells appears dark while the surrounding body is bright. The size of those nuclei seems to be about the same for both modalities. Density and spacing for both modalities are

presented in Tab. 11.2 here below. Dimensions computed with both modalities fall in the ranges characteristic for the RPE cells [119]. The small difference between the dimensions from the two modalities can be explained by a difference between the eccentricities where each image was taken or the age of subjects. Indeed, the closer to the center of the fovea, the higher the density of the RPE and in older subject the cells seem to be larger for the same regions[119].

	<b>Dark-field image</b>	<b>Autofluorescence image</b>
<b>Density (cells/mm<sup>2</sup>)</b>	4500	6250
<b>Cell spacing (<math>\mu\text{m}</math>)</b>	14.5	13

TABLE 11.2: Table showing the computed density of the RPE mosaic in dark-field and autofluorescence images.

These results have been carried out on two different subjects at different eccentricities. The aim was to show that we obtain mosaics looking alike and that in both techniques biomarkers evaluating spacing and density could be compared as well as the aspect of the cells. The next step is to acquire images with both technique in the same conditions, subject and eccentricity.

## 11.4 Conclusion: Towards functional imaging

In this Chapter we have only addressed a structural imaging of the RPE unlike previous Chs. 9 and 10 which have explored the prospective functional imaging for neurons and vessels. The RPE, contrary to photoreceptors and vessels, are more difficult to visualize. Therefore the first step before achieving functional analysis, which often implies the quantification of variations of the structure, is to achieve structural imaging. The images acquired with the AO-FIO using dark-field imaging on a healthy subject led to a mosaic whose characteristics suggest we might be imaging RPE. Even with a relatively low contrast, we have been able to characterize the mosaic by the computation of structural biomarkers such as spacing or density implying that our system can be used as a clinical tool to evaluate the good condition of the structure. A complementary imaging system for the RPE has been developed in the same hospital allowing the comparison between the two modalities and enabling a prospective mutual validation of the results.

Future work must be oriented to improve AO-FIO dark-field contrast by increasing its signal to noise ratio and explore the potential functional imaging of the instrument. Similarly, function imaging of the RPE can be contemplated with the NIR autofluorescence using AO-SLO. Indeed, further investigation on the link between melanin characteristics, like for instance its distribution, and the RPE functions should be carried out in order to explore potential functional biomarkers.



# Conclusion and Perspectives

## Conclusion

Visualizing the functions of retinal structures in addition to their morphology would lead to a better understanding of the physiological mechanisms carried out by retinal cells as well as helping obtain an earlier diagnosis. This functional analysis implies the extraction of functional biomarkers, which can only be achieved by imaging systems with cellular resolution *in-vivo*. Some research teams have addressed this challenge using Adaptive Optics Scanning Laser Ophthalmoscopy (AO-SLO) because of its outstanding resolution and contrast. However the performance of this system is limited by distortion and pixel rate leading to an uncertainty in the physiological topometry and restricted temporal resolution.

My thesis focused on the development of imaging modalities inspired from the microscopy field on an Adaptive Optics Flood Illumination Ophthalmoscope (AO-FIO) set-up improving the image quality, and particularly the contrast, of retinal images. The AO-FIO is a wide field system capable of high speed acquisitions and free from distortion, which combined with the enhancement of contrast provided by these implementations can achieve functional imaging of the retina.

As a first step I have contributed to the optimization of an AO-FIO by improving its robustness, ergonomics and image pre-processing. Then through the exploitation of the optimized system I derived two illumination geometries leading to the translation of microscopy-inspired modalities such as oblique back-illumination and structured illumination microscopy.

In a second phase, using these two illumination modulations I have implemented three imaging modalities which have improved the retinal image quality obtained with our AO-FIO. First, I have developed dark-field imaging in the AO-FIO system which led to the enhancement in contrast of hyporeflective structures previously invisible. In particular, I achieved the first visualization of, what appears to be, retinal pigment epithelium in AO-FIO on a healthy subject. Second, I implemented an instrument achieving pseudo-confocality in a wide field configuration, which benefits from the enhancement in contrast and optical sectioning due to the filtering of out of focus light comparable to the one obtained with the confocal pinhole but without the limitations of the scanning raster. Finally, the modulation of the illumination at the pupil plane led me to the development of an instrument allowing the variation of the illumination beam incidence and its use for two different applications, differential phase imaging and measurement of photoreceptor orientation, each requiring the implementation of specific image processing.

Then, I demonstrated the clinical applications of the implemented instruments by extracting structural biomarkers from various retinal structures, such as density in the case of neurons or wall to lumen ratio in the case of the vascular network, as well as functional biomarkers. Indeed, I proved that in addition to deriving the photoreceptors orientation,

perfusion could also be evaluated thanks to our modified AO-FIO. To achieve such functional analysis I contributed in the development and optimization of a specific image processing that led to the generation of perfusion maps as well as the measurement of capillaries speed, and therefore the characterization of the blood flow or perfusion function.

Finally, I participated in a study developing near infrared autofluorescence imaging of the retinal pigment epithelium at a new wavelength (757nm) with AO-SLO whose images I compared the pigment epithelium mosaic obtained with the dark-field imaging in our AO-FIO system. I showed complementary imaging techniques and thus the benefit of making new imaging techniques available to the ophthalmologic community.

## Perspectives

The results obtained during the three years of this work encourage us to further develop and exploit the modified AO-FIO system. In particular, the proof of concept of the three microscopy inspired modalities leading to dark-field, pseudo-confocal and phase imaging as well as the retinal goniometer incite us to continue optimizing these instruments in order to provide clinically useful imaging techniques. First, the acquisition of a more powerful light source as well as a new camera would lead to an increase in signal to noise ratio improving the image contrast for all modalities and to higher temporal resolution enabling the detection of faster physiological variations respectively. Second, the modalities ensuing from the modulation at a focal plane suffer from the technological restrictions, the high frequency noise as well as the diffraction effect of the spatial light modulator used to manipulate the illumination, and therefore future work should be oriented towards improving the set-up in order to obtain both dark-field and pseudo-confocal imaging in the whole AO-FIO field of view and in real-time imaging.

The retinal goniometer which with specific image processing could also be used to achieve phase imaging requires for both applications a pupil stabilization which would allow an accurate control of the illumination pupil position and thus of its angle of incidence. With this optimization of the instrument, the computation of the photoreceptors orientation could be achieved by developing the algorithm extracting the maximum intensity per photoreceptor from all the images obtain with various illumination incidences. Similarly, only a few tests have been done on a human retina in vivo for phase imaging. Further investigation of the angle and the appropriate image processing to obtain the best contrast should be conducted.

Finally, the last part of this thesis tackled the clinical applications that these implementations have given access to on the AO-FIO system, particularly showing the developed tools enabling functional imaging of photoreceptors orientation and retinal perfusion. This functional analysis opens new perspectives such as the study of neuro-vascular coupling. Since our imaging wavelength is in the near-infrared we can combine it with a visible stimulus and detect the vascular reaction and characterize the blood flow thanks to the previously described implementations.

## Appendix A

# Ocular safety for the Paris AO-FIO system

We determined the maximum power allowed by the European ocular safety norms (Norm ISO 15004-2 (2007)) to be used on the PARIS AOFIO.

### A.1 Context:

The light sources used in the PARIS AO-FIO are:

- Wavefront source WFS (point source of SuperLuminescent diode (SLED) type created by OMICRON centered at 750 nm and with a full width at half maximum of 20 nm)
- Imaging source IMA (large source of SLED type created by OMICRON centered at 860 nm and with a full width at half maximum of 20 nm with a field of view of 2° at the retina.)

The size of the illumination beams at the cornea is given by the size of a circular diaphragm placed at a pupil plane. We consider here a circular illumination beam on the cornea with an external diameter of  $\phi_{ext}=4.5\text{mm}$  and with an internal diameter of  $\phi_{int}=3\text{mm}$ . We consider the eye to have a focal length of  $f_{oeil}=20\text{mm}$ .

### A.2 ISO 15004-2 norm (2007):

The ISO 15004-2 norm establish the illumination limits for ophthalmic instruments. The norm divides the instruments into two categories: Group 1 and Group 2. The instruments of Group 1 do not represent "any danger linked to the radiation" while instruments from Group 2 represent "a potential danger linked to radiation". Given the wavelengths used in the PARIS AO-FIO as well as the beam sizes (defined by the circular diaphragm), the maximum illumination (maximum exposure allowed or MEA) can be given by the maximum exposure allowed at the eye lens or at the retina. In general the retina limits because of the thermal danger. According to the ISO 15004-2 (2007) document, the limit of the MEA is fixed and the illumination used in the PARIS AO-FIO must not exceed this limit:

$$\int_{380}^{1400} E(\lambda)R(\lambda)d\lambda \leq MEA$$

with  $E(\lambda)$  and  $R(\lambda)$  the spectral irradiance and the thermal danger weight factor. We consider our sources to be monochromatic, therefore:

$$E(\lambda)R(\lambda)d\lambda = E_{source}R(\lambda) \leq MEA$$

and therefore:

$$E_{source} \leq \frac{MEA}{R(\lambda)}$$

For WFS and IMA sources we have respectively  $R(\lambda_{WFS})=0.83$  and  $R(\lambda_{IMA})=0.52$ . The maximum power allowed for each source is computed separately:

We name  $E_x^{lim}$  the maximum irradiance in a given medium  $x$  (with  $x=cc$  at the eye lens and cornea and  $x=ret$  at the retina) and  $E_x$  the irradiance we send. We are looking for  $E_x \leq E_x^{lim}$ .

Yet,  $E_x=P_x/S_x$ ,  $P_x$  and  $S_x$  being the power we send in the medium  $x$  and the surface of the beam reaching the medium  $x$ , respectively. Therefore we have  $P_x \leq E_x^{lim} S_x$ , which leads to  $P_{MAX}=E_x^{lim} S_x$ .

We summarize in the following table the numerical application of the maximum surfaces and powers. We added the maximum irradiance allowed at the cornea and eye lens plane and the retina plane, for both illumination sources considered separately and depending on the group. The abbreviations Gr1 and Gr2 correspond to Group 1 and Group 2 respectively.

Medium	Surface	Exposure time limit		Maximum irradiance		Maximum power allowed		
		Gr1	Gr2	Gr1	Gr2	Gr1	Gr2	
Cornea	$S_{cc}= 8.83 \times 10^{-2} \text{ cm}^2$	$t_{exp} \leq 2h$	-	20mW/ $\text{cm}^2$	100mW/ $\text{cm}^2$	1760 $\mu$ W	8830 $\mu$ W	
Eye lens								
Retina	WFS source	$S_{ret}^{WFS}= 7.07 \times 10^{-6} \text{ cm}^2$	$t_{exp} \leq 2h$	$\delta_{ret}^{WFS} \leq 30\mu\text{m}$ et $t_{exp} \leq 2h$	0.84W/ $\text{cm}^2$	$t_{exp} \leq 2h$	6 $\mu$ W	341 $\mu$ W
	IMA source	$S_{ret}^{WFS}= 6.23 \times 10^{-3} \text{ cm}^2$	$t_{exp} \leq 2h$	$\alpha' \geq 2^\circ$ et $t_{exp} \leq 2h$	1.34W/ $\text{cm}^2$	2.7W/ $\text{cm}^2$	8340 $\mu$ W	16800 $\mu$ W

FIGURE A.1: Table with the numerical applications of the maximum values for power, irradiance and surfaces.

Our aim is to verify the ocular safety norms for Group 1. According to the ISO norms, in the case of two illumination sources, the maximum power is defined by: At the cornea plane:  $\frac{p^{WFS}}{1760\mu W} + \frac{p^{IMA}}{1760\mu W} \leq 1 \implies p^{IMA} \leq 1760\mu W - p^{WFS}$

At the retina plane:  $\frac{p^{WFS}}{6\mu W} + \frac{p^{IMA}}{8340\mu W} \leq 1 \implies p^{IMA} \leq 8340\mu W - 1390p^{WFS}$

The maximum power allowed to be sent in the PARIS AO-FIO given these two criteria are:

$$p^{WFS} \leq 4.75\mu W$$

$$p^{IMA} \leq 1750\mu W$$

# Bibliography

- [1] Caleb E Finch and David M Cohen. “Aging, metabolism, and Alzheimer disease: review and hypotheses”. In: *Experimental neurology* 143.1 (1997), pp. 82–102.
- [2] Tien Yin Wong et al. “Retinal microvascular abnormalities and their relationship with hypertension, cardiovascular disease, and mortality”. In: *Survey of ophthalmology* 46.1 (2001), pp. 59–80.
- [3] Yan Lu et al. “Retinal nerve fiber layer structure abnormalities in early Alzheimer’s disease: evidence in optical coherence tomography”. In: *Neuroscience letters* 480.1 (2010), pp. 69–72.
- [4] David R Hinton et al. “Optic-nerve degeneration in Alzheimer’s disease”. In: *New England Journal of Medicine* 315.8 (1986), pp. 485–487.
- [5] Edouard Koch et al. “Morphometric analysis of small arteries in the human retina using adaptive optics imaging: relationship with blood pressure and focal vascular changes”. In: *Journal of hypertension* 32.4 (2014), p. 890.
- [6] Sunil Ganekal. “Retinal functional imager (RFI): non-invasive functional imaging of the retina”. In: *Nepalese Journal of Ophthalmology* 5.2 (2013), pp. 250–257.
- [7] Junzhong Liang, David R Williams, and Donald T Miller. “Supernormal vision and high-resolution retinal imaging through adaptive optics”. In: *JOSA A* 14.11 (1997), pp. 2884–2892.
- [8] Austin Roorda et al. “Adaptive optics scanning laser ophthalmoscopy”. In: *Optics express* 10.9 (2002), pp. 405–412.
- [9] Toco YP Chui, Dean A VanNasdale, and Stephen A Burns. “The use of forward scatter to improve retinal vascular imaging with an adaptive optics scanning laser ophthalmoscope”. In: *Biomedical optics express* 3.10 (2012), pp. 2537–2549.
- [10] Toco YP Chui, Thomas J Gast, and Stephen A Burns. “Imaging of vascular wall fine structure in the human retina using adaptive optics scanning laser ophthalmoscopy”. In: *Investigative ophthalmology & visual science* 54.10 (2013), pp. 7115–7124.
- [11] Yusufu N Sulai et al. “Visualization of retinal vascular structure and perfusion with a nonconfocal adaptive optics scanning light ophthalmoscope”. In: *JOSA A* 31.3 (2014), pp. 569–579.
- [12] Drew Scoles, Yusufu N Sulai, and Alfredo Dubra. “In vivo dark-field imaging of the retinal pigment epithelium cell mosaic”. In: *Biomedical optics express* 4.9 (2013), pp. 1710–1723.
- [13] David Cunefare et al. “Automatic detection of cone photoreceptors in split detector adaptive optics scanning light ophthalmoscope images”. In: *Biomedical optics express* 7.5 (2016), pp. 2036–2050.
- [14] Drew Scoles et al. “In vivo imaging of human cone photoreceptor inner segments”. In: *Investigative ophthalmology & visual science* 55.7 (2014), pp. 4244–4251.

- [15] Ethan A Rossi et al. "Imaging individual neurons in the retinal ganglion cell layer of the living eye". In: *Proceedings of the National Academy of Sciences* 114.3 (2017), pp. 586–591.
- [16] Kate Grieve and Austin Roorda. "Intrinsic signals from human cone photoreceptors". In: *Investigative ophthalmology & visual science* 49.2 (2008), pp. 713–719.
- [17] Zhangyi Zhong et al. "In vivo measurement of erythrocyte velocity and retinal blood flow using adaptive optics scanning laser ophthalmoscopy". In: *Optics express* 16.17 (2008), pp. 12746–12756.
- [18] David Huang et al. "Optical coherence tomography". In: *Science* 254.5035 (1991), pp. 1178–1181.
- [19] Robert J Zawadzki et al. "Adaptive-optics optical coherence tomography for high-resolution and high-speed 3D retinal in vivo imaging". In: *Optics express* 13.21 (2005), pp. 8532–8546.
- [20] VJ Srinivasan et al. "In vivo functional imaging of intrinsic scattering changes in the human retina with high-speed ultrahigh resolution OCT". In: *Optics express* 17.5 (2009), pp. 3861–3877.
- [21] Siavash Yazdanfar, Andrew M Rollins, and Joseph A Izatt. "In vivo imaging of human retinal flow dynamics by color Doppler optical coherence tomography". In: *Archives of ophthalmology* 121.2 (2003), pp. 235–239.
- [22] Lin An and Ruikang K Wang. "In vivo volumetric imaging of vascular perfusion within human retina and choroids with optical micro-angiography". In: *Optics Express* 16.15 (2008), pp. 11438–11452.
- [23] Steven A Agemy et al. "Retinal vascular perfusion density mapping using optical coherence tomography angiography in normals and diabetic retinopathy patients". In: *Retina* 35.11 (2015), pp. 2353–2363.
- [24] Zhuolin Liu et al. "Imaging and quantifying ganglion cells and other transparent neurons in the living human retina". In: *Proceedings of the National Academy of Sciences* (2017), p. 201711734.
- [25] Kazuhiro Kurokawa et al. "method to investigate temporal dynamics of ganglion and other retinal cells in the living human eye". In: *Ophthalmic Technologies XXVIII*. Vol. 10474. International Society for Optics and Photonics. 2018, 104740W.
- [26] Scott B Stevenson, Austin Roorda, et al. "Correcting for miniature eye movements in high resolution scanning laser ophthalmoscopy". In: *Proc. SPIE*. Vol. 5688. 2005, pp. 145–151.
- [27] Alexander E Salmon et al. "An automated reference frame selection (ARFS) algorithm for cone imaging with adaptive optics scanning light ophthalmoscopy". In: *Translational vision science & technology* 6.2 (2017), pp. 9–9.
- [28] Adrian Podoleanu et al. "Correction of distortions in optical coherence tomography imaging of the eye". In: *Physics in Medicine & Biology* 49.7 (2004), p. 1277.
- [29] Jing Lu et al. "Adaptive optics parallel near-confocal scanning ophthalmoscopy". In: *Optics letters* 41.16 (2016), pp. 3852–3855.
- [30] Jungtae Rha et al. "Adaptive optics flood-illumination camera for high speed retinal imaging". In: *Optics express* 14.10 (2006), pp. 4552–4569.
- [31] Michel Paques et al. "Adaptive optics ophthalmoscopy: Application to age-related macular degeneration and vascular diseases". In: *Progress in retinal and eye research* (2018).

- [32] Igor Kozak. "Retinal imaging using adaptive optics technology". In: *Saudi Journal of Ophthalmology* 28.2 (2014), pp. 117–122.
- [33] David A Atchison, George Smith, and George Smith. "Optics of the human eye". In: (2000).
- [34] Pablo Artal. "Optics of the eye and its impact in vision: a tutorial". In: *Advances in Optics and Photonics* 6.3 (2014), pp. 340–367.
- [35] Susana Martinez-Conde, Stephen L Macknik, and David H Hubel. "The role of fixational eye movements in visual perception". In: *Nature Reviews Neuroscience* 5.3 (2004), p. 229.
- [36] M Millodot. *Dictionary of optometry and visual science (5: e appl.)*. s 107. 2000.
- [37] A Roorda et al. "What can adaptive optics do for a scanning laser ophthalmoscope?" In: *BULLETIN-SOCIETE BELGE D OPHTALMOLOGIE* 302 (2006), p. 231.
- [38] Jessica Jarosz. "Vers la conception d'un système d'optique adaptative pour la photocoagulation laser de la rétine". 2015PA066649. PhD thesis. 2015. URL: <http://www.theses.fr/2015PA066649/document>.
- [39] Pedro Mecê et al. "Fixational eye movement: a negligible source of dynamic aberration". In: *Biomedical optics express* 9.2 (2018), pp. 717–727.
- [40] David A Atchison and George Smith. "Chromatic dispersions of the ocular media of human eyes". In: *JOSA A* 22.1 (2005), pp. 29–37.
- [41] Larry N Thibos et al. "The chromatic eye: a new reduced-eye model of ocular chromatic aberration in humans". In: *Applied optics* 31.19 (1992), pp. 3594–3600.
- [42] Susana Marcos et al. "A new approach to the study of ocular chromatic aberrations". In: *Vision Research* 39.26 (1999), pp. 4309–4323.
- [43] Chi-Hsiu Liu et al. "Animal models of ocular angiogenesis: from development to pathologies". In: *The FASEB Journal* 31.11 (2017), pp. 4665–4681.
- [44] Jean-Pierre Barral and Alain Croibier. *Manual therapy for the cranial nerves*. Churchill Livingstone, 2008.
- [45] Ronald L Radius and Douglas R Anderson. "The course of axons through the retina and optic nerve head". In: *Archives of Ophthalmology* 97.6 (1979), pp. 1154–1158.
- [46] Brian A Wandell. *Foundations of vision*. Vol. 8. Sinauer Associates Sunderland, MA, 1995.
- [47] Jim Schwiegerling. "Field guide to visual and ophthalmic optics". In: Spie. 2004.
- [48] Olaf Strauss. "The retinal pigment epithelium in visual function". In: *Physiological reviews* 85.3 (2005), pp. 845–881.
- [49] P Henkind, RI Hansen, J Szalay, et al. "Ocular circulation". In: *Physiology of the human eye and visual system* (1979), pp. 98–155.
- [50] JP Campbell et al. "Detailed vascular anatomy of the human retina by projection-resolved optical coherence tomography angiography". In: *Scientific reports* 7 (2017), p. 42201.
- [51] Stéphane Fouquet et al. "The 3D Retinal Capillary Circulation in Pigs Reveals a Predominant Serial Organization". In: *Investigative ophthalmology & visual science* 58.13 (2017), pp. 5754–5763.
- [52] Joshua K McBee et al. "Confronting complexity: the interlink of phototransduction and retinoid metabolism in the vertebrate retina". In: *Progress in retinal and eye research* 20.4 (2001), pp. 469–529.

- [53] Brian M Kevany and Krzysztof Palczewski. "Phagocytosis of retinal rod and cone photoreceptors". In: *Physiology* 25.1 (2010), pp. 8–15.
- [54] Clément Viard et al. "Imaging microscopic structures in pathological retinas using a flood-illumination adaptive optics retinal camera". In: *Ophthalmic Technologies XXI*. Vol. 7885. International Society for Optics and Photonics. 2011, p. 788509.
- [55] Robert H Webb and George W Hughes. "Scanning laser ophthalmoscope". In: *IEEE Transactions on Biomedical Engineering* 7 (1981), pp. 488–492.
- [56] Minsky Marvin. *Microscopy apparatus*. US Patent 3,013,467. Dec. 1961.
- [57] Robert H Webb, George W Hughes, and Francois C Delori. "Confocal scanning laser ophthalmoscope". In: *Applied optics* 26.8 (1987), pp. 1492–1499.
- [58] Daniel X Hammer et al. "Hand-held digital line-scanning laser ophthalmoscope (LSLO)". In: *Ophthalmic Technologies XIV*. Vol. 5314. International Society for Optics and Photonics. 2004, pp. 161–170.
- [59] Daniel X Hammer et al. "Line-scanning laser ophthalmoscope". In: *Journal of biomedical optics* 11.4 (2006), p. 041126.
- [60] Matthew S Muller, Ann E Elsner, and Dean A Van Nasdale. "Low-cost Confocal Retinal Imaging with a Digital Light Projector Source". In: *Investigative Ophthalmology & Visual Science* 53.14 (2012), pp. 3099–3099.
- [61] Matthew S Muller et al. "Non-mydratic confocal retinal imaging using a digital light projector". In: *Emerging Digital Micromirror Device Based Systems and Applications VII*. Vol. 9376. International Society for Optics and Photonics. 2015, 93760E.
- [62] Kari V Vienola et al. "Parallel line scanning ophthalmoscope for retinal imaging". In: *Optics letters* 40.22 (2015), pp. 5335–5338.
- [63] DT Miller et al. "Adaptive optics and the eye (super resolution OCT)". In: *Eye* 25.3 (2011), p. 321.
- [64] Ravi S Jonnal et al. "Phase-sensitive imaging of the outer retina using optical coherence tomography and adaptive optics". In: *Biomedical optics express* 3.1 (2012), pp. 104–124.
- [65] Kyle Strimbu and Jorge A Tavel. "What are biomarkers?" In: *Current Opinion in HIV and AIDS* 5.6 (2010), p. 463.
- [66] Angelina Duan et al. "Reactivity in the human retinal microvasculature measured during acute gas breathing provocations". In: *Scientific reports* 7.1 (2017), p. 2113.
- [67] Phillip Bedggood and Andrew Metha. "Direct visualization and characterization of erythrocyte flow in human retinal capillaries". In: *Biomedical optics express* 3.12 (2012), pp. 3264–3277.
- [68] Darin A Nelson et al. "Special report: noninvasive multi-parameter functional optical imaging of the eye". In: *Ophthalmic Surgery, Lasers & Imaging Retina* 36.1 (2005), p. 57.
- [69] Peter J DeLint et al. "Slow optical changes in human photoreceptors induced by light". In: *Investigative ophthalmology & visual science* 41.1 (2000), pp. 282–289.
- [70] K Bizheva et al. "Optophysiology: depth-resolved probing of retinal physiology with functional ultrahigh-resolution optical coherence tomography". In: *Proceedings of the national academy of sciences* 103.13 (2006), pp. 5066–5071.
- [71] VJ Srinivasan et al. "In vivo measurement of retinal physiology with high-speed ultrahigh-resolution optical coherence tomography". In: *Optics letters* 31.15 (2006), pp. 2308–2310.

- [72] SB Stevenson, CK Sheehy, and A Roorda. “Binocular eye tracking with the tracking scanning laser ophthalmoscope”. In: *Vision research* 118 (2016), pp. 98–104.
- [73] Phillip Bedggood and Andrew Metha. “De-warping of images and improved eye tracking for the scanning laser ophthalmoscope”. In: *PloS one* 12.4 (2017), e0174617.
- [74] Bruno Emica. “Caractérisation des perturbations oculaires pour l’optimisation d’un système d’optique adaptative”. 2012PA066709. PhD thesis. 2012, 1 vol. (234 p.) URL: <http://www.theses.fr/2012PA066709>.
- [75] Mats GL Gustafsson. “Surpassing the lateral resolution limit by a factor of two using structured illumination microscopy”. In: *Journal of microscopy* 198.2 (2000), pp. 82–87.
- [76] Douglas B Murphy. *Fundamentals of light microscopy and electronic imaging*. John Wiley & Sons, 2002.
- [77] Lei Tian and Laura Waller. “Quantitative differential phase contrast imaging in an LED array microscope”. In: *Optics express* 23.9 (2015), pp. 11394–11403.
- [78] Tim N Ford, Kengyeh K Chu, and Jerome Mertz. “Phase-gradient microscopy in thick tissue with oblique back-illumination”. In: *Nature Methods* 9.12 (2012), p. 1195.
- [79] DK Hamilton, CJR Sheppard, and T Wilson. “Improved imaging of phase gradients in scanning optical microscopy”. In: *Journal of microscopy* 135.3 (1984), pp. 275–286.
- [80] Norbert Streibl. “Three-dimensional imaging by a microscope”. In: *JOSA A* 2.2 (1985), pp. 121–127.
- [81] H Rose. “Nonstandard imaging methods in electron microscopy”. In: *Ultramicroscopy* 2.0 (1976), pp. 251–267.
- [82] Zachary F Phillips, Michael Chen, and Laura Waller. “Single-shot quantitative phase microscopy with color-multiplexed differential phase contrast (cDPC)”. In: *PloS one* 12.2 (2017), e0171228.
- [83] Yao Fan et al. “Wide-field anti-aliased quantitative differential phase contrast microscopy”. In: *Optics Express* 26.19 (2018), pp. 25129–25146.
- [84] Rene A Claus et al. “Quantitative phase retrieval with arbitrary pupil and illumination”. In: *Optics express* 23.20 (2015), pp. 26672–26682.
- [85] Shalin B Mehta and Colin JR Sheppard. “Quantitative phase-gradient imaging at high resolution with asymmetric illumination-based differential phase contrast”. In: *Optics letters* 34.13 (2009), pp. 1924–1926.
- [86] DK Hamilton and CJR Sheppard. “Differential phase contrast in scanning optical microscopy”. In: *Journal of microscopy* 133.1 (1984), pp. 27–39.
- [87] Timothé Laforest et al. “A new microscopy for imaging retinal cells”. In: *arXiv preprint arXiv:1712.08472* (2017).
- [88] Sapna A Shroff. “Structured illumination imaging”. PhD thesis. University of Rochester. Department of Electrical and Computer Engineering, 2010.
- [89] Mark AA Neil, Rimas Juškaitis, and Tony Wilson. “Method of obtaining optical sectioning by using structured light in a conventional microscope”. In: *Optics letters* 22.24 (1997), pp. 1905–1907.
- [90] Roberto Baena-Galle, Laurent M Mugnier, and François Orieux. “Optical sectioning with structured illumination microscopy for retinal imaging: inverse problem approach”. In: 26ème Colloque sur le Traitement du Signal et des Images. GRETSI, 2017.

- [91] Jerome Mertz. *Introduction to optical microscopy*. Vol. 138. Roberts, 2010.
- [92] Nripun Sredar, Oladipo E Fagbemi, and Alfredo Dubra. “Sub-Airy Confocal Adaptive Optics Scanning Ophthalmoscopy”. In: *Translational vision science & technology* 7.2 (2018), pp. 17–17.
- [93] Tony Wilson. “Resolution and optical sectioning in the confocal microscope”. In: *Journal of microscopy* 244.2 (2011), pp. 113–121.
- [94] Matthew Stefan Muller. *Confocal imaging device using spatially modulated illumination with electronic rolling shutter detection*. US Patent 8,237,835. Aug. 2012.
- [95] Serge Meimon et al. “Manipulation of the illumination geometry on Adaptive Optics (AO) Flood Illumination Ophthalmoscope (FIO) for Dark Field imaging of the Retina”. In: *Investigative Ophthalmology & Visual Science* 59.9 (2018), pp. 4641–4641.
- [96] Dino Carpentras et al. “Effect of backscattering in phase contrast imaging of the retina”. In: *Optics express* 26.6 (2018), pp. 6785–6795.
- [97] Krishnakumar Venkateswaran, Austin Roorda, and Fernando Romero-Borja. “Theoretical modeling and evaluation of the axial resolution of the adaptive optics scanning laser ophthalmoscope”. In: *Journal of biomedical optics* 9.1 (2004), pp. 132–139.
- [98] Ran Yi, Kengyeh K Chu, and Jerome Mertz. “Graded-field microscopy with white light”. In: *Optics express* 14.12 (2006), pp. 5191–5200.
- [99] JS Werner et al. “Outer retinal abnormalities associated with inner retinal pathology in nonglaucomatous and glaucomatous optic neuropathies”. In: *Eye* 25.3 (2011), p. 279.
- [100] Jessica I Wolfing et al. “High-resolution retinal imaging of cone–rod dystrophy”. In: *Ophthalmology* 113.6 (2006), pp. 1014–1019.
- [101] Kaccie Y Li and Austin Roorda. “Automated identification of cone photoreceptors in adaptive optics retinal images”. In: *JOSA A* 24.5 (2007), pp. 1358–1363.
- [102] Xu Liu, Yudong Zhang, and Dai Yun. “An automated algorithm for photoreceptors counting in adaptive optics retinal images”. In: *6th International Symposium on Advanced Optical Manufacturing and Testing Technologies: Optoelectronic Materials and Devices for Sensing, Imaging, and Solar Energy*. Vol. 8419. International Society for Optics and Photonics. 2012, 84191Z.
- [103] Bai Xue et al. “Photoreceptor counting and montaging of en-face retinal images from an adaptive optics fundus camera”. In: *JOSA A* 24.5 (2007), pp. 1364–1372.
- [104] Donald L Budenz et al. “Determinants of normal retinal nerve fiber layer thickness measured by Stratus OCT”. In: *Ophthalmology* 114.6 (2007), pp. 1046–1052.
- [105] Viviane Guedes et al. “Optical coherence tomography measurement of macular and nerve fiber layer thickness in normal and glaucomatous human eyes”. In: *Ophthalmology* 110.1 (2003), pp. 177–189.
- [106] Omer P Kocaoglu et al. “Imaging retinal nerve fiber bundles using optical coherence tomography with adaptive optics”. In: *Vision research* 51.16 (2011), pp. 1835–1844.
- [107] Katie M Litts et al. “Photoreceptor-based biomarkers in AOSLO retinal imaging”. In: *Investigative ophthalmology & visual science* 58.6 (2017), BIO255–BIO267.

- [108] Chahira Miloudi et al. "The negative cone mosaic: a new manifestation of the optical Stiles-Crawford effect in normal eyes". In: *Investigative ophthalmology & visual science* 56.12 (2015), pp. 7043–7050.
- [109] Toco YP Chui et al. "Foveal avascular zone and its relationship to foveal pit shape". In: *Optometry and Vision Science* 89.5 (2012), p. 602.
- [110] David Rosenbaum et al. "Effects of age, blood pressure and antihypertensive treatments on retinal arterioles remodeling assessed by adaptive optics". In: *Journal of hypertension* 34.6 (2016), pp. 1115–1122.
- [111] Michel Paques. "Adaptive Optics Imaging of the Retina and Vessels". In: *Teleophthalmology in Preventive Medicine*. Springer, 2015, pp. 73–79.
- [112] David Rosenbaum et al. "Relationships between retinal arteriole anatomy and aortic geometry and function and peripheral resistance in hypertensives". In: *Hypertension Research* 39.7 (2016), p. 536.
- [113] Zhuolin Liu, Omer P Kocaoglu, and Donald T Miller. "3D imaging of retinal pigment epithelial cells in the living human retina". In: *Investigative ophthalmology & visual science* 57.9 (2016), OCT533–OCT543.
- [114] Jessica IW Morgan et al. "Light-induced retinal changes observed with high-resolution autofluorescence imaging of the retinal pigment epithelium". In: *Investigative ophthalmology & visual science* 49.8 (2008), pp. 3715–3729.
- [115] Charles E Granger, David R Williams, and Ethan A Rossi. "Near-infrared autofluorescence imaging reveals the retinal pigment epithelial mosaic in the living human eye". In: *Investigative Ophthalmology & Visual Science* 58.8 (2017), pp. 3429–3429.
- [116] Tao Liu et al. "Noninvasive near infrared autofluorescence imaging of retinal pigment epithelial cells in the human retina using adaptive optics". In: *Biomedical optics express* 8.10 (2017), pp. 4348–4360.
- [117] Charles E Granger et al. "Human retinal pigment epithelium: in vivo cell morphology, multi-spectral autofluorescence, and relationship to cone mosaic". In: *Investigative Ophthalmology & Visual Science* (2018).
- [118] Jessica IW Morgan et al. "In vivo autofluorescence imaging of the human and macaque retinal pigment epithelial cell mosaic". In: *Investigative ophthalmology & visual science* 50.3 (2009), pp. 1350–1359.
- [119] Shagun K Bhatia et al. "Analysis of RPE morphometry in human eyes". In: *Molecular vision* 22 (2016), p. 898.





## **Manipulation of the illumination of an Adaptive Optics Flood Illumination Ophthalmoscope for functional imaging of the retina in-vivo**

As the only transparent optical window of our body, the eye gives a unique access to the observation of neural and vascular networks. Today however, a new era is opening up for high-resolution imaging, which should no longer be limited to giving access to tissue structures, but may also tackle their functions. In fact, biomarkers for the functioning of the whole human body can be found in retinal imaging. Neurodegenerative diseases (Parkinson's, Alzheimer's) or arterial hypertension could thus be diagnosed early by high precision imaging of the retina. Adaptive optics, applied to retinal imaging as early as 1997, significantly improved the spatial resolution of retinal images, leading to many retinal studies by ophthalmoscopy. In particular, it was coupled with the scanning ophthalmoscope, which became the most popular choice for its superior spatial resolution and in optical sectioning compared to full-field.

However, unlike scanning systems, the full-field ophthalmoscope produces wide-field images with a high rate of acquisition and without distortion. In my thesis work, I intended to show how such a system, associated to imaging modalities adjusting geometrical settings of the illumination, could contribute to research on the retina.

To achieve this ambitious goal, we modified the full-field ophthalmoscope built at the National Hospital of Quinze-Vingts with a specific image processing and two new instruments inspired by full-field microscopy. We have integrated these instruments into the illumination path of the ophthalmoscope to manipulate the geometry of the retinal illumination. These new implementations allow us to make use of more advanced imaging techniques, such as dark field imaging or noninvasive near infrared angiography.

These imaging modalities have been exploited to image the retina functionally. We focused mainly on the light coupling function of photoreceptors and on blood perfusion.

**Keywords :** BIOMEDICAL IMAGING ; ADAPTIVE OPTICS ; FUNCTIONAL IMAGING

## **Manipulation de la géométrie de l'illumination pour l'imagerie fonctionnelle de la rétine par ophtalmoscope plein champ**

L'œil étant la seule fenêtre optique transparente de notre corps, il donne un accès unique à l'observation de réseaux neuronaux et vasculaires. Mais aujourd'hui une nouvelle ère s'ouvre pour l'imagerie haute résolution, qui ne doit plus se contenter de donner accès aux structures des tissus, mais aussi d'en apprécier les fonctions. En effet, on peut trouver dans l'imagerie rétinienne des biomarqueurs du fonctionnement de l'ensemble du corps humain. Des maladies neurodégénératives (Parkinson, Alzheimer) ou l'hypertension artérielle pourraient être ainsi précocement diagnostiquées par une imagerie de haute précision de la rétine. L'optique adaptative, adaptée à l'imagerie rétinienne dès 1997, a amélioré nettement la résolution spatiale des images rétiniennes entraînant la multiplication des études de rétine par ophtalmoscope. Elle a notamment été couplée avec l'ophtalmoscope à balayage, qui devint le choix le plus populaire par sa supériorité en résolution spatiale et sectionnement optique par rapport au plein champ.

Cependant, contrairement aux systèmes à balayage, l'ophtalmoscope plein champ produit des images grand champ à forte cadence d'acquisition et sans distorsion. Dans mon travail de thèse, j'ai cherché à montrer qu'un tel système, associé à des modalités d'imagerie jouant sur la géométrie d'éclairage, pourrait apporter à la recherche sur la rétine.

Pour atteindre cet objectif ambitieux, nous avons modifié l'ophtalmoscope plein champ construit au Centre Hospitalier National des Quinze-Vingts avec un traitement d'image spécifique et deux nouveaux instruments inspirés de la microscopie plein champ. Nous avons intégré ces instruments dans le trajet d'illumination de l'ophtalmoscope afin de manipuler la géométrie de l'éclairage de la rétine. Ces nouvelles implémentations nous permettent de mettre en œuvre des techniques d'imagerie plus avancées, comme par exemple l'imagerie en champ sombre ou l'angiographie non invasive en proche infrarouge.

Ces modalités d'imagerie ont été exploitées pour imager la rétine de façon fonctionnelle. Nous nous sommes intéressés principalement à la fonction de couplage de lumière des photorécepteurs et à la perfusion sanguine.

**Mots clés :** IMAGERIE BIOMEDICALE ; OPTIQUE ADAPTATIVE ; IMAGERIE FONCTIONNELLE

